Inelastic Deformation in Metals and Contacts

Comprehensive Treatises on Yielding and Hardening, the Yield Phenomenon and Dissipation

van Dokkum, J.S.

DOI
10.4233/uuid:bd755894-1386-4490-9ba0-c53aef05fb3f

Publication date
2023

Document Version
Final published version

Citation (APA)
van Dokkum, J. S. (2023). *Inelastic Deformation in Metals and Contacts: Comprehensive Treatises on Yielding and Hardening, the Yield Phenomenon and Dissipation*. [Dissertation (TU Delft), Delft University of Technology]. https://doi.org/10.4233/uuid:bd755894-1386-4490-9ba0-c53aef05fb3f

Inelastic Deformation in Metals and Contacts

Comprehensive Treatises on Yielding and Hardening, the Yield Phenomenon and Dissipation

Inelastic Deformation in Metals and Contacts

Comprehensive Treatises on Yielding and Hardening, the Yield Phenomenon and Dissipation

Proefschrift

ter verkrijging van de graad van doctor
aan de Technische Universiteit Delft,
op gezag van de Rector Magnificus Prof. dr. ir. T.H.J.J. van der Hagen,
voorzitter van het College voor Promoties,
in het openbaar te verdedigen
op donderdag 26 oktober 2023 om 15:00 uur

door

Jan Steven VAN DOKKUM

Master of Science in Materials Science and Engineering,
Technische Universiteit Delft, Nederland,
geboren te Heerenveen, Nederland.

Dit proefschrift is goedgekeurd door de promotors.

Samenstelling promotiecommissie:

Rector Magnificus,	voorzitter
Prof. dr. ir. J. Sietsma,	Technische Universiteit Delft, promotor
Dr. ir. S. E. Offerman,	Technische Universiteit Delft, promotor
Dr. ir. C. Bos,	Technische Universiteit Delft
	Tata Steel Research & Development, co-promotor
Onafhankelijke leden:	
Prof. dr. ir. C. H. Venner,	Universiteit Twente
Prof. dr. ir. L. J. Sluys,	Technische Universiteit Delft
Prof. Dr.-Ing. R. Schwab,	Hochschule Karlsruhe – Technik und Wirtschaft
Prof. Dr.-Ing. W. Volk,	Technische Universität München
Reserve lid:	
Prof. dr. M. J. Santofimia Navarro,	Technische Universiteit Delft

This research was carried out under project number T17019n in the framework of the Research Program of the Materials innovation institute (M2i) (`www.m2i.nl`) supported by the Dutch government.

Keywords: Inelasticity; Anelasticity; Plasticity; Viscoelasticity; Yield; Yield Point Phenomenon; Hysteresis in Contacts; Quasi-Static Solution.

Printed by: Gildeprint

Cover: Rachel Refael

Style: TU Delft House Style, with modifications by Moritz Beller
`https://github.com/Inventitech/phd-thesis-template`

ISBN 978-94-6384-479-6

An electronic version of this dissertation is available at
`http://repository.tudelft.nl/`.

Contents

Summary

Inelastic deformation is a common but often neglected phenomenon in experimental analysis of metal deformation and in contacts. This neglect leads to degraded measurement accuracy of material properties. Therefore a need arises for material models that *a priori* incorporate inelasticity. These material models must be simple and comprehensive to have the highest impact in society. This thesis addresses three main sources of inelasticity, namely anelasticity and plasticity in metals and viscosity in contacts. Inelasticity is a dissipative mode of deformation that is mechanically recoverable for anelasticity and viscosity, and irrecoverable for plasticity. We connect the fundamental properties and structures of metallic and soft matter constituents with experimentally accessible measures. The presented models will aid in the development of materials with specific properties that meet the needs of industry.

Chapter 2 presents an analytical model of the tensile test tangent moduli and yield points for single-crystallite metals with spatially uniform and nonuniform dislocation distributions across slip systems. The moduli and the onset of plastic flow show a notable dependence on initial dislocation character, spatial dislocation distribution, and loading direction with respect to crystallographic orientations. An improved methodology accounts for elastic compressibility and anisotropy, and the geometric structure of crystal lattices when one measures dislocation network geometry in single metallic crystallites.

Chapter 3 contains a seamless, unified stress-strain treatment of dislocation-driven deformation. This treatment combines the three deformation mechanisms of elastic bond stretching, stable dislocation glide, and unstable dislocation glide. The model's yield criterion connects the bowing out of local dislocation links and global dislocation multiplication. A semi-empirical relation is constructed for the evolution of the dislocation network structure with uniaxial loading.

Chapter 4 formulates a macromechanical model of the yield point phenomenon under invariant plane conditions. The heterogeneous stress state across the Lüders front and the plastic flow inside the Lüders band are accounted for. The Lüders band orientation with respect to the tensile direction is not unique; the orientation changes with material properties and tensile specimen geometry by the stress concentration at the front. The model serves to approximate constitutive parameters independent of the test conditions.

Chapter 5 elucidates the interplay between adhesion and roughness by modelling the retraction of rigid, wavy indenters from viscoelastic substrates. Viscoelasticity governs adhesive hysteresis across all loading rates, and even in the presence of roughness-induced mechanical instabilities. This confirms the central role that viscoelasticity must play in experimental measurements in the presence of adhesive interfaces in soft matter contacts.

Chapter 6 examines the static, quasi-static, and dynamic trajectories of a base-excited mass-spring-damper system in the presence of friction. The differences between the dynamic and the quasi-static solution in engineering problems with viscous, static, and dry friction are assessed. The omission of inertial contributions will under-predict dissipation at both low

and high excitation frequencies. This chapter is a guide for future (multi-scale) numerical modelling efforts on adhesion and interface friction, and the hysteretic deformation of metals.

Chapter 7 is a general discussion on the impact of inelasticity in metals, that follows from Chapters 2 and 3, the measurement of the yield point phenomenon in Chapter 4, and numerical modelling of dissipative contacts in Chapters 5 and 6. The four models as presented in Chapters 2-6 are readily applicable in experimental measurements and future numerical models. The importance of accounting for inelasticity in experimental measurement and modelling of the yield strength in metals, and adhesive dissipation in soft matter contacts is emphasised. Finally, the state of the art in research on the three main sources of inelasticity and potential applications of the presented models are enumerated, which serve as starting points of future research.

1

General Introduction

1

Interpreting experiments in the presence of inelastic deformation with models that are based on elastic deformation leads to discrepancies between observations, prediction, and postdiction. Elasticity is a mechanically and thermodynamically recoverable mode of deformation while inelasticity is dissipative. This presents a challenge in understanding the underlying mechanisms of material behaviour. Essential to materials mechanical behaviour are the fundamental properties and structures of, and interactions among, their constituents. While adjusting the elastic magnitude and tuning responses one minimises the observed discrepancies. The outcome still depends on the particular choices made when introducing this arbitrariness. Hence the *a priori* incorporation of the physics-based origins of inelasticity in models remains necessary. Only then the fundamental properties and structures of, and the interaction among, constituents will be measurable, which aids in the development of specific material properties to meet the needs of industry.

Traditionally, inelastic deformation is ignored when appreciable hysteresis is absent. Common sources of this hysteresis are mechanically and/or thermodynamically irreversible deformation. However hysteresis is omnipresent, even at small external loads and/or loading rates. In this thesis, we argue that inelastic deformation must be accounted for. Moreover, inelastic deformation as emergent behaviour in any model in the presence of localisation, multistability, adhesion and friction is non-trivial. One consequence of the neglect of inelastic deformation is the inability to accurately measure mechanical and material properties.

Simplifications are necessary in materials models as they remain essential tools to interpret complex problems in Materials Science. Furthermore, the most industrial impact is made when one can use a given model with minimal effort. However, more comprehensive physics-based descriptions are needed to obtain material properties independent of test conditions and to predict mechanical behaviour by (numerical) calculations where model simplification proves inadequate. Our goal in this thesis is to provide insights into the underlying mechanisms of inelasticity and their influence on their globally observed mechanical behaviour. While materials models must remain simple, it is crucial that we address shortcomings in current modelling efforts.

Inelastic deformation has various sources that include anelasticity, plasticity, and viscosity. The difference between anelasticity and viscosity is that the latter is a time-delayed material response and the former is instantaneous in *e.g.* metals. Anelasticity and plasticity are typical for metals and crystalline solids, while viscosity is more common in rubbers, polymers, and biological tissue. We treat in this thesis two material types: metals, with an emphasis on steels under tension; and, soft matter in adhesive contact and their friction with rigid surfaces. Note that the term anelasticity is used interchangeably with viscoelasticity in Polymer Science. Metals and polymers together with ceramics are among the most widely used engineering materials. One's thorough understanding of their mechanical properties is thus crucial for societal advancement.

The treatises we present in this thesis share a common theme, that is the difference between the globally observed mechanical behaviour of materials and the local inelastic materials deformation. We emphasise the importance of comprehending the underlying mechanisms of inelastic deformation to accurately capture the mechanical behaviour of materials. We show that describing local inelastic deformation helps capture the yield point, and unifying anelastic and plastic mechanisms in steels describes their global flow; secondly, the yield point phenomenon (YPP) can only be understood by addressing the local plastic

flow in the associated localisation. Similarly, local viscous dissipation governs the globally observed adhesive hysteresis; and, finally, we address the need to consider the full complexity in modelling friction as well as inelastic deformation. The common denominator of this thesis is the goal of developing comprehensive models of inelastic materials mechanics, that will aid to develop materials with specific properties that meet the needs of industry.

1.1 Outline

This thesis consists of three topics that we treat across this introduction, and the six subsequent chapters. The six subsequent chapters are grouped into three parts that follow this introduction's structure, where: *Part I* treats physics-based models of pre-, at- and post-yield dislocation-mediated deformation. Chapter 2 presents the tensile test tangent moduli and yield points in single-crystal metals and Chapter 3 a unified inelastic model under static loading conditions; *Part II* covers the YPP, with in Chapter 4 a macromechanical model of the Lüders front; and, *Part III* is an overview of the state of the art in modelling of adhesive soft matter contacts, and base-excited systems in the presence of friction. Chapter 5 treats the interplay between surface roughness and viscoelasticity in adhesive hysteresis and in Chapter 6 the ignorance of inertia by multi-scale models is assessed by means of a mass-spring-damper system with a single degree of freedom. This thesis finishes with a *General Discussion* in Chapter 7 on the contents we present in Parts I, II and III.

1.2 Part I: Inelasticity in Metals

Metals typically undergo significant deformation before they fracture. The force per unit area necessary to continue deformation increases with the previously applied plastic strain, which is called strain hardening or work hardening. Hence hardening is commonly associated with plasticity. A lesser studied type of deformation is anelasticity, *i.e.* recoverable nonlinear mechanical behaviour, as observed by [1–7]. Anelastic deformation is an additional strain component on top of the elastic lattice strain during loading and unloading. Li and Wagoner [7] show that anelastic deformation is dissipative yet mechanically recoverable, while plastic deformation is both thermodynamically and mechanically irrecoverable. The physical interpretation of yield thus is the transition from mechanically recoverable to mechanically irrecoverable deformation. Both types of deformation are inelastic, which literally means non-elastic, where elastic is defined as the lattice strain.

Industrial Background and Relevance

It is well known that during plastic deformation dislocations are introduced into the metallic microstructure that hardens. The degree of hardening is not only essential for the mechanical behaviour of the material, but also for possible subsequent (phase) transformations, since the defect density has a direct contribution to the free energy of the microstructural phases and thus influences nucleation. Within the framework of the DENS (Digitally Enhanced New Steel Product Development) programme, the aim is to bring through-process modelling for new product development to a maturity level where it can significantly shorten the time to market for new steel alloying and processing concepts without compromising on steel production efficiency. The main challenge addressed in the DENS programme is to connect state of the art available sub-models in one through-process model framework that can be

1

applied in practice for new steel product development. This reduces the number of tests and extends the efficiency of the experimental process route. In building this through-process modelling chain, it will be possible to identify the gaps and weakest links which can then be filled or improved. Having an offline through-process model is not sufficient to successfully develop and produce new steel grades. Therefore, the second scientific challenge addressed in this programme is the development of simplified models that are suitable for online control. Part I treats these challenges on the inelastic deformation and hardening of metals. This is required as an essential input for dynamic and static recrystallisation, and for online control of the predicted flow stress for control over the rolling process.

Scientific Background

At temperatures below about one-third of the melting point of metals, dislocation glide is the dominant mechanism of inelastic deformation [8]. It is common knowledge that the mechanical deformation of metals is chiefly governed by the generation, glide and storage of dislocations [9]. It is widely accepted that under these conditions for single crystallites, the constitutive behaviour is entirely governed by the dynamics of dislocations. The key microstructural feature thus is the dislocation network [8, 10].

The structure of the dislocation network is complex, with a distribution of dislocation-link lengths [8, 11]. The network is a continuous structure that consists of dislocation links delimited by microstructural features like precipitates, solute atoms, grain boundaries, and junctions with adjacent dislocations within the same net [9, 12]. Those points of interaction, which include all microstructural defects that impede local dislocation motion, are commonly known as pinning points [9]. A schematic representation of a dislocation link bound by two forest dislocations is presented in Fig. 1.1a. The motion of a given dislocation link, which is

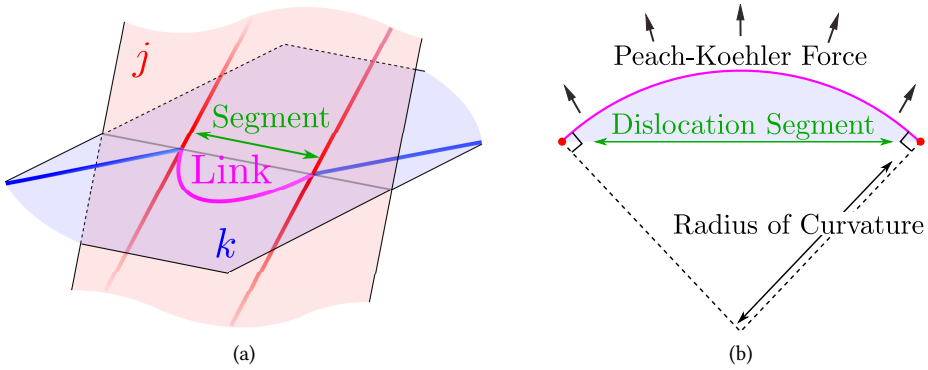

Figure 1.1: Schematic representation of (a) a dislocation link on slip system k pinned by two forest dislocations on slip system j, and (b) a Frank-Read source with an initially straight dislocation segment (Adapted from [13] and [4]).

an initially straight dislocation segment under zero Peach-Koehler force delimited by pinning points, was first described by Frank and Read, and a mobile link is known as a Frank-Read (FR) source [14, 15]. The Peach-Koehler force is the force per unit length of a dislocation loop [16]. A schematic representation of the FR source is given in Fig. 1.1b. While a given link, that is delimited by stable junctions, bows out on its glide plane and not yet attains

its critical, semicircular shape, the shear strain contribution is mechanically reversible [1]. The interaction between dislocations on non-parallel planes during Stage-II hardening forms these stable junctions that are strong obstacles to local dislocation motion [17]. The hardening stages-I⋯IV refer to the division of the stress-strain response of single crystals in discrete strain ranges with distinctly different plastic tangent moduli [18]. When a link attains its critical shape, the link starts acting as a so-called source [15]. The ensuing dislocation loop, if unimpeded, keeps expanding. The latter action is commonly referred to as the activation of FR sources, and herein, the main mechanism for dislocation density increase.

Post-yield mechanical deformation is commonly captured in work-hardening models, *e.g.* Kocks [19], Kocks and Mecking [20], Estrin and Mecking [21], Bergström [22, 23], Bergström-Van Liempt [24, 25] and internal-variable models [26, 27]. Lesser studied is the contribution of dislocations to the pre-yield constitutive behaviour. The nonlinear pre-yield mechanical behaviour, as observed by [2–6], is due to an additional strain component on top of the elastic lattice strain during loading and unloading. First Eshelby [1] and later Koehler and DeWit [2] connected the apparent elastic constants, which are lower than the constants due to lattice strains alone, to the bowing out of pinned dislocation segments. Knowledge of pre-yield mechanical behaviour has already proven important in the design of forming methods [28], micro-mechanical systems [29] and ultrasonic measurement techniques [30]. An outstanding example is the physical-phenomenological full-field numerical crystal plasticity model of isotropic anelasticity by Torkabadi *et al.* [28]. However, it has not been possible to accurately predict the apparent elastic constants after plastic deformation [5].

Chapter 2

The circular equilibrium shape of the FR source under an applied stress was first discussed by Frank and Read [14], and Schoeck [31]. However, for isotropic linearly elastic materials, it is well-known that the elastic energies per unit segment length of edge and screw dislocations are unequal for a non-zero Poisson's ratio. Edge and screw character dislocation are the two limits of the angle between the local dislocation line direction and the Burgers vector, where the latter is a measure of the magnitude and direction of the local distortion of a lattice. A mixed-character dislocation experiences an aligning torque towards its screw orientation because the self-energy of the edge dislocation is greater than the self-energy of the screw dislocation. Therefore, the equilibrium shape of FR sources in metals is non-circular.

Recently, Van Liempt and Sietsma [4] show that the pre-yield mechanical behaviour is a measure for the average properties of the dislocation network which they characterise by the total dislocation density and the average dislocation segment length. The method championed by Arechabaleta *et al.* [5, 6] allows for obtaining information on the characteristics of a dislocation network via mechanical testing. However, the crystallographic texture of a polycrystalline material is only taken into account by the Taylor factor and the assumed circular dislocation loop shape is only valid for highly compressible materials. Hereby, for one, the model predicts an isotropic anelastic response, and secondly, retrieves only spatially averaged quantities on a mesoscale.

Current models by [2–6] assume a uniform dislocation distribution over slip systems. Hereby, the models of Koehler and De Wit [2], and Agrawal and Verma [3] predict a linear anelastic mechanical response with cubic symmetry. The principal anelastic dislocation strain, however, increases non-linearly with the applied normal stress. Wherefore the tangent

modulus is an appropriate measure of anelasticity. The models of Van Liempt and Sietsma [4], and Arechabaleta *et al.* [5, 6] predict a non-linear mechanical response but with isotropic symmetry. However, the local response of a given crystallite depends on its spatially uniform or non-uniform dislocation distribution over slip systems. There is thus a distinct need for an anelastic model that takes the crystal structure into account and results in an expression for the anisotropic mechanical response. This is addressed in chapter 2 of this thesis.

Chapter 3

Plastic mechanical deformation is commonly captured in work-hardening models, *e.g.* [19–27], which make use of volume averaged quantities, *e.g.* the total dislocation density, average storage distance and average interaction range. Hardening models consist of two parts [32]. The *first* part describes the dislocation network evolution. The dislocation network structure evolves by the glide of activated dislocation links, commonly called mobile dislocations [9, 17]. The global dislocation density increases and the average dislocation segment length on a given (active) slip-system decreases [32]. Upon unloading, the stored, previously mobile, dislocation links reverse their motion. Yet, they might remain inactive as FR sources because the dislocation network refined concurrently. Plastic deformation is thus uniquely defined after unloading, *i.e.* the area swept by mobile dislocations whilst hardening minus the mechanically recoverable anelastic component of the total strain. Virtually all present work-hardening models neglect anelastic strain; the *second* part of hardening models consists of a flow rule that relates the current dislocation network geometry to the global flow strength. Commonly the relation between the flow strength and the dislocation density is assumed by a Taylor-type equation [33]. The Taylor relation is sometimes rationalised with the force necessary to activate dislocation links [34], under the assumption that the average segment length scales with the square root of the dislocation density [8, 32]. In the Taylor model, hardening is thus argued to depend on either the increase in global dislocation density [33] and/or the decrease of local dislocation segment lengths [34]. Taylor-type equations assume solely linear elastic pre-yield behaviour, although dislocations mechanics is modelled [33, 35]. Hence there are few studies, *e.g.* [36], that explicitly model dislocation glide over the entire stress-strain curve of metals. Currently, we are solely aware of the work by Torkabadi *et al.* [28], who use a mixed physical-phenomenological model. More common are hyperelasticity and Mroz-like multi-surface descriptions of continuum inelasticity, and complex path- and direction-dependent hardening models of continuum plasticity (See [7] for an extensive overview).

Several yield strength models do explicitly consider dislocation motion before massive dislocation multiplication initiates. Recently, Van Liempt and Sietsma [4] postulate a yield criterion based on the identification of the transition in dislocation behaviour from limited reversible glide in the pre-yield stage, without essential changes in the dislocation structure, to post-yield dislocation multiplication. Li and Wagoner [7] present a dissipative dislocation bow-out model that, they state, reproduces anelastic unloading-reloading hysteresis. These dislocation bow-out models [4, 7] excel in capturing the dissipative and mechanically reversible pre-yield deformation, however do not consider significant mechanically irreversible dislocation motion, that is at the origin of plastic strain and hardening. The flow strength description in current hardening models juxtaposed to bow-out models [4–7] leads to solely linear elastic behaviour; the majority of work-hardening models lack a description

of reversible dislocation motion and bow-out models [4–7] do not consider significant irreversible dislocation motion. From an engineering perspective, the total recoverable strain during loading and unloading governs the apparent elastic modulus [1–3, 37, 38], which is essential for materials models of cyclic loading and precision engineering [4, 7, 39], and in spring-back and thermomechanical processing of metal alloys [5, 28, 40]. Especially the nonlinear unloading-reloading behaviour in thermomechanical manufacturing processes is ill understood, which directly affects the process parameters, and assurance of products' properties and quality [41]. There is thus a distinct need for a unified inelastic model, where the physics-based descriptions of the anelastic and plastic strain are combined, that currently lacks in literature. This is addressed in Chapter 3 of this thesis.

Objectives

In summary, the objectives of Chapter 2 are the formulation of an anelastic model, that takes the crystal structure into account, and closed-form expressions for the anisotropic, inelastic mechanical response pre- and at-yield. This model must capture the dependence on initial dislocation character, spatial dislocation distribution and loading direction of the tangent modulus and inception of plastic flow. Chapter 2 thus presents a methodology that extends the model by Van Liempt and Sietsma [4], which yielded the dislocation density and a measure of dislocation segment lengths, to elastically anisotropic crystallites.

The objective of Chapter 3 is the formulation of a unified inelastic model of inelastic pre- and post-yield dislocation-mediated deformation. This model includes a novel yield criterion that is based on the local anelastic and global plastic compliances. Moreover, Chapter 3 presents a semi-empirical relation of dislocation network structure change that accompanies work hardening. This relationship thus rationalises the experimentally observed changes in initial apparent elastic constants with thermomechanical processing.

1.3 Part II: Yield Point Phenomenon

Materials that exhibit the YPP in a monotonic, uniaxial tensile test have a sudden transition from elastic to elastic-plastic behaviour. This transition in force-displacement is accompanied by a nominal strain region with constant nominal stress, where plastic deformation is heterogeneous, which is also referred to as yield point elongation or the Lüders phenomenon. Piobert *et al.* [42] and Lüders [43] described the YPP in mild steels first. Figure 1.2a is a schematic representation of a typically measured tensile curve of a metal that displays the YPP. The nominal stress and nominal strain are calculated on the basis of the specimen's initial geometry where localisation is ignored.

In contrast with the YPP, common metals display strain hardening, *i.e.* a change in nominal strain is accompanied by a finite, proportional change in nominal stress, and thus associated with ductility. Plastic deformation becomes heterogeneous solely when necking initiates and failure (rapidly) ensues. Heterogeneous deformation takes place in so-called Lüders bands for the YPP. A schematic representation of the Lüders band is given by the green coloured areas in the inserts in Fig. 1.2, that border the elastically and (elastic-)plastically deformed volumes. Herein, the Lüders band is a given volume where the material deforms plastically, and saturates to the so-called Lüders strain over an *a priori* unknown axial distance. Both necks and Lüders bands are associated with localisation [45]. The important distinction

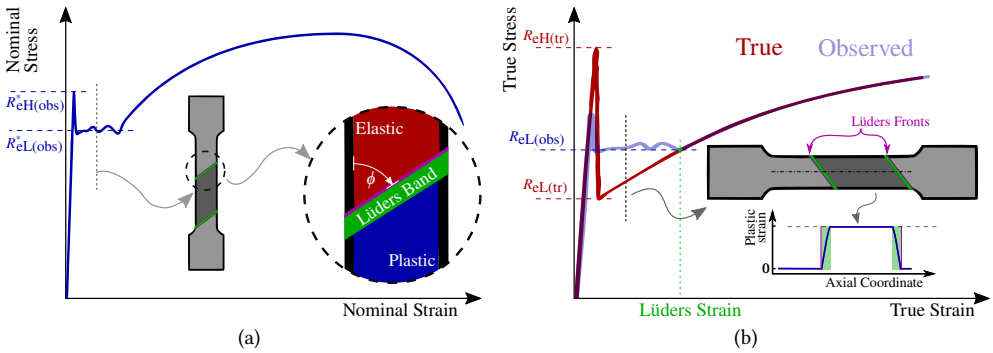

Figure 1.2: Schematic representations of (a) the nominal stress-nominal strain and (b) the true stress-true strain curves of the Yield Point Phenomenon (Adapted from [44]). The observed and true materials, mechanical behaviour is indicated by the upper and lower yield strengths, R_{eH} and R_{eL}, respectively. Here the superscript $R^*_{\bullet}$ indicates yield stresses $R_{\bullet}$ that are calculated across the specimens' original cross-section. The inserts in (a) and (b) depict a tensile specimen with two Lüders bands and fronts; and, in (b), a schematic representation of the magnitude of local plastic strain as a function of the axial coordinate.

from necking is that once Lüders bands traverse all elastic volume, the material continues to harden and the tensile specimen deforms homogeneously, whereas necking directly leads to fracture.

Materials Science research on the YPP focuses on micromechanical approaches, *e.g.* the Cottrell-Bilby theory [46] and dislocation multiplication mechanisms [47, 48]. The majority of these investigations elucidate the reasons for the YPP in metals, that include transformation induced plasticity [49]. Hall [50] presents a comprehensive summary on these treatises in the fifties and sixties. Research intensity on the YPP decreases over the last five decades, with efforts to quantify the Lüders strain [44]. Johnston and Gilman [47] find that although lithium fluoride crystals display the YPP, the initial dislocations do not move. Hahn [48] supports Johnston and Gilman's view, and states that the influence on the YPP by impurity atoms that lock dislocations in place [46] is overstated. They [47, 48] put the YPP down to rapid multiplication of new dislocations and these "locked" dislocations remain in place according to their view [46]. Hahn [48] applies their model [47] to mild steels as well. Most recently, Elliot *et al.* [51] report that sequential bake hardening and reverse loading is inconsistent with the carbon pinning model [46]. Currently, no single micromechanical model rationalises the occurrence of the YPP in low carbon steel.

Numerical research concentrates on modelling the YPP by means of the continuum finite element method [52]. The end of the last and the first decade of this century present a large body of constitutive models. Most notable are Hahn's [48] and the Up-Down-Up [53, 54] descriptions of the YPP. Yoshida *et al.* [55] and Žerovnik *et al.* [56] employ the former constitutive model; Giarola *et al.* [57] and Mazière and Forest [58] the latter. However, the finite element method has its own set of challenges when modelling the YPP [44, 52, 58, 59]. For an exhaustive overview of current numerical models of the YPP we refer to the work by Kim and Kim [52]. Despite the constant increase of computational power [60], the main drawback of numerical modelling remains tractability. Hence the aid of numerical modelling

in obtaining constitutive parameters of the YPP is tentative at best [56, 61, 62].

The works by Schwab and Ruff [44], Schwab [63] and Schwab and Harter [62], require special mention, because we discuss and reference them [44, 62, 63] extensively throughout Part II. They [44, 62, 63] present a "*completely new*", simple and fundamental macromechanical model to explain the nature of the YPP in plain carbon steels. Their [44, 62, 63] interesting assumption is a single strain-hardening law. Figure 1.2b is a schematic representation of the observed and true, stress–strain mechanical behaviour of a typical metal that displays the YPP. The true material mechanical behaviour after the elastic-plastic transition is based on hardening although this is not observed. For one, the true upper yield strength $R_{\mathrm{eH(tr)}}$ is much higher than the observed upper yield strength $R_{\mathrm{eH(obs)}}$; secondly, true material mechanical behaviour is strain hardening that starts with the true lower yield strength $R_{\mathrm{eL(tr)}}$; and, finally, the observed lower yield strength $R^{*}_{\mathrm{eL(obs)}}$ in Fig 1.2a is a result of the triaxial stress state [44, 64, 65], that develops on a plane that borders the elastic volume and the Lüders band. This plane is indicated by magenta lines on the inserted, dog-bone specimen in Fig. 1.2, and we refer to it as the Lüders front in the following.

The constitutive parameters for any model are difficult to measure experimentally when deformation is heterogeneous [66]; any experimental observation in a tensile test is not necessarily a material property when deformation is localised. Hence from an engineering standpoint the YPP presents a unique challenge. For one, the material's yield strength is potentially higher than the yield strength one observes; and, the constant nominal stress is not necessarily a material property [67]. Furthermore, strain hardening is not observed because it is obscured by a constant nominal stress [68] (See Fig. 1.2a). Finally, the Lüders strain depends on specimen geometry [67, 69].

Industrial Background and Relevance

The YPP represents a major drawback in metallic materials that leads to undesirable visible traces on the surface of final industrial products [69, 70]. The localised nature of Lüders bands is problematic in manufacturing processes of sheet metals and leads to "stretcher strain marks" [71–73]; Lüders bands induce surface roughness and limit industrial application [71, 74]. The prevention of the YPP thus equals stopping the formation of Lüders bands. Hence the deterioration in surface quality, *e.g.* due to the formation of stretcher strain marks, prompts extensive investigations into the YPP [75].

The formation of Lüders bands is usually eliminated by cold-working metallic sheets, where their thickness reduces by about a percentage point [76]. For example, when one produces cold-rolled steel sheets, the penultimate annealing process is followed by: skin-pass - or temper rolling; or, tension-levelling. The post-processing purpose is to eliminate the YPP, that creates undesirable surface marks when the steel sheets are industrially formed [77].

For annealed or aged steels, stretcher strains and fluting are critical defects that are induced by the YPP [78]. Pearce [79] explains that the roller-levelling process, with cyclic bending operations, induces mobile dislocations that diminish the yield-point elongation. The roller-levelling process is composed of multiple up-and-down bending operations with a series of offset rolls [78]. Theis [80] shows that plastic deformation generated from repeated bending-unbending, averts superficial defects for low carbon steel. Butler and Wilson [81] conclude that the surface of the rolled sheet is composed of yielded and virgin material volumes, which Lüders bands bound, and the plastic volume increases with thickness reduction.

Park and Yoon [54], Kim *et al.* [82] and Park *et al.* [83] conduct experimental studies on the onset condition and reduction of fluting and YPP related superficial defects, respectively. Park *et al.* [83] study tension-levelling conditions for reducing yield point elongation in order to prevent fluting and surface marks with press forming. However, post-processing is not always possible [76] and these surface marks continue to be a problem in some industrial applications, *e.g.* tin plated rings [84] and V-bending [78].

The YPP is beneficial in specific applications and is induced to enhance certain properties. Conventional steels with YPP are used as automotive, sheet material [85]. Holmberg and Thilderkvist [86] observe that a higher yield stress directly improves dent resistance. Hence bake hardening of pre-strained low carbon steel improves the dent resistance in automotive sheet metal forming [87]. These low-strength deep drawing steels initially offer low yield strength before forming, but they strengthen with forming and paint baking in automotive manufacturing [88]. When this higher yield stress is obtained by the YPP, after paint baking, low carbon steels show superior dent characteristics compared to steels without [87].

Scientific Background

In the fifties, Hundy [71] observes that for materials that display the YPP in tensile testing before skin-pass rolling, a light longitudinal stretching afterwards leads to surface markings perpendicular to the rolling direction. These areas correspond to yielded and virgin material volumes in the rolled sheet. Lake [89] analyses steel sheets submitted to the skin-pass under industrial conditions, and reveals Lüders bands similar to those already detected by Butler and Wilson [81]. Hosford and Caddell [72] state that, in general, the YPP is alleviated by temper rolling, also known as skin-pass rolling, which provides comparatively small strains to the material. The skin pass of carbon steel and ferritic stainless steels sheets eliminates the YPP and controls the sheet thickness and surface finish [90] as well. Yoshida *et al.* [91] numerically model temper rolling. Skin-pass rolling (or temper rolling) of steel sheets involves a thickness reduction of half to two percentage point, that follows hot rolling, annealing or galvanising [90–93]. It is important to know materials and processing specific, rolling conditions, because: excess thickness reduction induces defects; and, insufficient reduction retains defects related to the YPP. This unfortunately remains elusive [78]. Still low carbon steel often exhibits the YPP, even after the temper rolling because the material ages, for example, during the post-production colour coating process [78].

Steels that exhibit or lack the YPP have inferior respectively superior mechanical properties, which obviously depends on the final, industrial products' application. With the YPP one obtains an inferior surface finish after press forming [77]. Wherefore the YYP is an industrially important problem and investigated for several decades. Besides early studies on the mechanism of the YPP in low carbon steels, the influences of many factors such as: grain size [68, 73, 75, 94–99]; microstructure [73, 75, 96, 97, 99–105], strain rate [51, 96, 106–110], deformation temperature [105–107, 111]; and, carbon and nitrogen content [96, 101, 112], are studied. Despite solid experimental results reported in literature, no clear picture of the underlying mechanisms of the YPP has emerged [73]; while there is widespread consensus regarding the factors which influence the YPP, there are still gaps in the arguments that concern the underlying mechanisms. Depending on the application, one might mitigate, suppress, enhance or create the YPP. Hence it is crucial to understand the micromechanisms

of Lüders band formation and propagation [105].

Understanding the geometrical characteristics of Lüders bands that accompany the YPP in steels, particularly the orientation of these bands with respect to the loading axis, is imperative since they induce surface roughness during metal forming operations [74]. Such bands are experimentally measured extensively and studies address: band nucleation [109, 113–116]; growth [96, 114, 117–119]; kinematics [109, 114–120]; velocity [69, 96, 108, 109, 119, 121]; and, morphology [69, 74, 109, 117–121]. Earlier studies make significant effort on the morphological characteristics of Lüders bands [74, 117, 120] as well. In the early nineties, Anonthon and Hall [120] already note that literature reveals the important aspects of the tensile specimen's cross-section on the morphology of Lüders bands. While specimen thickness is thought to effect the nature of the bands [69], this is not given enough attention [114]. The experimentally obtained Lüders front angle varies in the range $45 \cdots 90$ degrees with respect to the tensile direction. Currently, no single model rationalises all these experimental observations. Although the YPP is investigated for more than hundred and seventy years, ones understanding of Lüders band formation lacks substantial support from experimental evidence [116]. The uncertainty on Lüders band characteristic orientation still exists due to the contradictions in the reported, experimental results [74]. The characteristics of Lüders band remain uncertain as well due to the limited number of experimental results reported.

Objectives

In summary, the objective of Chapter 4 is to formulate a macromechanical model of the YPP that accounts for the characteristics of, and the heterogeneous stress state at, the Lüders front. Moreover, Chapter 4 presents an alternative mechanism for the rotation of the Lüders band with material properties, specimen's geometry and test conditions. This results in a simple methodology to approximate the material properties from uniaxial tensile tests, independent of test conditions.

1.4 Part III: Dissipative Contacts

Bringing two surfaces into contact and separating them again is generally associated with net, rate-dependent energy loss [122]. Causes of this hysteresis are ageing, interlocking, relaxation and formation of capillaries. Other more recently recognised sources are multistability that originates surface roughness [123] and discontinuous motion of contact lines from surface heterogeneities [124]. The general critical aspect of contacts is that their contact deformation is mechanically reversible, yet energetically irreversible. This hysteresis is commonly observed as a larger intimate contact area during retraction than during indentation.

Industrial Background and Relevance

It is impossible to overstate the societal relevance of soft-materials adhesive contacts. Soft-Material adhesive contact is present in a large variety of engineering applications, that include: automotive [125–128]; aerospace [129, 130]; nano-engineering [131–135]; robotics [136–138]; bio-medics [139, 140]; and, bio-engineering [123, 141–144]. Understanding of the origins of adhesive hysteresis is thus paramount in the design, and for the operation of engineering applications [123, 129–149]. However, the physical mechanisms behind adhesive hysteresis

in soft materials contact with surface roughness present are ill understood [145–149].

The topical problem to address is when rough contacts are soft and adhesive, and emergent behaviour arises due to the interplay between adhesion and viscoelasticity [150]. The importance of this emergent behaviour, namely dissipative processes that occur at, and at a distance from, the interface, gives rise to the relevance of explicitly modelling solids [150]. The knowledge gap and future trends we identify are the lack of patterns that adhere to arbitrarily curved rough surfaces [151]; space debris remediation [152]; and, the growing demand for automated manipulation of objects in industrial miniaturisation. Costa *et al.* [151] remark on the importance of automated manipulation, where no longer only high adhesion but also release-ability is of importance. Soft-Matter adhesion in the presence of engineered surface topographies poses one route to obtain such tunable adhesion.

Scientific Background

It is well-known that adhesion between hard solids is difficult to observe on the macroscopic length scale, whilst adhesive forces are significant at micro- and meso-scales (*i.e.* the "adhesive paradox" [153]). Furthermore, it is shown theoretically [154–157], numerically [158, 159] and experimentally [141, 147, 155, 160, 161], that large surface roughness "destroys adhesion" [149]. The reduction and disappearance of perceptible adhesion with surface roughness is rationalised by the fact that energy is stored when a given surface roughness is flattened, and subsequently all stored energy is released in the retraction process in near-adiabatic contact. The additional energy needed to destroy, and subsequently create, two separate surface areas is then small compared to the stored (elastic) energy, and thus experimentally imperceptible and/or negligible in magnitude. Surprisingly though, the relationship between the observed adhesion and the surface roughness is non-monotonic [162–164].

The first observations of enhancement of adhesion (at pull-off) for small surface roughnesses is ascribed to Fuller and Tabor [162] by Papangelo and Ciavarella [149], and observed in experiments by Griggs and Biscoe [163], and Fuller and Roberts [164] as well. A seminal criterion for stickiness by Dahlquist [165, 166] is that the elastic Young's modulus is smaller than 1×10^6 Pa to perceive adhesion, even in the presence of surface roughness. Recently, this criterion is again experimentally verified by Tiwari *et al.* [142] and Dalvi *et al.* [157]. The enhancement in observed adhesion due to surface roughness is more complex than the single criterion by Dahlquist [165, 166] though.

A first insight is given by Persson and Tosatti [154], when they realised that surface roughness increases the total surface area. In perfect, continuous and intimate contact the total contact area increases, and hence so does the observed work of adhesion (known also as the Dupré surface energy). The relevance of this increase in the total surface area is shown experimentally by Peressadko *et al.* [141], theoretically by Dalvi *et al.* [157] and numerically by Pepelyshev *et al.* [167]. The contact theory by Persson and Tosatti [154] follows thermal equilibrium though, which calls for an additional source of dissipation [149].

Several origins of the observed hysteresis in the presence of adhesion are proposed. When adhesive forces are present in elastic contact between smooth surfaces, the normal loading and unloading force-displacement trajectories differ [168–170]. Which implies dissipation over a given loading/unloading cycle [168]. Dissipation is then exclusively due to the elastic jump-in and -out of contact, seminally known as "tack" [166, 171]. With surface roughness present, the mechanical response of bodies in contact is more complex [168]. Guduru [172]

proposes a contact-mechanics theory pertinent to the contact between an elastic ball and an axisymmetric rigid wavy surface. He [172] shows that in wavy, elastic contacts the equilibrium load-area curve is characterised by oscillations that lead to elastic mechanical instabilities. A representative load-indentation curve by Guduru and Bull [123] is given in Fig. 1.3a. The difference in location of the elastic jumps in the force-displacement trajectory

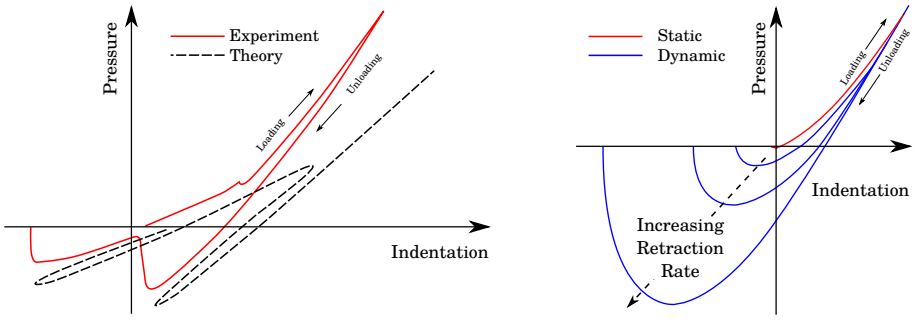

Figure 1.3: Schematic representations of the pressure-indentation curves for (a) axisymmetric, wavy elastic contact and (b) smooth, Hertzian viscoelastic contact (Adapted from [123] and [171], respectively).

between loading and unloading constitutes adhesive dissipation, that is induced by surface roughness. This theory [172] is: validated experimentally by Guduru and Bull [123] and numerically by Carbone *et al.* [173]; however, it is limited to cases where a single connected contact area is achieved.

Recent works with (spherical) indenters indicate that, in some cases, elastic instabilities triggered by surface roughness are rate determining for adhesion hysteresis [155, 157, 170]. Dalvi *et al.* [157], and Wang and Müser [170] state that surface heterogeneities pin the contact edge such that the retraction process de-pins with instantaneous jumps over small, localised microscopic areas (*i.e.* the Griffith theory [174]). Greenwood [175] extends the Fuller and Tabor multi-asperity model [162], and finds that adhesive hysteresis occurs because of elastic instabilities as well. In the contact between elastic bodies with surface roughness present, the most commonly recognised sources of dissipation are total contact area increase (of geometrical origin) [154, 157], and mechanical instabilities [123, 149, 172] (beyond elastic jump-in and -out of contact). Other chemical and mechanical sources of dissipation are chemical irreversibility [176, 177], heterogeneity of the surface properties [124, 178, 179], difference in bonding behaviour in tension *versus* compression [180], surface film transfer [128] and plasticity [181, 182].

The differences between experimental observation and theoretical prediction on the contact between elastic bodies are commonly attributed to viscoelastic effects [142, 147, 177, 183–187]. One reason is that despite attempts to approach adiabatic loading conditions, *e.g.* very low retraction rates in (vertical) unloading experiments, there is still perceptible dissipation due to viscoelasticity [124, 142, 147, 149, 177, 185, 188–191]. With viscosity the effective work of adhesion increases with retraction rate over several orders of magnitude [171]. Representative load-indentation curves, in smooth, elastomer contact by Barquins and Maugis [171]

are given in Fig. 1.3b.

Current understanding of different types of adhesive mechanics is dominated by the knowledge on simple adhesive elastic contact. Hence why a summary is called for. In adhesive circular contact, two well-known limits exist. One, the seminal work by Johnson, Kendall and Roberts (JKR) [192] on the adhesive contact between an elastic sphere in contact with an elastic (or rigid) half-space in the presence of short-range adhesion [193], *i.e.* adhesive forces outside the contact area are neglected [194]. On the other hand, in the Derjaguin-Muller-Toporov (DMT) approximation [195], *i.e.* rigid sphere behaviour [194, 196], the adhesive forces are taken into account, but the contact remains Hertzian. The transition from short- to long-range, *i.e.* JKR- to DMT-type, adhesive mechanics is treated analytically by Maugis [194] with a simple Dugdale potential [197] in smooth Hertzian contacts. The type of adhesion is then uniquely defined by the Tabor parameter [198], a measure of the surface roughness's curvature, effective elastic modulus, work of adhesion and "range of action" (of a given potential, *e.g.* [199, 200]) [194, 201]. Moreover, for a given adhesive contact the type of adhesion is determined by the spherical/cylindrical radius and the cubed adhesive interaction range (in the Dugdale potential [197]) [194, 201]. The most peculiar feature of both limiting types of adhesion is that the pull-off force is independent of the elastic modulus, and only a product of the spherical/cylindrical radius and the work of adhesion [193, 201]. Persson [202], and Gao and Yao [203] predict that the type of elastic jump-out of contact changes from the Bradley-type [196] prediction (*i.e.* uniform bond-breaking), towards the JKR-prediction (*i.e.* crack propagation), with indenter size and/or shape, respectively. Note that the works [192, 195, 201–204] omit viscous dissipation in soft-materials contact, and solely consider system-size (scale-)effects [205].

Chapter 5

Hysteresis due to viscous loss is distinct from hysteresis due to surface roughness in elastic contacts, as the former is rate dependent [206]. The influence of viscoelasticity is thus also felt across different length scales under finite deformation rates. Bulk viscosity clearly affects the contact mechanics, and causes hysteresis, which is trivial. However, viscoelasticity plays a significant role even when the indentation and retraction rate are small compared to the materials characteristic frequencies, which is experimentally verified by Chaudhury *et al.* [177], Lorenz *et al.* [147], Tiwari *et al.* [142], and Violano and Afferante [185], and later inferred by Papangelo and Ciavarella [149]. The significant role of viscosity is explained by *e.g.* the theory by Greenwood and Johnson [183]. They [183] note that high stress rates occur at low (normal) retraction rates, due to the existence of stress concentrations at the contacts' edges. When the retraction is slow enough for bulk stress to be related with the imposed normal strain through the relaxed modulus, the change in response due to viscosity is equivalent to that obtained through a given change in the (effective) work of adhesion [183]. In the latter case, the effect of viscoelasticity is oft described with a semi-empirical equation, that specifies an effective work of adhesion, which increases with crack-tip velocity [183, 204, 207–211]. Theoretical models reproduce dissipation at the contact edges by either the Barenblatt model [212–214], classic fracture mechanics [183, 204, 211, 215, 216] or crack-tip blunting [217–220]. The semi-empirical equation is thus used in theoretical treatises of smooth surface contacts [186, 187, 215, 221–223] and in experimental verification of models on nominally smooth (Hertzian) contacts [183, 187, 190, 191, 204, 221]. Most recently, Violano *et al.* [187] replace the adiabatic surface energy with an effective work of adhesion

which accounts for viscous dissipation in adhesive Hertzian contact [192]. The central assumption in the works [186, 187, 190, 191, 215, 221–223] is by Gent and Schultz [207–209], *i.e.* viscous dissipation resides in a volume by the edges of contact, this volume is small compared to the bodies.

Greenwood and Johnson [183] indicate that since traction is infinite at the edges of contact under JKR-theory, the stress and strain rates are infinite for any finite contact velocity. Therefore, any viscous material around the peeling edge would always be in the instantaneous limit (*i.e.* the Graham paradox [224]) [193]. Secondly, with the original framework of the JKR- and DMT-approximation, ignominiously applied to viscoelastic materials, the pull-off force is by definition independent of the retraction rate [193]. Obviously, both these analytical features are absent in experimental observations in the presence of viscous dissipation, where the pull-off force increases monotonically with the rate of retraction (*e.g.* [187]). Greenwood and Ciavarella [183, 193] already noted that the afformentioned analytical features are in conflict with experimental observations and therefore suggest to use more realistic descriptions of the crack tip. The Barenblatt model [212–214] is a good example of such a more realistic description. The previous theoretical treatises [183, 186, 187, 191, 193, 215, 221] implicitly model a cohesive zone though; they [183, 186, 187, 191, 193, 215, 221] essentially modify the JKR-solution by a given increase in the apparent work of adhesion [193]. The increase of pull-off force in JKR-type contacts is then obtained by considering some velocity-dependent elastic modulus at the crack tip by an increased effective work of adhesion via Gent and Schultz's theory (in [207–209]) [193]. Hence why a revision of current theoretical treatises of adhesive Hertzian contacts [194, 201] in the presence of viscoelasticity is inevitable.

Recent experimental investigations by Dorogin *et al.* [188], Beak *et al.* [225] and Deng and Kesari [226] show an increase in the pull-off force with pre-load (in the presence of surface roughness). Deng and Kesari [226] suggest that dissipation has two sources, one indentation independent, and one due to roughness [169]. Kroner *et al.* [227] and Lai *et al.* [228] observe a monotonous increase in pull-off force with pre-load, and a maximum, asymptotic force for high initial indentation depths. However, such findings disagree with tests on rough-surface, soft materials performed by Kesari *et al.* [155]. They [155] find a small enhancement of the pull-off force with pre-load, that is almost negligible compared with elastic contact, which is in agreement with Greenwood (in [175]) [191]. Moreover, for a patterned surface on a viscoelastic substrate, Violano *et al.* [191] find negligible or no dependence on pre-load at all. Dorogin *et al.* [188] find, for intimate contact across the entire apparent contact, that the pull-off force is independent of the pre-load. Similarly, Violano *et al.* [185] observe an almost constant pull-off force, while varying the initial load, in classic adhesion experiments between a spherical glass indenter and a soft material when unloading. Most recently, Das and Chasiotis [221] find that the pull-off force is independent of pre-load in the contact between crossed polymer nanofibres. In conclusion, the mechanism of adhesive hysteresis in soft materials *with surface roughness present* is still ill understood [145–149]; the predictions by theoretical treatises on rough surface, adhesive viscoelastic contacts remain tentative because of experimental difficulties [189] or tractability [229].

Of engineering interest is the influence of surface roughness and viscoelasticity on the rate dependencies of the apparent work of adhesion and the pull-off. The depicted state of the art highlights the absence of a model that is able to describe the real physics of the

adhesive interactions at rough contact interfaces, and captures the rate-dependent adhesive hysteresis without any assumptions on the location of viscous dissipation. Such a theoretical treatise or numerical investigation that satisfies both criteria has not been attempted in the presence of surface roughness, to the best of the author's knowledge.

Chapter 6

The quasi-static limit is used as an approximate to the fully dynamic solution in many engineering problems that involve frictional dissipation. Typically problems of interest in the field of mechanics of materials where viscous dissipation is active are the deformation of viscoelastic bodies, or the high temperature deformation of metals that is accompanied by grain-boundary sliding. For systems with solely viscous friction this estimate holds when the frequency of loading is low compared to the natural frequency. Even at room temperature, plastic deformation of metals occurs through the motion of dislocations, which is modelled without accounting for inertia, through a first-order differential equation. Ignoring inertia is done routinely, especially in the field of multi-scale modelling, where it is imperative to limit computational time. There are problems however where it is more difficult to make an estimate, like the ones where Coulomb friction is active concurrently with viscous dissipation. The terms static and dry friction are synonymous with Coulomb's dry contact friction, which is ubiquitous in Tribology.

When the loading frequency is low compared to the natural frequency and/or the motion is over-damped, the equation of motion is often reduced to a first-order differential equation. Notable examples are the drift equations for grain boundary and dislocation motion [17, 230]. The area of our particular interest is multi-scale numerical modelling [231]. Significant physical problems involve multi-scale physics, *e.g.* rubbing surfaces [232] and inelasticity [233]. Tractability necessitates simplification when one transitions from lower to higher temporal and spatial scales. Hysteretic behaviour under cyclic loading takes place in many engineering problems as well. One might thus be tempted to invoke simplifications and omit inertial forces, when static and dry friction is observed at the mesoscale. Static and dynamic friction are the principal sources of hysteresis, with static and dry friction the main sources at low frequencies. However, the solution under quasi-static assumption (no inertia) and the dynamic solution differ considerably depending on friction forces and loading frequency. It was indeed shown that the dynamic solution under quasi-static loading conditions does not necessarily correspond to the equivalent solution under the quasi-static assumption in a given mass-spring system [234]. Here, the quasi-static assumption implies the removal of inertial forces from the equation of motion. With the quasi-static loading limit, we mean the excitation frequency is only a fraction of the natural frequency of the given system. It is of engineering interest to know the parameter space where there are (no) differences between the solution under the quasi-static assumption and the dynamic solution.

Objectives

In summary, the objective of Chapter 5 is to present the interplay between adhesion and viscoelasticity in the presence of surface roughness. This answers the question of whether viscous and/or roughness-induced dissipation are/is the origin of adhesive hysteresis in soft matter contacts. The objective of Chapter 6 is to highlight the differences between the solution under the quasi-static assumption and the dynamic solution of a base-excited

system in the presence of friction. This is a guide for future inelastic multi-scale modelling efforts.

1.5 Preliminaries and Notations

We apply throughout this dissertation the direct tensor notation. Zeroth-order tensors/scalars are symbolised by italic letters (*e.g.* a, b, A and B), first-order tensors/vectors by italic lower case bold letters (*e.g.* $\boldsymbol{a} = a_i \boldsymbol{e}_i$ and $\boldsymbol{b} = b_j \boldsymbol{e}_j$), second-order tensors by italic uppercase bold letters (*e.g.* $\boldsymbol{A} = A_{ij} \boldsymbol{e}_i \otimes \boldsymbol{e}_j$ and $\boldsymbol{B} = B_{kl} \boldsymbol{e}_k \otimes \boldsymbol{e}_l$) and fourth-order tensors by italic uppercase bold calligraphic letters (*e.g.* $\boldsymbol{\mathcal{A}} = A_{ijkl} \boldsymbol{e}_i \otimes \boldsymbol{e}_j \otimes \boldsymbol{e}_k \otimes \boldsymbol{e}_l$) with basis $\boldsymbol{e}$. Moreover, the first-order zero tensor is given by an italic lowercase bold letter $\boldsymbol{o}$. In vector-matrix notation, vectors are denoted as upright lowercase sans serif bold letters (*e.g.*, normal $\mathsf{n} = (n_1, n_2, n_3)^\intercal$, with superscript $\bullet^\intercal$ indicating the transpose of $\bullet$) and matrices as upright uppercase sans serif bold letters (*e.g.* elastic matrix $\mathbf{C}^{\mathrm{el}}$).
For a real-valued Cartesian coordinate system and orthonormal basis, *e.g.* $\hat{\boldsymbol{e}}_i$, where the overscript $\hat{\bullet}$ indicates a unit vector, and origin $\boldsymbol{o}$, basic operations for tensors used are:

1 The tensor product: $\boldsymbol{a} \otimes \boldsymbol{b} = a_i b_j \hat{\boldsymbol{e}}_i \otimes \hat{\boldsymbol{e}}_j = \boldsymbol{C}$;

2 The double-dot product between two second-order tensors:
$\boldsymbol{A} : \boldsymbol{B} = A_{ij} B_{kl} \hat{\boldsymbol{e}}_i \otimes \hat{\boldsymbol{e}}_j : \hat{\boldsymbol{e}}_k \otimes \hat{\boldsymbol{e}}_l = A_{ij} B_{ji} = c$;

3 The double-dot product between fourth- and second-order tensors:
$\boldsymbol{\mathcal{A}} : \boldsymbol{B} = A_{ijkl} B_{mn} \hat{\boldsymbol{e}}_i \otimes \hat{\boldsymbol{e}}_j \otimes \hat{\boldsymbol{e}}_k \otimes \hat{\boldsymbol{e}}_l : \hat{\boldsymbol{e}}_m \otimes \hat{\boldsymbol{e}}_n = A_{ijkl} B_{lk} \hat{\boldsymbol{e}}_i \otimes \hat{\boldsymbol{e}}_j = \boldsymbol{C}$.

The Einstein summation convention is used where the Latin indices (*e.g.* i, j, k, l, ...) run through the values 1, 2 and 3. Throughout this work, we choose to denote the second-order stress and strain tensors, and derived variables by italic lowercase bold (Greek) letters (*e.g.* strain tensor $\boldsymbol{\epsilon}$). Finally, for a Bravais lattice with translation vectors $\boldsymbol{t}_i$, crystal direction $[uvw]$ is parallel to direction vector $\boldsymbol{d} = u\boldsymbol{t}_1 + v\boldsymbol{t}_2 + w\boldsymbol{t}_3$.

Part I: Inelasticity in Metals

2

Influence of Dislocations on the Apparent Elastic Constants in Single Metallic Crystallites: an analytical approach

Intricate knowledge of dislocation networks in metals has proven paramount in understanding the constitutive behaviour of these materials but current experimental methods yield limited information on the characteristics of these networks. Recently, the isotropic anelastic response of metals has been used to investigate complex dislocation networks through the well-known phenomenon that the observed elastic constants are influenced by dislocations. Considering the dependence of the behaviour of a Frank-Read (FR) source on its initial dislocation character and using discerning characteristics of dislocations, i.e. Burgers vector, line sense and slip system, the present paper takes dislocation character, crystal structure and dislocation network geometry into account and obtains the anisotropic mechanical response for a generic Poisson's ratio.

In this chapter, the tensile test tangent moduli and yield points are presented for spatially uniform and nonuniform dislocation distributions across slip systems. First, the reversible shear strain of the FR source is derived as a function of initial dislocation character. The area swept by a mobile and initially straight dislocation segment pinned at both ends is given as an explicit function of the line stress. Secondly, the anisotropic anelastic strain contribution of FR sources to the total pre- and at-yield strain in single crystallites is calculated. For a given normal stress and superposition of the principal infinitesimal linear elastic lattice strain and anelastic dislocation strain, the tangent moduli are presented. The moduli and the inception of plastic flow have a notable dependence on initial dislocation character, spatial dislocation distribution and loading direction.

This chapter is based on the scientific article: Van Dokkum, J. S., Bos, C., Offerman, S. E., Sietsma, J., Influence of dislocations on the apparent elastic constants in single metallic crystallites: an analytical approach. *Materialia*, 20, 101178, 2021.

NOMENCLATURE

Variable	Definition	Dimension (mass M, length L and time t)
α	proportionality coefficient	–
b	Burgers vector magnitude	L
$\boldsymbol{b}$	Burgers vector	L
$\hat{\boldsymbol{d}}$	tensile direction	–
C_1 & C_2	integration constants	L
$\boldsymbol{C}^{\mathrm{el}}$	elastic tensor	$\mathrm{ML^{-1}t^{-2}}$
E	Young's modulus	$\mathrm{ML^{-1}t^{-2}}$
$i,\ j$ & k	indices	–
L	initial segment length	L
M	Taylor factor	–
μ	shear modulus	$\mathrm{ML^{-1}t^{-2}}$
N	number	–
$\hat{\boldsymbol{n}}$	unit plane normal	–
ν	Poisson's ratio	–
$\boldsymbol{o}$	origin	L
$\{r,\theta,\phi\}$	spherical coordinates	$\{\mathrm{L},-,-\}$
$\{r',\theta\}$	polar coordinates	$\{\mathrm{L},-\}$
R	radius	L
R^2	coefficient of determination	–
ρ	dislocation density	$\mathrm{L^{-2}}$
S	swept-out area	L^2
$\boldsymbol{\sigma}$	stress	$\mathrm{ML^{-1}t^{-2}}$
$\boldsymbol{t}$	translation vector	L
$\boldsymbol{\tau}$	shear stress	$\mathrm{ML^{-1}t^{-2}}$
θ	azimuth angle	–
U	self-energy	$\mathrm{MLT^{-2}}$
V	volume	L^3
ϕ	dislocation character	–
$x,\ y$ & z	Cartesian coordinates	L
$\hat{\boldsymbol{\xi}}$	unit line-sense	–
Y	tangent modulus	$\mathrm{ML^{-1}t^{-2}}$
Z	Zener ratio	–

2.1 INTRODUCTION

In this chapter, we present an analytical model of the anisotropic tangent moduli and the yield points for nonuniform dislocation networks in single crystallites. First, the works by DeWit and Koehler [235], and Cash and Cai [30] are extended with an explicit formulation of the area swept by a single Frank-Read (FR) source as a function of the applied shear stress. We derive an explicit analytical expression for the dislocation character at both pinning points as a function of the line stress. Secondly, the behaviour of crystallites is considered. The dislocation network is described by the dislocation characters, densities and segment lengths per slip system. The spatial correlation is given in discrete terms of dislocation densities with

a given character on individual slip systems. The anelastic dislocation strain contribution is derived. The current definition of "anelastic" and "anelasticity" by Li and Wagoner [7] is adopted here: a mode of deformation that is mechanically recoverable and energetically dissipative, where for metals, nonlinear elasticity is implicit because of the bowing out of mobile dislocation segments. Loading/Unloading hysteresis thus is due to dissipation and the bow-out model captures the anelastic strain for a given stress state in metallic crystallites. Finally, combining the elastic and the anelastic mechanical response, we present the pre- and at-yield mechanical behaviour of crystallites as a function of the loading direction.

Inelastic deformation is considered by treating a dislocation model of the statistical distribution of dislocation-link lengths [236]. The probability of activation is determined by the link length; only certain link lengths with low line stresses contribute to inelastic deformation [236, 237]. Closed-form expressions are found for quasi-static loading conditions, where a range of segments are activated simultaneously [11, 236–238]. Anelastic deformation is governed by the same principles, but for static loading conditions only the longest segments are expected to be activated and determine the critical shear stress. It thus is necessary to use average statistical quantities, which characterise the ensemble of dislocations in the crystallite, when one constructs an inelastic constitutive model for static loading conditions.

Firstly, DeWit and Koehler [235] obtain a parametric function for the static equilibrium shape of the FR source as a function of the self-energy by calculus of variations. Following their seminal work [235], Kovacs [239] formulates a physical yield criterion depending on the initial dislocation character of the FR source. More recently, Cash and Cai [30] investigate the dislocation contribution to acoustic non-linearity in order to non-destructively monitor plastic deformation. They present an implicit analytical expression for the anelastic shear-strain contribution of initially straight edge and screw segments. Knowing the anelastic shear strain per FR source, Koehler and DeWit [2], and Agrawal and Verma [3] present in their seminal works the apparent Young's moduli for face-centred and body-centred cubic (FCC and BCC) crystallites, respectively. Nearly all crystals are elastically anisotropic, however a framework that emerges by assuming elastic isotropy is useful and reasonably accurate for most crystals [240].

A set of convenient formulae is presented, where every simplification is made to find the closed-form expression for the tangent moduli and yield strength of cubic crystals. We are unaware of any other publication which presents such an exhaustive treatise of tangent moduli of cubic crystallites without invoking additional phenomenological assertions as made by *e.g.* Yoshida *et al.* [241] and Sun and Wagoner [242]. The former [241] include the modulus degradation by varying the instantaneous modulus as an exponential function of strain. The latter [242] propose a Quasi-Plastic-Elastic model, which uses a two-yield-surface plasticity theory; a two-surface constitutive model in which the inner surface defines the transition between the linear and non-linear elasticity and the outer surface gives the yield criteria. Aforementioned models [241, 242, 242] are built based on computational convenience and lack a physical basis [36]. For recent and exhaustive discussions on anelasticity we refer to Torkabadi [36] and Li and Wagoner [7]. Our work is based on the underlying mechanism of dislocation-driven anelasticity, which gives a physical prediction with a minimum number of parameters and is computationally convenient as well. The central limitation in the present model is that the self-energy must adhere to the form of equivalent elastic constants [243]. Present work though is readily extended to cubic anisotropy following [243–247], which is

discussed comprehensively.

OUTLINE

In the following, we consider the isotropic response of polycrystalline materials. *Firstly*, our results for various dislocation densities are compared with the predictions made by Van Liempt and Sietsma [4]. The effects of compressibility and dislocation character on experimentally obtained total dislocation density and effective segment length are presented. Our method is directly applicable for analysis of experiments as preformed by Li and Wagoner [7]. *Secondly*, the anisotropic response for single crystallites is given and validated with the initial cubic Young's moduli obtained by Koehler and DeWit [2], and Agrawal and Verma [3]. *Thirdly*, the effects of a heterogeneous dislocation distribution over glide planes on the anisotropic symmetry of the apparent elastic constants and the yield point are discussed. A limit analysis of highly compressible and incompressible solids is performed for initial edge and/or screw character segments. The influences of compressibility and dislocation densities on the initial (apparent) shear modulus are given. *Finally*, a relevant engineering case is presented with Poisson's ratio $\nu = 1/3$. The feasibility of experimentally obtaining information, more than previously possible, on dislocation networks is discussed.

2.2 METHOD

2.2.1 FRANK-READ SOURCES

We consider the differential equation of equilibrium of the Frank-Read (FR) mechanism for the case of a uniform applied shear stress $\boldsymbol{\tau}$, with components: (1) the external applied shear stress $\boldsymbol{\tau}$ doing work on the dislocation; and (2), the potential energy changing as the dislocation bows out. In Fig. 2.1, an FR source is depicted. The self-energy per unit length U

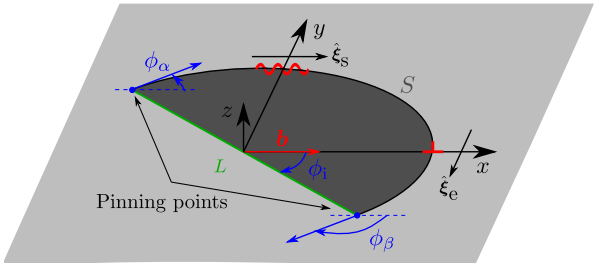

Figure 2.1: Schematic representation of a mixed character FR source ϕ_i in the light gray x-y plane with initial segment length L, dark gray swept-out area S and dislocation characters ϕ_α and ϕ_β at the pinning points.

of a dislocation segment for an elastically isotropic Volterra dislocation is approximated by the addition of pure screw b_s and pure edge b_e Burgers vector components, *i.e.*

$$U(\phi) \approx U_e + U_s = \frac{\mu^{el}}{2}\left(\frac{b_e^2}{1-\nu} + b_s^2\right), \tag{2.1a}$$

with

$$b_s = \|\boldsymbol{b}\|\cos(\phi), \qquad \text{and} \qquad b_e = \|\boldsymbol{b}\|\sin(\phi), \tag{2.1b}$$

where μ^{el} is the isotropic linear elastic shear modulus, ϕ indicates the dislocation character, *i.e.* it is the angle between the Burgers vector $\boldsymbol{b}$ and the local unit line-sense $\hat{\boldsymbol{\xi}}$, $\|\bullet\|$ the magnitude of the vector $\bullet$ and ν the Poisson's ratio. Here, the start-finish/right-hand convention is used. Note that long-range elastic interaction and the specific energy associated with the dislocation core are neglected. The line tension model is approximate because it considers the dislocation as a line that carries an energy per unit length along itself, and ignores the long-range interaction between different sections of the dislocation network. Only a single FR source is considered because the long-range interaction scales with the inverse of the range. Hence why line tension and self-interaction are low-order approximations. Self-interaction is the elastic interaction between dislocation segments across the same dislocation line. The exact expression for the dislocation energy involves a double integral along the whole loop [17, 248]. In order to attain closed-form analytical expressions, we solely consider line tension. Even with these approximations, the model is able to qualitatively capture physical behaviour of dislocations [240, 249], and hence is a useful model.

Following DeWit and Koehler [235], the static equilibrium of the FR source is determined by the method of the calculus of variation. Here, the x-y plane is the glide plane; the initial segment with length L lies along the line $y = x\tan(-\phi_{\text{i}})$, with initial dislocation character ϕ_{i}, is centred on the origin $\{0,0,0\}$ and is pinned at each end; the Burgers vector $\boldsymbol{b}$ is parallel to the x-axis; the line sense of a positive edge dislocation is anti-parallel to the y-axis; and, the unit plane normal $\hat{\boldsymbol{n}} \equiv \left(\hat{\boldsymbol{\xi}}_{\text{e}} \times \boldsymbol{b}\right) / \|\hat{\boldsymbol{\xi}}_{\text{e}} \times \boldsymbol{b}\|$ is parallel to the z-axis, which is defined as the slip system with a Cartesian coordinate system and axes $\{x, y, z\}$. The equilibrium shape of a pinned dislocation for a shear stress τ_{xz} as parametric functions is

$$x(\phi) \equiv \frac{1}{\tau_{xz} b}\left(U(\phi)\sin(\phi) + \frac{\partial U}{\partial \phi}\cos(\phi)\right) + C_1, \tag{2.2a}$$

and

$$y(\phi) \equiv \frac{1}{\tau_{xz} b}\left(U(\phi)\cos(\phi) - \frac{\partial U}{\partial \phi}\sin(\phi))\right) + C_2, \tag{2.2b}$$

where C_1 and C_2 are the integration constants. Substituting Eq. (2.1) in the equilibrium shape (2.2), we obtain the normalised FR source shape for a linear elastic isotropic material as

$$\frac{\tau_{xz} x(\phi)}{\mu^{\text{el}} b} = \frac{\left(1 + \nu\cos^2(\phi)\right)\sin(\phi)}{2(1-\nu)} + \frac{\tau_{xz} C_1}{\mu^{\text{el}} b}, \tag{2.3a}$$

and

$$\frac{\tau_{xz} y(\phi)}{\mu^{\text{el}} b} = \frac{(2 - 3\nu + \nu\cos(2\phi))\cos(\phi)}{4(1-\nu)} + \frac{\tau_{xz} C_2}{\mu^{\text{el}} b}, \tag{2.3b}$$

where C_1 and C_2 are the x- and y-coordinates of the mid-point of the major and the minor axis of the near-elliptical equilibrium shape, respectively. Here, the x- and y-coordinates are normalised with twice the seminal radius of curvature, which for a dislocation with character-independent energy ($\nu = 0$) by Schoeck [31] is the parametric function of a circle with radius $R = \mu^{\text{el}} b/(2\tau_{xz})$. As the shear stress τ_{xz} increases, the radius of curvature of the dislocation loop decreases. The bowing out of a FR source becomes critical when the applied shear stress equals the seminal maximum line stress $\tau_{\text{c}} = \mu^{\text{el}} b/L$. At shear stresses higher than the critical shear stress τ_{c}, the dislocation line stress $\mu^{\text{el}} b/(2R)$ does not compensate the

applied shear stress and the FR source is activated. The mixed character FR source in Fig. 2.1 is depicted for the critical shear stress τ_{xz}^{c}, by Kovacs [239]. Kovacs defined the critical shear stress τ_{xz}^{c} as the line stress τ_{xz} at which a diameter of the equilibrium shape coincides with the initially straight dislocation segment, *i.e.* $C_1 = C_2 \equiv 0$. The critical stress τ_{xz}^{c} is a function of the initial dislocation character ϕ_i and Poisson's ratio ν as well.

In order to calculate the anelastic dislocation shear strain contribution per FR source, the area S swept by the source is needed. The area enclosed by the initial and bowed-out segment is

$$S(\tau_{xz}) = \frac{1}{2}\int_{\phi_\beta(\tau_{xz})}^{\phi_\alpha(\tau_{xz})} \left(x\left(\phi'\right)\frac{\partial y\left(\phi'\right)}{\partial \phi'} - y\left(\phi'\right)\frac{\partial x\left(\phi'\right)}{\partial \phi'} \right) \mathrm{d}\phi', \tag{2.4}$$

where ϕ_α and ϕ_β represent the dislocation characters at the pinning points $\{x_\alpha, y_\alpha\}$ and $\{x_\beta, y_\beta\}$, respectively (See Fig. 2.1). To calculate the swept area, the dislocation characters ϕ_α and ϕ_β as a function of the line stress τ_{xz} are needed. The dislocation line stays attached to both pinning points when bowing out. The equilibrium shape must pass through $\{x_\alpha, y_\beta\}$ and $\{x_\beta, y_\beta\}$, which serves as physical boundary conditions to find the coordinates of the mid-point of the major and the minor axis of the near-elliptical equilibrium shape $\{C_1, C_2\}$. The two trigonometric polynomials, which relate the x- and y-distance between pinning points and the line stress, are formulated, *i.e.*

$$\frac{\tau_{xz} L \cos(\phi_i)}{\mu^{el} b} = \frac{\tau_{xz} x\left(\phi_\beta\right)}{\mu^{el} b} - \frac{\tau_{xz} x(\phi_\alpha)}{\mu^{el} b}, \tag{2.5a}$$

and

$$\frac{\tau_{xz} L \sin(\phi_i)}{\mu^{el} b} = \frac{\tau_{xz} y(\phi_\alpha)}{\mu^{el} b} - \frac{\tau_{xz} y\left(\phi_\beta\right)}{\mu^{el} b}. \tag{2.5b}$$

The domain of dislocation characters ϕ_α and ϕ_β at the pinning points is shifted to $[-\pi, \pi]$ by defining the difference angles $\Delta\phi_\alpha \equiv \phi_i - \phi_\alpha$ and $\Delta\phi_\beta \equiv \phi_\beta - \phi_i$. Inspecting Eq. (2.5), we find that $\Delta\phi_\alpha = \Delta\phi_\beta$ for $\phi_i = 0$, $\pi/2$, π and $3\pi/2$. Hence the axes of symmetry for an initial screw dislocation segment, with $\phi_i = 0$ and π, is the line $x = 0$ and for an initial edge dislocation, with $\phi_i = \pi/2$ and $3\pi/2$, the line $y = 0$. The Peach-Koehler force is parallel to the outward normal of each infinitesimal dislocation segment within the FR source and the newly created dislocation lines, on either half of the expanding loop, have the same self-energy. Hereby, the coordinate of the integration constant is $C_1 = 0$ for initial screw dislocation segments and $C_2 = 0$ for initial edge character segments [249].

Substituting Eqs. (2.3a) and (2.3b) into Eqs. (2.5a) and (2.5b), we obtain the relationship between the line stress, τ_{xz}, and the dislocation characters at both pinning points, ϕ_α and ϕ_β, by

$$\begin{aligned}\frac{(1-\nu)\tau_{xz} L}{\mu^{el} b}\cos(\phi_i) = \frac{1}{2}\Big(&\sin\left(\phi_\beta\right)\left(1+\nu\cos^2\left(\phi_\beta\right)\right) \\ &-\sin(\phi_\alpha)\left(1+\nu\cos^2(\phi_\alpha)\right)\Big);\end{aligned} \tag{2.6a}$$

$$\begin{aligned}\frac{(1-\nu)\tau_{xz} L}{\mu^{el} b}\sin(\phi_i) = \frac{1}{4}\Big(&\cos(\phi_\alpha)(2-3\nu+\nu\cos(2\phi_\alpha)) \\ &-\cos\left(\phi_\beta\right)\left(2-3\nu+\nu\cos\left(2\phi_\beta\right)\right)\Big).\end{aligned} \tag{2.6b}$$

The Kovacs condition, which indicates where the applied stress becomes critical [239], reads

$$\Delta\phi_\alpha^{\mathrm{c}} + \Delta\phi_\beta^{\mathrm{c}} = \pi, \tag{2.7}$$

where $\bullet^{\mathrm{c}}$ indicates the dependent variable $\bullet$ for the critical shear stress τ_{xz}^{c}. Substituting $\Delta\phi_\alpha^{\mathrm{c}}$, $\Delta\phi_\beta^{\mathrm{c}}$ and Eq. (2.7) into Eqs. (2.6a) and (2.6b), we obtain the relationships between the critical shear stress and the dislocation characters at both pinning points as

$$\frac{(1-\nu)L\tau_{xz}^{\mathrm{c}}}{\mu^{\mathrm{el}}b}\cos(\phi_{\mathrm{i}}) = \sin\left(\phi_{\mathrm{i}} + \Delta\phi_\beta^{\mathrm{c}}\right)\left(1+\nu\cos^2\left(\Delta\phi_{\mathrm{i}} + \phi_\beta^{\mathrm{c}}\right)\right); \tag{2.8a}$$

$$\frac{(1-\nu)L\tau_{xz}^{\mathrm{c}}}{\mu^{\mathrm{el}}b}\sin(\phi_{\mathrm{i}}) = -\frac{1}{2}\cos\left(\phi_{\mathrm{i}} + \Delta\phi_\beta^{\mathrm{c}}\right)\left(2-3\nu+\nu\cos\left(2\left(\phi_{\mathrm{i}} + \Delta\phi_\beta^{\mathrm{c}}\right)\right)\right). \tag{2.8b}$$

By solving Eqs. (2.8a) and (2.8b) simultaneously with a semi-analytical method, we find the critical values of the difference angles $\Delta\phi_\alpha^{\mathrm{c}}$ and $\Delta\phi_\beta^{\mathrm{c}}$, and critical shear stress τ_{xz}^{c}. The critical shear stress and associated difference angles are shown in Fig. 2.2. Similarly, character angles

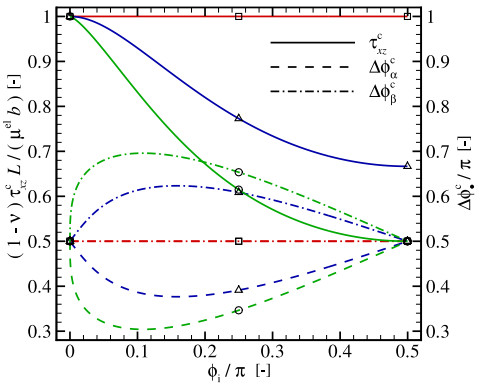

Figure 2.2: The normalised critical shear stress $(1-\nu)\tau_{xz}^{\mathrm{c}}L/(b\mu^{\mathrm{el}})$, the normalised critical difference angles $\Delta\phi_\alpha^{\mathrm{c}}/\pi$ and $\Delta\phi_\beta^{\mathrm{c}}/\pi$ as functions of normalised initial character ϕ_{i}/π for different Poisson's ratios $\nu = 0$, $1/3$ and $1/2$. The values at $\phi_{\mathrm{i}} = 0, \pi/4$ and $\pi/2$ for $\nu = 0, 1/3$ and $1/2$ are presented as square, triangle and circle symbols, respectively.

ϕ_α and ϕ_β are calculated as a function of line stress τ_{xz} with a generic initial dislocation character $\phi_{\mathrm{i}} \in (-\pi, \pi]$. Knowing the critical shear stresses τ_{xz}^{c}, we obtain difference angles $\Delta\phi_\alpha$ and $\Delta\phi_\beta$ as functions of τ_{xz} from Eqs. (2.6a) and (2.6b).

The difference angle $\Delta\phi_{\mathrm{s}}$ is defined as the monotonically increasing difference between the initial right-hand side (RHS) screw dislocation character, *i.e.* $\phi_{\mathrm{i}} \equiv 0$, and the dislocation characters $\phi_\alpha = -\Delta\phi_{\mathrm{s}}$ and $\phi_\beta = \Delta\phi_{\mathrm{s}}$. Substituting the definition of $\Delta\phi_{\mathrm{s}}$ in Eq. (2.6a), we obtain the normalised dislocation line stress as

$$\frac{\tau'_{xz}}{\tau_{\mathrm{c}}} = \left(1+\nu\cos^2(\Delta\phi_{\mathrm{s}})\right)\sin(\Delta\phi_{\mathrm{s}}), \tag{2.9}$$

with the scaled shear stress $\tau'_{xz} \equiv \tau_{xz}(1-\nu)$ and the range for τ'_{xz}/τ_c is $[-1, 1]$. Since $\cos^2(\Delta\phi_{\mathrm{s}}) \equiv \cos^2(\pi - \Delta\phi_{\mathrm{s}})$ and $\sin(\Delta\phi_{\mathrm{s}}) \equiv \sin(\pi - \Delta\phi_{\mathrm{s}})$, there are two branches of the solution for $\Delta\phi_{\mathrm{s}}$ as a function of shear stress τ_{xz}. The dislocation bows out under a given

applied shear stress $\tau_{xz} < \tau_{xz}^{\mathrm{c}}$. The diameter of the equilibrium shape is larger than the length of the initial dislocation segment with difference angle $0 \leq \Delta\phi_{\mathrm{s}} < \pi/2$. When the applied shear stress (originally $\tau_{xz} < \tau_{xz}^{\mathrm{c}}$) is subsequently removed, the bowed-out RHS screw dislocation returns to its original configuration parallel to the line $x = 0$. Hence the process is reversible. The corresponding branch with solutions $\Delta\phi_{\mathrm{s}}^{\mathrm{stable}}\left(\tau'_{xz}\right) < \pi/2$ is designated as "*stable*" because the swept-out area will only increase with increasing applied shear stress. This reversibility causes the pre-yield behaviour of FR sources. Secondly, for an applied shear stress τ_{xz} equal to the critical shear stress τ_{xz}^{c}, the diameter of the equilibrium shape coincides with the initial dislocation segment, *i.e.* the difference angle $\Delta\phi_{\mathrm{s}} = \pi/2$. When the applied shear stress (originally $\tau_{xz} = \tau_{xz}^{\mathrm{c}}$) is subsequently increased, the bowed-out dislocation line does not return to its initial configuration but keeps on expanding with difference angle $\pi/2 < \Delta\phi_{\mathrm{s}} \leq \pi$. The corresponding branch of the solution $\Delta\phi_{\mathrm{s}}^{\mathrm{unstable}}\left(\tau'_{xz}\right) \geq \pi/2$ is designated as "*unstable*" because the swept-out area will increase. This is the at- and post-yield behaviour of FR sources, which leads to plastic deformation and dislocation multiplication. Here $\tau_{xz} = \tau_{xz}^{\mathrm{c}}$ is part of the "*unstable*" solution because, although static equilibrium is attained, a small stress perturbation leads to the unstable state of continuing plastic deformation. Finally, it is trivial that $\Delta\phi_{\mathrm{s}}^{\mathrm{unstable}}\left(\tau'_{xz}\right) = \pi - \Delta\phi_{\mathrm{s}}^{\mathrm{stable}}\left(\tau'_{xz}\right)$.

The explicit equation of the difference angle for the stable equilibrium shape is

$$\Delta\phi_{\mathrm{s}}^{\mathrm{stable}} \equiv \sin^{-1}\left(2\sqrt{\frac{1+\nu}{3\nu}}\sin\left(\frac{1}{3}\sin^{-1}\left(\frac{3\sqrt{3\nu}}{2(\nu+1)}\frac{1}{\sqrt{(\nu+1)}}\frac{\tau'_{xz}}{\tau_{\mathrm{c}}}\right)\right)\right), \tag{2.10a}$$

for $\nu \neq 0$. In the limit $\nu \to 0$ the difference angle for the stable equilibrium shape is given by

$$\Delta\phi_{\mathrm{s}}^{\mathrm{stable}} \equiv \sin^{-1}\left(\frac{\tau_{xz}}{\tau_{\mathrm{c}}}\right), \tag{2.10b}$$

in agreement with Eq. (2.9). Secondly, the difference angle $\Delta\phi_{\mathrm{e}}$ is defined as the monotonically increasing difference between the initial positive edge dislocation character, *i.e.* $\phi_{\mathrm{i}} \equiv \pi/2$, and the characters $\phi_\alpha = \pi/2 - \Delta\phi_{\mathrm{e}}$ and $\phi_\beta = \pi/2 + \Delta\phi_{\mathrm{e}}$. Substituting the definition of $\Delta\phi_{\mathrm{e}}$ in Eq. (2.6b), we obtain the normalised dislocation line stress as

$$\frac{\tau_{xz}L}{\mu^{\mathrm{el}}b} = \frac{(2+3\nu-\nu\cos(2\Delta\phi_{\mathrm{e}}))\sin(\Delta\phi_{\mathrm{e}})}{2(1-\nu)} \equiv \frac{\tau_{xz}}{\tau_{\mathrm{c}}}. \tag{2.11}$$

The explicit equation of the difference angle for the stable equilibrium shape is

$$\Delta\phi_{\mathrm{e}}^{\mathrm{stable}} \equiv \sin^{-1}\left(2\sqrt{\frac{1-2\nu}{3\nu}}\sinh\left(\frac{1}{3}\sinh^{-1}\left(\frac{3\sqrt{3\nu}}{2(1-2\nu)}\sqrt{\frac{(1-\nu)^2}{1-2\nu}}\frac{\tau_{xz}}{\tau_{\mathrm{c}}}\right)\right)\right), \tag{2.12a}$$

for $\nu \neq 0$ and $\nu \neq 1/2$. Note that for Poisson's ratio $\nu = 0$, Eq. (2.10b) holds. Since $\cos(2\Delta\phi_{\mathrm{e}}) \equiv \cos(2(\pi - \Delta\phi_{\mathrm{e}}))$, again two branches of the solution for $\Delta\phi_{\mathrm{e}}$ are $\Delta\phi_{\mathrm{e}}^{\mathrm{unstable}}(\tau_{xz}) \equiv \pi - \Delta\phi_{\mathrm{e}}^{\mathrm{stable}}(\tau_{xz})$. In the limit $\nu \to 1/2$ the difference angle for the stable equilibrium shape is

$$\Delta\phi_{\mathrm{e}}^{\mathrm{stable}} \equiv \sin^{-1}\left(\sqrt[3]{\frac{\tau_{xz}}{\tau_{\mathrm{c}}}}\right). \tag{2.12b}$$

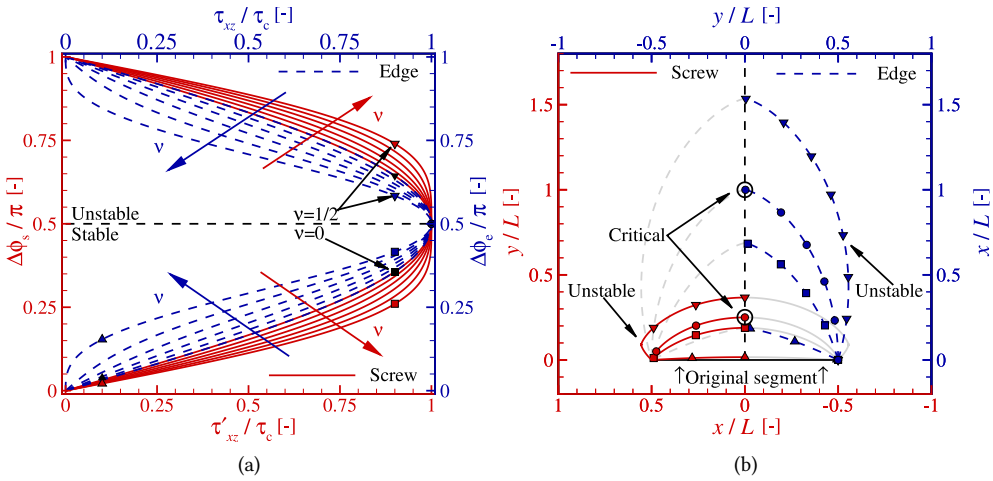

Figure 2.3: (a) The normalised difference angles $\Delta\phi_s/\pi$ and $\Delta\phi_e/\pi$ as a function of the normalised line stresses τ'_{xz}/τ_c and τ_{xz}/τ_c for Poisson's ratios $\nu = 0,\ 1/10,\ 1/5,\ 3/10,\ 2/5$ and $1/2$. The coloured arrows indicate an increase in Poisson's ratio ν across equivalently coloured lines. (b) The normalised half equilibrium shapes $\{x/L, y/L\}$ with shear stresses τ_{xz}/τ_c=τ'_{xz}/τ_c= $1/10,\ 9/10$ and 1, and Poisson's ratio $\nu = 1/2$.

Intermediate steps in the derivation of Eqs. (2.10) and (2.12) are given in Appendix A.II.

In Fig. 2.3a, the difference angles as a function of the line stress are presented. The difference angles for line stresses τ_{xz}/τ_c=τ'_{xz}/τ_c= $1/10,\ 9/10$ and 1 are indicated with triangle, square, circle and gradient symbols with Poisson's ratios $\nu = 0$ in black and for $\nu = 1/2$ in red and blue in Fig. 2.3. The gradient symbols correspond to an unstable static equilibrium solution with normalised line stress τ_{xz}/τ_c=τ'_{xz}/τ_c= $9/10$. In the following, the equilibrium shapes and swept-out areas for these stresses and Poisson's ratios are studied in more detail. In Appendix A.I, the equations for the equilibrium shape of a given FR source as a function of the angles ϕ_α and ϕ_β are given. Hereby, the static equilibrium shape of a given FR source $\{x(L,\tau_{xz}), y(L,\tau_{xz})\}$ as an explicit function of the line stress is obtained. In Fig. 2.3b, the equilibrium shapes of the FR sources with RHS screw and positive edge character are presented for Poisson's ratio $\nu = 1/2$. Since the shapes are symmetric, half is shown in colour, half in grey. The triangle and square symbols indicate the stable shapes, the circle symbols the critical shapes and the gradient symbols the unstable shapes. These symbols indicate the shapes for the line stresses τ_{xz}/τ_c=τ'_{xz}/τ_c= $1/10,\ 9/10$ and 1 as indicated in Fig. 2.3a. When the applied shear stress increases so does the circumference of the FR source and the swept-out area S. For Poisson's ratio $\nu = 1/2$, the equilibrium shapes are markedly different between initial RHS screw and initial positive edge FR sources. For isotropic elasticity, the energy per unit edge character line length is a factor $1/(1-\nu)$ times higher than that for pure screw character. This is why the dislocation line aligns towards a majority of screw character and line length with edge character is minimised. However, because the dislocation line must remain continuous, locally sharp corners appear for both "*stable*" and "*unstable*" geometries with increased Poisson's ratio ν. As expected for the maximum dislocation line stress [239], the given diameter of the critical equilibrium shape coincides with the

initial dislocation segment, *i.e.* $\Delta\phi_s = \pi/2$ and $\Delta\phi_e = \pi/2$. Dislocation dynamics governs line shape under quasi-static loading conditions in both the "*stable*" and "*unstable*" regime. However, for static loading conditions, we show in [249] that the dislocation loop orients in the lowest line-tension direction as well when self-interaction is included. When the applied stress is increased beyond the critical shear stress τ^c_{xz}, the FR source continues to expand as depicted by the (dashed) lines with gradient symbols in Fig. 2.3b. This leads to the well known dislocation multiplication mechanism. Note that once the critical stress is exceeded, no stable quasi-static equilibrium is attained. The time-dependent relation can solely be found solving the inherently dynamic problem. However, the tendency of the dislocation loop to orient itself in the lowest self-energy direction remains. This is only captured by the unstable quasi-static equilibrium solution, which also represents the shape for $\tau_{xz} > \tau^c_{xz}$. Notwithstanding, the present unstable equilibrium solution is relevant beyond purely theoretical interest. We repeat the realistic numerical calculations by Fitzgerald *et al.* [247] for isotropic elasticity [249]. Long-range elastic interaction across the dislocation loop is incorporated. The line tension model is qualitatively consistent with the results which include self interaction [240, 249]. The self interaction suppresses the bowing out of the FR source. As a result, for the same magnitude of applied shear stress, the inclusion of long-range interaction reduces the swept out area. It is demonstrated that loops remain "*stable*" even when the applied stress surpasses the maximum dislocation line stress by about a factor two. The FR source attains static equilibrium beyond the approximate half-ellipse shape. Secondly, we reason that within a dislocation network, activated FR sources will experience long-range stresses from adjacent dislocation segments. These stresses are known as back stresses and allow for attaining a equilibrium with dislocation loop shapes comparable to the unstable equilibrium.

The area swept by a given FR source as a function of the difference angles is given in Appendix A.III. Combining Eqs. (2.10) and (2.12), and Eqs. (A.14) and (A.15), respectively, we obtain the explicit equation for the swept area $S(\tau_{xz})$. For the sake of brevity, only two limiting cases are given, namely the positive edge segment and only the normalised areas for the stable equilibrium shape, being

$$\frac{S(\tau_{xz})}{L^2} = \frac{1}{8(\tau_{xz}/\tau_c)^2}\left(2\sin^{-1}\left(\frac{\tau_{xz}}{\tau_c}\right) - \sin\left(2\sin^{-1}\left(\frac{\tau_{xz}}{\tau_c}\right)\right)\right), \tag{2.13a}$$

and

$$\begin{aligned}\frac{S_e(\tau_{xz})}{L^2} = \frac{1}{128(\tau_{xz}/\tau_c)^2}\Bigg(&60\sin^{-1}\left(\sqrt[3]{\frac{\tau_{xz}}{\tau_c}}\right) - 45\sin\left(2\sin^{-1}\left(\sqrt[3]{\frac{\tau_{xz}}{\tau_c}}\right)\right) - \cdots \\ &\cdots 9\sin\left(4\cos^{-1}\left(\sqrt[3]{\frac{\tau_{xz}}{\tau_c}}\right)\right) - \sin\left(6\sin^{-1}\left(\sqrt[3]{\frac{\tau_{xz}}{\tau_c}}\right)\right)\Bigg),\end{aligned} \tag{2.13b}$$

for $\nu = 0$ and $1/2$, respectively. In Fig. 2.4, the dislocation line stress is presented in relation with the swept area. The axes are chosen as such to readily relate with tensile curves, but note that hardening is not considered here. The calculated stress is the stress needed to accomplish plastic strain by a single dislocation loop. The triangle, square, circle and gradient symbols in Fig. 2.4 correspond to those in Fig. 2.3. We observe that the area-to-stress relation has a continuously changing slope and zero gradient for the critical shear stress τ^c_{xz}. Initially

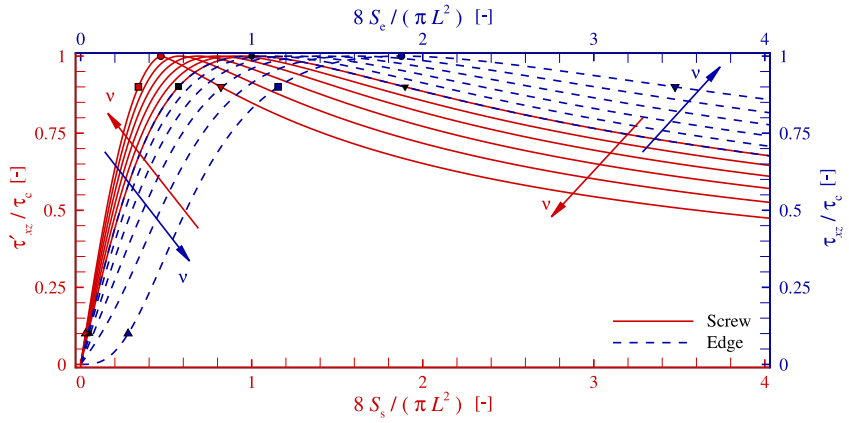

Figure 2.4: The normalised line stresses τ'_{xz}/τ_c and τ_{xz}/τ_c as a function of the normalised swept-out areas $8S_s/(\pi L^2)$ and $8S_e/(\pi L^2)$ for Poisson's ratios $\nu = 0$, 1/10, 1/5, 3/10, 2/5 and 1/2. The arrows indicate an increase in Poisson's ratio ν across equivalently coloured lines, from $\nu = 0$ to 1/2.

the dislocation line stress increases with swept area S. The line stress increase depends on the Poisson's ratio ν and is largest for an initial screw dislocation segment because mixed character dislocation line is formed upon expansion of the dislocation loop. *Vice versa*, the dislocation loop of an initial edge character FR source easily expands, which gives rise to a high local gradient $\partial S/\partial\tau_{xz}$. Secondly, the local gradient of the area-to-stress relation depends on the length and orientation of the formed dislocation line. The length of the loop with a majority of edge character is minimised while the formation of predominant screw character dislocation lines requires less work (See Fig. 2.3b). However, given that the dislocation line cannot terminate within the bulk of the material, parts of the loop must attain orientations with higher self-energy. Hereby, the dislocation line stress increases rapidly upon the formation of approximately pure edge character dislocation line as witnessed between the red square and circle symbols in Fig. 2.4 ($0.9 \leq \tau'_{xz}/\tau_c \leq 1$). And, contrary, an initial edge character FR source sweeps a large area between shear stresses $0.9 \leq \tau_{xz}/\tau_c \leq 1$ (the blue square and circle symbols in Fig. 2.4). The unloading curve will be the same as the loading curve because dissipation is not taking place in the static solution here. It should be noted that the present model reproduces the anelastic strain for a given stress state but not the symmetric unloading/loading curves as reported in *e.g.* [4–7]. The maximum dislocation line stress is highest for screw character FR sources because a pure edge character dislocation line is formed. Once the applied stress matches the critical shear stress, the line stress reduces upon further expansion of the dislocation loop. The dislocation loop will expand and the potential energy is minimised. This "*unstable*" line stress equals the minimum applied stress needed for the loop to continue expanding. Unimpeded expansion of the loop results in softening which is expected when a single FR source is considered and work-hardening is excluded.

2.2.2 Strain in Uniaxially Loaded Crystallites

For an arbitrary stress $\boldsymbol{\sigma}$ in the crystal frame, the corresponding strain $\boldsymbol{\epsilon}$ is a superposition of the elastic and anelastic strains, $\boldsymbol{\epsilon}^{\mathrm{el}}$ and $\boldsymbol{\epsilon}^{\mathrm{an}}$, respectively. The crystal frame is a Cartesian coordinate system with axes $\{x', y', z'\}$ with right-hand orthonormal basis $\hat{\boldsymbol{e}}_i \parallel \boldsymbol{t}_i$, with translation vectors $\boldsymbol{t}_i$. In Fig. 2.5, a schematic representation of the crystal frame is given. The second-order elastic lattice strain tensor $\boldsymbol{\epsilon}^{\mathrm{el}}$ is derived through a linear mapping

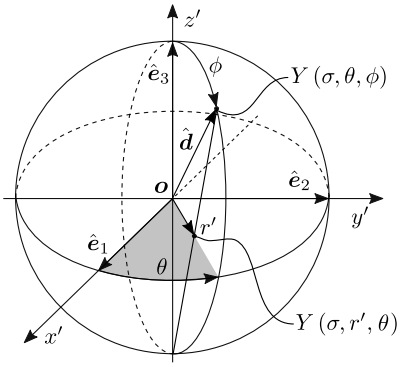

Figure 2.5: Schematic representation of the tangent modulus Y on a unit sphere in the crystal frame and the stereographic projection onto the plane with its normal parallel to $\hat{\boldsymbol{e}}_3$ containing the origin $\boldsymbol{o}$.

of the infinitesimal second-order stress tensor $\boldsymbol{\sigma}$ with a fourth-order tensor $\left(\boldsymbol{C}^{\mathrm{el}}\right)^{-1}$ called the inverse elastic (*i.e.* stiffness) tensor [250–252]. The stiffness tensor has major and minor symmetry. For a given slip system with Burgers vector $\boldsymbol{b}$ and unit slip-plane normal $\hat{\boldsymbol{n}}$ in the crystal frame, the Orowan equation [253] is used and the second-order infinitesimal anelastic strain is

$$\boldsymbol{\epsilon}^{\mathrm{an}}(\boldsymbol{\sigma}) = \frac{N}{2}\frac{S(\boldsymbol{\sigma})}{V}\mathrm{Sym}(\boldsymbol{b}\otimes\hat{\boldsymbol{n}}), \tag{2.14}$$

where N/V is the number of FR sources with length L per unit volume V and $\mathrm{Sym}(\bullet)$ is the symmetric part of tensor $\bullet$. Hereby, slip is solely a function of the resolved shear stress.

For given stress tensor $\boldsymbol{\sigma} = \sigma\hat{\boldsymbol{d}}\otimes\hat{\boldsymbol{d}}$, where $\hat{\boldsymbol{d}}$ is a unit vector parallel to the normal stress with magnitude σ, the corresponding principal strain is $\epsilon = \boldsymbol{\epsilon} : \hat{\boldsymbol{d}}\otimes\hat{\boldsymbol{d}}$. The unit vector in the loading direction is

$$\hat{\mathsf{d}} = (\cos(\theta)\sin(\phi), \sin(\theta)\sin(\phi), \cos(\phi))^{\mathsf{T}}, \tag{2.15}$$

where θ is the azimuth angle, ϕ from here on the polar angle. The infinitesimal principal strain ϵ in the crystal frame is a superposition of the elastic and anelastic components ϵ^{el} and ϵ^{an}. The principal elastic lattice and anelastic strains are

$$\epsilon^{\mathrm{el}}\left(\sigma, \hat{\boldsymbol{d}}\right) = \sigma\hat{\boldsymbol{d}}\otimes\hat{\boldsymbol{d}} : \left(\boldsymbol{C}^{\mathrm{el}}\right)^{-1} : \hat{\boldsymbol{d}}\otimes\hat{\boldsymbol{d}} \tag{2.16a}$$

and,

$$\epsilon^{\mathrm{an}}\left(\sigma, \hat{\boldsymbol{d}}\right) = \hat{\boldsymbol{d}}\otimes\hat{\boldsymbol{d}} : \boldsymbol{\epsilon}^{\mathrm{an}}(\boldsymbol{\sigma}), \tag{2.16b}$$

respectively. In order to employ computational algebra to calculate the spatial representation of the moduli, the well-known Voigt scheme is used [249]. If the material is devoid of

dislocations, the well-known definition of the linear elastic Young's modulus $E \equiv \sigma/\epsilon^{\mathrm{el}}$ is obtained. Contrary, with dislocations present the tangent modulus $Y \equiv \partial\sigma/\partial\epsilon$ depends on the direction $\hat{\boldsymbol{d}}$, the magnitude of the normal stress σ and the dislocation structure. Furthermore, the left-hand side of Eq. (2.16a) is not limited to isotropic or cubic elasticity but valid for any symmetric elastic tensor $\boldsymbol{C}^{\mathrm{el}}$. We note that the effective Poisson's ratio is unaffected because volume is conserved during dislocation glide. Hence the scaled effective Poisson ratio $\nu(\theta,\phi)/\nu^{\mathrm{el}}$ remains a unit sphere.

The scaled linear elastic Young's modulus $E(\theta,\phi)/E^{\mathrm{el}}$ can be graphically represented in spherical coordinates $\{r,\theta,\phi\}$, with $r \equiv \|E(\theta,\phi)/E^{\mathrm{el}}\|$. For isotropic linear elastic materials devoid of dislocations [251, 252], the Young's modulus is a unit sphere. Equivalent to the frequently used spherical representation of linear elastic anisotropy, the tangent modulus can be shown in spherical coordinates with $r \equiv \|Y(\sigma,\theta,\phi)/E^{\mathrm{el}}\|$. A two-dimensional representation by means of a stereographic projection onto the plane with its normal parallel to $\hat{\boldsymbol{e}}_3$ and containing the origin $\boldsymbol{o}$ is possible since $Y(\hat{\boldsymbol{d}}) = Y(-\hat{\boldsymbol{d}})$. The polar angle is expressed as $\phi = 2\tan^{-1}\left(r'\right)$, with the polar coordinates $\{r',\theta\}$ [251]. The stereographic projection is included in Fig. 2.5.

2.3 Results

2.3.1 Isotropic Mechanical Response

In the following, we present the results for virtual tensile tests on polycrystalline materials. For an isotropic mechanical response, the principal strain is

$$\epsilon(\sigma) = \frac{\sigma}{E^{\mathrm{el}}} + \epsilon^{\mathrm{an}}(\sigma). \tag{2.17}$$

In Appendix B, the relation between the normal stress and resolved shear stress, and the principal anelastic strain and anelastic shear strain by the Taylor factor M [4, 254, 255] is revisited. Assuming FR sources to be uniformly distributed over $k = 12$ slip systems with dislocation density ρ^{slip} each, *i.e.* the total dislocation density $\rho^{\mathrm{total}} = \sum_k \rho_k^{\mathrm{slip}} \equiv k\rho^{\mathrm{slip}}$, and substituting Eqs. (2.14) and (B.4) in Eq. (2.17), we give the total principal strain as

$$\epsilon(\sigma) = \frac{\sigma}{E^{\mathrm{el}}} + \frac{b}{M}\left(\frac{\rho_{\mathrm{e}}^{\mathrm{total}} S_{\mathrm{e}}(\sigma)}{L_{\mathrm{e}}} + \frac{\rho_{\mathrm{s}}^{\mathrm{total}} S_{\mathrm{s}}(\sigma)}{L_{\mathrm{s}}}\right), \tag{2.18}$$

with $\rho^{\mathrm{total}} \equiv \rho_{\mathrm{s}}^{\mathrm{total}} + \rho_{\mathrm{e}}^{\mathrm{total}}$, where $\rho_{\mathrm{s}}^{\mathrm{total}}$ and $\rho_{\mathrm{e}}^{\mathrm{total}}$, and L_{s} and L_{e} are the dislocation densities and effective segment lengths of screw and edge dislocations, respectively. In the works by Van Liempt and Sietsma [4] and Arechabaleta *et al.* [5, 6], the equilibrium shape of the FR source is circular and the total principal strain is

$$\epsilon_{\mathrm{iso}}(\sigma) \approx \frac{\sigma}{E^{\mathrm{el}}} + \frac{M\rho^{\mathrm{total}}\left(E^{\mathrm{el}}\right)^2 b^3}{32(\nu+1)^2\sigma^2 L}\left(2\sin^{-1}\left(\frac{2(1+\nu)\sigma L}{ME^{\mathrm{el}}b}\right) - \sin\left(2\sin^{-1}\left(\frac{2(1+\nu)L\sigma}{ME^{\mathrm{el}}b}\right)\right)\right), \tag{2.19}$$

with L independent of dislocation character. Here, four cases are considered, namely: (1) the results by Van Liempt and Sietsma [4]; (2) only screw dislocation segments (*i.e.* $\rho_{\mathrm{s}}^{\mathrm{total}} = \rho^{\mathrm{total}}$ and $\rho_{\mathrm{e}}^{\mathrm{total}} = 0$) with length $L_{\mathrm{s}} = L$; (3) only edge dislocation segments (*i.e.* $\rho_{\mathrm{s}}^{\mathrm{total}} = 0$ and $\rho_{\mathrm{e}}^{\mathrm{total}} = \rho^{\mathrm{total}}$) with length $L_{\mathrm{e}} = L$; (4) mixed dislocation densities $\rho_{\mathrm{s}}^{\mathrm{total}} = \rho_{\mathrm{e}}^{\mathrm{total}} = \rho^{\mathrm{total}}/2$

with lengths $L_e = L_s = L$. First, the total dislocation density $\rho^{\text{total}} = 10^{14}$, 5×10^{14} and 10^{15} m^{-2} is varied while the effective segment length $L = 140$ nm is kept constant; secondly, the effective segment length $L = 100$, 140 and 200 nm changes while the total dislocation density $\rho^{\text{total}} = 5\times10^{14}$ m^{-2} remains constant. In Fig. 2.6, the tensile results are presented with Young's modulus $E^{\text{el}} = 210\times10^{9}$ Pa, Poisson's ratio $\nu = 0.3$, Taylor factor $M = 3.06$ [256–258] and Burgers vector magnitude $b = 0.25$ nm. In Fig. 2.6, the elastic response is represented

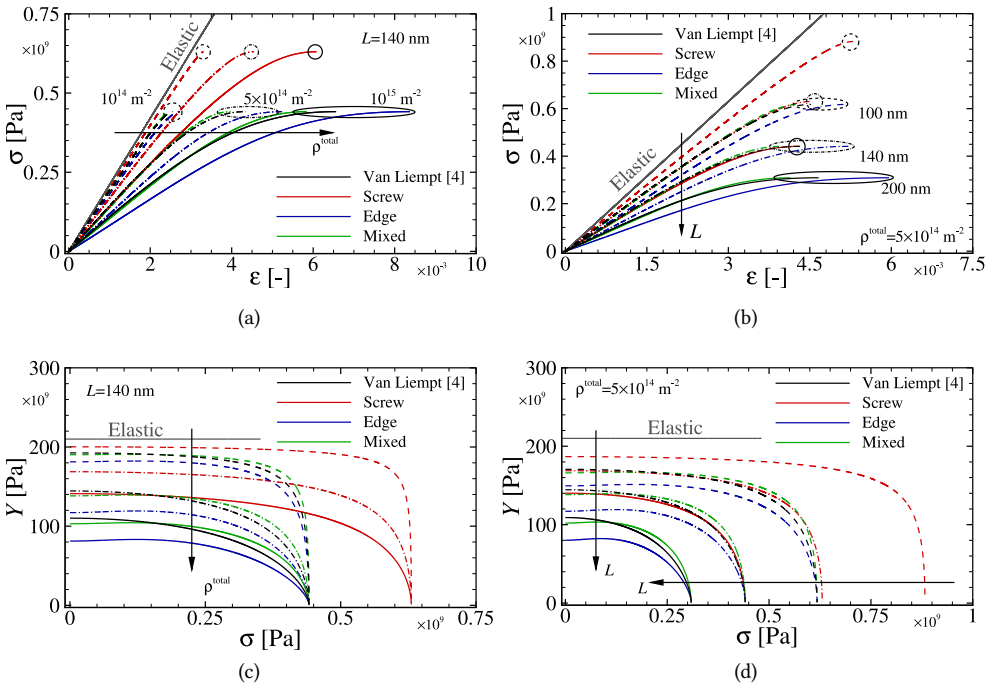

Figure 2.6: The normal stress σ as a function of principal strain ϵ for (a) effective segment length $L = 140$ nm and total dislocation densities $\rho^{\text{total}} = 10^{14}$, 5×10^{14} and 10^{15} m^{-2}, and (b) density $\rho^{\text{total}} = 5\times10^{14}$ m^{-2} and lengths $L = 100$, 140 and 200 nm. The tangent modulus Y as a function of the normal stress σ in (c) and (d). The arrows in (a) and (c) indicate an increase in total dislocation density ρ^{total}, and in (b) and (d) an increase in effective segment length L across lines with a given colour.

by a solid gray line marked "Elastic". The results with constant effective segment length $L = 140$ nm and total dislocation densities $\rho^{\text{total}} = 10^{14}$, 5×10^{14} and 10^{15} m^{-2} are indicated by dashed, dash-dotted and solid lines, respectively. The same line patterns hold for results with constant density $\rho^{\text{total}} = 5\times10^{14}$ m^{-2} and lengths $L = 100,$ 140 and 200 nm.

While varying the total dislocation density for the effective segment length $L = 140$ nm, we observe in Fig. 2.6a that the principal strain increases with dislocation density. The principal anelastic strain is the horizontal distance between the line $\sigma \equiv E^{\text{el}}\epsilon$ and any point on the tensile curve. When the dislocation density per slip plane is increased, and in turn, so is the anelastic dislocation strain (See Eq. 2.14). In Fig. 2.6b, the dislocation density $\rho^{\text{total}} = 5\times10^{14}$ m^{-2} and the effective segment length is varied. We observe that the principal anelastic strain increases with effective increasing segment length. The anelastic dislocation

shear strain scales with the area swept by an FR source, which scales with the square of the effective segment length, $S \propto L^2$. Furthermore, the normal stress for a given anelastic strain is inversely proportional to the effective segment length because the self-stress scales with the curvature of the bowed-out dislocation. In the present work dissipation is not accounted for, hence why the initial modulus deviates from the isotropic linear elastic modulus from the start of loading. Furthermore, the tangent modulus vanishes when the applied stress matches the line tension, because upon further expansion of the FR loops the line stress decreases.

The differences between the prediction by Van Liempt and Sietsma [4] and the results for solely screw or edge dislocations are striking. Between screw dislocations and the prediction by [4], the normal stress for a given total principal strain differ up to a factor $1/(1-\nu)$, *i.e.* on the order of 50%. Also for a given stress the principal anelastic strains differ up to a factor $(1-\nu)$. Hence the normal stress is underestimated and total principal strain overestimated. While the range of normal stresses is unaffected between edge dislocations and the prediction by [4], the anelastic dislocation strains differ a factor $1/(1-\nu)$, hence the total principal strain is underestimated. The observed differences are easily rationalised by considering an elliptical equilibrium shape and with the results in Fig. 2.4 for initial screw and edge character sources. The prediction by [4] and the results for mixed dislocation segments match closely.

In order to present the tangent modulus, we take the inverse of the derivative of Eq. (2.19) with respect to the normal stress and obtain the isotropic tangent modulus [4], *i.e.*

$$Y_{\mathrm{iso}}(\sigma) \approx \left(\frac{1}{E^{\mathrm{el}}} + \frac{\rho^{\mathrm{total}} L b}{2M\sigma} \frac{\left(ME^{\mathrm{el}}b\right)^2}{(2(\nu+1)\sigma L)^2} \left(\sqrt{\frac{(2(\nu+1)\sigma L)^2}{\left(ME^{\mathrm{el}}b\right)^2 - (2(\nu+1)\sigma L)^2}} - \sin^{-1}\left(\frac{2(\nu+1)\sigma L}{ME^{\mathrm{el}}b} \right) \right) \right)^{-1} . \tag{2.20}$$

In Figs. 2.6c and 2.6d the tangent modulus as a function of the normal stress (extended Kocks-Mecking plot [4]) is presented. These correspond to Figs. 2.6a and 2.6b, respectively. In Fig. 2.6c, we observe that the initial modulus decreases with increasing total dislocation density. Furthermore, in Fig. 2.6d, the given change in segment length affects the initial moduli. The inverse relationship between the yield stress and the effective segment length is clearly visible in Fig. 2.6d. Considering the prediction by Van Liempt and Sietsma [4] and the results for mixed dislocation segments, we observe that the tangent moduli are close as well.

Arechabaleta *et al.* [5] evaluated the validity of the model with approximate circular equilibrium shape [4] by comparison with dislocation densities from X-Ray Diffraction (XRD) measurements. The dislocation densities $10^{12} < \rho^{\mathrm{total}} \leq 10^{14}$ m^{-2} obtained through aforementioned model [4] were consistent with those obtained by XRD. We note that the prediction by [4] approximates the results for isopycnic dislocation densities in Fig. 2.6. Isopycnic means of, relating to, or marked by equal or constant density. Hereby, the experimental XRD diffraction and tensile-test measurements of the total dislocation density ρ^{total} might have agreed too.

It is of interest to study the effect of different screw and edge dislocations densities on previously experimentally obtained total dislocation densities and effective segment lengths. They were calculated by means of Eqs. (2.19) and (2.20) [4–6]. Here, a set of virtual tensile tests is performed for various edge and screw dislocation densities $\rho_{\mathrm{s}}^{\mathrm{total}}/\rho^{\mathrm{total}} = 1 - \rho_{\mathrm{e}}^{\mathrm{total}}/\rho^{\mathrm{total}} = 0$, 1/8, 1/4, 3/8, 1/2, 5/8, 3/4, 7/8, 15/16, 99/100 and 1. In Fig. 2.7, the tensile results are given by solid black lines with screw dislocation densities $\rho_{\mathrm{s}}^{\mathrm{total}}/\rho^{\mathrm{total}} = 0,\ 1/2,\ 3/4$ and 1, total dis-

location density $\rho^{\text{total}} = 10^{15}$ m^{-2} and effective segment length $L = 140$ nm. Here the dashed

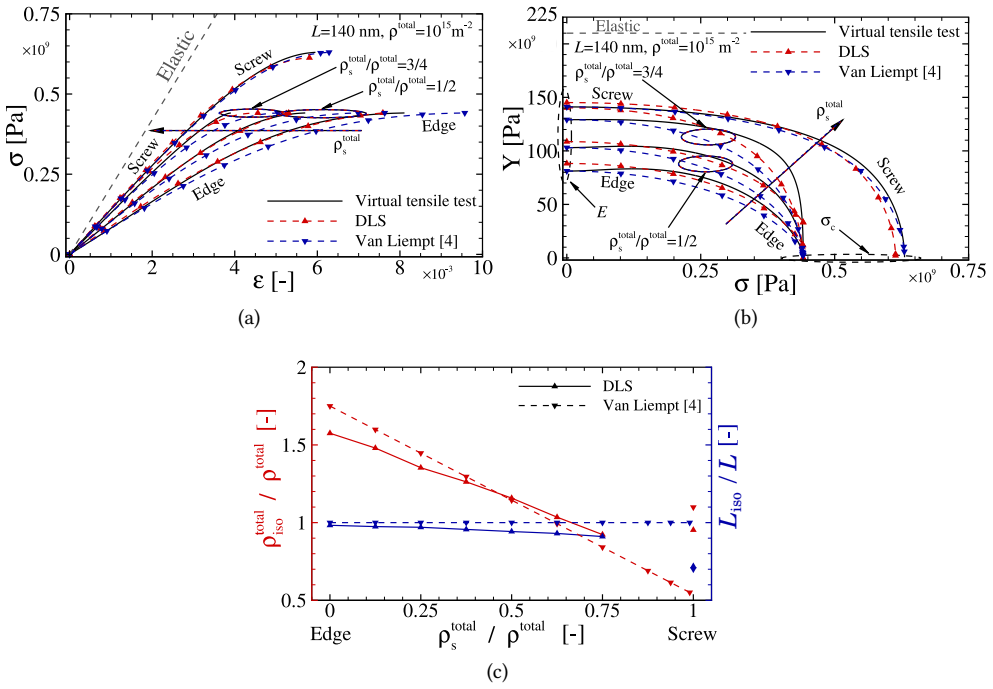

Figure 2.7: (a) The normal stress σ as a function of the principal strain ϵ and (b) the tangent modulus Y as a function of the normal stress σ with screw dislocation densities $\rho_{\text{s}}^{\text{total}}/\rho^{\text{total}} = 0,\ 1/2,\ 3/4$ and 1, total density $\rho^{\text{total}} = 10^{15}$ m^{-2} and effective segment length $L = 140$ nm. The arrows in (a) and (b) indicate an increase in total screw dislocation density $\rho_{\text{s}}^{\text{total}}$ across equivalently coloured lines. (c) The ratios $\rho_{\text{iso}}^{\text{total}}/\rho^{\text{total}}$ and L_{iso}/L as a function of the scaled screw dislocation density $\rho_{\text{s}}^{\text{total}}/\rho^{\text{total}}$ via the damped least-squares (DLS) method and the method by Van Liempt and Sietsma [4].

gray line marked "Elastic" indicates the linear elastic response; in Fig. 2.7b, the tangent modulus as a function of the normal stress is given. Subsequently, a non-linear fitting and the fitting procedure as followed by Van Liempt and Sietsma [4] are preformed on the tensile-test data sets. The former method is the damped least-squares (DLS) method [259, 260] with Eq. (2.19), $L = L_{\text{iso}}$ and $\rho^{\text{total}} = \rho_{\text{iso}}^{\text{total}}$. In the latter method, the effective segment length L_{iso} is obtained at the yield points with critical normal stress $\sigma_{\text{c}} \equiv M\mu^{\text{el}}b/L_{\text{iso}}$; the initial Young's modulus, *i.e.* $E \equiv \lim_{\sigma\to 0} Y(\sigma)$, is used to determine the effective dislocation density $\rho_{\text{iso}}^{\text{total}}$. The numerical fits by DSL method and the method by Van Liempt and Sietsma are indicated by solid blue and dashed red lines, respectively, in Figs. 2.7a and 2.7b solely for $\rho_{\text{s}}^{\text{total}}/\rho^{\text{total}} = 0,\ 1/2,\ 3/4$ and 1. In Fig. 2.7c, the obtained ratios L_{iso}/L and $\rho_{\text{iso}}^{\text{total}}/\rho^{\text{total}}$ are presented. The red triangle and blue gradient symbols in Figs. 2.7a and 2.7b indicate results of the DLS method and the method by Van Liempt and Sietsma [4], respectively. The symbols in Fig. 2.7c correspond to the tensile-test data with varying screw dislocation density $\rho_{\text{s}}^{\text{total}}$. The (dashed) lines connecting these symbols are guides to the eye. The results for solely screw dislocations are indicated separately. They represent a limit case given the difference in yield

strength from finite edge dislocation densities. The goodness of fit is assessed by calculating the coefficient of determination R^2. The obtained coefficients of determination are between $R^2 = 0.96$ and 1. The non-linear fits by DLS method for ratio $3/4 \leq \rho_s^{\text{total}}/\rho^{\text{total}} < 1$ do not converge to the global minimum and are therefore omitted.

The effective dislocation density $\rho_{\text{iso}}^{\text{total}}$ is significantly affected by the ratio between edge and screw dislocations. In the limit of solely edge dislocations, the total dislocation density ρ^{total} is overestimated. The observed effective segment length L_{iso} differs far less from the actual length L because the yield strength $\sigma_c \propto 1/L$. For an approximately elliptic dislocation loop, the observed total dislocation density $\rho_{\text{iso}}^{\text{total}}$ and segment length L_{iso} agree well with density ρ^{total} and length L when the ratio $\rho_s^{\text{total}}/\rho^{\text{total}} \approx 1/(2-\nu)$. For Poisson's ratio $\nu = 1/3$ this screw dislocation density $\rho_s^{\text{total}}/\rho^{\text{total}} \approx 0.58$ and in agreement with the observed unit ratios between $\rho_s^{\text{total}}/\rho^{\text{total}} \approx 0.62-0.64$. The method by Van Liempt and Sietsma underestimates the total dislocation density ρ^{total} for a majority of screw dislocations, *i.e.* $1/2 << \rho_s^{\text{total}}/\rho^{\text{total}} < 1$. Finally, for solely screw dislocations, the effective segment length is underestimated by a factor ~ 0.3 because the critical shear stress is $\tau_c/(1-\nu)$. The effective dislocation density $\rho_{\text{iso}}^{\text{total}}$ differs marginally from the given total density ρ^{total}. This is non-trivial. Quantifying the observational error in previous works is however only possible if additional information on the geometry of the given dislocation network was measured. The method here does not need additional observations on the dislocation network geometry. The orientation of individual dislocations and a generic Poisson's ratio are *a priori* incorporated.

2.3.2 Anisotropic Mechanical Response

In the following, we present the results for virtual tensile tests on single crystallites with cubic crystal lattices. In the supplementary material [249], the slip systems in face- and body-centred (FCC and BCC) crystallites, respectively, are given. For BCC crystallites, only twelve $\langle 111 \rangle \{110\}$ slip systems are considered. They form the six main glide planes at low temperatures [240], instead of the forty-eight potential slip systems which include $\{112\}$ and $\{123\}$ planes. In order to present the effect of a nonuniform dislocation distribution, the effective segment length $L_s = L_e = L$ is kept constant and solely the density ρ^{slip} is varied. The present method is not limited to the same fractions of initial dislocation segments with a given character per slip-system either. Though under static loading conditions it remains necessary to use effective segment lengths which characterise the ensemble of dislocations in a given crystallite.

Dislocations are spread homogeneously across each active slip-system contained within a single crystallite. The total dislocation density per slip system $\rho^{\text{slip}} \equiv \rho_s^{\text{slip}} + \rho_e^{\text{slip}}$, where ρ_s^{slip} and ρ_e^{slip} are the screw and edge dislocation densities per slip system. We choose to limit the results to pure (or a mixture of pure) screw and edge character segments. The present method is not limited to these assumptions, but needs numerical root-finding to approximate the equilibrium solution for an arbitrary initial dislocation character ($\phi_i \neq -\pi/2$, 0, $\pi/2$ and π) for Poisson's ratio $\nu \neq 0$, while the closed-form expressions for initial pure edge and screw character segments do not. The dislocation density on each glide plane is defined as the sum of its constituent slip systems. Here, we use the seminal proportionality coefficient $\alpha \equiv \left(L\sqrt{\rho^{\text{total}}}\right)^{-1} = 1/3$ which was both experimentally [6] ($\alpha \approx 0.4$) and theoretically [261] obtained.

In order to validate our method with the works by Koehler and DeWit [2], and Agrawal and Verma [3], we take the series expansion of Eq. (2.13a) around zero applied shear stress and obtain the engineering shear strain

$$\gamma_{xz}^{\mathrm{an}} = \frac{b\rho^{\mathrm{slip}}}{L} S(\tau_{xz}) \simeq \frac{\rho^{\mathrm{slip}} L^2}{6} \frac{\tau_{xz}}{\mu^{\mathrm{el}}}. \tag{2.21}$$

Assuming the dislocation density ρ^{slip} to be constant across all slip systems and Poisson's ratio $\nu = 0$, we give the fourth-order inverse anelastic tensor in vector-matrix notation as

$$\begin{pmatrix} \epsilon_{11}^{\mathrm{an}} \\ \epsilon_{22}^{\mathrm{an}} \\ \epsilon_{33}^{\mathrm{an}} \\ 2\epsilon_{23}^{\mathrm{an}} \\ 2\epsilon_{13}^{\mathrm{an}} \\ 2\epsilon_{12}^{\mathrm{an}} \end{pmatrix} \simeq \frac{\rho^{\mathrm{slip}} L^2}{12\mu^{\mathrm{el}}} \begin{pmatrix} \frac{8}{3} & -\frac{4}{3} & -\frac{4}{3} & 0 & 0 & 0 \\ -\frac{4}{3} & \frac{8}{3} & -\frac{4}{3} & 0 & 0 & 0 \\ -\frac{4}{3} & -\frac{4}{3} & \frac{8}{3} & 0 & 0 & 0 \\ 0 & 0 & 0 & \frac{8}{3} & 0 & 0 \\ 0 & 0 & 0 & 0 & \frac{8}{3} & 0 \\ 0 & 0 & 0 & 0 & 0 & \frac{8}{3} \end{pmatrix} \cdot \begin{pmatrix} \sigma_{11} \\ \sigma_{22} \\ \sigma_{33} \\ \sigma_{23} \\ \sigma_{13} \\ \sigma_{12} \end{pmatrix}. \tag{2.22}$$

This corresponds to the results for a uniform distribution of dislocations across all glide planes in FCC by Koehler and DeWit [2] and in BCC by Agrawal and Verma [3].

For a single active glide plane with two active slip systems in FCC and BCC, we find Tetragonal *versus* Rhombic anisotropic symmetry because of the difference in angles between the Burgers vectors $\langle 110\rangle/2$ and $\langle 111\rangle/2$. Inactive slip systems and/or glide planes are devoid of dislocations and active ones have isopycnic dislocation densities. For two active glide planes Rhombic *versus* Tetragonal anisotropic symmetry is found. In addition the angles between glide plane normals, $\{111\}/\sqrt{3}$ and $\{110\}/\sqrt{2}$, differ. The anisotropic symmetry is unique for any (non)uniform distribution of dislocations and depends on the crystal structure as well. Furthermore, the obtained anisotropic symmetry is independent of Poisson's ratio ν and a given normal stress below the yield stress. We find it notable that for distributions with differing edge and screw dislocation densities the number of symmetry planes reduces. The anisotropic ratio [262] and index [263] do depend on dislocation distribution, densities and characters. In the supplementary material [249], the normalised initial Young's moduli E/E^{el} for nonuniform distributions of dislocations in FCC and BCC are presented. Finally, as expected for the uniform distribution of dislocations across all glide planes, the initial modulus has cubic anisotropy as seen in Fig. 2.8.

2.3.3 Limit Analysis

In the following, we consider the compressibility and incompressibility limits, *i.e.* Poisson's ratios $\nu = 0$ and $1/2$. In the supplementary material [249], the normal stress-strain relations are presented in five rational tensile directions for several nonuniform dislocation distributions in FCC and BCC. For tensile tests on single crystallites, it is well-known that the normal stress at yield is predicted by means of the Schmid factor and the often used critical shear stress $\tau_{\mathrm{c}} \equiv \mu^{\mathrm{el}} b/L$ [264]. Hence the yield stress decreases, or remains the same, as more glide planes become active. The normal stress-strain relationships for a uniform distribution of dislocations are the same for FCC and BCC. From here on, only cubic lattices with uniform dislocation distributions are considered.

In Fig. 2.9, the tensile results are presented with Poisson's ratio $\nu = 1/2$, edge or screw dislocations and rational tensile directions $\langle 100\rangle$, $\langle 110\rangle$ and $\langle 111\rangle$. In Fig. 2.9, the rational

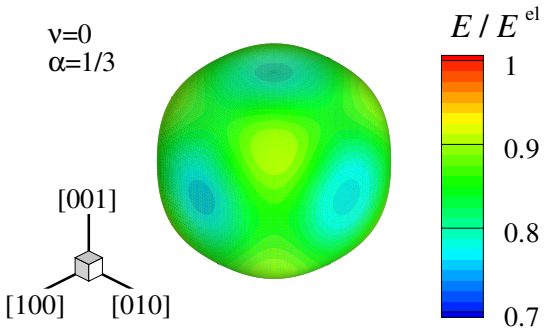

Figure 2.8: The normalised initial Young's modulus E/E^{el} in spherical coordinates for a cubic crystallite with Poisson's ratio $\nu = 0$ and a uniform distribution of dislocations across all glide planes.

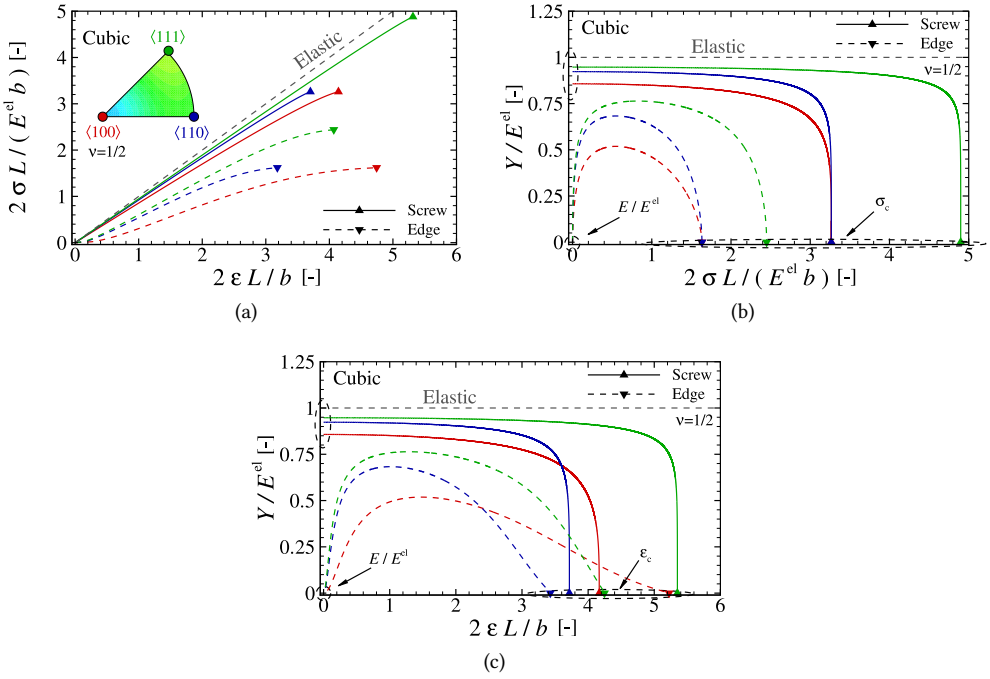

Figure 2.9: (a) The normalised normal stress $2\sigma L/(E^{\mathrm{el}}b)$ as a function of normalised principal strain $2\epsilon L/b$, (b) the normalised tangent modulus Y/E^{el} as a function of the normalised stress $2\sigma L/\left(E^{\mathrm{el}}b\right)$, and (c) the normalised strain $2\epsilon L/b$ with Poisson's ratio $\nu = 1/2$ in rational tensile directions ⟨100⟩, ⟨110⟩ and ⟨111⟩.

tensile directions are indicated by coloured dots on the inserted stereographic projection of Fig. 2.8. The stress σ_{c} and strain ϵ_{c} at yield are depicted by coloured triangle and gradient symbols in Fig. 2.9. Note that the choice of normalisation originates from $E^{\mathrm{el}}/2 \equiv \mu^{\mathrm{el}}$ for Poisson's ratio $\nu = 0$. It is obvious that the strain ϵ is not obtained by the linear elastic stiffness alone because FR sources contribute significantly to the total principal strain. As

expected, we obtain the largest anelastic dislocation strain contribution for edge character segments and Poisson's ratio $\nu = 1/2$. Intermediate values are found for Poisson's ratio $\nu = 0$ independent of initial dislocation character (See Fig. 2.10) and the smallest anelastic strain contribution results for screw dislocations and Poisson's ratio $\nu = 1/2$. The anisotropy is not affected by the dislocation character.

In Figs. 2.9b and 2.9c, the normalised tangent moduli Y/E^{el} as a function of the normalised stress $2\sigma L/\left(E^{\mathrm{el}}b\right)$, and the normalised strain $2\epsilon L/b$, respectively, are presented. The flow-stress σ_{c} and critical principal strain ϵ_{c} are the intersects of given tangent modulus with $Y/E^{\mathrm{el}} = 0$. During tensile experiments the observed tangent modulus does not reduce to zero for critical normal stress σ_{c} [4–6, 265, 266]. Before the tensile curve becomes horizontal, work-hardening initiates with shear stress contribution τ_{w} and plastic shear strain γ_{p}. The flow stress is $\sigma_{\mathrm{f}} \simeq \sigma_{\mathrm{c}} + \sigma_{\mathrm{w}}$ and the work-hardening gradient $\Theta \equiv \partial\sigma_{\mathrm{f}}/\partial\epsilon_{\mathrm{p}}$. Values of constant gradient Θ during Stage-I/II/III work-hardening are typically one to three orders of magnitude smaller than the elastic Young's modulus [20]. Hence plastic deformation commences when the tangent modulus, Y, equals the work-hardening gradient, Θ. Moreover, the critical stress σ_{c} and strain ϵ_{c} are the upper bounds of the yield point.

In Fig. 2.9, we observe a marked difference between the tangent moduli for edge or screw dislocation segments. Regarding initial edge character segments in the limit $\sigma \to 0$, we find that the initial tangent modulus approaches zero. This is readily understood by taking the limit $\lim_{\tau_{xz}\to 0} \partial\Delta\phi_{\mathrm{e}}/\partial\tau_{xz}$ of Eq. (2.12b). It is intuitive that with a given change of dislocation character at both pinning points, the total dislocation line length either increases or decreases, and the local line sense changes. The associated change in potential energy can be split into: (1) a contribution solely due to line length change with constant dislocation character; and (2), a change in self-energy with dislocation character for a constant line length. Even though the line length increases when a given FR source with initial pure edge character bows out, the increase in potential energy associated with total segment length is lowered because dislocation character changes along the dislocation loop. From pure edge character, which has the maximum self-energy for a finite Poisson's ratio, the local line sense changes to a mixed character. In the limit of an incompressible solid, the total energy change is zero because the increase in potential energy per unit dislocation line length with constant character equals the reduction in self-energy with dislocation character. Contrarily, when a given FR source with initial pure screw character bows out, the potential energy increases with both dislocation line length and the change of character. Hence the apparent elastic constants depend on the initial dislocation character and compressibility.

It is of interest to compare our results with the isotropic predictions by Van Liempt and Sietsma [4]. Moreover, a mix of initial edge and screw characters segments is incorporated. In Fig. 2.10, the tensile results are presented with Poisson's ratios $\nu = 0$ and $1/2$, and isopycnic dislocation densities. In Fig. 2.10a, the normal stress-strain relation is given and the isotropic results for Taylor factor $M = 3.06$ are represented with dashed and solid black lines. The solid and dashed lines correspond to Poisson's ratios $\nu = 0$ and $1/2$, respectively. Comparing Figs. 2.9a and 2.10a for Poisson's ratio $\nu = 1/2$, we observe that the yield stress is determined by the initial edge dislocation segments. These segments attain their critical shape before initial screw segments as predicted by Kovacs [239]. The principal strain for a given stress decreases compared to solely edge dislocations since $\rho_{\mathrm{e}}^{\mathrm{total}} < \rho^{\mathrm{total}}$ (See Fig. 2.9 and 2.10). The predicted critical normal stress σ_{c} by Van Liempt and Sietsma [4] agrees well with single

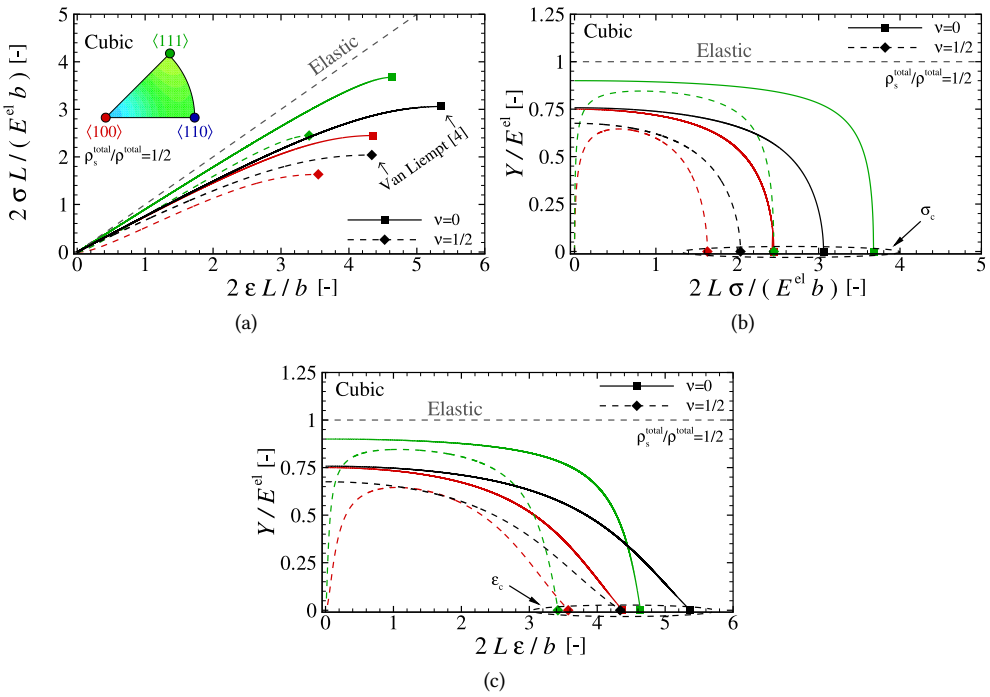

Figure 2.10: (a) The normalised normal stress $2\sigma L/(E^{\mathrm{el}}b)$ as a function of normalised principal strain $2\epsilon L/b$ with Poisson's ratios $\nu = 0$ and $1/2$, screw dislocation density $\rho_{\mathrm{s}}^{\mathrm{total}}/\rho^{\mathrm{total}} = 1/2$ and rational tensile directions $\langle 100\rangle$ and $\langle 111\rangle$. The normalised tangent modulus Y/E^{el} as a function of (b) the normalised stress $2\sigma L/\left(E^{\mathrm{el}}b\right)$ and (c) the normalised strain $2\epsilon L/b$. The dashed and solid black lines indicate the isotopic results in Eqs. (2.19) and (2.20) by Van Liempt and Sietsma [4].

crystallite results because the critical shear stress is $\tau_{\mathrm{e}}^{\mathrm{c}} \equiv \mu^{\mathrm{el}}b/L$. However, the predicted total principal strain at yield ϵ_{c} by Van Liempt and Sietsma [4] is an overestimate because the anelastic shear strain across different slip systems is the same (See Appendix B). Contrarily, here the anelastic shear strain depends on slip system orientation. Hence not every slip system contributes equally in the given tensile direction. The exaggerated anelastic strain in the isotropic model [4] leads to overestimating the total dislocation density (See Sec. 2.3.1).

The cubic tangent moduli and the isotropic tangent modulus by Van Liempt and Sietsma [4] are given in Figs. 2.10b and 2.10c. The Taylor factor M proportionally scales the isotropic curves. For Poisson's ratio $\nu = 0$, the functional forms of our results and the isotropic prediction by [4] agree. For Poisson's ratio $\nu = 1/2$, we observe a large disparity between our results and the isotropic tangent modulus by [4]. Notable are the differences in tangent moduli for small normal stresses and principal strains. This is readily understood because the self-energy in the isotropic prediction by Van Liempt and Sietsma [4] is independent of dislocation character. Hereby, the potential energy always increases with dislocation line length. Hence the gradient of the normal stress/strain-to-modulus relation is negative for any normal stress (and principal strain).

2

In order to illustrate the effects of compressibility, ν, and dislocation densities ρ_s^{total} and ρ_e^{total}, the normalised initial shear modulus, $\mu/\mu^{\text{el}} \equiv \lim_{\tau_{xz}\to 0} \mu(\tau_{xz})/\mu^{\text{el}}$, is given as a function of the Poisson's ratio ν and density $\rho_s^{\text{slip}}/\rho^{\text{slip}}$ in Fig. 2.11. The densities are varied from solely edge to only screw dislocations in increments of $\Delta\rho_s^{\text{slip}} = \rho^{\text{slip}}/5$ across coloured (dashed) lines in Fig. 2.11a. The shear moduli are presented for the given proportionality

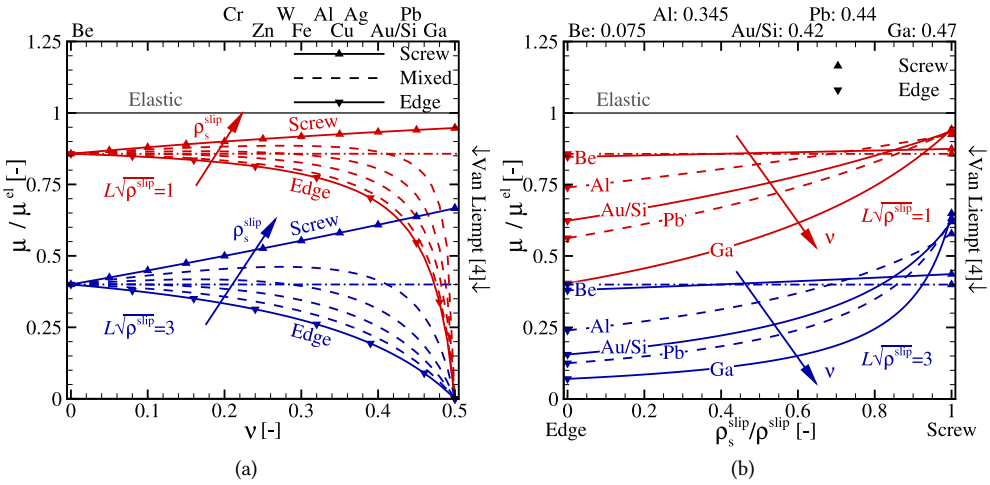

Figure 2.11: The normalised initial shear modulus μ/μ^{el} as a function of (a) the Poisson's ratio ν and (b) the scaled screw dislocation density $\rho_s^{\text{slip}}/\rho^{\text{slip}}$ with inverse coefficients $L\sqrt{\rho^{\text{slip}}} = 1$ and 3. The arrows indicate an increase in (a) screw dislocation density ρ_s^{slip} and (b) Poisson's ratio ν across equivalently coloured lines.

coefficients $(L\sqrt{\rho^{\text{slip}}})^{-1}$ =1/3 and 1 in a single active slip system. Several metals are depicted in Fig. 2.11a with their horizontal loci corresponding to their respective Poisson's ratios, *e.g.* Au and Si with $\nu = 0.42$, and Cr with $\nu = 0.21$. The initial shear moduli predicted by Van Liempt and Sietsma [4] are depicted by horizontal dashed-dotted lines. The initial modulus as a function of the screw dislocation density is given in Fig. 2.11b, for several Poisson's ratios. As expected, we observe that the initial modulus is only independent of dislocation character for Poisson's ratio $\nu = 0$. Otherwise, when a given FR source with initial pure screw character bows out, the potential energy increases with dislocation line length and the change of local line sense towards a mixed character. Hereby, the initial shear modulus increases with Poisson's ratio ν and screw dislocation density ρ_s^{slip}. Juxtaposed, the increase in potential energy with line length is lowered because of the formation of mixed character dislocation line from an initial pure edge dislocation. Hence the initial modulus depends on the fractions of screw and edge dislocations. For a given increase in Poisson's ratio $\nu \geq 0.4$ and/or edge dislocation density ρ_e^{slip}, the initial shear modulus tends to zero. As expected, the initial modulus decreases with increasing coefficient $L\sqrt{\rho^{\text{slip}}}$. A given decrease in proportionality coefficient α implies an increase in dislocation density and/or initial segment length. Apart from an increase in dislocation density after plastic deformation, the accompanying changes in dislocation character affect the initial moduli.

This might explain why accurate predictions of the apparent linear elastic constants after plastic deformation proved impossible up to now [5].

2.3.4 Cubic Crystallites

In the following, we study materials with Poisson's ratio $\nu = 1/3$ which is commonly used for steels and aluminium. It is well-known that at low temperatures BCC iron contains predominantly screw dislocations [267]. Furthermore, BCC related non-Schmid effects [268], *e.g.* the lack of mirror symmetry with respect to planes orthogonal to the dominant $\langle 111 \rangle$ slip directions and the structure of the screw cores, are not considered here. Recently, Cash and Cai [30] discussed the surplus of edge dislocations in fatigued FCC metals. Given that a dislocation network is continuous and cannot terminate inside the bulk, a single character segment distribution is rare. Here, dislocation densities $\rho_s^{\text{total}}/\rho^{\text{total}} = 1/4$ and $3/4$ are considered. The virtual tensile results are presented in Fig. 2.12. As expected [239],

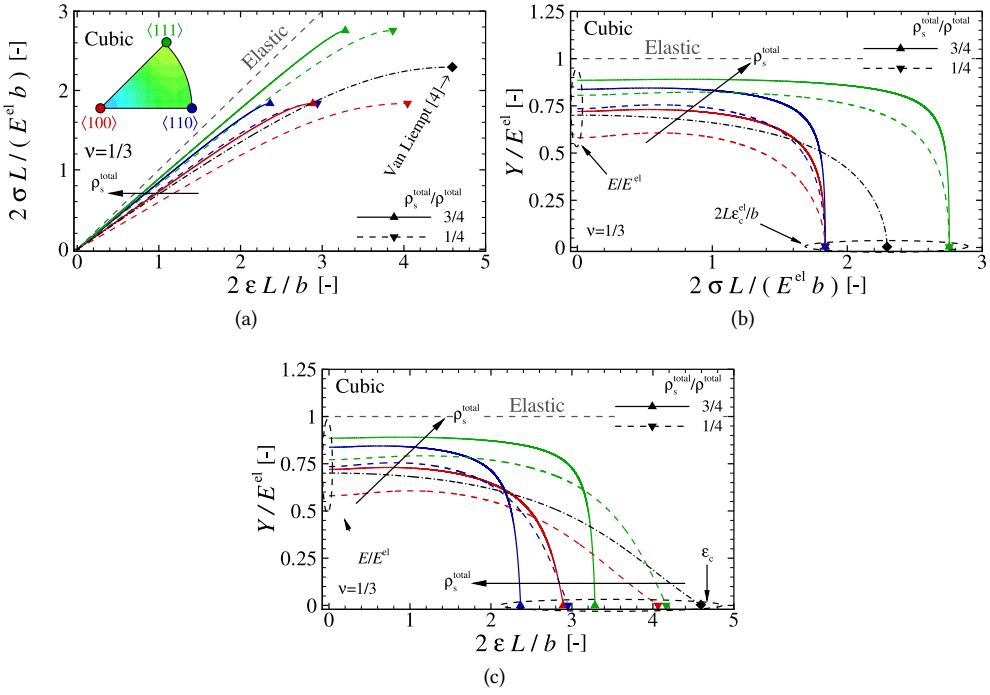

Figure 2.12: (a) The normalised normal stress $2\sigma L/(E^{\text{el}}b)$ as a function of normalised principal strain $2\epsilon L/b$ with densities $\rho_s^{\text{total}}/\rho^{\text{total}} = 1/4$ and $3/4$, and rational tensile directions $\langle 100 \rangle$, $\langle 110 \rangle$ and $\langle 111 \rangle$. The normalised tangent modulus Y/E^{el} as a function of (b) the normalised stress $2\sigma L/\left(E^{\text{el}}b\right)$ and (c) the normalised strain $2\epsilon L/b$. The black arrows marked with ρ_s^{total} indicate an increase in screw dislocation density ρ_s^{total} across lines with a given colour. The dashed-dotted black line indicates the isotopic results in Eqs. (2.19) and (2.20) by Van Liempt and Sietsma [4].

the yield strength is independent of screw dislocation density ρ_s^{total}. Here, the initial segment lengths are equal $L_s = L_e$. Thus edge character FR sources become critical first; when $L_s > L_e/(1-\nu)$, screw character FR sources become critical before edge character segments.

Hence the yield strength depends on the length of edge character segments, or the segment length of screw dislocations. This is a general observation. The isotropic prediction by Van Liempt and Sietsma [4] with Taylor factor $M = 3.06$ is indicated by a dashed-dotted black line with diamond symbols in Fig. 2.12. In accordance with Fig. 2.11, the initial Young's modulus E/E^{el} increases with increasing screw dislocation density $\rho_{\mathrm{s}}^{\mathrm{total}}$. We note that the gradients of the cubic tangent moduli Y/E^{el} are initially positive. The positive initial gradient is markedly different from the prediction by Van Liempt and Sietsma [4]. The principal strain increases with edge dislocation density $\rho_{\mathrm{e}}^{\mathrm{total}}$. The increase in anelastic strain is most apparent at the yield stress (See Figs. 2.12b and 2.12c). Given that the anelastic strain increases with (edge) dislocation density, the linear elastic stiffness cannot *a priori* predict the principal strain in compressible materials either.

In order to experimentally obtain information on a physical dislocation network, the quantitative and qualitative change in stress-strain relationship, with a given change in dislocation densities, has to be observable. It is obvious that this criterion is satisfied for Poisson's ratio $\nu = 1/2$ (See Figs. 2.9-2.11). However, many engineering materials are compressible due to which the difference in initial moduli decreases (See Fig. 2.11). Fortunately, the anelastic strain, and in turn the tangent moduli, differ significantly for Poisson's ratio $\nu = 1/3$. This is most apparent between the tensile results in the $\langle 100 \rangle$ directions. These display a difference in initial moduli E of about a tenth of the linear elastic Young's modulus E^{el}; the difference in principal strains ϵ_{c} is about half the elastic strain $\epsilon_{\mathrm{c}}^{\mathrm{el}}$ for σ_{c} (See Fig. 2.12b). The latter is intuitive because an initial edge character FR source sweeps out a large area S near activation of the FR source.

Nearly all crystals are elastically anisotropic, at least to some extent. For several technically important engineering materials with cubic anisotropy the Zener ratio $Z \equiv 2C_{44}/(C_{11} - C_{12})$ [269]. In materials with low Zener ratios, the FR source equilibrium shape is approximately elliptical because self-energy chiefly depends on dislocation character. As the anisotropy ratio increases, discrete segments of the dislocation loop tend to align themselves along directions which are not necessarily screw orientations. Even so, Fitzgerald [244] showed that the critical shear stress τ_{xz}^{c} of various initial dislocation segment orientations, in BCC iron at room temperature, is approximated within an order of magnitude by an equivalent elastically isotropic material provided that $Z < 5$. When the ratio $Z \geq 2.5$, depending on the Burgers vector and slip system, sharp corners emerge in the dislocation loop equilibrium shape. Contrary to the elastically isotropic case, these corners are not directly associable with dislocation character [244]. Those sharp corners are due to thermodynamic instability of certain dislocation orientations [246] as a given crystallite's anisotropy ratio increases with, *e.g.*, temperature. The influences of Zener ratio and dislocation orientation in α-iron are comprehensively discussed in [244–247].

Firstly, we argue that aluminium is a promising candidate to perform single crystal tensile-test upon. Foremost, aluminium is considered a "fairly isotropic" FCC material with anisotropy ratio 1.23 (equal to the Zener ratio for cubic anisotropy [262]). The Poisson's ratio $\nu \approx 0.33$ is high enough to experimentally obtain distinguishable changes in tangent modulus and yield point with a given change in dislocation density, effective segment length and dislocation character. Furthermore, the emergence of a surplus of edge character dislocation segment is expected for a fatigued specimen [30]. This warrants a noticeable change in tensile behaviour. Secondly, for crystallites with cubic anisotropic elasticity,

Scattergood and Bacon [243] developed a method to calculate effective elastic isotropic moduli with dislocations in mind. Note that these effective elastic isotropic moduli are not the apparent elastic moduli, but similar to the Voigt [270] and Reuss [271] average elastic moduli, which were developed to model the aggregate behaviour of poly-crystallites. The effective moduli are defined as explicit functions of the pre-logarithmic part of the self-energy of straight screw and edge dislocations in a given slip system. Aubry *et al.* [246] showed that one can model dislocation loop equilibrium shapes in BCC crystallites using the isotropic elasticity and Scattergood and Bacon's approximation. According to [246], the Scattergood and Bacon model produces results in reasonable agreement with the full anisotropic numerical calculations of a a given dislocation loops on a given slip system. Our framework distinguishes between different slip systems and allows for tailoring the effective elastic constants per glide plane, and even per initial line sense and Burgers vector. This allows one to model the tangent moduli and yield points in crystallites with high Zener ratios, e.g, in single iron crystallites with $Z \approx 8$ as the α-γ transition is approached [272]. The present elastic-anelastic constitutive model takes account of anisotropic effects on a per-grain basis. For crystallographically textured materials, with *e.g.* cubic elasticity, an additional level of abstraction is necessary beyond the present constitutive model, which is satisfied by probabilistic or full-field crystal plasticity methods.

2.4 Conclusions

In this chapter, the anisotropic tangent moduli and the yield points for heterogeneous dislocation networks in single crystallites are presented. First, the explicit expression for the area swept by a FR source pre-, at- and post-yield is derived. Secondly, the geometries of the slip systems in FCC and BCC single crystallites are incorporated. Making use of well known methods from linear elastic theory, we visualise the apparent elastic constants.

It is shown that the previously predicted isotropic tangent modulus by Van Liempt and Sietsma [4] only yields accurate results for highly compressible material. For a finite Poisson's ratio, previous analysis was prone to over- and/or underestimate the total dislocation density and effective segment length. Varying the dislocation density across slip systems to describe a (non)uniform dislocation distribution, we observe:

- The pre-yield mechanical response for a given dislocation network in a linear elastic isotropic material is anisotropic. The anisotropic symmetry and the magnitude of anisotropy depend on the dislocation distribution, density and character;

- The initial moduli depend on the ratio between edge and screw dislocations for a finite Poisson's ratio. They decrease with increasing edge dislocation density and Poisson's ratio. For incompressible solids with a finite edge dislocation density, the apparent initial Young's modulus vanishes;

- The yield strength of single crystals depends on the initial lengths of edge or screw dislocation segments. The anelastic dislocation strain increases with (edge) dislocation density. Hence the total principal strain at yield cannot be predicted by the linear elastic stiffness alone.

3

Static Unified Inelastic Model: pre- and post-yield dislocation-mediated deformation

Modelling dislocation glide over the initial part of a stress-strain curve of metals received little attention up to now. However, dislocation glide is essential to ones understanding of the fundamental relationship between inelastic deformation and the evolution of the dislocation network structure. Therefore, we present a model of dislocation-driven deformation under static loading conditions.

In this chapter, we reproduce repeated cyclic uniaxial tensile tests on Interstitial-Free and Low-Alloy steels. The elastic mechanical behaviour is described by isotropic linear elasticity, pre-yield anelastic mechanical behaviour by a dislocation bow-out model with dissipation, and the post-yield evolution of dislocation network structure by a statistical storage model. We hypothesise that when the local anelastic compliance is lower than the global plastic compliance, deformation is mechanically recoverable, and vice versa. This hypothesis is corroborated with the classical Taylor relation. We report the relation between stable and unstable dislocation glide using this prototypical modelling framework.

We find four structural variables, that are based on dislocation physics, to describe the stress-strain curve: total dislocation density, average dislocation segment length, dislocation junction formation rate, and average dislocation junction length. Firstly, we quantify the dislocation network evolution during uniaxial monotonic loading, and verify work-hardening by dislocation junction formation and a Taylor-type equation for flow. Finally, we present a semi-empirical relation for the evolution of the dislocation network structure. Which allows us to: refine the physical interpretation of the Taylor relationship, and rationalise experimental observations on apparent modulus degradation by thermomechanical processing. Both these findings circumvent the limitations of current, physics-based hardening models.

NOMENCLATURE

Variable	Definition	Dimension (mass M, length L and time t)
α	proportionality	–
α'	Taylor relationships' constant	–
b	Burgers vector magnitude	L
β	junction formation rate	–
$\bar{\beta}$	work-hardenability	–
C	constant	– & L^{-1}
γ	shear strain	–
E	elastic modulus	$ML^{-1}t^{-2}$
ϵ	strain	–
Θ	tangent modulus	$ML^{-1}t^{-2}$
j & k	slip-system indices	–
l	segment length	L
M	Taylor factor	–
μ	shear modulus	$ML^{-1}t^{-2}$
N	number	–
ν	Poisson's ratio	–
ξ	junction length	L
R	radius	L
RMSE	root mean-square error	–, L^{-2} & $ML^{-1}t^{-2}$
R^2	coefficient of determination	–
ρ	dislocation density	L^{-2}
$\hat{q}^{-1}$	hardening ratio	–
S	area	L^2
σ	stress	$ML^{-1}t^{-2}$
τ	shear stress	$ML^{-1}t^{-2}$
V	volume	L^3
ϕ	angle	–
x & z	Cartesian coordinates	L

3.1 INTRODUCTION

In this chapter, we construct a model of inelastic deformation under static loading conditions. We propose a novel yield criterion that encompasses both the local behaviour of individual sources and the global dislocation interactions that constitute hardening. First, we ensure that the bow-out model [273] and a statistical storage [274] model share the same set of dislocation structural variables, which is the *unification* in the present work. Then, we hypothesise that when the local anelastic compliance is higher than the global plastic compliance, deformation is mechanically irrecoverable, and *vice versa*. The unified inelastic model consists of three parts: part *one* describes the anelastic deformation in the absence of structural change in the dislocation network, *i.e.* the dissipative dislocation bow-out model [7]. Here, we simplify the quasi-static bow-out model by Benzerga *et al.* [273]; part

This chapter is based on the scientific article: Van Dokkum, J. S., Bos, C., Offerman, S. E., Sietsma, J. Static Unified Inelastic model: dislocation-mediated deformation pre-, at- and post-yield. *Materialia*, 101694, 2023.

two describes the structural change of the dislocation network with plastic strain. Here, we re-interpret the proto(type)-statistical storage model by Kocks [19]; and, part *three* is the physics-based criterion that identifies the transition from mechanically recoverable to irrecoverable deformation. In the remainder of the present work, we consider static loading conditions [17], *i.e.* time-dependent (dislocation) interactions that take place at much shorter timescales than the rate of loading and unloading. The present model must be: *general*, to apply to various metals; *concise*, to represent dislocation physics; *consistent*, to incorporate commonplace material properties; and, *transparent*, to uniquely capture the stress-strain curves shape. These steps allow us to define the four unique physical, structural variables of total dislocation density, average segment length, junction formation rate and average junction length. Herewith we finalise our unified model, that we use to analyse uniaxial tensile force-displacement curves.

All is performed under the following main assumption: *the proportionality α between the square root of the dislocation density $\sqrt{\rho}$ and the number of junctions per unit dislocation length $1/\langle l \rangle$ is constant for monotonic uniaxial loading in each cycle.* This is based on the relation between the the proportionality α and the Taylor relationships' constant α' [33] as proposed by Arechabaleta *et al.* [6]. The proportionality $\alpha \equiv 1/\left(\langle l \rangle \sqrt{\rho}\right)$ thus represents the geometry of the dislocation network, wherein the global dislocation density is connected to the local dislocation-link structure as described by average dislocation segment length $\langle l \rangle$. From a physics perspective, we identify a disparity between the invariance of the Taylor relationships' constant α' during work hardening, which is widely accepted, and the different functional forms of the proportionality α. Several works find that the proportionality α is constant [6, 31, 32], while others [5, 7, 8] report that it decreases with plastic deformation.

Outline

The following results are presented and discussed: *first*, we corroborate our definition of yield with the square root dependence of the yield strength on dislocation density. Wherefore we analyse the experimental force-displacement results of asymmetric stress, low cyclic, uniaxial ratcheting of single phase, Interstitial-Free and Low-Alloy, steels [5, 6]. Moreover, we find our definition of yield to be in keeping with the Taylor relationship [33]; *then*, we reproduce the evolution of average dislocation segment length and density with plastic monotonic uniaxial loading. Combining these findings, we construct the statistical storage-base work-hardening model. The statistical storage-based work-hardening model allows us to verify that the Taylor relationship captures the flow stress increase with dislocation network structure evolution; *finally*, we find that the proportionality α decreases monotonically with plastic strain, yet distinctly different from previous reports [6, 7]. These observations prompt us to experimentally quantify the evolution of the dislocation network structure. Hence we derive a new, semi-empirical relation of proportionality change that accompanies work hardening. This relation then allows us to: present a new physical interpretation for the Taylor relationships' constant α'; rationalise previous experimental observations [28, 38, 41, 275–278] on the changes in initial apparent moduli with thermomechanical processing; and, finally, we propose a first step towards improving the current unified inelastic model.

3.2 THEORY

For an isotropic mechanical response and uniaxial loading σ, the total principal strain is

$$\epsilon(\sigma) = \epsilon_{\text{el}}(\sigma) + \epsilon_{\text{in}}(\sigma) = \frac{\sigma}{E} + \epsilon_{\text{an}}(\sigma) + \epsilon_{\text{pl}}(\sigma), \tag{3.1}$$

with elastic lattice strain ϵ_{el}, inelastic strain ϵ_{in}, and anelastic and plastic strains, ϵ_{an} and ϵ_{pl}, respectively, where E is the isotropic linear elastic modulus. Here, the Roman subscript $\cdot$ indicates a given mean-field property $\bullet$. In the following, we consider solely isothermal deformation conditions.

3.2.1 ANELASTIC STRAIN

A pinned dislocation segment with length l lays along the x-axis with the applied shear stress τ^{PK} in Fig. 3.1. Benzerga *et al.* [273] solved the differential equation of motion, under

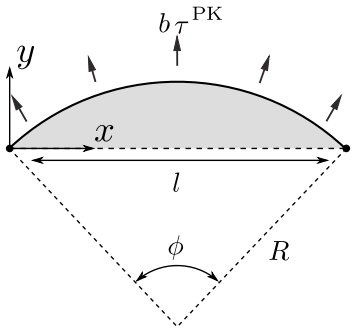

Figure 3.1: Schematic representation of a dislocation link with radius of curvature R, subtended angle ϕ and swept area S indicated by a grey semicircle (Adapted from [4]).

quasi-static loading conditions, of a single dislocation link for a constant Peach-Koehler force $\tau^{\text{PK}}b$, with the Burgers vector magnitude b. The Roman superscript $^{\cdot}$ indicates a given specification $\bullet$. These quasi-static loading conditions mean that the solution of the differential equation of motion is approximated by omission of inertia [279]. Under static equilibrium, the velocity of the dislocation line vanishes and the given link's curvature is

$$\frac{1}{R} = \frac{2\tau^{\text{PK}}}{\mu b}, \tag{3.2}$$

where $\mu = E/(2(1+\nu))$ is the linear elastic shear modulus, with Poisson's ratio ν. The area swept by the given link is

$$S(\phi) = \begin{cases} -\pi R^2 - \frac{1}{2}R^2(\phi - \sin(\phi)), & -\pi \geq \phi > -2\pi; \\ \frac{1}{2}R^2(\phi - \sin(\phi)), & \pi > \|\phi\| \geq 0; \\ \pi R^2 - \frac{1}{2}R^2(\phi - \sin(\phi)), & \pi \leq \phi < 2\pi; \end{cases}, \tag{3.3}$$

with the subtended angle

$$\phi(R/l) = \begin{cases} -2\pi - 2\sin^{-1}(l/(2R)), & R < -\frac{l}{2}; \\ 2\sin^{-1}(l/(2R)), & \|R\| \leq \frac{l}{2}; \\ 2\pi - 2\sin^{-1}(l/(2R)), & \frac{l}{2} < R; \end{cases} . \tag{3.4}$$

Substituting Eqs. (3.2) and (3.4) in Eq. (3.3), we obtain the swept area for shear stress $\tau^{\mathrm{PK}} < \mu b/l$ as

$$S\left(\tau^{\mathrm{PK}}, l\right) = \frac{l^2}{8}\left(\frac{\tau^{\mathrm{c}}}{\tau^{\mathrm{PK}}}\right)^2\left(2\sin^{-1}\left(\frac{\tau^{\mathrm{PK}}}{\tau^{\mathrm{c}}}\right) - \sin\left(2\sin^{-1}\left(\frac{\tau^{\mathrm{PK}}}{\tau^{\mathrm{c}}}\right)\right)\right), \tag{3.5}$$

with the critical line stress $\tau^{\mathrm{c}} \equiv \mu b/l$. In the following, pre-yield dislocation motion is limited to planar glide.

We take the local Peach-Koehler force $\tau^{\mathrm{PK}} b$ equal to $\tau_k b$, with resolved shear stress τ_k in slip system k. Note that the Italic subscript $_k$ is not the index notation, but indicates a given slip system $\bullet$. The anelastic shear strain is

$$\gamma_k^{\mathrm{an}}(\tau_k) = \frac{b\rho_k}{\langle l_k \rangle} S(\tau_k, \langle l_k \rangle), \tag{3.6}$$

where the average segment length $\langle l_k \rangle$ is related to the dislocation density ρ_k on slip system k. We thus consider a dislocation-link length-distribution, that we model implicitly by representative, volumetric mean, dislocation structural properties $\bullet$ indicated by $\langle \bullet \rangle$.

3.2.2 Statistical Storage Model

Kocks [19, 274] constructed a self-styled statistical dislocation storage and dynamic recovery model. This early model, often called prototype [280] and/or Kocks-Mecking model, is *a posteriori* rationalised by the empirical Palm-Voce equation [281, 282]. The formulation is originally based on the forest strengthening model [10, 261], although this is not advocated as such in the earliest publication [19]. Furthermore, the dislocation interaction is confined to interaction between mobile and forest dislocations, and the model was formulated for zero Kelvin as well. In order to relate the flow strength at 0 K to the glide flow stress at finite temperatures and applied strain rates, one can use, following [19, 280, 283], a simple Arrhenius expression for thermally activated glide. We extend this proto-statistical storage-based model.

Mobile dislocation links travel a given distance till they interact with microstructural obstacles and/or (other) dislocations. The latter interaction predominantly forms stable junctions between dislocation lines on the given slip system and/or forest planes. We refer to this process as dislocation storage and gave a schematic representation thereof in Fig. 1.1a. Another part of the dislocation density annihilates because oppositely signed dislocations meet, or they reach free surfaces and grain boundaries. We thus write the forest dislocation structure evolution as:

$$\frac{\partial \rho_j}{\partial \epsilon_{\mathrm{pl}}} = \frac{\partial \rho_j^+}{\partial \epsilon_{\mathrm{pl}}} - \frac{\partial \rho_j^-}{\partial \epsilon_{\mathrm{pl}}}. \tag{3.7}$$

The forest structure evolution describes the creation and loss of a given part of the junction density ρ_j, where slip systems j form junctions with a given slip system k. Note that the

junction density ρ_j is the number of potential junction sites to be formed between a given mobile dislocation link on slip system k with the given dislocation link on system j. Here, the first term on the right-hand side of Eq. (3.7) is defined by the chance that a mobile dislocation encounters a potential junction and, subsequently, forms a (stable) junction. Therefore, assuming a model with the mean free path on slip system k given by the effective junction spacing $\left(\sqrt{\rho_j} \left\langle \beta_{kj} \right\rangle \right)^{-1}$, we write the storage term as:

$$\frac{\partial \rho_j^+}{\partial \epsilon_{\mathrm{pl}}} = \left\langle \beta_{kj} \right\rangle \rho_k^{\mathrm{m}} \sqrt{\rho_j} \frac{\partial \langle R_k \rangle}{\partial \epsilon_{\mathrm{pl}}}, \tag{3.8}$$

3

where $\mathrm{d}\langle R_k \rangle$ is the average distance travelled by mobile dislocation lines per unit of volume ρ_k^{m} during a principal strain increment $\mathrm{d}\epsilon_{\mathrm{pl}}$. Furthermore, the mean junction formation rate $\left\langle \beta_{kj} \right\rangle$ [284, 285] is assumed to be temperature independent, and, as will be shown, an effective measure that relates the dislocations on slip system k to the dislocation densities on all slip systems, which include system k. The double Italic subscripts $\bullet_{kj}$ indicate the interaction matrix $\bullet$ of a given dislocation property of slip j on a given dislocation property of slip system k. The individual components of these interaction matrices are not determined herein, but their effective values on a polycrystalline level are in the following.

The second term on the right-hand side of the structure evolution equation (3.7) describes a recovery or a rearrangement process that occurs on junctions when impinged by mobile dislocations. The number of potential recovery sites a mobile dislocation meets during the principal strain increment $\mathrm{d}\epsilon_{\mathrm{pl}}$ is defined as:

$$\mathrm{d}N_{kj}^{\mathrm{recov}} \equiv \rho_j \left(\epsilon_{\mathrm{pl}} \right) \mathrm{d}\langle S_k \rangle, \tag{3.9}$$

where $\langle S_k \rangle$ is the average area swept by a mobile dislocation on slip system k. An average junction length $\left\langle \xi_{jk} \right\rangle$ of the junction density ρ_j gets recovered at each potential recovery site [19]. We thus find that the average, recovered junction length per unit of volume V is

$$\frac{\partial \rho_j^-}{\partial \epsilon_{\mathrm{pl}}} = \frac{\rho_j \left\langle \xi_{jk} \right\rangle}{V} \frac{\partial \langle S_k \rangle}{\partial \epsilon_{\mathrm{pl}}}. \tag{3.10}$$

Typically, one increases $\left\langle \xi_{jk} \right\rangle$ by means of a power law to describe cross-slip of screw dislocations at low to intermediate temperatures and vacancy assisted climb from intermediate up to high temperatures [280].

The assumption is made that the probability of a recovery event per unit of distance a dislocation travels is proportional to the number of times that a potential recovery site is contacted by a moving dislocation, *i.e.*,

$$\rho_k^{\mathrm{m}} \mathrm{d}\langle R_k \rangle \propto \mathrm{d}\langle S_k \rangle / V. \tag{3.11}$$

This is equivalent to the Orowan equation and therefore we write:

$$\frac{\partial \gamma_k^{\mathrm{pl}}}{\partial \epsilon_{\mathrm{pl}}} \approx b \rho_k^{\mathrm{m}} \frac{\langle R_k \rangle}{\epsilon_{\mathrm{pl}}} \approx \frac{b}{V} \frac{\partial \langle S_k \rangle}{\partial \epsilon_{\mathrm{pl}}}, \tag{3.12}$$

where γ_k^{pl} is the plastic shear strain on slip system k. By substituting Eqs. (3.8), (3.10) and (3.12) in Eq. (3.7) and using the chain rule, we find:

$$\frac{\partial \rho_j}{\partial \gamma_k^{\mathrm{pl}}} = \frac{\left\langle \beta_{kj} \right\rangle \sqrt{\rho_j}}{b} - \frac{\left\langle \xi_{jk} \right\rangle \rho_j}{b}. \tag{3.13}$$

We relate the potential junction-dislocation density to average area per junction on given slip system k, and take $\rho_j\left(\epsilon_{\mathrm{pl}}\right) \equiv \alpha_{jk}^2 \rho_k\left(\epsilon_{\mathrm{pl}}\right)$ for a dislocation net with homogeneous junction spacing, *i.e.* uniformly distributed junction sites characterised by the length scale $\langle l_k \rangle$. The density increase on given plane thus reads

$$\frac{\partial \rho_k}{\partial \gamma_k^{\mathrm{pl}}} = \frac{\left\langle \beta_{kj} \right\rangle \sqrt{\rho_k}}{\alpha_{jk} b} - \frac{\rho_k \left\langle \xi_{jk} \right\rangle}{b}, \tag{3.14}$$

where we assume that the proportionality $\alpha_{jk} \equiv \left(\sqrt{\rho_k} \langle l_k \rangle \right)^{-1}$ is constant during monotonic plastic straining in each loading cycle. This is approximately satisfied for monotonic plastic strain $\epsilon_{\mathrm{m}}^{\mathrm{pl}} \lessapprox 5 \times 10^{-3}$ as shown in the following.

Contrary to the number of potential junctions per area of slip plane ρ_j, density ρ_k is the dislocation density on slip system k. Substituting the proportionality α_{jk} into Eq. (3.14), the evolution of the average dislocation segment length is given by the ordinary differential equation

$$\frac{\partial \langle l_k \rangle}{\partial \gamma_k^{\mathrm{pl}}} = \frac{\left\langle \xi_{jk} \right\rangle \langle l_k \rangle}{2b} - \frac{\left\langle \beta_{kj} \right\rangle \langle l_k \rangle^2}{2b}. \tag{3.15}$$

When the network refinement $\mathrm{d}\langle l_k \rangle$ equals zero, we find the minimum segment length $\lim \langle l_k \rangle \left(\epsilon_{\mathrm{pl}} \to \infty\right) \sim \left\langle \xi_{jk} \right\rangle / \left\langle \beta_{kj} \right\rangle$, *i.e.* the scaled projection of average junction length $\left\langle \xi_{jk} \right\rangle$ is recovered at each recovery site, and the network no longer refines.

3.2.3 Yield Strength

The definition of global, plastic flow strength before yield is ambiguous because dislocation mediated deformation is limited without the glide of activated dislocation links. However, when mobile dislocation loops are present with radii larger than the average dislocation segment length, they move at Peach-Koehler forces that are a fraction of those necessary to maintain pre-yield reversible deformation. Moreover, these dislocation loops shear across larger areas than dislocation links do at pre-yield stress. So we hypothesise that when the local anelastic compliance is lower than the global plastic compliance, deformation is mechanically recoverable. *Vice versa*, once the local anelastic compliance is higher than the global plastic compliance, inelasticity is mechanically irrecoverable. The least compliant type of deformation thus describes post-yield mechanical deformation. Compliance is the ratio of strain to stress with units of inverse stress, analogue to the inverse of the stiffness.

In Fig. 3.2, a schematic representation of the yield-point by shear stress-inelastic strain curves is given. At yield, we then ensure the flow curve and tangent modulus are continuous and write the criteria:

$$\Theta_k^{\mathrm{pl}}\Big|_{\tau_k = \tau_k^{\mathrm{y}}} \equiv \Theta_k^{\mathrm{an}}\Big|_{\tau_k = \tau_k^{\mathrm{y}}}; \qquad \text{and,} \qquad \lim_{\tau_k \to \left(\tau_k^{\mathrm{y}}\right)^+} \gamma_k^{\mathrm{pl}} \equiv \lim_{\tau_k \to \left(\tau_k^{\mathrm{y}}\right)^-} \gamma_k^{\mathrm{an}}, \tag{3.16}$$

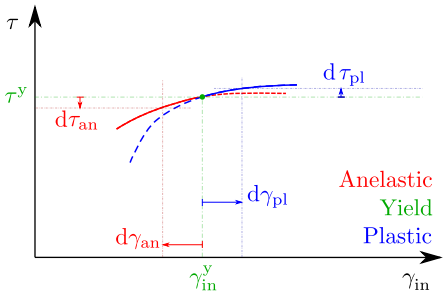

Figure 3.2: Schematic representation of the novel yield criterion by shear stress-inelastic shear strain curves.

i.e. at yield the anelastic and plastic compliance are equal. The post-yield tangent modulus thus is larger for plastic than for anelastic deformation, which is obvious from experiments [4–7]. Note that by the right-hand side of Eq. (3.16), the pre-yield anelastic deformation becomes plastic deformation when yield occurs, and we choose to neglect pre-yield micro-plasticity. A finite yield stress based on a Taylor-style relations considers forest dislocations [286], junction strengthening [287] and/or a combination of both [35]. A potential plastic flow rule thus is defined as:

$$\tau_k\left(\epsilon_{\mathrm{pl}}\right) \equiv \alpha_{kj}\mu b\sqrt{\rho_j(\epsilon_{\mathrm{pl}})}. \tag{3.17}$$

The novel yield criterion and the Taylor-type equation (3.17) are distinct herein.

3.3 Calculation

We use the relation between the normal stress and resolved shear stress, and the principal inelastic strain and inelastic shear strain as given by the Taylor factor M. Assuming dislocation lines to be, *one*, homogeneously dispersed, and *two*, uniformly distributed over k slip-systems with dislocation density ρ_k each, *i.e.* the total dislocation density $\sum_k \rho_k \equiv k\langle\rho_k\rangle$, we approximate the resolved shear stress and principal inelastic strain by

$$\tau \approx \frac{\sigma}{M}, \qquad \text{and} \qquad \epsilon_{\mathrm{in}}(\sigma) \approx \frac{1}{M}\sum_k \gamma_k^{\mathrm{in}}(\tau), \tag{3.18}$$

respectively.

In the following, the average junction length $\langle\xi_k\rangle$, the mean junction formation rate $\langle\beta_k\rangle$ and proportionality α_k are assumed to represent dislocation statistics of $\left\langle\xi_{jk}\right\rangle$, $\left\langle\beta_{kj}\right\rangle$ and α_{jk}, respectively, which is necessary for the Taylor homogenisation. This requires the average junction length $\langle\xi_k\rangle$, the mean junction formation rate $\langle\beta_k\rangle$ and proportionality $\alpha_k = \left(\sqrt{\rho_k}\langle l_k\rangle\right)^{-1}$ to be solely properties of the given slip system k. Variable with the given Roman subscript **.**, and several without, *e.g.* proportionality α_k, thus are spatially averaged values, here across grains, that represent the given, more complex polycrystalline morphology.

3.3.1 Flow Curve

In this work, the plastic shear strain γ_k^{pl} relates to the dislocation density ρ_k via

$$\frac{\partial \rho_k}{\partial \gamma_k^{\mathrm{pl}}} = \frac{\langle \beta_k \rangle}{\alpha_k b} \sqrt{\rho_k \left(\gamma_k^{\mathrm{pl}}\right)} - \frac{\langle \xi_k \rangle}{b} \rho_k \left(\gamma_k^{\mathrm{pl}}\right). \tag{3.19}$$

The maximum dislocation density is $\rho_k^{\max} = (\alpha_k \langle \xi_k \rangle / \langle \beta_k \rangle)^{-2}$, which corresponds with the total density of created dislocation line being recovered. The flow strength is

$$\tau_k \left(\gamma_k^{\mathrm{pl}}\right) = \alpha_k \mu b \sqrt{\rho_k (\gamma_k^{\mathrm{pl}})} = \mu b / \langle l_k \left(\gamma_k^{\mathrm{pl}}\right) \rangle, \tag{3.20}$$

where the average dislocation-link length is equal to the mean potential junction spacing. The inelastic shear strain $\gamma_k^{\mathrm{in}} = \gamma_k^{\mathrm{an}} + \gamma_k^{\mathrm{pl}}$ on slip system k is derived in Appendix C. Given the anelastic and plastic tangent moduli, Eqs. (C.3) and (C.6), respectively, are symmetric, and substituting them into the left-hand side term of Eq. (3.16), we obtain the inverse hardening ratio

$$\hat{q}_k = \frac{1}{\dfrac{\bar{\tau}_k^{\mathrm{y}}}{\sqrt{1-\left(\bar{\tau}_k^{\mathrm{y}}\right)^2}} - \sin^{-1}\left(\bar{\tau}_k^{\mathrm{y}}\right)} \left(\frac{\langle \beta_k \rangle}{\sqrt{1-\left(\bar{\tau}_k^{\mathrm{y}}\right)^2}} - \frac{\langle \beta_k \rangle}{\bar{\tau}_k^{\mathrm{y}}} \sin^{-1}\left(\bar{\tau}_k^{\mathrm{y}}\right) - 4\left(\bar{\tau}_k^{\mathrm{y}}\right)^2 \alpha_k^2 \right), \tag{3.21}$$

where $\hat{q}_k^{-1} \equiv \langle l_k \rangle / \langle \xi_k \rangle$ is a measure of the capacity of the dislocation network to refine the average link length, *i.e.* harden. Herein, the overhat $\hat{\bullet}$ indicates a given scaled variable $\bullet$.

Li and Wagoner [7] constructed a dissipative bow-out (DB) model. The increment of energy dissipated is conceptually provided by a reduction of the resolved shear stress with a static friction shear stress τ_{f}. The physical interpretation of the static friction shear stress τ_{f} is a local strengthening mechanism by various microstructural obstacles to glide, that is particularised to the experiment's materials in the following. The principle inelastic strain is

$$\epsilon_{\mathrm{in}}(\sigma) \approx \frac{b}{M\langle l \rangle} \begin{cases} 0, & 0 \le \sigma \le \sigma_{\mathrm{f}}; \\ \frac{1}{8\alpha^2 \left(\bar{\tau}'\right)^2} \left(2\sin^{-1}\left(\bar{\tau}'\right) - \sin\left(2\sin^{-1}\left(\bar{\tau}'\right)\right)\right), & \sigma_{\mathrm{f}} < \sigma \le \sigma_{\mathrm{y}}; \\ \frac{1}{8\alpha^2 \left(\bar{\tau}'_{\mathrm{y}}\right)^2} \left(2\sin^{-1}\left(\bar{\tau}'_{\mathrm{y}}\right) - \sin\left(2\sin^{-1}\left(\bar{\tau}'_{\mathrm{y}}\right)\right)\right) + \frac{2}{\hat{q}} \ln\left(\dfrac{1-\frac{\hat{q}\bar{\tau}'_{\mathrm{y}}}{\beta}}{1-\frac{\hat{q}\bar{\tau}'}{\beta}}\right), & \sigma_{\mathrm{y}} < \sigma < \sigma_{\mathrm{s}}; \end{cases} \tag{3.22a}$$

with normalised effective resolved shear stress and yield strength,

$$\bar{\tau}' = \frac{(\sigma - \sigma_{\mathrm{f}})}{M} \frac{\langle l \rangle}{b\mu}, \qquad \text{and} \qquad \bar{\tau}'_{\mathrm{y}} = \frac{\left(\sigma_{\mathrm{y}} - \sigma_{\mathrm{f}}\right)}{M} \frac{\langle l \rangle}{b\mu}, \tag{3.22b}$$

respectively, where $\sigma_{\mathrm{f}} = M\tau_{\mathrm{f}}$ is the static friction stress and σ_{s} the saturation stress. Here, α, β and $\hat{q}^{-1} = \langle l \rangle / \xi$ are the proportionality, junction formation rate and hardening ratio at the polycrystalline level. Herein, the overbar $\bar{\bullet}$ indicates a given normalised variable $\bullet$. To facilitate the subsequent numerical regression, we normalise the structural parameters in the following.

3.3.2 NORMALISATION

As plastic straining continues, the total dislocation density approaches the maximum density, $\rho \sim \rho^{\max}$, *i.e.* the shear flow stress asymptotically approaches the saturation shear stress

$$\tau_{\mathrm{s}} \sim \alpha\mu b \sqrt{\rho^{\max}(\gamma)} = \frac{\beta\mu b}{\xi}. \tag{3.23}$$

The tangent modulus thus decreases with increasing strain, *i.e.* $\partial\Theta/\partial\epsilon \leq 0$, which we rewrite as

$$\frac{\partial^2\tau}{\partial\gamma_{\mathrm{in}}^2} = \frac{\tau\hat{q}^2}{4} - \frac{\beta\hat{q}}{4} \leq 0. \tag{3.24}$$

Then the minimum mean junction formation rate becomes

$$\beta_{\min} \equiv \frac{4\alpha^2\left(\bar{\tau}_{\mathrm{y}}\right)^3\sqrt{1-\left(\bar{\tau}_{\mathrm{y}}\right)^2}}{\bar{\tau}_{\mathrm{y}} - \sqrt{1-\left(\bar{\tau}_{\mathrm{y}}\right)^2}\sin^{-1}\left(\bar{\tau}_{\mathrm{y}}\right)}, \tag{3.25}$$

that is equivalent to no recovery taking place, *i.e.* when the average dislocation junction length at the polycrystalline level $\xi \sim 0$, and allows for scaling the junction formation rate β over the range $(0,1)$. Here, the inverted scaled mean junction formation rate $\bar{\beta} = \beta_{\min}/\beta$. The inverted scaled junction formation rate $\bar{\beta}$ thus is the measure of work-hardening capacity, where the limit zero equals perfect plasticity, and unity the absence of anelasticity and solely hardening. From here on we refer to $\bar{\beta}$ as the work-hardenability, that is unrelated to the depth to which a material is hardened after putting it through a heat treatment process [288]. Substituting the work-hardenability $\bar{\beta}$ and inverse hardening ratio $\hat{q}$ in Eq. (C.5), we define the scaled dimensionless shear stress as $\hat{\bar{\tau}} \equiv \tau'/\tau_{\mathrm{s}} = \bar{\tau}'(1-\bar{\beta})/\bar{\tau}_{\mathrm{y}}$. This allows for scaling the normalised resolved shear stress $\hat{\bar{\tau}} \in (0,1)$ as well. Hence the average dislocation segment length $\langle l\rangle$ is uniquely defined by

$$\frac{\sigma_{\mathrm{s}}\langle l\rangle}{M\mu b}\frac{1-\bar{\beta}}{\bar{\tau}_{\mathrm{y}}} \sim 1. \tag{3.26}$$

Substituting work-hardenability $\bar{\beta}$ and scaled normalised resolved shear stress $\hat{\bar{\tau}}$ in Eq. (3.22a) and normalising the inelastic shear strain with the anelastic strain at-yield $\bar{\gamma}_{\mathrm{an}}\left(\tau_{\mathrm{y}}\right)$ (right-hand side of Eq. (3.16)), we obtain the scaled inelastic shear strain as

$$\hat{\gamma}_{\mathrm{in}}\left(\tau/\tau_{\mathrm{s}}\right) \equiv \frac{\gamma_{\mathrm{in}}(\tau)}{\gamma_{\mathrm{an}}\left(\tau_{\mathrm{y}}\right)} = \begin{cases} \left(\frac{1-\bar{\beta}}{\hat{\bar{\tau}}}\right)^2 \frac{2\sin^{-1}\left(\frac{\hat{\bar{\tau}}\bar{\tau}_{\mathrm{y}}}{1-\bar{\beta}}\right) - \sin\left(2\sin^{-1}\left(\frac{\hat{\bar{\tau}}\bar{\tau}_{\mathrm{y}}}{1-\bar{\beta}}\right)\right)}{2\sin^{-1}\left(\bar{\tau}_{\mathrm{y}}\right) - \sin\left(2\sin^{-1}\left(\bar{\tau}_{\mathrm{y}}\right)\right)}, & 0 < \hat{\bar{\tau}} \leq 1-\bar{\beta}; \\ 1 + \frac{\sin^{-1}\left(\bar{\tau}_{\mathrm{y}}\right) - \frac{\hat{\bar{\tau}}_{\mathrm{y}}}{\sqrt{1-\hat{\bar{\tau}}_{\mathrm{y}}^2}}}{2\sin^{-1}\left(\bar{\tau}_{\mathrm{y}}\right) - \sin\left(2\sin^{-1}\left(\bar{\tau}_{\mathrm{y}}\right)\right)} \frac{4\bar{\beta}}{(1-\bar{\beta})} \ln\left(\frac{1-\hat{\bar{\tau}}}{\bar{\beta}}\right), & 1-\bar{\beta} < \hat{\bar{\tau}} < 1; \end{cases} . \tag{3.27}$$

Here, solely in equation (3.27) the friction stress is neglected for readability, *i.e.* $\sigma_{\mathrm{f}} = 0$; in the remainder of this work, the friction stress is accounted for. Note that the constant proportionality α linearly scales the inelastic strain because it is removed by scaling with the anelastic shear strain at yield. Equations (3.18), (3.22) and (3.26) thus allow one to uniquely obtain the proportionality coefficient α, work-hardenability $\bar{\beta}$ and normalised yield strength $\bar{\tau}_{\mathrm{y}}$, all at the polycrystalline level.

3.4 Method

In previous methodology [4–6], graphical estimates are made by means of the initial degradation of the apparent moduli [31] and a distinct transition point on the tangent modulus. Van Liempt and Sietsma [4] formulated a novel method to determine the yield stress of metals from tensile curves. The transition point is determined by a clearly distinguishable feature in a given plot of the tangent modulus versus the uniaxial normal stress. Arechabaleta *et al.* [5, 6] propose an accessible, cheap and accurate method to quantify the dislocation network in metals, based on tensile tests and the aforementioned method [4]. A similar approach is used by Li and Wagoner [7], who closely reproduce experimental results on Dual-Phase, Transformation- and Twinning-Induced Plasticity steels. The present unified model allows us to advance this methodology, that yields the total dislocation density ρ and average segment length $\langle l \rangle$ at the polycrystalline level.

By means of the unified model, we analyse repeated cyclic uniaxial tensile tests on Interstitial-Free and Low-Alloy steels. We characterise the dislocation network evolution in relation to the macroscopic stress-strain behaviour. The present model is rooted in dislocation physics, yet general, so applicable to a wide range of metals [7]. Herein, we perform non-linear regressions on experimental force-displacement measurements. Numerical computation is limited to non-linear regression by an existing software package [289].

3.4.1 Experimental

Repeated cyclic tensile tests are performed on Low-Alloy (LA) and Interstitial-Free (IF) steel [6]. Both are single-phase ferritic steels. The main alloying elements for the LA steel are 0.08 wt% C, 0.30 wt% Mn and 0.10 wt% Si, and for the IF steel 0.0047 wt% C, 0.15 wt% Mn and 0.049 wt% Ti. Specimens of 275×10^{-3} m total length, 60×10^{-3} m gauge length and 12.5×10^{-3} m gauge width, with a thickness of 0.7×10^{-3} m are used. Note that we choose to present our results in a coherent system of units. Static loading conditions are achieved when deformation is applied slowly. The resultant static load then varies slow compared to phonon drag and thermally-activated dislocation motion [9, 17].

The repeated cyclic tests consisted at most of twenty successive loading and unloading cycles with a strain rate in the order of 10^{-5} s^{-1}. In each of these cycles the stress reduces to $\sigma_f \approx 10 \times 10^6$ Pa after the application of $\Delta\epsilon_m^{pl} \approx 5 \times 10^{-3}$ true principal plastic strain. We choose to keep the friction stress constant because of the finite positive stress at load reversal. Detailed descriptions of the methodologies, specimens geometries and tensile tester is given in the works [5, 6] by Arechabaleta *et al.*.

3.4.2 Numerical

By means of the present method, the dislocation network structure is approximated. The present, numerical methodology is as follows (See also Fig. 3.3): (1) the measured force-displacement curve is transformed to the normal stress vs. principal strain curve, and the friction stress σ_f and strain σ_f/E are subtracted from the normal stress σ and the total principal strain ϵ, respectively; (2) the principal elastic strain ϵ_{el} is subtracted from total principal strain ϵ via Eq. (3.1), and the resolved shear stress τ and inelastic strain γ_{in} are approximated by Eq. (3.18); (3) the plastic hardening rate Θ_{pl} is numerically obtained by a finite-difference method, and the normalised saturation shear stress $\tau_s/(\mu b)$ is obtained by a linear fit on the plastic tan-

gent modulus of Stage-II hardening; (4) the shear stress τ is normalised by the saturation stress τ_s, and the dislocation shear strain γ_{in} by the anelastic strain at-yield $\gamma_{an}(\tau_y)$, *i.e.* we obtain the scaled inelastic shear strain $\hat{\gamma}_{in}$; (5) the scaled dimensionless shear stress is multiplied by negative one, and subsequently unity is added (*i.e.* the scaled dimensionless shear strain-stress curve is mirrored in the vertical axis through the origin, and then shifted in the positive stress direction); and (6), the natural logarithms of the scaled shear stress, and of the scaled inelastic shear strain, *i.e.* $\ln(1-\tau/\tau_s)$ and $\ln\left(\gamma_{in}/\gamma_{an}(\tau_y)\right)$, respectively, are calculated. A schematic representation of the steps (2-6) is given in Fig. 3.3. We ob-

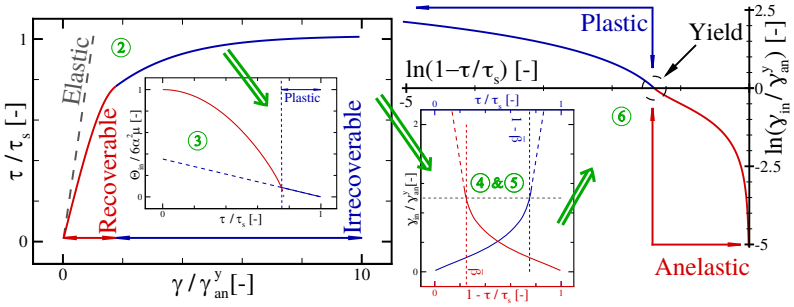

Figure 3.3: Schematic representation of the present numerical methodology in steps (2-6).

tain the dependent variables α, $\tilde{\beta}$ and $\bar{\tau}_y$ by a given non-linear regression with Eq. (3.27). Subsequently, we calculate the effective segment length $\langle l \rangle$ by means of Eq. (3.26) and the dislocation density as $\rho = (\alpha \langle l \rangle)^{-2}$ on the polycrystalline level. Note that the yield criterion is not restricted to our choice of strain-hardening model. However, the set of structural variables changes with the hardening models' description of dislocation network structure. The current unified model is limited to Stage-II work-hardening of a polycrystalline material. The storage and loss parameters, $\beta/\alpha b$ and ξ/b are thus obtained via Eqs. (3.25) and (3.21), respectively. However, there is not limitation to the choice of work-hardening model. For example, towards higher applied plastic strains, a phenomenological description of the complex process of Stage-III can serve a useful purpose [17].

3.5 RESULTS

The loading and unloading periods are determined from the time-step vs. displacement curves, with a constant time-step period of 5×10^{-3} seconds across $> 1.8 \times 10^5$ data points. The cyclic true normal stress vs. true principal strain curves are determined from the force vs. engineering strain curves, under the assumption of a constant volume, and corrected for, by the initial engineering strain at (re)loading. The datasets of true normal stress vs. true principal strain are combined per cycle and sorted by true normal stress. The mean and the root mean square error (RMSE) are determined by a rectangular windowing function across ten neighbouring data points of equal and/or increased true normal stress. The standard deviation in true principal strain serves then used as weight in the successive non-linear regressions. In Fig. 3.4, the cyclic true normal stress as a function of the cyclic true principal strain is given; successive cyclic results are shifted by 5×10^{-3} strain and indicated with five different, four times repeated, colours. The plastic tangent modulus is obtained by first

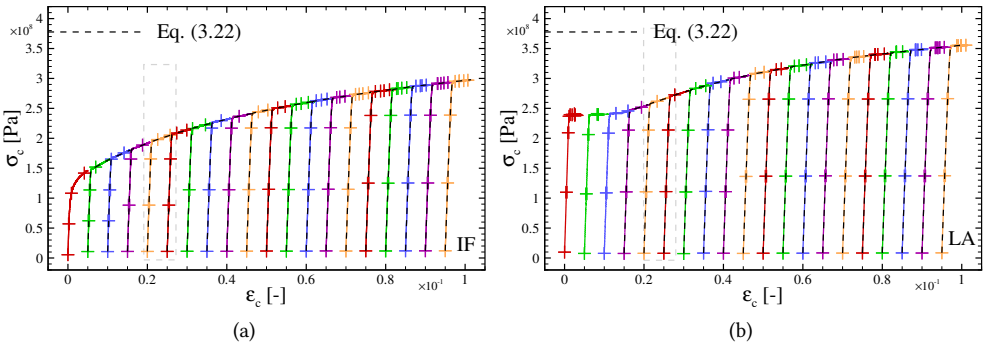

Figure 3.4: The cyclic normal true stress σ_c as a function of the cyclic principal true strain ϵ_c for (a) IF and (b) LA, and the unified model prediction (3.22) indicated by dashed black lines. The error bars indicate the RMSEs in stress and strain per data point.

filtering the monotonic average true normal stress vs. average true principal strain data by convolution with a block function with a width of a hundred neighbouring data points with a plastic strain range $\Delta\epsilon_{pl} \approx 10^{-6}$. Subsequently, the tangent modulus is calculated by the central-difference method. A linear regression is performed on the plastic tangent modulus, from a minimum true normal plastic stress defined with the ≤ 0.002 off-set method on the cyclic average normal stress vs. average true principal strain curves. The saturation stress σ_s is calculated by equating the Stage-II hardening model's plastic tangent modulus to zero. In Appendix D, this method is briefly summarised. The saturation stress $\sigma_s = 320 \pm 1 \times 10^6$ and $380 \pm 3 \times 10^6$ Pa for IF and LA, respectively. Here, $\pm\bullet$ indicates RMSE for independent and standard error for dependent variables. We calculate a single saturation stress σ_s for each steel grade across all loading-unloading cycles. Whereby we consider any changes in deformation conditions negligible, *e.g.* a changes in specimen temperature across these successive cycles. Furthermore, we find that the stress-strain range satisfies the Considère criterion [290] for uniform deformation.

The dependent variables β, α and $\bar{\tau}_y$ are obtained by first a non-linear regression on an hundredth of all data points. Herein, the non-linear regression is by the damped least-squared method [259, 260]. We use a single set of material parameters, namely: elastic shear modulus $\mu = 83.8 \times 10^9$ Pa. The alloying content of IF and LA lowers the elastic modulus less than 1% of the value for pure α–Iron [291]; Poisson's ratio $\nu = 0.3$; Burgers vector magnitude $b = 2.48 \times 10^{-10}$ m [5]; and, Taylor factor $M = 3.06$ [292],[293] for body-centred cubic polycrystalline material.

Because the dependent variable $\bar{\tau}_y$ lies near the edge of the permissible range $[0, 1]$, we use the natural logarithm-transformation to ensure convergence: $\bar{\tau}_y \equiv \bar{\tau}_y^{\min} + \left(1 - \bar{\tau}_y^{\min}\right) / \left(1 + e^{-\hat{\bar{\tau}}_y}\right)$, with the lower boundary $\bar{\tau}_y^{\min} = 0.9$ and the scaled normalised yield strength $\hat{\bar{\tau}}_y \in \mathfrak{R}$. The latter is related to, but distinct from the normalised yield strength $\bar{\tau}_y \in (0, 1]$ and scaled dimensionless stress $\hat{\tau} \in (0, 1)$. Although dependent variable $\bar{\beta}$ shares its permissible range with $\bar{\tau}_y$, no transformation is found necessary. The initial guess for the dependent variables, informed by their geometric meaning [294], are varied across the ranges $\bar{\tau}_y \in [0.9, 0.99]$, $\alpha \in [0.1, 0.9]$

and $\bar{\beta} \in [0.1, 0.9]$, and converge to a unique set of best-fit parameters. Subsequently, the set of best-fit parameters is used to initialise the non-linear regression on the mean cyclic true normal stress vs. cyclic mean true principal strain results as presented here. The covariance matrix is determined, and the standard errors and correlation coefficients are used to calculate the standard error of the remaining physical, structural parameters, *i.e.* dislocation density ρ, average segment length $\langle l \rangle$ and storage rate β/α. Note that the normalised average junction length ξ/b is already uniquely defined when the saturation stress σ_s is kept constant.

The model reproductions (3.22) are indicated in Fig. 3.4 by dashed black lines. The predictions are omitted for the first loading cycle of IF and the first three of LA, due to poorness of fit and the yield point phenomenon, respectively. The former is thought to be in part due to: micro-plasticity observed in virgin materials, as discussed by Li and Wagoner [7]; internal stresses [6]; and, imperfect alignment in the samples [6]. In Fig. 3.5a, the cyclic normal true stress σ_c as a function of the cyclic principal true strain ϵ_c, and the fit for cycle #5 are presented; the stress-strain ranges are indicated in Fig. 3.4 by dashed light-gray

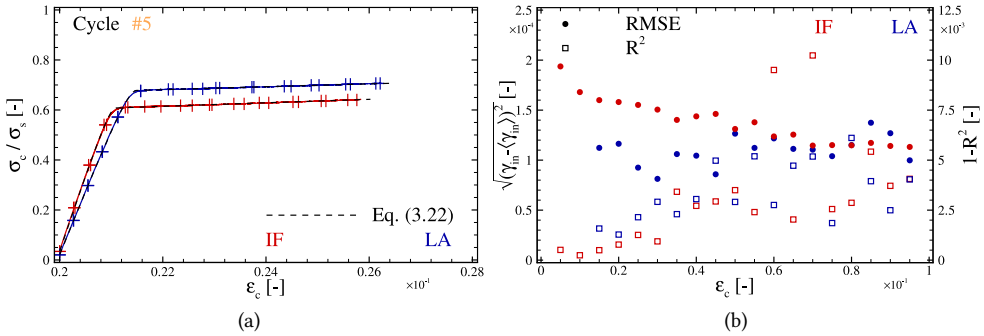

Figure 3.5: (a) The scaled cyclic normal true stress σ_c/σ_s as a function of the cyclic principal true strain ϵ_c for cycle #5 in 3.4a IF and (b) LA, and the unified model prediction (3.22) indicated by dashed black lines. The error bars indicate the RMSEs in stress and strain per data point. (b) The root mean-square error (RMSE) and shifted coefficient of determination $1-R^2$ as functions of the cyclic true principal strain ϵ_c for IF and LA, are indicated by coloured dots and open squares, respectively.

rectangles. The total cyclic inelastic strain, per cycle, is $2\times10^{-4}\cdots12\times10^{-4}$ for both steel grades. This fraction of the total cyclic inelastic strain, per cycle, increases by $1:17\cdots1:4$ and $1:10\cdots1:5$ between cycle #3 and #20, for IF and LA, respectively.

The RMSE and coefficient of determination R^2 are given in Fig. 3.5b; the solid, coloured circles indicate the RMSE in strain over each loading cycle, and the open, coloured squares the shifted coefficient of determination $1-R^2$. The ranges of the coefficient of determination R^2 are $(0.989, 0.999)$ and $(0.994, 0.999)$ for IF and LA, respectively.

In Fig. 3.6, the proportionality α, scaled normalised work-hardenability $\bar{\beta}/\alpha$, and yield stress σ_y and scaled normalised yield stress $\hat{\bar{\tau}}_y$ are presented. In Fig. 3.7, the total dislocation density ρ, the average dislocation segment length $\langle l \rangle$ and the storage rate β/α are presented. The statistical measures and the physical parameters in Fig. 3.5a, and Figs. 3.6 and 3.7, respectively, are spaced by the applied cyclic 5×10^{-3} strain so they correspond with the cyclic strains at reloading in Fig. 3.4.

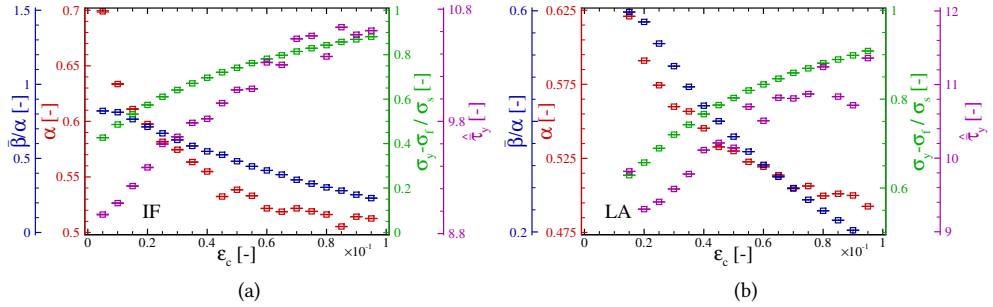

Figure 3.6: The proportionality α, scaled normalised work-hardenability $\bar{\beta}/\alpha$, normalised yield stress $\left(\sigma_{\mathrm{y}}-\sigma_{\mathrm{f}}\right)/\sigma_{\mathrm{s}}$ and scaled normalised yield stress $\hat{\bar{\tau}}_{\mathrm{y}}$ as functions of the cyclic principal true strain ϵ_{c} for (a) IF and (b) LA. The error bars indicate the standard error in the experimentally obtained physical parameters.

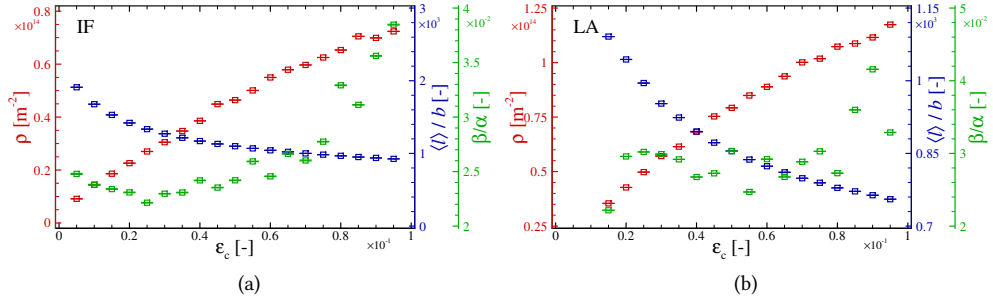

Figure 3.7: The total dislocation density ρ, scaled average segment length $\langle l\rangle/b$ and storage rate β/α as functions of the cyclic principal true strain ϵ_{c} for (a) IF and (b) LA. The error bars indicate the standard error in the experimentally obtained physical parameters.

3.6 Discussion

3.6.1 Yield Strength

The Taylor relationship reads

$$\sigma_{\mathrm{y}} = \sigma_0 + \alpha' M \mu b \sqrt{\rho}, \tag{3.28}$$

where $\sigma_0 \equiv M\tau_0$ is a strength contribution due to other microstructural obstacles than dislocations and α' constant. Note that equations (3.17) and (3.28) differ by a factor α/α', that is not necessarily unity, because the proportionality is allowed to vary each cycle while the Taylor relationships' constant is not. Moreover, the difference between the maximum line stress σ^{c} (See Sec. 3.2.1) and the present observed yield strength σ_{y} requires explanation. It stands within reason that dislocation segments whose lengths are several times greater than the mean segment length exist [8]. Those of "*greater length*" than the average segment length are expected to control the onset of flow [32]. Considering this physical property of the dislocation network, we thus limit the present definition of the observed yield strength

by

$$\sigma_y \simeq \sigma_f + M\frac{\mu b}{\langle l \rangle}. \tag{3.29}$$

Here, the difference between theoretical and observed yield strength is exceedingly small, but finite, due to the distributive nature of dislocation-link lengths, that comprise the given dislocation network. *It has since long been accepted that the so-called Taylor equation describes the relation between yield stress and dislocation density* [6], which warrants the validation of our hypothesis. In Fig. 3.8, the yield stress σ_y is given as a function of the square root of the dislocation density $\sqrt{\rho}$; the dashed gray line indicates the classic Taylor relation-

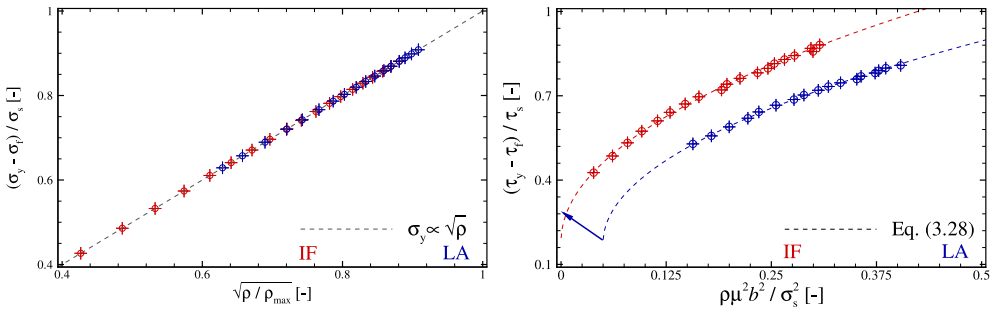

Figure 3.8: (a) The scaled yield stress $\left(\sigma_y - \sigma_f\right)/\sigma_s$ as a function of the square root of the scaled dislocation density $\sqrt{\rho/\rho^{max}}$, and (b) the scaled shear flow stress $\left(\tau_y - \tau_f/\right)\tau_s$ as a function of the normalised dislocation density $\rho\mu^2 b^2/\sigma_s^2$ for IF and LA. The blue arrow indicates the original position of the origin of LA and the error bars indicate the standard error and the RMSE.

ship (*i.e.* $\alpha'\mu b\sqrt{\rho}$ [33]). Note that the maximum dislocation density and saturation stress are constants across loading-unloading cycles. Moreover, the maximum dislocation density ρ^{max} is defined by Eq. (3.23), so the scaled dislocation density ρ/ρ^{max} is independent of proportionality α.

It is clear that the classic Taylor relationship holds, with RMSEs 1.11×10^3 and 1.22×10^3 Pa, for IF and LA, respectively. Where the maximum (latter) absolute error is less than 0.1% of the saturation stress σ_s. The present definition of the observed yield strength is thus corroborated by the square root dependency of the yield stress on dislocation density. Which is testament to the success of the classic Taylor relationship [33], even though the latter is based on the force necessary for a single-character dislocation to move through a regular spaced grid of like-signed infinite straight Volterra dislocation lines. We find the physics-based local yield criterion as postulated by Gurrutxaga *et al.* [279], and Van Liempt and Sietsma [4], and employed by Torkabadi *et al.* [28] and Li and Wagoner [7]. In Fig. 3.8b, the shear yield stress τ_y is presented as a function of the dislocation density ρ; the dashed coloured lines indicate the Taylor relationship (3.28). The origin for LA is shifted for clarity, the blue arrow indicates its original position. The constant and strength contribution $\left\{\alpha'\ [\text{-}], \tau_0 - \tau_f\ \left[10^6\ \text{Pa}\right]\right\} = \{0.410, 18.7\}$ and $\{0.345, 34.0\}$; and, the RMSEs are 57×10^4 and 28×10^4 Pa for IF and LA, respectively. Standard errors are exceedingly small hence omitted here. Note that stresses σ_0 and σ_f are

not necessarily equal because the former is a global strength contribution due to other microstructural obstacles than dislocations, while the latter is a local strengthening mechanism by dislocation links that "jump over" other soft pins [4, 7]. Moreover, the normalised dislocation density $\rho\mu^2 b^2/\sigma_s^2$ does depend on the measured proportionality α. Present definition of the observed yield strength thus is in keeping with the Taylor relationship (3.28) as well.

3.6.2 Dislocation Network Evolution

The statistical storage model describes the dislocation network structure evolution with plastic strain. Integrating the average segment length evolution (3.15) by parts and solving for the principal plastic strain, we define a scaled average dislocation segment length $\left\langle \hat{l}\left(\epsilon_{\mathrm{pl}}\right)\right\rangle \equiv \left\langle l\left(\epsilon_{\mathrm{pl}}\right)\right\rangle / \left\langle l\left(\epsilon_{\mathrm{pl}}\to\infty\right)\right\rangle$, that decreases as:

$$\left\langle \hat{l}\left(\epsilon_{\mathrm{pl}}\right)\right\rangle = \left(\left(\left\langle \hat{l}(0)\right\rangle^{-1} - 1\right) e^{-M\epsilon_{\mathrm{pl}}\xi/(2b)} + 1\right)^{-1}. \tag{3.30}$$

Integrating equation (3.19) by parts and solving for plastic strain once more, we define a scaled dislocation density $\hat{\rho}\left(\epsilon_{\mathrm{pl}}\right) = \rho\left(\epsilon_{\mathrm{pl}}\right)/\rho\left(\epsilon_{\mathrm{pl}}\to\infty\right)$, that increases as:

$$\hat{\rho}\left(\epsilon_{\mathrm{pl}}\right) = \left(\left(\sqrt{\hat{\rho}(0)} - 1\right) e^{-M\epsilon_{\mathrm{pl}}\xi/(2b)} + 1\right)^2. \tag{3.31}$$

Equations (3.30) and (3.31) constitute the evolution of dislocation structural parameters in the present *statistical storage model*.

We assume that physics-based structural parameters obtained at a given loading cycle are an indication of the dislocation network structure when unloading initiates in the preceding loading-unloading cycle; the dislocation network structure is preserved between unloading and subsequent reloading upto yield. Furthermore, we expect no local transformation of the dislocation structure into persistent slip bands [295] under our loading conditions [296, 297]. Torkabadi *et al.* [28] show aforementioned assumptions to hold for Advanced High Strength Steels by comparison of monotonic and repeated cyclic uniaxial tensile test results. Hence we keep these assumptions in the remainder of the present work, which our experimental observations on the monotonic (flow) stress curves in Sec. 3.6.3 support.

In Fig. 3.9, the scaled dislocation density $\hat{\rho}$ is presented as a function of the monotonic plastic strain ϵ_{pl}; the scaled average dislocation segment length $\left\langle \hat{l}\right\rangle$ is given as well; the proportionality α is scaled by its number average $\langle\alpha\rangle$ over all loading-unloading cycles of a particular type of steel; and, the coloured dashed lines indicate the evolution of average dislocation segment length, dislocation density and proportionality by Eqs. (3.30) and (3.31), respectively.

In Fig. 3.10, the average junction length ξ is presented as a function of the monotonic plastic strain ϵ_{pl}; the physical, structural parameter ξ/b per cycle is indicated by coloured circles (See Sec. 3.5). The constant average junction lengths ξ for monotonic loading are determined as described in this section by Eq. (3.31), and for Stage-II hardening in Eq. (D.3). The former and latter results are indicated by solid and dashed coloured lines, respectively, and their standard errors by equivalently coloured shaded areas. The average junction

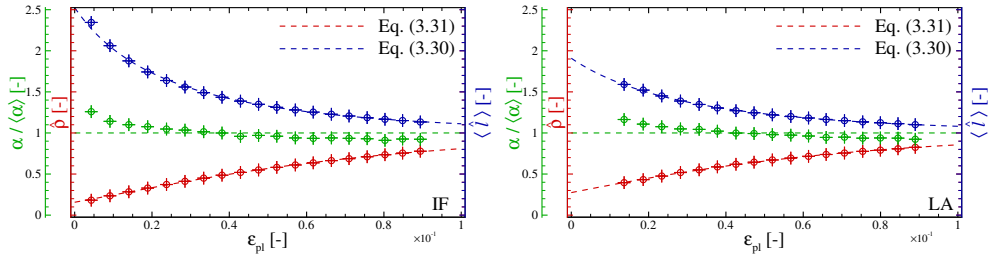

(a) (b)

Figure 3.9: The scaled dislocation density $\rho/\rho\left(\epsilon_{\mathrm{pl}} \to \infty\right)$, scaled average dislocation segment length $\langle l \rangle / \left\langle l\left(\epsilon_{\mathrm{pl}} \to \infty\right)\right\rangle$ and scaled proportionality $\alpha/\langle\alpha\rangle$ as functions of the monotonic plastic strain ϵ_{pl} for (a) IF and (b) LA. The error bars indicate the standard error and RMSE, and the dashed coloured lines the statistical storage model.

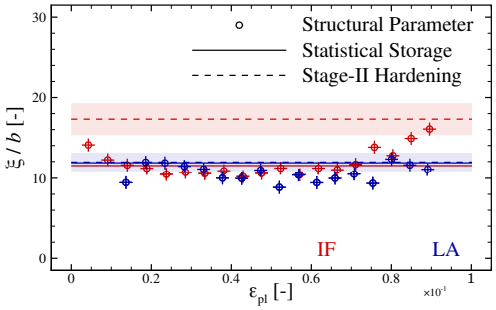

Figure 3.10: The normalised average junction length ξ/b as a function of the monotonic plastic strain ϵ_{pl} for IF and LA. The error bars indicate the standard errors and RMSE, and the coloured circles the scaled junction lengths ξ/b per cycle; the solid and dashed coloured lines indicate the junction lengths ξ/b for monotonic loading, and the coloured shaded areas their standard errors.

lengths ξ differ within 30% of each other. We argue that the origin of these differences are due to the assumption of a constant proportionality α in the present statistical storage model, and noise of the experimental signals in the first derivative of the stress-strain curves, respectively. Moreover, the storage parameter $\beta/(\alpha b)$ is presumed to be constant for Stage-II work-hardening (See Sec. 3.2.2). The storage rate β/α in Fig. 3.7 increases with the cyclic principal true strain ϵ_{c} due to the decrease in proportionality α as shown in Figs. 3.9, when the junction formation rate β remains constant.

The main assumption in the statistical storage model on the dislocation structure is the constant proportionality $\alpha \equiv \left(\langle l \rangle \sqrt{\rho}\right)^{-1}$ for Stage-II work-hardening. Obviously, this holds when one combines equations (3.30) and (3.31). Even so, the measured proportionality α, as displayed in Figs. 3.6 and 3.9, decreases with plastic strain. This is as rationalised by Li and Wagoner [7], who expect the proportionality α to decrease with forest dislocation density. Moreover, they [7] present an empirical linear decrease of the squared proportionality α^2 with flow stress $\sigma \propto \sqrt{\rho}$ and expect the proportionality α to saturate with significant strain hardening. The proportionality α is obviously not constant with increasing

plastic strain across the monotonic loading curve. Yet, the differences across successive loading and unloading cycles are tenths of their number average. So, we find that proportionality α is approximately constant and equal to $1/\left(\sqrt{\rho}\langle l\rangle\right)$ over monotonic plastic strain ranges $\epsilon_{\mathrm{pl}} \lessapprox 5\times10^{-3}$. The measured scaled mean segment length $\langle\hat{l}\rangle$ and scaled density $\hat{\rho}$ in Fig. 3.9 are independent of the measured proportionality α though. Moreover, the evolution of the average dislocation segment length $\langle l\rangle$ and dislocation density ρ are independent across (successive) cycles. Hence the equations (3.19) and (3.15) predict the evolution of average segment length and dislocation density for monotonic loading, which is testament to the versatility of the proto-statistical storage model [19]. However, the main assumption of the present model (See Sec. 3.1) is violated for monotonic loading, which we address in the following.

3.6.3 Work Hardening

With the square root dependency of the observed yield strength (See Sec. 3.6.1) and the statistical storage model (See Sec. 3.6.2), we predict the plastic flow curve under monotonic loading. The work-hardening model is a combination of the dislocation network structural evolution (3.31) and the potential flow rule (3.17). Here we choose to describe the dislocation network by the total dislocation density alone, and use the Taylor relationship, respectively. Aforementioned combination we call the *statistical storage-based work-hardening* model.

In Fig. 3.11, the monotonic (flow) stress is given as a function of the monotonic inelastic strain; numerical analysis of experimental results in this section is limited to the plastic

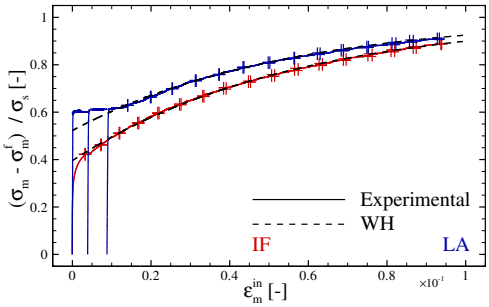

Figure 3.11: The scaled, monotonic (flow) stress $\left(\sigma_{\mathrm{m}}-\sigma_{\mathrm{m}}^{\mathrm{f}}\right)/\sigma_{\mathrm{s}}$ as functions of the monotonic inelastic strain $\epsilon_{\mathrm{m}}^{\mathrm{in}}$ for IF and LA. The dashed black lines indicate the reproduction via the work-hardening (WH) model. The error bars indicate the RMSEs per data point.

strain ranges as defined in the present work (See Secs. 3.4 and 3.5); we ignore the first loading cycle of IF and first three of LA, respectively (See Sec. 3.5 as well), and the deformation pre-yield in our numerical analysis here. The dashed black lines in Fig. 3.11 indicate the reproduction by the statistical storage-based work-hardening (WH) model. The RMSEs across the plastic strain ranges considered in Sec. 3.5 are 1.1×10^{6} and 1.6×10^{6} Pa for IF and LA, respectively. Equivalently, the error bars that indicate the RMSEs per data point are omitted across the stress-strain ranges that are omitted from the current numerical analysis. The monotonic flow curves are indicated by the coloured lines and globally smooth, which supports the dislocation network structure to be preserved between unloading and

subsequent yield [28] (See Sec. 3.6.2).

We include in Fig. 3.11 the monotonic stress-monotonic inelastic strain curves of the first loading cycle of IF and the first three of LA. A given work-hardening model is obviously incapable of reproducing these stress-inelastic strain curves pre-yield, which is one of the main reasons to conduct this study. However, all experimental data is presented in Fig. 3.11 because they facilitate the discussion in the following.

For one, it is clear that $\sigma \propto \sqrt{\rho}$ holds during work hardening; under static loading conditions, the flow strength increase with dislocation density is captured by the Taylor relationship. Secondly, we indeed find that the (inelastic) strain in the initial cycle(s) appears to be captured by neither anelasticity nor plasticity. A potential reason is rearrangement in the dislocation network structure during the initial loading cycle [7]. For LA, the yield point elongation phenomenon is distinct; and, our method inadvertently predicts a lower yield strength [44, 62, 63]. We find that the confirmation between our model reproductions and the experimentally obtained (plastic) results for IF and LA steels notable; notable is that the reproductions indicated by dashed black lines are based on the total dislocation density ρ as measured in Sec. 3.6.2, and not obtained by regression on the experimental results as indicated by the coloured solid lines in Fig. 3.11. Finally, the assumption that the storage rate β/α is constant during unidirectional loading in Sec. 3.2.2 seems to hold, at least up to the first-order. Herewith we verify that the statistical storage-based WH model captures the monotonic plastic deformation. Still the functional difference between proportionality α and the Taylor relationships' constant α' requires rationalisation.

3.6.4 Proportionality

Recalling the Taylor relation (3.28), we think that the constant α' is potentially perceived as the quantitative measure between the global dislocation densities ρ and the local average dislocation segment length $\langle l \rangle$ [34], *i.e.* the main descriptors of dislocation network geometry. This implies that the proportionality α is an equivalent quantifier for the dislocation network geometry, and thus remains constant whilst work hardening takes place [6]. However, we find that the proportionality α decreases during plastic straining (See Sec. 3.6.2), while a large body of experimental evidence a constant $\alpha' \approx 0.1 \ldots 0.4$ *ditto* the present work.

The success of the Taylor relation is the prediction of the flow strength increase with dislocation density whilst hardening takes place (See Sec. 3.6.3); the success of the bow-out model is the relation between global yield strength and the local dislocation structural feature of dislocation segment length [6]. As we demonstrate in Sec. 3.6.1, the Taylor relation for the shear flow strength and present definition of observed yield strength are equivalent, *i.e.*

$$\tau_k^{(0)} + \alpha' \mu b \sqrt{\rho \left(\gamma_k^{\mathrm{pl}} \right)} \simeq \tau_k^{\mathrm{f}} + \frac{\mu b}{\left\langle l_k \left(\gamma_k^{\mathrm{pl}} \right) \right\rangle}, \tag{3.32}$$

where $\tau_k^{(0)}$ is the strength contribution on slip system k other than dislocation strengthening equivalent to σ_0 in Eq. (3.28). When assuming the local yield and global flow strength to increase equally in strain hardening, taking the derivative with respect to the plastic strain ϵ_{pl}

and using the chain rule twice, we find the ordinary differential equation

$$\frac{\partial \left\langle l\left(\epsilon_{\mathrm{pl}}\right)\right\rangle}{\partial \rho\left(\epsilon_{\mathrm{pl}}\right)}=-\frac{\alpha^{\prime}\left\langle l\left(\epsilon_{\mathrm{pl}}\right)\right\rangle^{2}}{2\sqrt{\rho\left(\epsilon_{\mathrm{pl}}\right)}}. \tag{3.33}$$

This equation is an implicit equation of the dislocation network structure evolution with plastic strain, at the polycrystalline level. We solve the ordinary differential equation (3.33), with the initial conditions of average dislocation segment length $\langle l(0)\rangle$ and dislocation density $\rho(0)$ at zero plastic strain, and find that the proportionality decreases as:

$$\alpha\left(\rho\left(\epsilon_{\mathrm{pl}}\right)\right)=\alpha^{\prime}+\frac{\alpha(0)-\alpha^{\prime}}{\sqrt{\rho\left(\epsilon_{\mathrm{pl}}\right)/\rho(0)}}, \tag{3.34}$$

with an initial proportionality $\alpha(0)\equiv\left(\langle l(0)\rangle\sqrt{\rho(0)}\right)^{-1}$. It is trivial that the Taylor relationship's constant $\alpha^{\prime}\sim\alpha(\rho\rightarrow\infty)$.

In Fig. 3.12, the proportionality α is given as a function of the dislocation density ρ; the

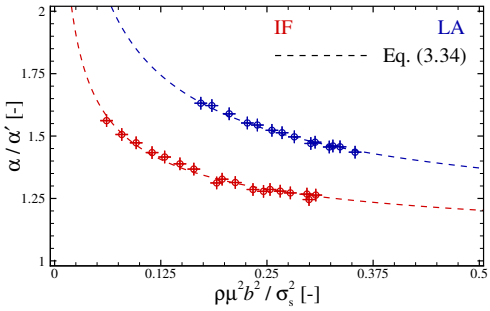

Figure 3.12: The scaled proportionality $\alpha/\alpha^{\prime}$ as a function of the normalised dislocation density $\rho\mu^2b^2/\sigma_s^2$ for IF and LA. The error bars indicate the standard errors; the dashed coloured lines indicate the semi-empirical relation (3.34).

coloured dashed lines in Fig. 3.12 indicate the proportionality $\alpha(\rho)$, obtained by non-linear regression with Eq. (3.34), where the constant and initial, average dislocation segment length $\left\{\alpha^{\prime},\langle l(0)\rangle/b\right\}=\{0.406\pm0.004,4510\pm130\}$ and $\{0.343\pm0.003,2450\pm30\}$ for IF and LA, respectively. Different from Arechabaleta *et al.* [6], and akin to Li and Wagoner ($\alpha\propto\rho^{-1/4}$) [7], we find the proportionality α has a non-linear dependence on the dislocation density ρ. The latter work [7] treats more complex microstructures beyond the present work though, *e.g.* various Transformation- and Twinning-Induced Plasticity Steels.

We argue that the proportionality $\alpha(\rho)$ is the appropriate implicit quantitative measure of the dislocation network structure evolution with plastic deformation. Coercive is the minimal difference between the constants $\alpha^{\prime}$ obtained in Sec. 3.6.1 ($\alpha^{\prime}=0.410$ and 0.345 for IF and LA, respectively) and the current section, which are obtained independently. Moreover, the RMSEs are 4.4×10^{-3} and 2.1×10^{-3} and 7.0×10^{-3}, for IF and LA, respectively, and the shifted coefficient of determination $1-\mathrm{R}^2<10^{-4}$. The minimum proportionality $\alpha\left(\gamma_{\mathrm{pl}}\right)\sim\alpha^{\prime}$ is obviously only achieved when dislocation recovery or rearrangement processes are absent.

The constant α' thus is a lower limit of the quantitative representation of the dislocation network geometry α, *i.e.* a physics-based, yet theoretical, asymptote. We issue a warning to the reader here on the physical interpretation of constant α'. It seems tempting to relate the constant α' directly with the forest strengthening [7], as the projection of dislocation links that intersect a given glide plane is constant. Detractive is the change in constant α' with steel type though, which can be remedied by changing the elastic shear modulus. However, use of the Taylor factor to relate principal inelastic strain and normal stress to local inelastic shear strain and shear stress, convolutes any such interpretation. Furthermore, the proportionality α in Eq. (3.22) is an effective measure at the polycrystalline level, that neglects the notion of active and inactive slip-systems. The success of equation (3.34) combined with the present statistical storage model, excludes the seminal interpretation of the Taylor relationships' constant α' as the measure of dislocation-dislocation interaction on a single slip-system though. Hence we interpret the Taylor relationship as a combination of forest interactions and junction strengthening, akin to Kubin *et al.* [35]. Here, the proportionality α thus is the effective measure of junction strengthening on the crystallite level (See Sec. 3.2.2), that changes with plastic strain through forest interactions [7].

Equation (3.32) remains an *a posteriori* constructed semi-empirical relation, that is based solely on the interpretation of the experimental results with our present model (*i.e.* with a constant proportionality α per loading-unloading cycle). Use of the ordinary differential equation (3.33) in the present statistical storage model, in Sec 3.2.2, will enforce the equivalence in Eq. (3.32). Then, the interpretation of the constant α' is set *a priori*, which we think severely weakens the results herein. The current work thus presents the next step [6] towards the final interpretation of the Taylor relationship.

In the present model, we consider solely monotonous, unidirectional loading wherefore the current modelling framework, as the works [4–7] show, is adequate. For pre-yield tension-compression asymmetry Zhu *et al.* [39] recently present a combined experimental-modelling approach. We do not account for strain gradients or internal stresses, which are postulated as critical in understanding anelasticity under reciprocal loading conditions [7]. Full-Field crystal plasticity methods are the only way to satisfy mechanical equilibrium and strain compatibility throughout a polycrystal. Hence they will give more realistic results than our Taylor homogenisation, *e.g.* the influence of the accumulation of dislocations at grain boundaries, which we do not capture in this model (See Sec. 3.3). However, the present experimental data leads to over-fitting when one employs a more sophisticated full-field crystal plasticity method. Our framework is accepted in inelastic deformation modelling, and demonstrates its usefulness in anelasticity by *e.g.* Li and Wagoner [7] and plasticity by *e.g.* Sendrowic *et al.* [298] to date. In the following, we summarise several universal, experimental observations that support our findings.

3.6.5 Apparent Modulus

Given that the elastic modulus is virtually constant with strain, the degradation in apparent modulus is primarily due to anelastic deformation [1]. With successive loading-unloading cycles the dislocation density ρ increases and the average segment length $\langle l \rangle$ decreases (See Sec. 3.6.2). The associated change in dislocation network is such that the product $b\rho\langle l \rangle$ (See Eq. (3.6)), *i.e.* the anelastic strain magnitude, increases with each loading-unloading cycle (See Sec. 3.5). For a given applied uniaxial, cyclic tension, σ_c, well below the yield

strength σ_y, the anelastic modulus thus decreases, *i.e.* the apparent modulus degradates.

Ma *et al.* [41] present a series of continuous loading-unloading-reloading experiments on a near-alpha high-strength titanium alloy within the cold and warm forming domains. They [41] find that the chord modulus under cold deformation is degraded dramatically at a low plastic strain level and then gradually gets a saturated state with dislocation density. Chamakura *et al.* [278] experimentally observe independent of the unified model herein that the modified chord modulus, which is proportional to the chord modulus but can be an order of magnitude higher, decreases with dislocation density in cyclic loading-unloading tensile tests on fully martensitic stainless steel. Most recently, Vitzthum *et al.* [38] presents continuous cyclic tensile test on a DP and IF steel, that are similar to those herein. They [38] observe that the loading and unloading chord moduli decrease with increasing plastic strain, where in the beginning of plastic deformation, these moduli decrease rapidly until they converge with further plastic deformation.

The initial anelastic modulus reads $\Theta_{an} \propto \alpha^2$. Hence the now known proportionality evolution, $\alpha(\rho)$, allows us to rationalise the following observations: *one*, the variation of the apparent modulus depends on prior plastic straining [38, 41, 276–278]; *two*, the apparent modulus decreases to a certain extent, and then saturates with work hardening, *i.e.* successive plastic deformation does not lead to an experimentally observable decrease in modulus [38, 41, 276]; *three*, (recovery) heat treatment increases/restores the apparent modulus [41, 275]; and *four*, the apparent modulus approaches the theoretical elastic modulus after bake-hardening [28], while the flow strength is unaffected, *i.e.* the dislocation density is virtually constant.

We find that: *one*, with work hardening and ensuing plastic deformation the proportionality decreases with dislocation density; *two*, because of the recovery and/or rearrangement process in Stage-II strain-hardening, the dislocation density saturates, similarly the change of initial anelastic modulus with plastic strain does. Similar to our findings (not presented in this work), Vitzthum *et al.* [38] find the loading modulus for single-phase material decreases less with increasing plastic strain then the loading modulus of Dual-Phase steel; *three*, heat treatment reduces the dislocation density by increased dislocation recovery, which leads to a higher apparent modulus. This is inline with the extensive experimental results on warm deformation by Ma *et al.* [41]. They [41] show that the modulus degradation and its strain dependence decrease with forming temperature; and *four*, interstitials diffuse to dislocation lines, so the average dislocation segment lengths decrease with bake-hardening, yet dislocation recovery is minimal, so the proportionality α increases. For the influences of metals lattices, local dislocation network structure and compressibility, we refer to our previous work on the influence of dislocations on the apparent elastic constants in single metallic crystallites [37, 39].

To accurately predict the apparent modulus (i.e the anelastic strain) after plastic deformation, one needs a dislocation network structure model which *a priori* incorporates the evolution of proportionality $\alpha\left(\epsilon_{pl}\right)$. The relationship given by Eq. (3.33) is not enforced in the current statistical storage-based WH model though. However, future storage models are to be amended with the now known dependence of the proportionality α on the dislocation density ρ.

3.7 CONCLUSIONS

In this chapter, we present a static inelastic model. The elastic mechanical behaviour is described by isotropic linear elasticity, anelastic mechanical behaviour by the dissipative dislocation bow-out model and the dislocation network structure evolution by the statistical storage model. We analyse repeated cyclic tensile tests on Interstitial-Free and Low-Alloy steels. The yield point is determined by the compliance of anelastic and plastic deformation. We ascertain the two premises in physical metallurgy of the Taylor relationship and the statistical storage-based work-hardening. Finally, we present a measure for the changes in initial apparent modulus with thermomechanical processing.

Under the assumption that the dislocation network structure is preserved between unloading from the plastic regime and subsequent reloading up to yield, we draw the following conclusions: the statistical storage model predicts the evolution of average segment length and dislocation density with plastic strain; and, the statistical storage-based work-hardening model is experimentally verified, and successfully predicts monotonic uniaxial plastic deformation at least upto the first-order.

The fundamental understanding on the evolution of dislocation network geometry during plastic deformation is expanded as well. The implicit semi-empirical relation of the proportionality, $\alpha(\rho) \propto 1/\sqrt{\rho}$, captures the average dislocation segment length decrease and dislocation density increase with work hardening, *i.e.* the chance in dislocation network structure. Moreover, this findings rationalise the previous experimental observations [28, 38, 41, 275–278] on the changes in initial apparent moduli with thermomechanical processing.

Part II: Yield Point Phenomenon

4

On the Characteristics of the Lüders Front: the yield point phenomenon under invariant plane conditions

The plastic deformation of metals that exhibit the yield point phenomenon is confined to Lüders bands. Current knowledge on the Lüders band characteristics is derived from numerical and experimental observations, but a more comprehensive constitutive relation is needed. We present an analytical model that determines the Lüders front orientation relative to the uniaxial tensile direction, taking into account the heterogeneous stress states across the front. Moreover, we verify this model by means of full-field numerical calculations.

Plastic flow in the Lüders front maximises global dissipation and vanishes parallel to it. These are the characteristics of the Lüders front under invariant plane conditions. The change in front inclination originates from the local stress concentration. Hence the Lüders front orientation depends on the ratio between upper and lower yield strength, and tensile specimen geometry. Our results provide an additional explanation beyond test conditions for the wide range of Lüders band orientations in experiments.

We present a methodology to approximate the lower yield strength measuring force-displacement and the Lankford coefficient. The here presented description of the yield point phenomenon provides an experimental method for future studies, that is independent of test conditions.

This chapter is based on the scientific article: Van Dokkum, J. S., Bos, C., Offerman, S. E., Sietsma, On the Characteristics of the Lüders Front, (In preparation).

NOMENCLATURE

Variable	Definition	Dimension (mass M, length L and time t)
a & b	scalars	–
α	Lüders front inclination	–
C_1	axial coordinate	L
$\bar{C}_2$	Lüders band ratio	–
E	elastic modulus	$\mathrm{ML^{-1}t^{-2}}$
$\boldsymbol{\epsilon}$	strain	–
f	Von Mises criterion	$\mathrm{ML^{-1}t^{-2}}$
h	specimen height	L
H	plastic modulus	$\mathrm{ML^{-1}t^{-2}}$
i & j	indices	–
l	specimen length	L
λ	proportionality	$\mathrm{M^{-1}Lt^2}$
$\hat{\boldsymbol{n}}$	Plane normal	–
ν	Poisson's ratio	–
Ω	volume	$\mathrm{L^3}$
$\bar{q}$	contraction ratio	–
$\bar{r}$	inverse yield strength ratio	–
R_e	flow strength	$\mathrm{ML^{-1}t^{-2}}$
$R_{\mathrm{eH(obs)}}$	observed upper yield strength	$\mathrm{ML^{-1}t^{-2}}$
$R_{\mathrm{eL(obs)}}$	observed lower yield strength	$\mathrm{ML^{-1}t^{-2}}$
$R_{\mathrm{eH(tr)}}$	true upper yield strength	$\mathrm{ML^{-1}t^{-2}}$
$R_{\mathrm{eL(obs)}}$	true lower yield strength	$\mathrm{ML^{-1}t^{-2}}$
$\mathcal{R}$	yield surface	$\mathrm{ML^{-1}t^{-2}}$
$\mathcal{R}_\mathrm{H}$	upper yield criterion	$\mathrm{ML^{-1}t^{-2}}$
$\mathcal{R}_\mathrm{L}$	lower yield criterion	$\mathrm{ML^{-1}t^{-2}}$
$\boldsymbol{s}$	deviatoric stress	$\mathrm{ML^{-1}t^{-2}}$
$\mathcal{S}$	observation area	$\mathrm{L^2}$
$\boldsymbol{\sigma}$	stress	$\mathrm{ML^{-1}t^{-2}}$
τ	shear stress	$\mathrm{ML^{-1}t^{-2}}$
t	time	t
$\boldsymbol{u}$	displacement	L
$\boldsymbol{v}$	velocity	$\mathrm{Lt^{-1}}$
ϕ	Lüders front angle	–
w	gauge width	L
x, y & z	Cartesian coordinates	L
ζ	azimuth angle	–

4.1 Introduction

Seminally, the deformation in the Lüders front is pure shear [117, 299, 300] or a combination of initial shear and subsequent, plastic flow [68, 301, 302]. In both hypotheses the Lüders front forms parallel to the plane of maximum shear stress [120, 303] and/or the plane of maximum projected shear stresses [299, 300]. The experimentally obtained Lüders front angle is thus expected to be close to $\phi = 45$ degrees with respect to the tensile direction. This angle ϕ is indicated on the insert in Fig. 1.2a. The mesomechanical explanation by Lomer [68] and Jaoul [299] is that the YPP occurs by pure shear under a characteristic angle between the front and the tensile axis, that originates from the average slip orientation in individual grains. Lomer [68] reasons that the kink at the Lüders band introduces bending moments that influence the Lüders front angle ϕ. The macromechanical rational by Butler [68, 300] states that the orientation of the front on the specimen's faces change in order to minimise the misalignment caused by plastic shear with Lüders strain. They [300] report that the Lüders angle remains constant with $\phi = 50$ degrees, but increases to 90 degrees on the tensile specimen's widest face. Delwiche and Moon [117] find that the Lüders front propagates with the angle $\phi = 45$ degrees, *i.e.* parallel to planes of maximum shear stresses. The global orientation of the Lüders front maximises the stress intensity factor on one side of the shear kink, and remains constant under a constant load [117]. Ananthan and Hall [120] find that the direction of shear is not parallel with the greatest slope in the Lüders front, which points to grip constraints and/or the bending moment of the specimen that influence the orientation of the Lüders front. Notable is that the works [68, 117, 300] attribute the plastic flow to the tensile test conditions; plastic flow is not a characteristic of the Lüders front.

The experimental works [50, 68, 109, 117, 118, 304] report a constant Lüders angle $\phi = 45$ degrees; Joaul [299] and Pomey *et al.* [305] find that the Lüders front angle varies across specimens with $\phi = 45 \cdots 55$, and the average $\phi = 50.1$ degrees. The works [50, 53, 115, 116, 299, 306, 307] report a constant Lüders angle of $\phi \approx 55$ degrees; Cai *et al.* [69] report a constant Lüders angle of $\phi = 60$ degrees, and Louche and Chrysochoos [308] $\phi = 70.5$ degrees; The observations in [119, 309] give a constant Lüders front angle $\phi = 90$ degrees; and, Nagaran *et al.* [74] and Van Rooyen[64] obtain Lüders front angles that vary between $\phi = 62.5 \cdots 76.4$ for a constant strain rate, and $\phi = 47.5 \cdots 68.5$ degrees with strain rate, respectively. Notable experimental observations are the works by Butler [300] and Ananthan and Hall [120] that report Lüders angles that increase $\phi = 50 \cdots 90$ with the Lüders strain, and varies between $\phi = 45 \cdots 76$ degrees with tensile specimens' geometry, respectively.

Mechanics research into the occurrence of the YPP covers both mesomechanical, *e.g.* Lomer [68], Jaoul [299] and Butler [300], and macromechanical approaches, *e.g.* Nadai [310] and Van Rooyen [64]: *firstly*, Nadai [310] states that the plastic extension parallel to the Lüders front is zero because the adjoining portions of non-yielding material do not participate in the deformation [311]. Experimental observations on the Lankford coefficient [307, 312] support the hypothesis by Nadai [310], that plastic flow parallel to the Lüders front is zero. When the ratio between specimen height and width increases, Nadai [310] states that the Lüders front angle decreases towards $\phi = 45$ degrees. They [310] connect this decrease in angle to the dominant plane strain state in the interior of the tensile specimen. Thomas [311, 313] and Thomas [314] use the method of characteristics [315] to find the Lüders front inclination under plane stress condition, with Hencky's stress-strain and Prandtl-Reuss stress-strain increment relationships, respectively. Both Nadai [310] and Thomas [311, 313, 314], yet

commonly ascribed to Hill [316], find the seminal Lüders front angle $\phi \approx 54$ degrees under the plane stress condition. Park and Kim [317] rewrite the former method by Thomas [311] to plane strain condition; and, Tokuoka and Saito [318] the latter method [314] for orthothropic anisotropy by Hill [319]. Savoie *et al.* [307] report the experimental observation that the Lüders front angle varies between $\phi = 52.2$ and 64.3 degrees from the rolling to the transverse direction; and, Mengi *et al.* [320] extend the works by Thomas [311, 313, 314] to how the Lüders front angle ϕ increases with Poisson's ratio ν. The Lüders front angle $\phi = 45$ [310, 317] and $\phi \approx 54$ [310, 311, 313, 314, 318, 320] degrees for an incompressible solid under plane strain and stress conditions, respectively. Notable is that the stress state at the Lüders front in the works [310, 311, 313, 314, 316–318] is homogeneous [310, 311, 313, 314, 317] and/or uniaxial tensile [316, 318] because they [310, 311, 313, 314, 316–318] consider a single true, and thus observed, yield strength, *i.e.* $R_{\mathrm{eL(tr)}} = R_{\mathrm{eH(tr)}}$. The Lüders front angle thus changes with a given materials elastic compressibility and tensile specimen geometry but not with a change in material specific micromechanisms (excluding orthothropic plastic anisotropy [318]). *Secondly*, the work by Van Rooyen [64] is the first that treats the stress concentration at the Lüders front. A stress concentration is a location where the local stress is significantly different from the global stress. This heterogeneous stress state across the Lüders front qualitatively accounts for most of the experimentally observed yield-point phenomena in low-carbon steel [64, 65]. Notable is that Van Rooyen [64, 65] treats a uniaxial stress across the Lüders front and the increase in Lüders front angle ϕ is empirical. Burg and Harris [302] are the first to notice that the Lüders front angle, that they define as the direction of no finite elongation [310], varies between $\phi = 45$ and 90 degrees with the ratio of applied stresses in rocks [302]. Similarly, Watterson [321] treats the effect of plastic dilatation on the orientation of no finite extension under plane strain condition, and the subsequent failure surfaces, in brittle fracture of rocks. They [302, 321] self-evidently omit the conditions necessary for the associated triaxial stress state in uniaxial tensile tests of metals. Even so, the majority of Materials Science studies ignore the stress concentration at the Lüders front [44, 64]. Most recently, Schwab and Ruff [44], Schwab [63], and Schwab and Harter [62] are the first to present a closed-form expression for the Lüders front angle ϕ as a function of the material properties. Their [44] significant hypothesis is that the Lüders front is the plane, where the maximum shear stress acts. This assumption is inline with the observations in [117, 299, 300]. Both Van Rooyen [64, 65] and Schwab *et al.* [44, 62, 63] postulate that the Lüders front angle ϕ depends on the stress concentration, and require this angle to increase with the constant nominal stress, *i.e.* the lower observed yield strength $R^{*}_{\mathrm{eL(obs)}}$ in Fig. 1.2a. The majority of the mechanical investigations took place in the fifties and sixties, and focus on the orientation of the Lüders front [310, 311, 313, 314, 316–318]. Others, which start with Van Rooyen [64, 65] and continue till today [44, 62, 63], treat the heterogeneous stress state at the Lüders front. However, a comprehensive, mechanical framework that explains the YPP misses.

OUTLINE

We present a macromechanical model of the YPP. We divide the current, macromechanical descriptions of the YPP into two general categories: models that consider a discontinuity in displacement and stress along the Lüders front but with a homogeneous stress state, *e.g.* [310, 314, 317, 320]; and, models [44, 64, 65] that treat the discontinuity in stress along the Lüders front with a stress concentration at the Lüders front. The former's limitation is

that the heterogeneous stress state is prerequisite to the YPP [44, 64, 65]; the latter's stress state is independent of the specimen's geometry and the Lüders front orientation changes with the discontinuity in displacement [310, 315, 316]. These simplifications were necessary at the time, yet limit the applicability of resulting analytical models. Hence our goal is to combine these macromechanical descriptions of the YPP to provide an explanation for experimental observations. We use material mechanical behaviour as inputs to the (numerical) models and the micromechanical origin of the YPP remains open-ended. The experimentally obtained Lüders front angle varies between 45 and 90 degrees [50, 53, 64, 68, 74, 109, 115–120, 299, 300, 304, 306–309] with respect to the tensile direction. No general, mechanical model of the Lüders front exist, that captures these observations, to the best of the authors knowledge. Hence we study the characteristic orientation of the Lüders front.

The following results are presented and discussed: *firstly*, we present the YPP in a generic, uniaxial tensile test, where the Lüders front is modelled in a rigid-plastic framework. Herein, plastic flow in the Lüders front is maximised and comparatively negligible parallel to it. These are the characteristics of the Lüders front we propose; *secondly*, we limit the analyses to invariant-plane conditions, that allow us to present open-form expressions with minimal simplification; *thirdly*, we use the Finite Element Method as presented by Schwab and Harter [62] to model tensile tests under uniaxial tension. Via the numerical results, we obtain closed-form expressions under plane strain and stress conditions, and corroborate the characteristics of the Lüders front; *fourthly*, we verify the main feature of our model under plane stress conditions: the change in Lüders front angle ϕ with the stress concentrations, which depends on the ratio between the upper and lower yield strength; *finally*, our model allows one to approximate constitutive parameters by the common-place uniaxial tensile test. A simple methodology with the force-displacement and Lankford coefficients [322] measurement is discussed to approximate material properties, independent of test conditions.

The major outcomes are the characteristics of the Lüders front. Moreover, we discuss an alternative mechanism for the rotation of the Lüders band with material properties, specimen geometry and testing conditions. The outcomes herein are for future use in experimental works to obtain constitutive parameters by the common-place uniaxial tensile test.

4.2 Problem Definition

We consider a tensile specimen with a prismatic cross-section. The specimen's material is homogeneous and displays isotropic material mechanical behaviour. This distinction between material mechanical and observed mechanical behaviour is necessary because the materials parameters one measures experimentally are not necessarily material properties when deformation is heterogeneous [66]. Away from the tensile specimen shoulders a single Lüders band covers the whole cross-section and moves from one towards the opposite end of the specimen length. On either side, a given distance away from this band, the applied stress is uniaxial tension. A typical tensile specimen shape is shown schematically in Fig. 4.1.

The Lüders front has two degrees of freedom that correspond to the local direction of its normal. To uniquely capture this front, we attach a Cartesian coordinate system with orthonormal basis $Ox'y'z'$ to the specimen geometry. The prime $\bullet'$ and double primes $\bullet''$ with coordinate $\bullet$ indicate coordinate transforms. Here, the x'-direction is parallel with the applied tensile direction, and the z'-plane parallel with the widest specimen face. The local Lüders front is represented by a unit vector $\hat{\boldsymbol{n}}' = [\cos(\alpha), \sin(\zeta)\sin(\alpha), -\cos(\zeta)\sin(\alpha)]$,

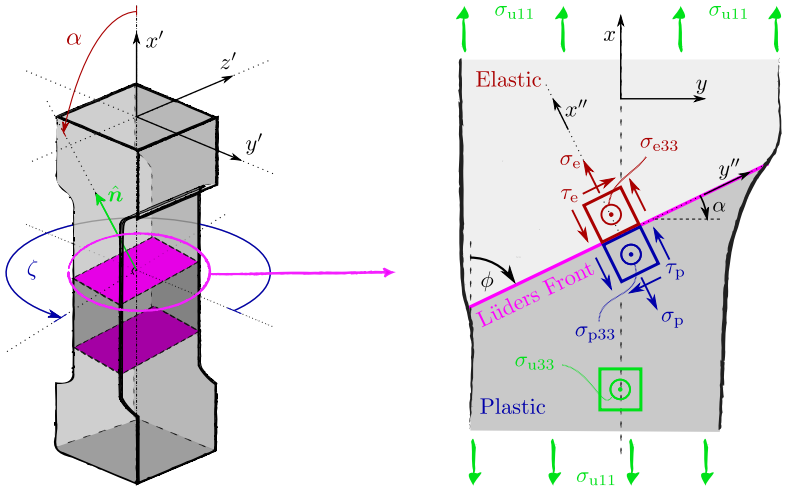

Figure 4.1: Schematic representation of the Lüders front with the stress states in material points in the still-elastic, just-plastic and uniaxial tensile volumes in a typical, dog-bone tensile specimen (after [44]).

with the polar angle $\alpha \in [-\pi/2, \pi/2]$ and azimuth angle $\zeta \in [-\pi, \pi]$, and has the coordinates $\left(x'(t), y'(t), z'(t)\right)$ at time t. Here, the hat $\hat{\bullet}$ indicates a unit vector $\bullet$. We take the convention that the materials volume on the positive side of the vector $\hat{\boldsymbol{n}}'$ is elastic.

In the remainder of this work, the Lüders front moves with a constant velocity $v_{x'}$, that remains undefined but whose magnitude is small enough for dissipative contributions beyond plasticity to be negligible, *e.g.* phonon damping. For convenience sake, we attach a local orthogonal Cartesian reference system to the Lüders front, where the x-axis remains parallel to the tensile x'-direction and the z-axis is in the Lüders front. Wherefore we construct a Cartesian coordinate system with orthonormal basis $Oxyz$ and unit vectors $\hat{\boldsymbol{e}}_1 = [100]$, $\hat{\boldsymbol{e}}_2 = [010]$ and $\hat{\boldsymbol{e}}_3 = [001]$, with $\hat{\boldsymbol{e}}_3 \cdot \hat{\boldsymbol{n}} \equiv 0$. Hence the front is uniquely captured by the Lüders angle $\phi(y) = \pi/2 - \alpha(y)$, with $\alpha \in [0, \pi/2]$ and the coordinate translation $x = x' - v_{x'}t$. Finally, for convenience of notation, we attach a second local orthogonal Cartesian reference system to the Lüders front. This Cartesian coordinate system has the orthonormal basis basis $Ox''y''z$ and unit vectors $\hat{\boldsymbol{e}}_1 = [\cos(\alpha)\ \sin(\alpha)\ 0]$, $\hat{\boldsymbol{e}}_2 = [-\sin(\alpha)\ \cos(\alpha)\ 0]$ and $\hat{\boldsymbol{e}}_3 = [0\ 0\ 1]$ in the local basis $Oxyz$ (See Fig. 4.1). In the following, the angle α is the inclination in the $\hat{\boldsymbol{e}}_3$-plane between the unit vector $\hat{\boldsymbol{e}}_2$ and the Lüders front; the Lüders front has the unit normal $\hat{\boldsymbol{n}} = [\cos(\alpha)\ \sin(\alpha)\ 0]$; and, the angle ϕ is the smallest angle between the tensile $x'-$direction and the Lüders front y''. We assume that the inclination α is independent of the $y'-$ and z'-coordinates in the following as well, *i.e.* the Lüders front is a plane.

Material both in the elastic and plastic volume, away from the Lüders front, experiences the observed uniaxial tensile stress σ^*_{u11}, where the superscript $\sigma^*_\bullet$ indicates stresses $\sigma_\bullet$ that are calculated across the specimen's original geometry. Directly at the Lüders front, two material states (still-elastic and just-plastic) coexist. As the front traverses the gauge length a given material point is initially in the elastic state, until an upper yield criterion $\mathcal{R}_{\mathrm{H}}$ is met. This instance coincides with the given material point entering the Lüders band. Inside the Lüders band the material point starts to deform plastically, but with a lower yield criterion $\mathcal{R}_{\mathrm{L}} \leq \mathcal{R}_{\mathrm{H}}$.

In Fig. 1.2b, a schematic representation of the material mechanical behaviour is given in red. In the remainder of this section and Sec. 4.3 the transition in stress space between both yield surfaces $\mathcal{R}_\bullet$ is void of plastic deformation.

The Von Mises criterion for plastic yielding is

$$f\left(\sigma_{ij}, R_\mathrm{e}\right) = \tilde{\sigma}^2 - R_\mathrm{e}^2, \tag{4.1a}$$

with the equivalent stress,

$$\tilde{\sigma} \equiv \sqrt{3 s_{ij} s_{ij}/2}, \tag{4.1b}$$

where R_e is the flow strength, s_{ij} deviatoric stress and the circumflex $\tilde{\bullet}$ indicates an equivalent measure of tensor $\bullet$. Using the yield criterion (4.1), we obtain the yield strengths

$$R_{\mathrm{eH(tr)}} \equiv \frac{1}{\sqrt{2}} \sqrt{(\sigma_{\mathrm{e}1} - \sigma_{\mathrm{e}2})^2 + (\sigma_{\mathrm{e}2} - \sigma_{\mathrm{e}3})^2 + (\sigma_{\mathrm{e}3} - \sigma_{\mathrm{e}1})^2}; \tag{4.2a}$$

$$R_{\mathrm{eL(tr)}} \equiv \frac{1}{\sqrt{2}} \sqrt{\left(\sigma_{\mathrm{p}1} - \sigma_{\mathrm{p}2}\right)^2 + \left(\sigma_{\mathrm{p}2} - \sigma_{\mathrm{p}3}\right)^2 + \left(\sigma_{\mathrm{p}3} - \sigma_{\mathrm{p}1}\right)^2}; \tag{4.2b}$$

and,

$$R_{\mathrm{eL(obs)}} \equiv \frac{1}{\sqrt{2}} \sqrt{(\sigma_{\mathrm{u}1} - \sigma_{\mathrm{u}2})^2 + (\sigma_{\mathrm{u}2} - \sigma_{\mathrm{u}3})^2 + (\sigma_{\mathrm{u}3} - \sigma_{\mathrm{u}1})^2}, \tag{4.2c}$$

where $R_{\mathrm{eH(tr)}}$ and $R_{\mathrm{eL(tr)}}$ are the true upper and lower yield strengths, and $R_{\mathrm{eL(obs)}}$ the lower observed yield strength. Here, the stresses σ_{ei} are the principal stresses in a material point in the elastic volume, where $\bullet_{ei}$ is the index notation with $i = \{1,2,3\}$. We observe the Mohr's circle convention, where the principal components $\bullet_3 \leq \bullet_2 \leq \bullet_1$, and the given $\bullet_1$ indicates the major, $\bullet_2$ the middle and $\bullet_3$ the minor principal component of second-order tensor $\bullet$. Moreover, $\sigma_{\mathrm{p}i}$ and $\sigma_{\mathrm{u}i}$ are the principal stresses in a material point in the plastic and uniaxial tensile volumes. The *still-elastic* and *just-plastic* material points are indicated schematically in Fig. 4.1 by a red and a blue square, respectively. A material point in the plastic volume under uniaxial tension, with the true stresses $\sigma_{\mathrm{u}11}$ and $\sigma_{\mathrm{u}22} = 0$, is indicated by a green square in Fig. 4.1 as well.

The problem is governed by the traction continuity condition:

$$\left[\left[\sigma''_{ij}\right]\right] n''_j = \left[\left[\sigma''_{i1}\right]\right] = 0, \tag{4.3}$$

where $\left[\left[\sigma_{ij}\right]\right] \equiv \sigma_{\mathrm{p}ij} - \sigma_{\mathrm{e}ij}$ are the differences in stresses across the Lüders front, in the still-elastic and just-plastic volumes. The normal stress to the Lüders front is $\sigma_\bullet \equiv \sigma''_{\bullet 11}$ and the shear stress parallel to the Lüders front $\tau_\bullet \equiv \sigma''_{\bullet 12}$, where $\bullet = \{\mathrm{e,u,p}\}$ indicates the elastic, uniaxial tensile and plastic volumes, respectively. These stresses in the still-elastic, just-plastic and uniaxial material points are indicated in Fig. 4.1 by red, blue and green arrows, respectively. Note that the stresses parallel to the Lüders front, $\sigma''_{\bullet 22}$ and $\sigma''_{\bullet 33}$, and shear stresses $\sigma''_{\bullet 23}$ and $\sigma''_{\bullet 13}$, are not necessarily equal.

Incompressible rigid-plastic deformation is given by the associated Levy-Mises hypothesis,

$$\mathrm{d}\epsilon_{\mathrm{p}ij} \equiv s_{\mathrm{p}ij}\mathrm{d}\lambda, \tag{4.4a}$$

with,

$$\mathrm{d}\epsilon_{\mathrm{p}1} + \mathrm{d}\epsilon_{\mathrm{p}2} + \mathrm{d}\epsilon_{\mathrm{p}3} \equiv 0, \tag{4.4b}$$

where $\mathrm{d}\epsilon_{\mathrm{p}ij}$ is the plastic strain increment and $0 \leq \mathrm{d}\lambda$ the plastic multiplier. We neglect elastic deformation, *i.e.* elastic deformation is small compared with plastic deformation. Material in the elastic state is thus rigid and in the plastic state displays typical hardening behaviour which we leave unspecified till Sec. 4.4.

We propose two kinematic conditions:

$$\mathrm{d}\epsilon''_{\mathrm{p}22} = 0, \tag{4.5a}$$

parallel to the Lüders front; and,

$$\mathrm{d}\epsilon_{\mathrm{p}12} = 0, \qquad \text{and} \qquad \mathrm{d}\epsilon_{\mathrm{p}13} = 0, \tag{4.5b}$$

perpendicular to the uniaxial tensile direction. Condition (4.5a) equals a velocity discontinuity/localisation [316] under uniaxial tension. Similarly, we locate the Lüders front parallel to the directions of zero extension [314]; condition (4.5b) ensures maximum, global plastic dissipation and was postulated by Irvin [323], *i.e.* direction of the major principal plastic strain increment is parallel with the tensile direction. These are the characteristics of the Lüders front we propose. Notable is that kinematic conditions (4.5) hold for a homogeneous stress state [314, 318], yet not necessarily for a heterogeneous stress state across the Lüders front, which we consider in the following.

Herein, the dependent variables are the observed lower yield strength $R_{\mathrm{eL(obs)}} \in \left[R_{\mathrm{eL(tr)}}, R_{\mathrm{eH(tr)}}\right]$ and the Lüders front angle $\phi \in (0, \pi/2]$ because of plane symmetry. The independent variables are the true upper and true lower yield strengths $R_{\mathrm{eH(tr)}}$ and $R_{\mathrm{eL(tr)}}$, respectively. The remaining unknowns are the twelve stresses $\sigma_{\bullet ij}$, nine on each side of the Lüders front of which at least six sets are equal. Equations (4.2)-(4.5) are the governing equations; and, the inverse yield strength ratio $\bar{r} \equiv R_{\mathrm{eL(tr)}}/R_{\mathrm{eH(tr)}} \in (0, 1]$, where the overbar $\bar{\bullet}$ indicates a scaled scalar $\bullet$. From these we construct open-form expressions for the lower yield strength $R_{\mathrm{eL(obs)}}$ and the Lüders front angle ϕ in the following.

4.3 Model

The problem definition presents an underdetermined system. We thus need five more functions that relate the macroscopic quantities of the lower observed yield strength $R_{\mathrm{eL(obs)}}$ and the Lüders front angle ϕ to the yield strength ratio $R_{\mathrm{eH(tr)}}/R_{\mathrm{eL(tr)}}$. We choose the invariant plane condition, that reduces the number of additional expressions to two. Wherefore we define three analytical expressions, one under plane strain and two under plane stress condition, and present their physics-based bounds in the following.

4.3.1 Plane Strain Analysis

Under plane strain condition, the displacement is zero perpendicular to the invariant plane, *i.e.*

$$\epsilon_{3i} = 0, \tag{4.6}$$

and the two remaining principal strain directions reside in the invariant plane.

Uniaxial Tensile Volume

The principal stresses in the (plastic) uniaxial tensile areas

$$\sigma_{\mathrm{u}1} = 2R_{\mathrm{eL(obs)}}/\sqrt{3}; \qquad \sigma_{\mathrm{u}2} = R_{\mathrm{eL(obs)}}/\sqrt{3}; \quad \text{and,} \quad \sigma_{\mathrm{u}3} = 0, \tag{4.7}$$

with the observed lower uniaxial tensile strength

$$R_{\mathrm{eL(obs)}} = \sqrt{3}\sigma_{\mathrm{u11}}/2, \tag{4.8}$$

for an incompressible solid and the uniaxial yield strength (4.2c).

Just-Plastic Volume

Using the plastic incompressibility (4.4b), we obtain the principal plastic strain increments in the invariant plane

$$\mathrm{d}\epsilon_{\mathrm{p3}} = -\mathrm{d}\epsilon_{\mathrm{p1}}, \tag{4.9a}$$

with the out of plane strain increment

$$\mathrm{d}\epsilon_{\mathrm{p33}} = \mathrm{d}\epsilon_{\mathrm{p2}} = 0. \tag{4.9b}$$

Substituting the principal plastic strain increments (4.9) in the kinematic conditions (4.5), we find that Lüders front angle

$$\phi = \frac{\pi}{4}, \tag{4.10}$$

that is independent of the heterogeneous stress state across the Lüders front.

Using the Levy-Von Mises hypothesis (4.4a), the plane strain boundary condition (4.6) and the kinematic condition (4.5b), we obtain the stresses in the just-plastic volume

$$\sigma_{\mathrm{p33}} = \frac{1}{2}\left(\sigma_{\mathrm{p11}} + \sigma_{\mathrm{p22}}\right); \qquad \sigma_{\mathrm{p13}} = 0; \qquad \sigma_{\mathrm{p23}} = 0; \quad \text{and,} \quad \sigma_{\mathrm{p12}} = 0. \tag{4.11}$$

The normal and shear stress in the just-plastic volume

$$\sigma_{\mathrm{p}} = \frac{1}{2}\left(\sigma_{\mathrm{p11}} + \sigma_{\mathrm{p22}}\right); \quad \text{and,} \quad \tau_{\mathrm{p}} = \frac{1}{2}\left(\sigma_{\mathrm{p11}} - \sigma_{\mathrm{p22}}\right). \tag{4.12}$$

Using the principal stresses in the just-plastic volume $\sigma_{\mathrm{p}\bullet}$ and the yield strength (4.2b), we find the true lower yield strength

$$R_{\mathrm{eL(tr)}} = \sqrt{3}\tau_{\mathrm{p}}. \tag{4.13}$$

Still-Elastic Volume

Under plane strain condition (4.6) for an incompressible solid, the out of plane (shear) stresses

$$\sigma_{\mathrm{e33}} = \frac{1}{2}(\sigma_{\mathrm{e11}} + \sigma_{\mathrm{e22}}); \quad \sigma_{\mathrm{e23}} = 0; \quad \text{and} \quad \sigma_{\mathrm{e13}} = 0. \tag{4.14}$$

The normal and shear stress in the just-plastic volume

$$\sigma_{\mathrm{e}} = \frac{1}{2}(\sigma_{\mathrm{e11}} + 2\sigma_{\mathrm{e12}} + \sigma_{\mathrm{e22}}); \quad \text{and,} \quad \tau_{\mathrm{e}} = \frac{1}{2}(\sigma_{\mathrm{e11}} - \sigma_{\mathrm{e22}}), \tag{4.15}$$

respectively. Using the principal stresses in the still-elastic volume $\sigma_{\mathrm{e}\bullet}$ and the yield strength (4.2a), we obtain the true upper yield strength

$$R_{\mathrm{eH(tr)}} = \sqrt{3\left(\tau_{\mathrm{e}}^2 + \sigma_{\mathrm{e12}}^2\right)}. \tag{4.16}$$

YIELD STRENGTHS

The lower yield point limit corresponds with the yield strength ratio that approaches unity, *i.e.* $\bar{r} \sim 1$. Using the boundary conditions (4.3), and the true lower and upper yield strengths (4.13) and (4.16), respectively, we find the shear stress in the invariant plane is obviously zero, *i.e.* $\sigma_{e12} \sim 0$. The shear stress in the Lüders front is trivially $\tau \sim R_{eL(obs)}/\sqrt{3}$. The upper yield point limit corresponds with the inverse yield strength ratio $\bar{r} \sim 0$. The shear stress in the Lüders front thus approaches zero, *i.e.* $\tau \equiv \tau_p = \tau_e \sim 0$. The angle of the Lüders front $\phi = \pi/4$ is invariant under plane strain condition.

Combining the boundary conditions (4.3), and true yield strengths (4.13) and (4.16), we obtain the shear stress in the invariant plane and the still-elastic volume

$$\sigma_{e12} = \frac{\sqrt{1-\bar{r}^2}}{\bar{r}}\tau. \tag{4.17}$$

The two remaining independent variables are the normal and shear stresses in the Lüders front $\sigma \equiv \sigma_p = \sigma_e$ and τ, respectively. Using the true lower uniaxial yield strength (4.13), we find the shifted and scaled, major and minor principal stresses

$$\frac{(\sigma_{p1}-\sigma)}{R_{eL(tr)}} = \frac{(\sigma-\sigma_{p2})}{R_{eL(tr)}} = \frac{1}{\sqrt{3}}; \tag{4.18a}$$

the shifted middle principal stress $\sigma_{p2} - \sigma = 0$ in the just-plastic volume; and, the shifted and scaled, major, middle and minor principal stresses

$$\frac{(\sigma_{e1}-\sigma)}{R_{eL(tr)}} = \frac{1-\sqrt{1-\bar{r}^2}}{\sqrt{3}\bar{r}}; \qquad \frac{(\sigma_{e2}-\sigma)}{R_{eL(tr)}} = -\frac{\sqrt{1-\bar{r}^2}}{\sqrt{3}\bar{r}};$$
$$\text{and,} \qquad \frac{(\sigma_{e3}-\sigma)}{R_{eL(tr)}} = -\frac{1+\sqrt{1-\bar{r}^2}}{\sqrt{3}\bar{r}}, \tag{4.18b}$$

respectively, in the still-elastic volume. Hence the true yield strengths ratio is independent of the normal stress in the Lüders front σ, that solely translates both sets of principal stresses and remains unknown. In Fig. 4.2, the shifted and scaled Mohr's circles are given for yield strength ratio $R_{eH(tr)}/R_{eL(tr)} = 2$ under plane strain condition; the xy-, xz- and yz-planes that contain the given plane normal $\hat{\boldsymbol{n}}$ are indicated with solid, dashed and dotted lines, respectively; and, the stresses in the just elastic σ_{eij} and just-plastic σ_{pij} volumes are indicated in red and blue, respectively. The shear stress τ in the Lüders front is highlighted by a gray dashed circle.

Substituting the shear stress in the invariant plane (4.17) in the true upper yield strength (4.2a), and using the definition of the inverse yield strength ratio $\bar{r}$, we rewrite the scaled true lower and upper yield strengths as

$$\frac{R_{eL(tr)}}{R_{eL(obs)}} = \bar{r}\frac{R_{eH(tr)}}{R_{eL(obs)}} = \frac{\sqrt{3}\tau}{R_{eL(obs)}}. \tag{4.19}$$

The scaled shear stress in the Lüders front $\tau/R_{eL(obs)}$ is then the independent variable. In accordance with Eqs. (4.18) and (4.19), the heterogeneous stress state is the result of the yield strength ratio $1 < R_{eH(tr)}/R_{eL(tr)} = \bar{r}^{-1}$ and the stress concentration increases with it. The

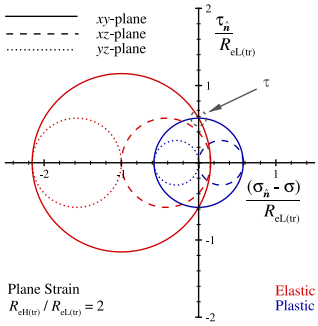

Figure 4.2: The scaled shear stress $\tau_{\hat{\boldsymbol{n}}}/R_{\mathrm{eL(tr)}}$ as a function of the shifted and scaled normal stress $(\sigma_{\hat{\boldsymbol{n}}}-\sigma)/R_{\mathrm{eL(tr)}}$ on a plane with normal $\hat{\boldsymbol{n}}$ in the still-elastic and just-plastic volumes for yield strength ratio $R_{\mathrm{eH(tr)}}/R_{\mathrm{eL(tr)}} = 2$ under plane strain condition.

challenge thus remains to find the functional form of the relation between the observed lower yield strength $R_{\mathrm{eL(obs)}}$ and the shear stress in the Lüders front τ as a function of the material properties of the yield strength ratio $R_{\mathrm{eH(tr)}}/R_{\mathrm{eL(tr)}}$.

4.3.2 Plane Stress Analysis

Under plane stress condition, the only non-zero stresses are in the invariant plane, *i.e.*

$$\sigma_{3i} = 0, \tag{4.20}$$

and one principal stress direction is perpendicular to the invariant plane.

Uniaxial Tensile Area

The principal stresses in the uniaxial tensile areas are

$$\sigma_{\mathrm{u1}} = R_{\mathrm{eL(obs)}}; \qquad \sigma_{\mathrm{u2}} = 0; \quad \text{and} \quad \sigma_{\mathrm{u3}} = 0, \tag{4.21}$$

with the observed lower uniaxial tensile strength

$$R_{\mathrm{eL(obs)}} = \sigma_{\mathrm{u11}}, \tag{4.22}$$

for the yield strength (4.2c).

Just-Plastic Area

Using the kinematic conditions (4.5), we find the stresses in the invariant plane on the just-plastic area

$$\sigma_{\mathrm{p22}} = \left(1 - \frac{2}{3\cos(2\alpha)+1}\right)\sigma_{\mathrm{p11}}; \qquad \text{and,} \qquad \sigma_{\mathrm{p12}} = 0. \tag{4.23}$$

The normal and shear stress in the Lüders front on the just-plastic area

$$\sigma_{\mathrm{p}} = \frac{4\cos(2\alpha)}{3\cos(2\alpha)+1}\sigma_{\mathrm{p11}}; \quad \text{and,} \quad \tau_{\mathrm{p}} = \frac{\sin(2\alpha)}{3\cos(2\alpha)+1}\sigma_{\mathrm{p11}}, \tag{4.24}$$

respectively. Using the principal stresses on the just-plastic area,

$$\sigma_{\mathrm{p1}} = \sigma_{\mathrm{p11}}; \qquad \sigma_{\mathrm{p2}} = \sigma_{\mathrm{p22}}; \quad \text{and} \quad \sigma_{\mathrm{p3}} = 0, \tag{4.25}$$

and the yield strength (4.2b), we obtain the true lower yield strength

$$R_{\mathrm{eL(tr)}} = \sqrt{9\cot^2(2\alpha) + 3\csc^2(2\alpha)}\tau_{\mathrm{p}}. \tag{4.26}$$

Hence the true lower yield strength depends on the shear stress τ_{p} in and the inclination α of the Lüders front.

Still-Elastic Area

The normal and shear stress in the Lüders front on the still-elastic area are

$$\begin{aligned} \sigma_{\mathrm{e}} &= \cos^2(\alpha)\sigma_{\mathrm{e11}} + \sin(2\alpha)\sigma_{\mathrm{e12}} + \sin^2(\alpha)\sigma_{\mathrm{e22}}; \qquad \text{and,} \\ \tau_{\mathrm{e}} &= \frac{1}{2}\sin(2\alpha)\sigma_{\mathrm{e11}} - \cos(2\alpha)\sigma_{\mathrm{e12}} - \frac{1}{2}\sin(2\alpha)\sigma_{\mathrm{e22}}, \end{aligned} \tag{4.27}$$

respectively. Using the principal stresses on the still-elastic area σ_{e}. and the yield strength (4.2a), we find the trivial true upper yield strength

$$R_{\mathrm{eH(tr)}} = \sqrt{\sigma_{\mathrm{e11}}^2 - \sigma_{\mathrm{e11}}\sigma_{\mathrm{e22}} + \sigma_{\mathrm{e22}}^2 + 3\sigma_{\mathrm{e12}}^2}. \tag{4.28}$$

Yield Strengths

Using the true lower yield strength (4.26), the shear stress on the just-plastic area (4.24) and the observed lower tensile strength (4.22), we find that in the lower yield point limit the Lüders front inclination $\alpha \sim \tan^{-1}\left(\sqrt{8}\right)/2$ radian (*i.e.* the seminal Lüders front angle $\phi \approx 54.74$ degrees [310]). The shear stress in the Lüders front $\tau \equiv \tau_{\mathrm{u}} \sim \sqrt{2}R_{\mathrm{eL(obs)}}/3$. Using the true upper yield strength (4.28) and the normal and shear stresses (4.27), we find that the shear stress in the invariant plane on the still-elastic area σ_{e12} is obviously zero as well, *i.e.* a uniaxial tensile stress state exists. Using the true lower and upper yield strengths (4.26) and (4.28), we find that in the upper yield point limit the shear stress in the Lüders front τ vanishes as well, and the Lüders front angle $\phi \sim \pi/2$ radian. Hence the Lüders front angle $\phi \approx 55\cdots \sim 90$ degrees increases with the yield strength ratio $R_{\mathrm{eH(tr)}}/R_{\mathrm{eL(tr)}}$under plane stress condition. Notable is that the major and middle principal stresses are positive, *i.e.* $0 \leq \sigma_{\mathrm{p2}}/\sigma_{\mathrm{p1}} < 1/2$, and the maximum shear stress on the just-plastic area $\left(\sigma_{\mathrm{p1}} - \sigma_{\mathrm{p3}}\right)/2$ resides on a plane at a $\pi/4$ radian angle to the tensile direction out of the invariant plane.

Using Eq. (4.24) and the boundary condition (4.3), we obtain the normal stress in the Lüders front

$$\sigma = 4\cot(2\alpha)\tau. \tag{4.29}$$

Combining the boundary condition (4.3), the normal stress in the Lüders front (4.29), and yield strengths (4.26) and (4.28), we find the shear stress in the invariant plane on the still-elastic area

$$\sigma_{\mathrm{e12}} = \left(2\cos(2\alpha) + \sqrt{\frac{3\left(1-\bar{r}^2\right)}{8\bar{r}^2}\left(3\cos(4\alpha)+5\right)}\right)\tau. \tag{4.30}$$

The two remaining independent variables are the shear stresses τ in, and the inclination α of, the Lüders front.

Using the true lower yield strength (4.26) and the Lüders front ratio $\bar{\alpha} \in [0,1]$, we rewrite the scaled, true lower and upper yield strengths as

$$\frac{R_{\mathrm{eL(tr)}}}{R_{\mathrm{eL(obs)}}} = \bar{r}\frac{R_{\mathrm{eH(tr)}}}{R_{\mathrm{eL(obs)}}} = \frac{3}{\sqrt{2}}\frac{\tau}{\bar{\alpha}R_{\mathrm{eL(obs)}}}. \tag{4.31}$$

The scaled shear stress in the Lüders front $\tau/R_{\mathrm{eL(obs)}}$ is one remaining independent variable. With the Lüders front ratio $\bar{\alpha}$, we rewrite the Lüders front inclination as

$$\alpha = \frac{1}{2}\cos^{-1}\left(\sqrt{1-\frac{8\bar{\alpha}^2}{6\bar{\alpha}^2+3}}\right), \tag{4.32}$$

which aids the formulation of a closed-form expression for the Lüders front angle ϕ as a function of the yield strength ratio $R_{\mathrm{eH(tr)}}/R_{\mathrm{eL(tr)}}$ in the following.

Using the true lower yield strength (4.26) and the definition of the Lüders front ratio $\bar{\alpha}$ in (4.32), we find the shifted and scaled, major and middle principal stresses

$$\frac{4\sigma_{\mathrm{p1}}-3\sigma}{2R_{\mathrm{eL(tr)}}} = \frac{3\sigma-4\sigma_{\mathrm{p2}}}{2R_{\mathrm{eL(tr)}}} = \frac{\sqrt{2\bar{\alpha}^2+1}}{\sqrt{3}}, \tag{4.33a}$$

on the just-plastic area; and, the major and minor principal stresses

$$\begin{aligned}\frac{4\sigma_{\mathrm{e1}}-3\sigma}{2R_{\mathrm{eL(tr)}}} &= \frac{1}{3}\sqrt{6(\bar{\alpha}^2-1)+\frac{9}{\bar{r}^2}+6\sqrt{(2\bar{\alpha}^2-3)\frac{1-\bar{r}^2}{\bar{r}^2}}}-\sqrt{\frac{1-\bar{r}^2}{\bar{r}^2}}; \quad \text{and,}\\ \frac{4\sigma_{\mathrm{e3}}-3\sigma}{2R_{\mathrm{eL(tr)}}} &= -\frac{1}{3}\sqrt{6(\bar{\alpha}^2-1)+\frac{9}{\bar{r}^2}+6\sqrt{(2\bar{\alpha}^2-3)\frac{1-\bar{r}^2}{\bar{r}^2}}}-\sqrt{\frac{1-\bar{r}^2}{\bar{r}^2}},\end{aligned} \tag{4.33b}$$

respectively, on the still-elastic area, with the normal stress in the Lüders front,

$$\frac{\sigma}{R_{\mathrm{eL(tr)}}} = \frac{2}{3}\sqrt{3-2\bar{\alpha}^2}. \tag{4.33c}$$

The ratio between principal stresses, within and between both sets, are thus independent of the shear stress τ; the shear stress τ in the Lüders front solely scales all principal stresses $\sigma_{\bullet i}$. In Fig. 4.3, the scaled Mohr's circles are given for yield strength ratios $R_{\mathrm{eH(tr)}}/R_{\mathrm{eL(tr)}} = 2$ and $5/2$, and Lüders front angles $\phi = 60$ and 80 degrees under plane stress condition; the yield strength ratio increases from $R_{\mathrm{eH(tr)}}/R_{\mathrm{eL(tr)}} = 2$ to $5/2$ between Figs. 4.3a, and b and c; and, the Lüders front angle increases from $\phi = 60$ to 80 degrees, between Figs. 4.3a and b, and c. The shear stress τ in, and the normal stress σ on, the Lüders front are highlighted by a gray dashed circle. Furthermore, the ×-shaped markers on the horizontal axis in Fig. 4.3b indicate the principal stresses $\sigma'_{\bullet 1}$ and $\sigma'_{\bullet 2}$ on the widest face of a tensile specimen. The heterogeneous stress state is then the result of the yield strength ratio $1 < R_{\mathrm{eH(tr)}}/R_{\mathrm{eL(tr)}}$ and/or a decrease in Lüders front inclination $\alpha < \tan^{-1}\left(\sqrt{8}\right)/2$ radian. The stress concentration increases with the yield strength ratio $R_{\mathrm{eH(tr)}}/R_{\mathrm{eL(tr)}}$ and Lüders front angle ϕ as well. The challenge that remains under plane stress conditions is to find the functional form of the relation between the Lüders front angle ϕ and the material properties of the yield strength ratio $R_{\mathrm{eH(tr)}}/R_{\mathrm{eL(tr)}}$, which we address in the following.

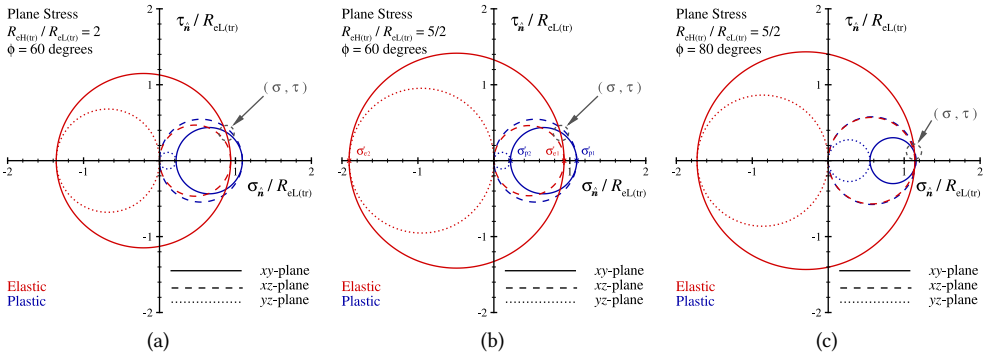

Figure 4.3: The scaled shear stress $\tau_{\hat{\boldsymbol{n}}}/R_{\mathrm{eL(tr)}}$ as a function of the scaled stress $\sigma_{\hat{\boldsymbol{n}}}/R_{\mathrm{eL(tr)}}$ on a plane with normal $\hat{\boldsymbol{n}}$ in the still-elastic and just-plastic areas for yield strength and Lüders front ratios (a) $\left\{R_{\mathrm{eH(tr)}}/R_{\mathrm{eL(tr)}}; 4\phi/\pi\right\} = \{2; 4/3\}$, (b) $\{5/2; 4/3\}$ and (c) $\{5/2; 16/9\}$ under plane stress condition.

4.4 Numerical Approach

We use the method as presented by Schwab and Harter [62] to obtain the numerical results. We carry out the numerical calculations with the Abaqus/Standard code version 6.14 [324], with finite deformations, dynamic two-dimensional solid (continuum) elements, and without mass scaling. Rayleigh damping of 10^{-6} s stabilises the implicit calculations and the volumetric mass density is 7.85×10^{3} kg/m^3. Time increments are limited to a maximum and minimum of 1×10^{-3} s and 1×10^{-15} s, respectively, and the remaining criteria are kept as supplied by Abaqus 6.14 [324]. The geometry, mesh and boundary conditions are presented schematically in Fig. 4.4. The geometry is that of a typical dog-bone tensile specimen with

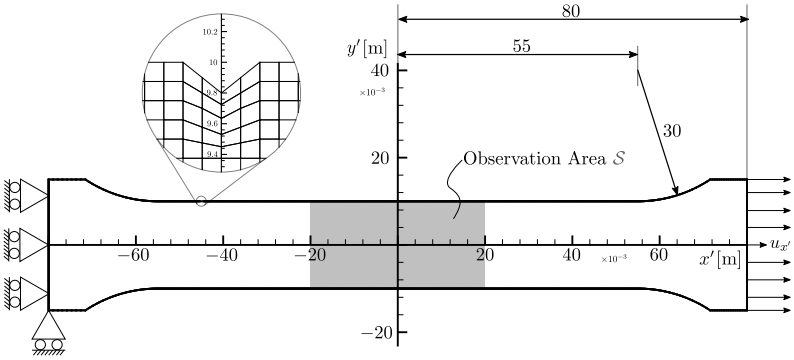

Figure 4.4: Diagram of the tensile specimen, mesh and the displacement boundary conditions. All spatial dimensions are in $\times10^{-3}$ m.

gauge width $w = 2\times10^{-2}$ m and total length $l = 1.6\times10^{-1}$ m. The gauge length is maximised to avoid influence of the shoulder shape and initiation of the Lüders bands. We create a trigger point for these bands by means of a triangular cutout at $\{x', y'\} = \{-45, 10\}\times10^{-3}$ m, that reduces the specimen cross-sectional area by one hundredth. This trigger point is

shown in the insert in Fig. 4.4. The specimen thickness is $h = 1 \times 10^{-3}$ m for computational convenience.

The mesh consists of predominantly, square eight-node two-dimensional solid elements with reduced integration under plane strain and stress conditions, which are termed *CPE8R* and *CPS8R* in Abaqus [324], respectively. The discretization varies symmetrically around the y'-axis, where the mesh coarsens a factor two across the shoulders to increase computational tractability. The maximum element's aspect ratio is kept below two. The discretization is constant with square elements over the central rectangular section with 12.5×10^{-5} m sides (See the insert in Fig. 4.4). We limit mechanical behaviour to elasticity for the rectangular parts of the specimen shoulders to increase computational tractability as well.

The material mechanical behaviour is described by isotropic linear elasticity, with the elastic modulus $E = 210 \times 10^9$ Pa and Poisson's ratio $\nu = 0.3$; and, the isotropic plastic behaviour is described by a simple Up-Down-Up plasticity model [325]. The material flow strength is

$$R_{\mathrm{e}} = R_{\mathrm{eL(tr)}} + H\tilde{\epsilon}_{\mathrm{p}}, \tag{4.34a}$$

during hardening, with the equivalent plastic strain,

$$\tilde{\epsilon}_{\mathrm{p}} \equiv \sqrt{2\epsilon_{\mathrm{p}ij}\epsilon_{\mathrm{p}ij}/3}, \tag{4.34b}$$

and the plastic modulus ratio $H = E/10$. The softening modulus is kept constant in the following with $-260E$. We find this ensures computational tractability and simplifies the further analysis of our model that is independent of softening/hardening behaviour (See Sec. 4.3). The boundary conditions are selected as those by Mazière and Forest [58]. This ensures predominantly uniaxial tension across the tensile specimen. Only the displacement rate $\dot{u}_{x'}$ is kept constant across the outer faces of the prismatic part of the specimen shoulders. Here the overdot $\dot{\bullet}$ indicates a derivative with respect to time t. This results in a strain rate $\dot{\epsilon}_{11} \approx 10^{-4}$ s^{-1}, where the hardening response is independent of loading rate. The Up-Down-Up plasticity model [325] induces strain localisation [62]. This steep drop of stress at first yielding poses problems with stability and mesh dependence.

It is well known that conventional strain localisation is associated with spurious mesh dependence due to the loss of ellipticity of the set of partial differential equations [326]. Due to the hardening behaviour that follows the softening convergence is still achieved [58]. However, it has been demonstrated that simulations of Lüders band formation is prone to spurious mesh dependencies, and the observed lower yield strength $R_{\mathrm{eL(obs)}}$ and Lüders strain ϵ^{L} cannot be predicted with high accurately due to the presence of mesh-dependent oscillations on the overall curve [59, 61, 88]. This dependence on the relative orientation between element edges and loading direction is evidenced by Mazière and Forest [58], and pronounced under plane stress condition. We counteract this by: (1) limiting our observations to only a section of the tensile specimen with a well-developed Lüders front; and (2), an extensive mesh-sensitivity study. Closure and corroboration of our simple rigid-plastic model is the goal, for which we find the numerical approach suffices [44, 62, 63].

4.5 Numerical Results

In the remainder, we limit our observations to an area $\mathcal{S}$, that is one-fourth of the tensile specimen's length, $l/4$, centred around the origin with a volume $\Omega = \mathcal{S}h$. This area we

shade light grey in Fig. 4.4 and refer to, from hereon, as the observation area. The observed quantities are reported in the original orthonormal basis $Ox'y'z'$ in the following (See the Problem Definition 4.2).

We find it necessary to make special mention of the method by which we visualise and quantify the Lüders front. Firstly, the (physical) quantity one chooses depends on ones understanding of the characteristics of the Lüders front. Secondly, not all (observable) quantities are easily accessible in an experiment. Numerical analysis allows us to choose any spatial quantity, yet we find the equivalent plastic strain gradient $\|\nabla\tilde{\epsilon}_{\mathrm{p}}\|$ most suitable. The spatial difference in equivalent plastic strain gradient is maximised perpendicular to, and minimised parallel to the Lüders band. This makes it particularly suitable for visualising the Lüders front by means of the global coordinates $\left\{x', y'\right\}$ of the local maxima in the equivalent plastic strain gradient. This is similar to the analysis method of experimental results in [69, 74]. The Lüders front that we consider is a plane (See Problem Definition 4.2). Hence we use linear regression [289] with

$$x' = C_1 + \bar{C}_2 y', \tag{4.35}$$

where C_1 is the axial coordinate of the Lüders band and $\alpha \equiv \tan^{-1}\left(\|\bar{C}_2\|\right)$ the inclination of the Lüders front, with Lüders band ratio $\bar{C}_2$.

4.5.1 Tensile Test

The volume averaged Von Mises stress $\langle\tilde{\sigma}\rangle$ as a function of the volume averaged equivalent plastic strain $\langle\tilde{\epsilon}_{\mathrm{p}}\rangle$ for yield strength ratios $R_{\mathrm{eH(tr)}}/R_{\mathrm{eL(tr)}} = 7/4,\ 2,\ 5/2,\ 3,\ 7/2$ and 4, is presented in Figs. 4.5a and b; the dashed-dotted grey line indicates materials strain hardening $R_{\mathrm{e}}\left(\tilde{\epsilon}_{\mathrm{p}}\right)$; the coloured solid markers the numerical results; and, the solid and dashed coloured lines the means and a single standard deviations, respectively. We determine the observed lower yield strength $R_{\mathrm{eL(obs)}}$ by averaging the volume averaged Von Mises stress $\langle\tilde{\sigma}\rangle$ over the volume averaged equivalent plastic strain $\langle\tilde{\epsilon}_{\mathrm{p}}\rangle$, *i.e.*

$$R_{\mathrm{eL(obs)}} \equiv \frac{1}{\tilde{\epsilon}_{\mathrm{p}}^{\mathrm{L}}} \int_0^{\tilde{\epsilon}_{\mathrm{p}}^{\mathrm{L}}} \langle\tilde{\sigma}\rangle \,\mathrm{d}\langle\tilde{\epsilon}_{\mathrm{p}}\rangle, \tag{4.36a}$$

with the volume averaged scalar function,

$$\langle\bullet\rangle \equiv \frac{1}{\Omega} \iiint_{\Omega} \bullet \,\mathrm{d}x' \,\mathrm{d}y' \,\mathrm{d}z', \tag{4.36b}$$

where $\tilde{\epsilon}_{\mathrm{p}}^{\mathrm{L}}$ is the volume averaged equivalent plastic Lüders strain. Here the roman superscript $\bullet^{\mathrm{L}}$ indicates the quantity $\bullet$ at the instant the Lüders band swept the observation area $\mathcal{S}$. Three of these instants are highlighted by black circles in Figs. 4.5a and b.

Under plane stress in Fig. 4.5a and plane strain condition in 4.5b, the observed lower yield strength $R_{\mathrm{eL(obs)}}$ increases with yield strength ratio $R_{\mathrm{eH(tr)}}/R_{\mathrm{eL(tr)}}$. The equivalent plastic Lüders strain $\tilde{\epsilon}_{\mathrm{p}}^{\mathrm{L}}$ increases as well. Notable is that the standard deviation in the volume averaged Von Mises stress is larger under plane strain than plane stress conditions. Whereof one reason is that the axial length of the Lüders band along the x'-axis is longer under plane strain than under plane stress condition. Plastic deformation across the shoulders thus

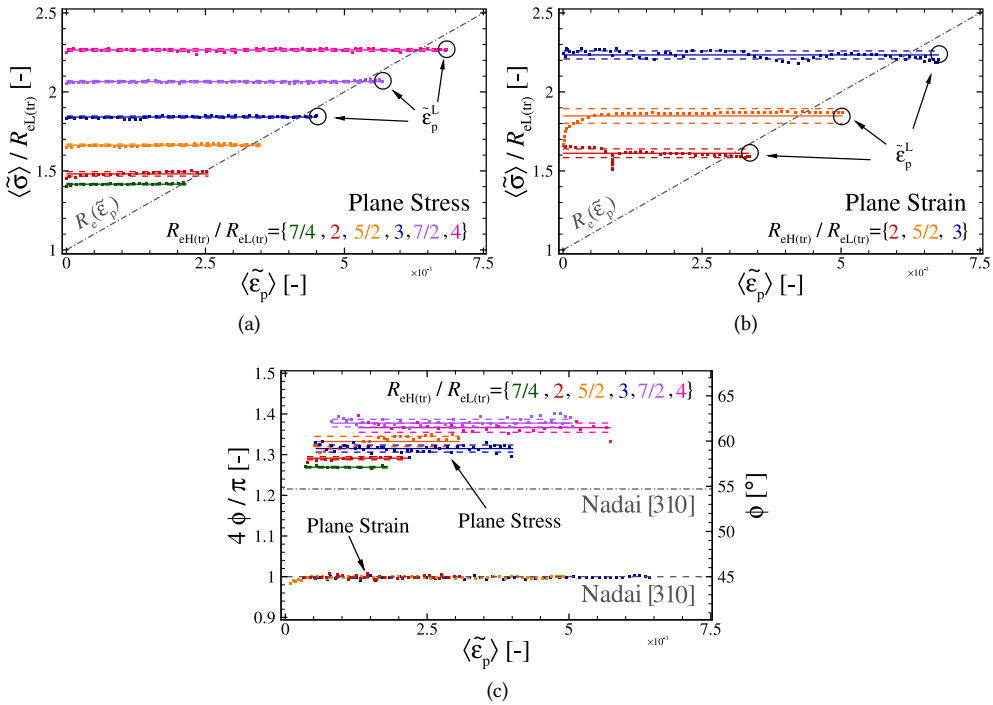

Figure 4.5: (a,b) The scaled volume averaged Von Mises stress $\langle\tilde{\sigma}\rangle/R_{eL(tr)}$ and (c) the scaled Lüders front angle $4\phi/\pi$ as functions of the volume averaged equivalent plastic strain $\langle\tilde{\epsilon}_p\rangle$, under (a,c) plane stress and (b,c) plane strain conditions for yield strength ratios $R_{eH(tr)}/R_{eL(tr)}$ =7/4, 2, 5/2, 3, 7/2 and 4. The solid coloured lines indicate the mean over the given equivalent plastic strain ranges, and the dashed dotted lines a single standard deviation.

influences the initial volume averaged Von Mises stress $\langle\sigma\rangle$ with volume averaged equivalent plastic strain range $\langle\tilde{\epsilon}_p\rangle \leq 1\times10^{-3}$ over the observation area $\mathcal{S}$. Notable is that equivalent plastic Lüders strain $\tilde{\epsilon}_p^L$ for the given yield strength ratio $R_{eH(tr)}/R_{eL(tr)}$ is larger than the plastic strain $\left(R_{eL(obs)} - R_{eL(tr)}\right)/H$, *i.e.* the intersection of the given solid coloured line and the slanted dashed-dotted grey line in Figs. 4.5a and b. The magnitude of this difference increases with yield strength ratio $R_{eH(tr)}/R_{eL(tr)}$, which we discuss in Sec. 4.6.2.

The Lüders front angle ϕ as a function of the volume averaged equivalent plastic strain $\langle\tilde{\epsilon}_p\rangle$ for yield strength ratios $R_{eH(tr)}/R_{eL(tr)} = 7/4,\ 2,\ 5/2,\ 3,\ 7/2$ and 4, is shown in Fig. 4.5c; the dashed and dashed-dotted grey lines indicate the plane strain and plane stress results by Nadai [310] of angles $\phi = 45$ and ≈ 55 degrees, respectively. We omit the mean and standard deviation of the Lüders front angle $\phi \approx 45$ degrees under plane strain condition because the standard deviations are negligible compared with those under plane stress condition. The means and the standard deviations are over the volume averaged equivalent plastic strain range $0\cdots\tilde{\epsilon}_p^L$. We find that the Lüders front angle ϕ increases with yield strength ratio $R_{eH(tr)}/R_{eL(tr)}$ under plane stress condition. However, we limit the plastic strain range under plane stress condition, that we display and integrate with, to when then the Lüders band covers the whole specimens width w (See Fig. 4.4). The standard deviation in the

Lüders front angle ϕ increases because the fronts' morphology curves with yield strength ratios $R_{\mathrm{eH(tr)}}/R_{\mathrm{eL(tr)}} = 5/2 \cdots 4$ [120] under plane stress condition. This we discuss in Sec. 4.6.2 as well.

4.5.2 Macroscopically Observed Quantities

The scaled shear stresses in the Lüders front (4.19) and (4.31), and the Lüders front ratio (4.32) present underdetermined systems under plane strain and stress conditions, respectively. Hence we construct two first-order approximations for these independent variables that satisfy the bounds that we present in Sec. 4.3. Using a linear approximation, we give the scaled observed lower yield strength as

$$\frac{R_{\mathrm{eL(obs)}}}{R_{\mathrm{eL(tr)}}} \approx 1 - a\left(1 - \frac{1}{\bar{r}}\right), \tag{4.37}$$

with scalar $a \in (0,1)$. Herewith we assume that the observed lower yield strength $R_{\mathrm{eL(obs)}}$ is directly related to the shear stress in the Lüders front τ as a function of the yield strength ratio $R_{\mathrm{eH(tr)}}/R_{\mathrm{eL(tr)}}$, the Lüders front angle ϕ and the in-plane condition. This is our alternative to a condition by Schwab and Ruff [44]. They [44] keep the shear stress in the Lüders front τ the same as that in the nominal, uniaxial tensile volume τ_{u}^{*} (*i.e.* on a plane parallel with the Lüders front outside the Lüders band), which is not necessarily satisfied under invariant plane conditions. By means of a linear fit of Eq. (4.37), we obtain the scalars $a = 0.606 \pm 0.038$ and 0.436 ± 0.046 under plane strain and stress conditions, respectively. Here the plus-minus sign $\pm\bullet$ indicates the standard deviation. The observed lower yield strength $R_{\mathrm{eL(obs)}}$ is presented as a function of the yield strength ratio $R_{\mathrm{eH(tr)}}/R_{\mathrm{eL(tr)}}$ in Fig. 4.6a. the red and

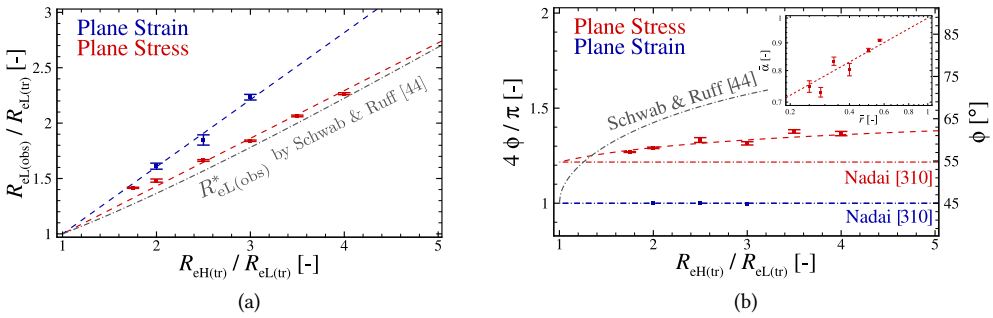

Figure 4.6: (a) The scaled lower observed yield strength ratio $R_{\mathrm{eL(obs)}}/R_{\mathrm{eL(tr)}}$ and (b) the scaled Lüders front angle $4\phi/\pi$ as functions of the yield strength ratio $R_{\mathrm{eH(tr)}}/R_{\mathrm{eL(tr)}}$. The error bars indicate a single standard deviation; the dashed coloured lines the reproductions by means of (a) Eq. (4.37), and (b) Eqs. (4.10) and (4.32).

blue coloured markers correspond with the numerical results under plane stress and strain conditions, respectively; and, the error bars indicate a single standard deviation as displayed in Fig. 4.5. The reproductions by Eq. (4.37) are indicated in Fig. 4.6a by coloured dashed lines.

Under plane strain condition, the Lüders front angle $\phi \approx \pi/4$ radian and independent of the yield strength ratio $R_{\mathrm{eH(tr)}}/R_{\mathrm{eL(tr)}}$ (See Fig. 4.5c). By means of a linear fit, we obtain the Lüders front inclination $4\alpha/\pi = 1.000$ radian with a standard deviation that is less than a five

hundredth of this mean. The (numerical) Lüders front angles ϕ are shown as a function of the yield strength ratios $R_{eH(tr)}/R_{eL(tr)}$ in Fig. 4.6b; the blue coloured markers correspond with the numerical results under plane strain condition; and, the reproduction is indicated by the dashed blue line in Fig. 4.6b. Under plane stress condition, the Lüders front angle ϕ increases with the yield strength ratio $R_{eH(tr)}/R_{eL(tr)} = 5/2 \cdots 4$ (See Fig. 4.5c). We use an exponential function for the Lüders front ratio $\bar{\alpha} \approx \bar{r}^b$ with the scalar $b \in (0,1]$, that satisfies the lower and upper yield point limits, *i.e.* Lüders front ratios $\bar{\alpha} = 1$ and ~ 0, respectively. This is the second first-order approximation for the now dependent variable of the Lüders front angle ϕ. By means of a linear fit of Eq. (4.32), we obtain the scalar $b \approx 1/5$, with $b = 0.201 \pm 0.001$. The insert in Fig. 4.6b is this linear fit of a Lüders front ratio $\bar{a}(\bar{r})$ on a Log-Log scale. The numerical results are indicated by red solid square symbols and a single standard deviation by red coloured error bars in Fig. 4.6b. The reproduction via Eq. (4.32) is indicated by a dashed red line. Herewith we obtain four closed-form expressions, two for the observed lower yield strengths $R_{eL(obs)}$ and two for the Lüders front angle ϕ under invariant plane conditions.

4

4.5.3 Lüders Band

The principal stresses σ'_i and plastic strains ϵ'_{pij} on the invariant plane as a functions of the distance x'' from the Lüders front are presented in Fig. 4.7 for yield strength ratio $R_{eH(tr)}/R_{eL(tr)} = 3$; the principal stresses $\sigma_\bullet$ are shifted with the volume averaged stress $\langle\sigma_\bullet\rangle$

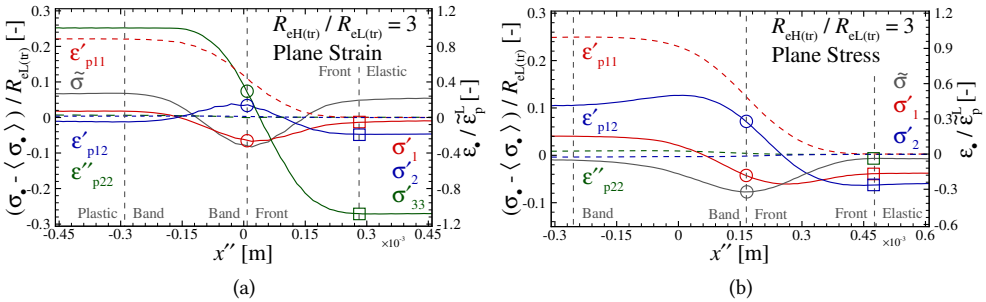

Figure 4.7: The shifted and scaled stress $(\sigma_\bullet - \langle\sigma_\bullet\rangle)/R_{eL(tr)}$ and the scaled strain $\epsilon_\bullet/\tilde{\epsilon}^L_p$ as a function of the distance x'' from the Lüders front for yield strength ratio $R_{eH(tr)}/R_{eL(tr)} = 3$ under (a) plane strain and (b) plane stress condition. Stresses are indicated by solid lines and strains by dashed coloured lines.

and indicated by solid coloured lines. The plastic strain $\epsilon_\bullet$ is scaled with the equivalent plastic Lüders strain $\tilde{\epsilon}^L_p$ and indicated by dashed coloured lines. The vertical dashed grey lines divide the distances from the Lüders front x'' into four regions, that are labelled *elastic*, *front*, *band* and *plastic*. These regions are delimited by yield $0 < d\tilde{\epsilon}_p$ and softening $d\tilde{\sigma} < 0$, between the elastic and front regions; hardening $0 < d\tilde{\sigma}$ and $0 < d\tilde{\epsilon}_p$ between the front and band regions; and, $d\tilde{\sigma} = 0$ and $d\tilde{\epsilon}_p = 0$ in the plastic region. The Von Mises stress $\tilde{\sigma}$ is indicated by a solid grey line in Fig. 4.7 as well.

In Fig. 4.7, the principal and equivalent stresses in the still-elastic and just-plastic volume/area are indicated by coloured squares and circles, respectively. We make this choice because the former coincide with initial yielding, that is related to the upper yield strength $R_{eH(tr)}$;

and, the latter with global hardening, that we capture with the lower yield strength $R_{\mathrm{eL(tr)}}$. The scalar stress and strain field are shifted back to the origin $x' - C_1$ by means of the axial coordinate C_1 and averaged over the equivalent plastic strain ranges as Fig. 4.5c displays. Notable is that because of the (numerical) method we choose, the high softening tangent modulus and Lüders band morphology (See Secs. 4.5.1 and 4.5.2), the change in stresses are smoothed compared with our analytical analysis in Sec. 4.3.

In Fig. 4.7, the major principal stresses σ'_1 are the major stresses σ_{e1} and σ_{p1}, which depend on their distance x'' from the Lüders front. The minor principal stress σ'_2 is not necessarily the middle principal stress $\sigma_{\bullet 2}$. Similarly, the stress on the invariant plane σ'_{33}, that we use to approximate the minor or middle principal stress (σ_{e3} and σ_{p2}) under plane strain condition in Fig. 4.7a, depends on the in-plane condition as well. The stress on the invariant plane σ'_{33} is obviously zero under plane stress condition in Fig. 4.7b and thus omitted. With the scaling of the stresses we choose in Fig. 4.7 the relative magnitudes between the middle and minor principal stresses $\sigma_{\bullet 2}$ and $\sigma_{\bullet 3}$ are retained.

We make the following observations on the principal stresses under plane strain condition in Fig. 4.7a: the maximum principal stresses in both still-elastic and just-plastic volume are positive with $0 < \sigma_{\mathrm{p1}} < \sigma_{\mathrm{e1}}$; the middle principal stress in the just-plastic volume is larger than the middle principal stress in the still-elastic volume with $\sigma_{\mathrm{e2}} \leq \sigma_{\mathrm{p2}}$; and, the minor principal stress in the just-plastic volume is $\sigma_{\mathrm{e3}} < 0$, while the minimum principal stress in the just-plastic volume is $\sigma_{\mathrm{p3}} < 0$, with $\sigma_{\mathrm{e3}} \leq \sigma_{\mathrm{p3}}$. The latter two observations agree with the analytical model in Sec. 4.3.1. The former observation is partly due to the elastic compressibility in our numerical results (with Poisson's ratio $\nu = 0.3$) and hardening that our analysis both omits (See Secs. 4.2 and 4.3.1). Moreover, under plane stress condition in Fig. 4.7b: the maximum principal stresses in both still-elastic and just-plastic area are positive with $\sigma_{\mathrm{e1}} \lessapprox \sigma_{\mathrm{p1}}$; the middle principal stress in the still-elastic area is $\sigma_{\mathrm{e2}} = 0$, while the middle principal stress in the just elastic area is $0 \leq \sigma_{\mathrm{p2}}$, with $\sigma_{\mathrm{e2}} \leq \sigma_{\mathrm{p2}}$; and, the minimal principal stress in the still-elastic area is $\sigma_{\mathrm{e3}} \leq 0$, while the minimum principal stress in the just-plastic area is $\sigma_{\mathrm{p3}} = 0$, with $\sigma_{\mathrm{e3}} \leq \sigma_{\mathrm{p3}}$. The latter two observations agree with the analytical model in Sec. 4.3.2. The former difference in major principal stress magnitudes is small. The numerically obtained principal stresses' signs and relative magnitudes agree with our model framework in Sec. 4.2. The difference in the ratio between principal stresses under plane stress condition is due to the numerical method that accounts for hardening as well. This is discussed further in Sec. 4.6.1.

The plastic shear strain ϵ'_{p12} is below a hundredth of the plastic strain ϵ'_{p11}, and approaches zero in the front. Likewise the plastic strain $\epsilon''_{\mathrm{p22}}$ is less than a twentieth of plastic strain ϵ'_{p11} strain. In the Lüders front the plastic extension $\epsilon''_{\mathrm{p22}}$ is less than a fiftieth of the equivalent plastic Lüders strain $\tilde{\epsilon}^{\mathrm{L}}_{\mathrm{p}}$. Notable is that the plastic shear strain ϵ'_{p12} remains an order of magnitude smaller than the plastic strain ϵ'_{p11} in the plastic region as well. However, the plastic extension $\epsilon''_{\mathrm{p22}}$ increases throughout the Lüders band under plane stress condition in Fig. 4.7b. These observations in Fig. 4.7 support the characteristics (4.5) under invariant plane conditions in the Lüders front, which are the characteristics of the Lüders front we propose herein.

4.6 Discussion

4.6.1 Stress Concentration under Uniaxial Tension

In Fig. 4.8a, the equivalent stress $\tilde{\sigma}$, and the principal stresses on the still-elastic and just-plastic side of the Lüders front, $\sigma_{e\bullet}$ and $\sigma_{p\bullet}$, respectively, are presented; a thin ten-

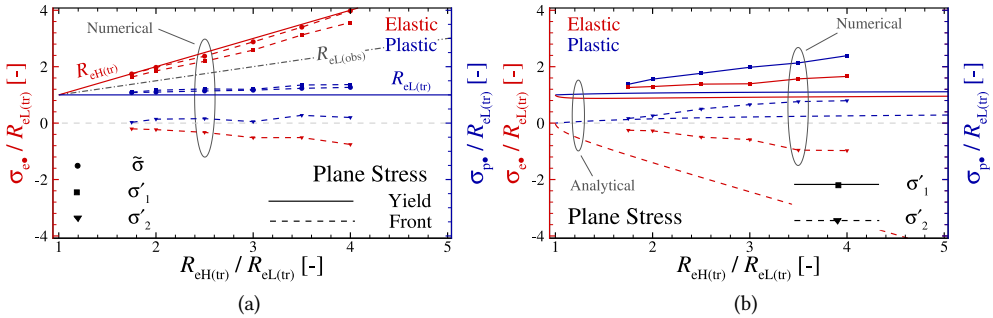

Figure 4.8: The scaled principal stresses $\sigma_{e\bullet}/R_{eL(tr)}$ and $\sigma_{p\bullet}/R_{eL(tr)}$ in a material point (a) on the elastic and plastic sides of the Lüders front and (b) in the elastic and plastic area in front and inside the Lüders band as functions of the yield strength ratio $R_{eH(tr)}/R_{eL(tr)}$. The solid lines in (a) are the true, lower and upper yield strengths $R_{eL(obs)}$ and $R_{eH(tr)}$, respectively; and, the grey dashed-dotted line the observed lower yield strength (4.37) with scalar $a = 1/2$. The solid and dashed coloured lines in (b) indicate the analytical major and middle/minor principal stresses (4.33) with scalar $b = 1/5$, respectively. The dashed coloured lines in (a,b) and the solid lines in (b) that connect solid symbols with a given shape are guides to aid the reader.

sile specimen is considered under plane stress condition; the red and blue coloured symbols indicate the stresses on the still-elastic $\sigma_{e\bullet}$ and just-plastic side $\sigma_{p\bullet}$ of the Lüders front, respectively; and, the numerical equivalent stress $\tilde{\sigma}$ and principal stresses $\sigma'_\bullet$ are indicated by solid circular, and square and gradient symbols, respectively. Numerical results are obtained within a square with an area $4\times10^{-5}\ w^2$, that is centred on the origin $\{x', y'\} = \{0, 0\}$ (See Fig. 4.4). The red and blue solid coloured lines indicate the true upper and lower yield strengths $R_{eH(tr)}$ and $R_{eL(tr)}$, respectively; and, the grey dashed-dotted line the observed lower uniaxial tensile strength $R_{eL(obs)}$ via Eq. (4.37) with scalar $a = 1/2$.

The major and minor principal stresses σ_{e1} and σ_{e3} (*i.e.* σ'_1 and σ'_2 in red, respectively) correspond with the maximum numerical Von Mises stress $\tilde{\sigma}_e \approx R_{eH(tr)}$ on the still-elastic side of the Lüders front. The major and middle principal stresses σ_{p1} and σ_{p2} (*i.e.* σ'_1 and σ'_2 in blue, respectively) correspond with the minimum numerical Von Mises stress $\tilde{\sigma}_p \approx R_{eL(tr)}$ on the just-plastic side of the Lüders front. These numerical maximum and minimum Von Mises stresses are indicated by solid circles with red and blue colours, respectively, that are connected by dashed lines as well.

On the elastic side of the front, the minor principal stress σ_{e3} is negative and decreases; on the plastic side of the front, the middle principal stress σ_{p2} is positive and increases. The stress concentration increases each side of the Lüders front with yield strength ratio $R_{eH(tr)}/R_{eL(tr)}$. Stress concentration is here the ratio between the major principal stresses σ_{e1} and σ_{p1}, and the observed lower tensile strength $R_{eL(obs)}$; and, the minor and middle principal stresses σ_{e3} and σ_{p2}, respectively, and the volume averaged stress $\langle \sigma'_{22} \rangle = 0$. The major principal stresses $\sigma_{\bullet 1}$ differ from the observed lower tensile strength $R_{eL(obs)}$. This difference increases

with yield strength ratio $R_{eH(tr)}/R_{eL(tr)}$ as well. These results corroborate the signs of the principal stresses in our model, which is straightforward when one compares the intersects of the Mohr circles with the horizontal axis in Fig. 4.3b and the numerical results in Fig 4.8. Secondly, we confirm once again that the stress concentration increases with yield strength ratio $R_{eH(tr)}/R_{eL(tr)}$, which is the original contribution by Van Rooyen [64, 65]. Notably this increase in stress concentration coincides with the increase in Lüders front angle ϕ (See Fig. 4.6b). This confirms the Lüders band orientation changes with yield strength ratio $R_{eH(tr)}/R_{eL(tr)}$ due to the heterogeneous stress state at the Lüders front, at least for thin tensile specimens.

Because of the elastic-plastic material behaviour in the numerical calculations (See Sec. 4.4) the maximum middle principal stress σ_{p2} resides in the Lüders band. Similarly, the minimum middle principal stress σ_{e2} occurs in front of the Lüders front. In Fig. 4.8b, the principal stresses and on either side of the Lüders front, *i.e.* $\sigma_{e\bullet}$ in front and $\sigma_{p\bullet}$ inside the Lüders band, under plane stress condition are shown; the solid and dashed coloured lines indicate the analytical major principal stress $\sigma_{\bullet 1}$ and middle/minor principal stresses $\sigma_{\bullet 2}$ and $\sigma_{\bullet 3}$ in Eq. (4.33) in the invariant plane as well. Comparable with the representation in Fig. 4.8a, major principal stresses $\sigma_{\bullet 1}$ correspond with the maximum middle principal stress σ_{p2} inside the Lüders band and the minimum minor principal stress σ_{e3} in front of the Lüders front. The latter stresses are indicated by blue and red solid gradient symbols, respectively. The major numerical principal stresses σ_{e1} and σ_{p1} are indicated by solid coloured square symbols and connected by solid coloured lines; and, the numerical minor principal stress σ_{e3} and middle principal stress σ_{p2} by gradient symbols and dashed lines that guide the reader as well.

In front of the Lüders band the minor principal stress σ_{e3} is negative and its magnitude increases with the yield strength ratio $R_{eH(tr)}/R_{eL(tr)}$. The analytical results show a larger minor principal stress magnitude $\|\sigma_{e3}\|$ than the numerical results, which is intuitive because the latter accounts for the elastic contraction perpendicular to the loading direction. Hence the ratio $-\sigma_{e3}/\sigma_{e1}$ is smaller in the numerical results than in the analytical postdiction (4.33). We can reduce the modulus ratio $H/E < 10$ to decrease this difference, however that increases the oscillations in the numerical force-displacement response and Lüders front angle. Inside the Lüders band the middle principal stress σ_{p2} is positive and increases with the yield strength ratio $R_{eH(tr)}/R_{eL(tr)}$. The analytical results show a larger middle principal stress magnitude σ_{p2} than the numerical result because the material point hardens in the Lüders band, which is not accounted for in our modelling framework (See Sec. 4.3). In turn the major principal stress σ_{p1} increases because the material hardens as well. The numerical results agree qualitatively with the analytical *postdiction* (4.33) with scalar $b = 1/5$. Quantitative agreement between the numerical and analytical results are not expected because the latter does not account for elasticity, neglects softening and hardening, and solely considers the traction continuity on the Lüders front (See Sec. 4.2). Still we find with our characteristics of the Lüders front (4.5) that the signs and magnitudes of the principal ratios σ_{e3}/σ_{e1} and σ_{p2}/σ_{p1}, and the scaled differences $\left(\sigma_{p1}-\sigma_{e1}\right)/R_{eL(tr)}$ and $-\left(\sigma_{p2}-\sigma_{e2}\right)/R_{eL(tr)}$ are of the same order of magnitude in the analytical postdiction and the numerical results. The latter two differences are readily inferred from Fig. 4.8b.

4.6.2 Experimental Methodology

Several works relate the so-called Lankford coefficient [322] to the orientation of localised necking [316, 327] and plastic anisotropy [319, 328]. Lesser known are the works by Daniel *et al.* [312] and Savoie *et al.* [307] that connect the rapid changes in Lankford coefficient under heterogeneous plasticity to the orientation of the Lüders front. The latter is based on their [307, 312] hypotheses that the Lüders band is parallel to the direction of zero extension [329] and plastic shears perpendicular to the loading direction are zero. This only necessarily holds for the yield strength ratio $R_{\mathrm{eH(tr)}}/R_{\mathrm{eL(tr)}} = 1$. Defining the contraction ratio $\bar{q} \equiv -\epsilon'^{\mathrm{L}}_{22}/\epsilon'^{\mathrm{L}}_{11}$, we find the approximation of the Lüders front inclination

$$\hat{\alpha} \approx \tan^{-1}\left(\sqrt{\bar{q}}\right). \tag{4.38}$$

Here, the hat $\hat{\bullet}$ indicates the approximate of scalar $\bullet$. This allows one to measure the Lüders band orientation without the need for advanced methodology, *e.g.* digital image correlation technology [69, 74, 118]. Yu *et al.* [329] verify this approximation for the Portevin-Le Chatelier band orientation in aluminium alloy sheets. However they [307, 312, 329] relate change in Lüders front orientation with metallic sheets' rolling texture. Hence the Lüders band angle is related to the crystallographic texture and plastic anisotropy [307, 312, 328], and the stress concentration at the Lüders front.

In Fig. 4.9a, the difference between the numerical inclination α via (4.35) and the approximation $\hat{\alpha}$ via Eq. (4.38) is given as a function of the yield strength ratio $R_{\mathrm{eH(tr)}}/R_{\mathrm{eL(tr)}}$; the red solid square markers indicate the numerical results and the coloured dashed lines

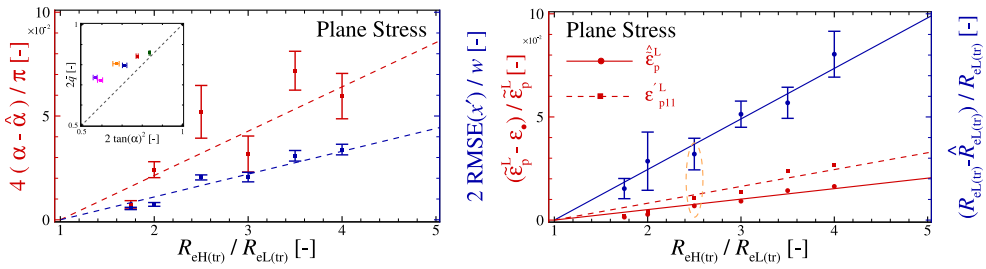

Figure 4.9: (a) The scaled Lüders front inclination $4(\alpha-\hat{\alpha})/\pi$ and the scaled root mean square error $2\mathrm{RMSE}\left(x'\right)/w$, and (b) the scaled plastic Lüders strain $\left(\tilde{\epsilon}^{\mathrm{L}}_{\mathrm{p}}-\epsilon^{\mathrm{L}}_{\bullet}\right)/\tilde{\epsilon}^{\mathrm{L}}_{\mathrm{p}}$ and scaled lower yield strength $\left(R_{\mathrm{eL(tr)}}-\hat{R}_{\mathrm{eL(tr)}}\right)/R_{\mathrm{eL(tr)}}$ as functions of the yield strength ratio $R_{\mathrm{eH(tr)}}/R_{\mathrm{eL(tr)}}$ under plane stress condition. The (dashed) coloured lines are guides to the eye.

are linear fits through the origin as guides to the eye. In Fig. 4.9a, the root-mean square error RMSE$\left(x'\right)$ of the linear fit with Eq. (4.35) is presented as well; the blue solid markers indicate this numerical result and the error bars a single standard deviation.

Clearly the difference between the estimated and numerical Lüders front inclination $\alpha-\hat{\alpha}$ increases with the yield strength ratio $R_{\mathrm{eH(tr)}}/R_{\mathrm{eL(tr)}}$. One reason is that the Lüders band curves when the true upper yield strength $R_{\mathrm{eH(tr)}}$ increases. As the Lüders band curves the root mean square error RMSE$\left(x'\right)$ increases as well. This confirms that our assumption of a planar Lüders front (See Sec. 4.2) breaks down at higher yield strength ratios $2 << R_{\mathrm{eH(tr)}}/R_{\mathrm{eL(tr)}}$,

which is one reason the approximation via Eq. (4.38) deteriorates. This only occurs under plane stress, where under plane strain condition the Lüders front remains planar. Furthermore, the plastic flow is more complex than Daniel *et al.* [312] and Savoie *et al.* [307] assume. The plastic shear strain $\epsilon'_{\mathrm{p}12}$ is finite at the border between the Lüders band and the plastic area in Fig. 4.7b for yield strength ratio $R_{\mathrm{eH(tr)}}/R_{\mathrm{eL(tr)}} = 3$. The plastic extension parallel to the Lüders front $\epsilon''_{\mathrm{p}22}$ is finite in the plastic area as well. In the insert in Fig. 4.9a, the contraction ratio $\bar{q}$ is presented as a function of the squared ratio $\tan^2(\alpha)$ for the yield strength ratios $R_{\mathrm{eH(tr)}}/R_{\mathrm{eL(tr)}} = 7/4,\ 2,\ 5/2,\ 3,\ 7/2$ and 4. The colours of the markers in the insert correspond with those in Fig. 4.5. Even though the difference between the ratios $\tan^2(\alpha) - \bar{q}$ increases with yield strength ratio $R_{\mathrm{eH(tr)}}/R_{\mathrm{eL(tr)}}$, the contraction ratio $\bar{q}$ decreases monotonically.

Because the plastic flow in the Lüders front is not necessarily equal to uniaxial extension, the plastic contraction ratio is $0 < 2\bar{q}_{\mathrm{p}} \leq 1$ in the Lüders band, where $\bar{q}_{\mathrm{p}} \equiv -\epsilon'^{\mathrm{L}}_{\mathrm{p}22}/\epsilon'^{\mathrm{L}}_{\mathrm{p}11}$. This allows one to approximate the equivalent plastic Lüders strain $\tilde{\epsilon}^{\mathrm{L}}_{\mathrm{p}}$ from the Lüders strain $\epsilon^{\mathrm{L}}_{11}$. Using the definition of the equivalent plastic strain (4.34b), plastic incompressibility (4.4b) and the Lüders front characteristics (4.5), we approximate the equivalent plastic strain by

$$\hat{\tilde{\epsilon}}^{\mathrm{L}}_{\mathrm{p}} \approx \frac{2\epsilon'^{\mathrm{L}}_{\mathrm{p}11}}{\sqrt{3}} \sqrt{\bar{q}_{\mathrm{p}}^2 - \bar{q}_{\mathrm{p}} + 1}, \tag{4.39}$$

that is $\epsilon'^{\mathrm{L}}_{\mathrm{p}11}$ under uniaxial tension.

In Fig. 4.9, the difference between the estimated equivalent plastic Lüders strain $\hat{\tilde{\epsilon}}^{\mathrm{L}}_{\mathrm{p}}$ and the numerical equivalent plastic Lüders strain $\tilde{\epsilon}^{\mathrm{L}}_{\mathrm{p}}$ is presented as a function of the yield strength ratios $R_{\mathrm{eH(tr)}}/R_{\mathrm{eL(tr)}} = 7/4,\ 2,\ 5/2,\ 3,\ 7/2$ and 4; and, the difference with the plastic Lüders extension $\epsilon'^{\mathrm{L}}_{\mathrm{p}11}$ is included. The former is indicated by red solid circular markers and a solid red line, and the latter by square markers and a dashed line. These lines are guides to the eye as well.

As expected differences between the plastic Lüders extension $\epsilon'^{\mathrm{L}}_{\mathrm{p}11}$, the estimated $\hat{\tilde{\epsilon}}^{\mathrm{L}}_{\mathrm{p}}$ and the equivalent plastic Lüders strain $\tilde{\epsilon}^{\mathrm{L}}_{\mathrm{p}}$ approach zero when the yield strength ratio $R_{\mathrm{eH(tr)}}/R_{\mathrm{eL(tr)}}$ tends to unity. The difference between the plastic extension and the equivalent plastic strain $\tilde{\epsilon}^{\mathrm{L}}_{\mathrm{p}} - \epsilon'^{\mathrm{L}}_{\mathrm{p}11}$ increases with yield strength ratio $R_{\mathrm{eH(tr)}}/R_{\mathrm{eL(tr)}}$ because the plastic deformation in the Lüders band is no longer that of uniaxial extension, *i.e.* $\bar{q}_{\mathrm{p}} < 1/2$. The difference between the estimated and the numerical equivalent plastic Lüders strain $\tilde{\epsilon}^{\mathrm{L}}_{\mathrm{p}} - \hat{\tilde{\epsilon}}^{\mathrm{L}}_{\mathrm{p}}$ increases because the characteristics of the Lüders front do not necessarily hold throughout the Lüders band (See Sec. 4.5.3). Even so, the presented differences reduce with a third, when the plastic contraction $\bar{q}_{\mathrm{b}}$ inside the Lüders band is accounted for.

With linear hardening (4.34) we approximate the true lower yield strength as

$$\hat{R}_{\mathrm{eL(tr)}} \approx R_{\mathrm{eL(obs)}} - H\hat{\tilde{\epsilon}}^{\mathrm{L}}_{\mathrm{p}}. \tag{4.40}$$

This methodology is similar to method of Schwab *et al.* [62, 63]. In Fig. 4.9, the difference between the true lower yield strength $R_{\mathrm{eL(tr)}}$ and estimated lower yield strength $\hat{R}_{\mathrm{eL(tr)}}$ is presented; the numerical result are indicated by blue solid circular markers; and, the solid blue line is a guide to the eyes. Clearly, the lower yield strength is underestimated via Eqs. (4.39) and (4.40). The difference between estimated $\hat{R}_{\mathrm{eL(tr)}}$ and the true lower yield strength $R_{\mathrm{eL(tr)}}$

increases with yield strength ratio $R_{eH(tr)}/R_{eL(tr)}$ as well. One reason is that the equivalent plastic Lüders strain $\tilde{\epsilon}_p^L$ is underestimated via Eq. (4.39) by up to a ratio $\hat{\tilde{\epsilon}}_p^L/\tilde{\epsilon}_p^L \approx 2\times10^{-2}$. However, the lower yield strength $\hat{R}_{eL(obs)}$ is underestimated by twice this factor. Another reason is that the material flow strength $R_{eL(obs)} < R_e\left(\tilde{\epsilon}_p^L\right)$ once the Lüders band has passed.

In Fig. 4.10, tensile stress-axial strain and equivalent stress-equivalent plastic strain responses are given for yield strength ratio $R_{eH(tr)}/R_{eL(tr)} = 5/2$; the in-plane condition is plane

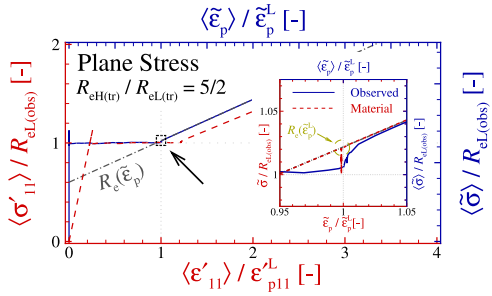

Figure 4.10: The scaled volume averaged tensile stress $\langle\sigma'_{11}\rangle/R_{eL(obs)}$ as a function of the scaled volume averaged axial strain $\langle\epsilon'_{11}\rangle/\epsilon'^L_{p11}$, and the scaled volume averaged Von Mises stress $\langle\tilde{\sigma}\rangle/R_{eL(obs)}$ as a function of the scaled volume averaged equivalent plastic strain $\langle\tilde{\epsilon}_p\rangle/\tilde{\epsilon}_p^L$ for yield strength ratio $R_{eH(tr)}/R_{eL(tr)} = 5/2$. The hardening behaviour (4.34) is indicated by a dashed-dotted grey line and marked $R_e\left(\tilde{\epsilon}_p\right)$.

stress. The observed uniaxial tensile response is indicated in red and the equivalent response in blue. Material hardening is given by a dashed-dotted grey line of the flow strength R_e.

The uniaxial tensile stress $\left\langle\sigma'_{11}\right\rangle$ and the observed lower yield strength $R_{eL(obs)}$ are obviously the same during yield elongation. Figure 4.5a, where the given equivalent plastic Lüders strains $\tilde{\epsilon}_p^L$ are highlighted by black circles, shows that the observed lower yield strength $R_{eL(tr)} \lessapprox R_e\left(\tilde{\epsilon}_p^L\right)$. The true lower yield strength is underestimated similarly by $\hat{R}_{eL(tr)}$ in Fig. 4.9b. This is expected because the Lüders band forms along a stress concentration due to local softening when the material is loaded up to the upper yield surface $\mathcal{R}_H$. This means that the material flow strength $R_e\left(\tilde{\epsilon}_p^L\right)$ is not necessarily the same as the observed uniaxial stress $\left\langle\sigma'_{11}\right\rangle$. The material solely hardens uniformly under uniaxial tension once the Lüders band has traversed the gauge length; the tensile stress-axial strain and the equivalent stress-equivalent plastic strain responses are parallel in Fig. 4.10, where the latter shifts upwards due the subtraction of the elastic extension.

In the insert in Fig. 4.10, the materials, mechanical response in a single material point near the origin $\left\{x', y'\right\} = \{0, 0\}$ and the observed equivalent response are presented. This inserted plot's area is demarcated by a black dashed square in the main figure. The materials equivalent stress-equivalent plastic strain response is indicated by a red dashed line. Note that hardening is included in the insert with a dashed-dotted grey line that is covered by this material point response. The material flow strength $R_e\left(\tilde{\epsilon}_p^L\right)$ is highlighted by a metallic green coloured dashed circle in the insert in Fig. 4.10.

The material hardens in the Lüders band and local stress state changes in the plastic area so the Von Mises stress $\tilde{\sigma}_p \leq R_e\left(\tilde{\epsilon}_p^L\right)$. The then remaining elastic volume continues to deform heterogeneously. Only once the Lüders bands traverses the whole gauge length the

material start to harden homogeneously; the local and global mechanical response coincide, and the observed uniaxial tensile response and the Von Mises stress-equivalent plastic strain response are parallel (See main figure 4.10). The material flow strength must thus be obtained as the intersect of the equivalent Lüders strain $\tilde{\epsilon}_{\mathrm{p}}^{\mathrm{L}}$ and the materials hardening behaviour, that is herein linear hardening.

Considering the stress concentration at the Lüders front and the plastic flow in the Lüders band, we highlight that: *firstly*, the estimated true lower yield strength $\hat{R}_{\mathrm{eL(tr)}}$ depends on the Lüders front angle ϕ via the plastic contraction ratio $\bar{q}_{\mathrm{p}}$ over the volume traversed by the Lüders front, while plastic deformation is inhomogeneous; *secondly*, the axial plastic Lüders strain $\epsilon_{\mathrm{p11}}^{\prime\mathrm{L}}$ is equal to or lower than the equivalent plastic Lüders strain $\tilde{\epsilon}_{\mathrm{p}}^{\mathrm{L}}$; and, *thirdly*, the observed lower yield strength $R_{\mathrm{eL(obs)}}$ is not necessarily the uniaxial yield strength $R_{\mathrm{e}}\left(\tilde{\epsilon}_{\mathrm{p}}^{\mathrm{L}}\right)$ of the material once the Lüders band passed.

4

One can approximate the true lower yield strength $R_{\mathrm{eL(tr)}}$ without the need for advanced methodology either, *e.g.* decarburisation or sandwich-structured tensile specimens [67]. The material flow strength $R_{\mathrm{e}}\left(\tilde{\epsilon}_{\mathrm{p}}^{\mathrm{L}}\right)$ can be graphically estimated (See the insert in Fig. 4.10), and substituted for the observed lower yield strength $R_{\mathrm{eL(obs)}}$ in Eq. (4.40). The scaled difference $\left(R_{\mathrm{e}}\left(\tilde{\epsilon}_{\mathrm{p}}^{\mathrm{L}}\right) - R_{\mathrm{eL(tr)}}\right)/R_{\mathrm{eL(obs)}} \approx 2\times10^{-2}$, approaches the difference of the estimated lower yield strength $\hat{R}_{\mathrm{eL(tr)}}$ that we highlight in Fig. 4.9b by a metallic green coloured, dashed ellipse. By measuring the Lankford coefficient $\bar{q}/(1-\bar{q})$ one can approximate the plastic contraction $\bar{q}_{\mathrm{p}}$ under the assumption of uniaxial tension $R_{\mathrm{eL(obs)}}$ as well. All these input parameters are measurable in a single uniaxial tensile test on a metallic sheet material that displays the yield point phenomenon (YPP). The proposed methodology will improve the accuracy of the experimentally obtained lower yield strength $R_{\mathrm{eL(tr)}}$ in future studies.

4.6.3 Lüders Front Characteristics

The seminal consensus was that deformation in the Lüders front initiates by pure shear [68, 117, 299–301]. The self-evident hypothesis thus is that the Lüders front is the plane where the maximum shear stress acts [44, 117]. However, we find this hypothesis is inconsistent with the plane stress condition, where the Lüders front does not reside on the plane of the maximum shear stress; the plane of the maximum shear stress, $(\sigma_{\mathrm{e1}}-\sigma_{\mathrm{e3}})/2$, is perpendicular to the y-plane but not parallel to the Lüders front (See Fig. 4.1 and Sec. 4.3.2). Moreover, the plastic shear in the Lüders front decreases with the yield strength ratio $R_{\mathrm{eH(tr)}}/R_{\mathrm{eL(tr)}}$ and vanishes in the upper yield point limit, where flow is perpendicular to the Lüders front, *i.e.* the plastic strain increments $-\mathrm{d}\epsilon_{\mathrm{p33}}^{\prime} = \mathrm{d}\epsilon_{\mathrm{p11}}^{\prime}$ (See Sec. 4.3).

Nadai [310] contributes the decrease in Lüders front angle $\phi \approx 54\ldots45$ degrees to in-plane strains, that increase with tensile specimen's width; and, Thomas [313] an increase in the Lüders front angle $\phi = 54\cdots90$ degrees to compressibility. Notable is that Van Rooyen [64, 65] reports the Lüders front angle ϕ to increase with yield strength ratio yet their force balance is based on the plane strain condition. The analytically obtained Lüders front angles under plane strain and plane stress conditions by Nadai [310] are indicated by blue and red, dashed-dotted horizontal lines in Fig. 4.6b.

We present an alternative reason for the increase in Lüders front angle ϕ with the yield strength ratio $R_{\mathrm{eH(tr)}}/R_{\mathrm{eL(tr)}}$. This interpretation is similar to that of rock fracture, that occurs parallel to the direction of zero extension, by Burg and Harris [302]. The main

difference is that the occurrence of the normal stress ratio $0 < 2\sigma'_{p2}/\sigma'_{p1} < 1$ is due to the stress concentration at the Lüders front in uniaxial tensile tests on metals. The Lüders front angle ϕ thus changes with localisation and maximises global plastic dissipation. Hence we posit that the variation in Lüders front angle ϕ with the given yield strength ratio $R_{eH(tr)}/R_{eL(tr)}$ depends on tensile specimen geometry as well.

Butler [300] shows that Lüders front angle increases $\phi = 50 \cdots 90$ degrees, with Lüders strain $0 \cdots 0.15$, in thin tensile specimens with various grain sizes and deformation rates. They [300] suggest that the azimuth angle ζ (See Fig. 4.1) changes to correct the misalignment through sheet bending, which is easier across the specimen's thickness than its width. Pomey *et al.* [305] observe an angle $\phi = 90$ degrees on the widest specimen's face and 50 degrees with respect to the tensile axis through thickness. In accordance with our analytical and numerical results in Sec. 4.5 we find that the Lüders front angle increases with the yield strength ratio $R_{eL(tr)}/R_{eL(obs)}$. Herein, the Lüders front is perpendicular to the invariant plane whereby the front solely rotates in that plane. This alternative is inline with the experimental measurements in Figure 13 on page 329 by Butler [300] as well.

Van Rooyen's [64] and Schwab *et al.*'s [44, 62] descriptions of YPP are independent of tensile specimen's geometry. In their work [44, 64] an increase in the Lüders front angle ϕ is pre-requisite for the increase in yield strength ratio $R_{eH(tr)}/R_{eL(tr)}$. However, this is not necessarily so as we demonstrate under plane strain condition (See Fig. 4.6b). The grey dashed-dotted lines in Fig. 4.6 are the analytical predictions by Schwab and Ruff [44] for the lower observed uniaxial yield strength $R^*_{eL(obs)}$ and the Lüders front angle ϕ. We find that the observed uniaxial yield strength $R_{eL(obs)}$ differ quantitatively, and the Lüders front angle ϕ is predominantly over-predicted. The former can be due to the different calculations of the observed lower yield strengths 4.36a here and $R^*_{eL(obs)}$ in [44, 62]. Notable is that Schwab and Ruff [44] over-predict the Lüders front angle relative to their numerical finite element results as well. The latter was already noted by Schwab *et al.* [44, 63], which we contribute to the in-plane conditions of the Lüders front, that depend on *e.g.* tensile specimen geometry and boundary conditions. Later work by Schwab [63] attributes the change in Lüders front angle ϕ to bending stresses that result from heterogeneous (plastic) deformation. We contribute this overestimate [63] in part to the hypothesis by Schwab and Ruff [44] on the in-plane condition as well.

Hall [67] in their seminal book on the YPP states that the Lüders front's morphology depends on tensile specimen's geometry. This year, Van der Heijde and Samad [330, 331] present the effect of tensile specimen thickness h on the YPP. They [330, 331] are the first to the authors' knowledge, who systematically and simultaneously, experimentally quantify the effect of thickness h on the Lüders strain ϵ'_{11} and band orientation ϕ in low-carbon steel. They [330, 331] employ digital image correlation and find that: the lower observed yield strength changes non-monotonically with specimens thickness; the Lüders strain decreases with increased specimen thickness; and, the angle between the Lüders front and tensile direction sharpens with specimen thickness. The former observation holds in similar experiments for aluminium alloys by Cai *et al.* [69]. Our analytical result that present the influence of invariant plane conditions are supported by the reported dependencies on specimen's geometry [69, 331]. Moreover, we present an alternative mechanism where the Lüders strain increases with the scaled observed yield strength $R_{eL(obs)}/R_{eL(tr)}$ [62, 63, 68] via the contraction ratio $\bar{q}$. Here, the contraction ratio $\bar{q}$ depends on the Lüders band orientation.

Note that we do not consider tensile specimens with a generic thickness in this chapter though.

Moon [332], and Ananthan and Hall [120] reason that the Lüders front angle increases with the bending moment due to shear flow. The analytical results in Sec. 4.3 are valid for an infinite solid and this bending moment is not accounted for. The numerical results in Secs. 4.4 and 4.5 are not constrained to uniaxial tension. We take special care of the Neumann boundary conditions that allow for displacement in the y-direction and volume changes (See Fig. 4.4), which reduce the bending moment compared to clamped boundary conditions [327]. However, the moment, thus the discrepancy between analytical model and numerical calculation, increases with Lüders strain as well. We have not noticed any such influence on our numerical results though. Even so the bending moment due to clamping conditions and/or heterogeneous deformation must be considered in future analytical works.

4.7 Conclusions

In this chapter, we present a macromechanical model of the Lüders front to investigate the yield point phenomenon. We model the orientation of Lüders front and lower observed yield strength that depend on the ratio between the upper and lower yield strengths. We verify that the plastic flow parallel to the Lüders front vanishes and maximises the global dissipation. These we find are the characteristics of the Lüders front under invariant plane conditions.

The orientation of the Lüders front depends on the heterogeneous stress state, tensile specimen's geometry and loading conditions, as well as the material properties. In particular the ratio between the upper and lower yield strengths influences the Lüders front angle and the observed lower yield strength. However the former angle depends on the tensile specimen cross-section as well, of which we present the two limits of plane stress and plane strain conditions. This explains the wide range of front angles observed in experiments.

We find that plastic shear perpendicular to the Lüders front is orders of magnitude smaller than the plastic extension in the tensile direction across it. Plastic extension in the Lüders band is an order of magnitude smaller than the Lüders strain under plane stress condition as well. The stress concentration at the Lüders front and the Lüders front angle increase with the true upper yield strength in thin tensile specimens. One can approximate the Lüders band angle from a single uniaxial tensile test by measuring the Lankford coefficient during inhomogeneous plastic deformation. Additionally, via the force-displacement measurement during homogeneous plastic deformation, one can obtain the material property of true lower yield strength.

The characteristics of the Lüders front and the experimental methodology herein serve to obtain constitutive parameters in future experiments, that will serve to advances ones understanding of the yield point phenomenon.

Part III: Dissipative Contacts

5

Adhesive Hysteresis in Soft Matter Contacts

Soft matter adhesive contact is present in a large variety of engineering applications, covers a wide range of length- and time-scales, and involves mechanics, physics and chemistry. A critical aspect of these contacts is that they display adhesive hysteresis. Recognised mechanical sources of dissipation are surface roughness and viscoelasticity, but their interplay is not yet clear, especially due to experimental difficulties and strong assumptions in theoretical work. In numerical simulations of smooth contacts, viscoelasticity is found to change adhesion from short- to long-ranged. This finding poses limitations on the validity of the two most common assumption on which theoretical work is based: adhesion is short-ranged; and, viscous dissipation is confined to the edges of intimate contact.

In this chapter, we aim at elucidating the interplay between adhesion and roughness, by modelling the retraction of rigid, wavy indenters from a viscoelastic substrate. To this end we use an extended Green's function molecular dynamics technique, which allows us to compute the intimate contact area and the pull-off load of indenters with various waviness, material and interfacial properties, and at different loading rates.

Results of the simulations show, for the first time, that at moderate loading rates viscoelasticity effectively dampens the adiabatic mechanical instabilities caused by waviness. However, when the instantaneous limit is approached, mechanical instabilities reoccur. At finite retraction rates, the mechanism of interfacial toughening by roughness-induced instabilities is present, also with viscous dissipation. In conclusion, viscoelasticity governs adhesive hysteresis, even in the presence of roughness-induced mechanical instabilities.

This chapter is based on the scientific article: Pérez-Ràfols, F., Van Dokkum, J. S., Nicola, L. On the Interplay between Roughness and Viscoelasticity in Adhesive Hysteresis, *Journal of the Mechanics and Physics of Solids*, 105079, 2022; and the presentation in symposium 4, *Contact, Friction, Adhesion: Mechanics of Interfaces Across Scales*, during the *10th International Conference on Multiscale Materials Modeling*, October 2022, Baltimore, MD, USA.

NOMENCLATURE

Variable	Definition	Dimension (mass M, length L and time t)
a	width	L
A	amplitude	L
α	normalised amplitude	–
β	normalised wavelength	–
$\delta_{\max}$	interaction length	L
E	modulus	$\mathrm{ML^{-1}t^{-2}}$
f_r	modulus ratio	–
g	gap width	L
$\Delta\gamma$	work of adhesion	$\mathrm{Mt^{-2}}$
h	profile	L
$\mathcal{L}$	periodic width	L
λ	Maugis parameter	–
m	ratio	–
p	pressure	$\mathrm{ML^{-1}t^{-2}}$
$\boldsymbol{q}$	wave vector	$\mathrm{L^{-1}}$
R	Hertzian radius	L
σ	traction	$\mathrm{ML^{-1}t^{-2}}$
t	time	t
τ	relaxation time	t
u	displacement	L
w	load	$\mathrm{Mt^{-2}}$
x, y & z	Cartesian coordinates	L
ζ	wavelength	L

5

5.1 INTRODUCTION

In this chapter, we address the combined effect of the two "perceived main" [333] sources of hysteresis in soft materials: surface roughness; and, viscoelasticity. Wavy roughness results in waviness of the load-approach curve, and increases the pull-off force compare with the smooth elastic case [192] (See Fig. 1.3a). The energy dissipated in these elastic jumps, equivalent to the area enclosed between the trajectories of a given jump and the stable, static elastic equilibrium on the force-displacement curve, increases the interfacial toughness. This enhances the observed adhesion.

Viscous dissipation plays a significant role even when the indentation and retraction rates are small compared to the materials characteristic frequencies [142, 147, 177, 185]. The time-dependent behaviour for slow retraction is due to a high stress rate near the edges of intimate contact. Those edges of contact are therefore treated as opening cracks [205, 207–209, 217, 229, 334, 335]. The increase in effective work of adhesion, as measured in *e.g.* Fig. 1.3b by Barquins and Maugis [171], due to viscous dissipation, is equivalent or several orders of magnitude larger than that due to elastic mechanical instabilities [123, 172]. The main question thus is: *What is the origin of adhesive hysteresis in soft matter contacts: viscous or roughness-induced dissipation in contacts?*[1].

[1]Paraphrase of one of the questions posed by Martin Müser (Saarland University) at WeSST 2021: "*One thing*

With viscous dissipation present adhesion is not necessarily short-range and departs from JKR-theory [192]. Concurrently, yet separately, Ciavarella [193] and us [335] come to a similar, improved understanding by introducing two Tabor (in the latter Maugis [335]) parameters. One parameter corresponds with the relaxed, and one with the instantaneous modulus. The work of adhesion thus is constant with the relaxed magnitude, *i.e.* viscous dissipation is no-longer an interfacial property; the effective Tabor/Maugis parameter changes with the decrease in compliance of the viscoelastic material at the contact edges. *Firstly*, with increased retraction rate, the effective Tabor/Maugis parameter is reduced towards the instantaneous value [335]; *secondly*, deviation from the JKR-type adhesive behaviour is observed as the instantaneous limit is approached [193, 335]; *thirdly*, a "very large" [193] relaxed Tabor/Maugis parameter is needed to approach JKR-type adhesion in viscoelastic contacts [193, 335]. The type of adhesion is delimited by two Tabor/Maugis parameters. Hence the apparent Tabor/Maugis parameter depends on the ratio between retraction rate and characteristic frequency, and the ratio between relaxed and instantaneous modulus. Independently, Müser and Persson [205] find similar results by means of a Boundary-Element method as well. Notably, they find [205] that with "large" retraction rates dissipation occurs pre-dominant "far away" from the contact edges. Which is the effect of long-range adhesion, *i.e.* the decrease in effective Maugis parameter. Moreover, they [205] show that the load at jump-out of contact at high retraction rates is characterised by "quasi-uniform" bond breaking [202].

The assumption by Gent and Schultz [207–209] is recently scrutinised by: Van Dokkum *et al.* [335] by means of a Boundary Element method, where adhesion is described by the Dugdale potential [197] in cylindrical contact; and, Afferante and Violano [229] by means of a Finite Element model, where adhesion is described by the Lennard-Jones potential [199, 200] in Hertzian contact. Both [229, 335], and later Müser and Persson [205], show that the prediction(s) of the crack propagation models by Greenwood [334] or(/and) Persson and Brenner [217] are (equally) accurate. Violano and Afferante [229] discuss the validity of the Gent and Schultz assumption [207–209] as well. They [229] show that viscous dissipation does occur in the bulk material at (extremely) high retraction rates. The likelihood that the central assumption by Gent and Schultz [207–209] is violated thus increases with retraction rate [229, 335]. Two other Finite Element implementations of note are presented by Lin and Hui [146] and Jaing *et al.* [135], who consider adhesive contact between viscoelastic spheres, where adhesion is modelled by the Dugdale potential [197], and adhesive contact between a rigid sphere and an axisymmetric viscoelastic half-space, with the Lennard-Jones potential [199, 200], respectively.

Despite the assumption by Gent and Schultz [207–209] breaks down for high retraction rates [335, 337], it is at the basis of current studies on non-smooth viscoelastic adhesive contacts, that include wavy [333], patterned [223] and multi-asperity [190, 191] roughnesses. Ciavarella and Papangelo [333] generalise the works by Guduru [172], and Guduru and Bull [123] to the case of a viscoelastic material. The resultant differential equation, that is a combination of Guduru *et al.* works [123, 172] and the assumption by Gent and Schultz [207–209], is then solved numerically; Papangelo and Ciavarella [223] explicitly introduce the effect of the rate-dependent work of adhesion in the model of McMeeking *et al.* [338], in

I (Martin) *would like to know is if the origin of adhesive hysteresis, that we often see* (in experiments)*, is due to viscoelasticity or due to multistability in contacts*?". [336]

the presence of an axisymmetric single-scale roughness. The resultant ordinary differential equation is solved numerically as well; and, Violano *et al.* [191] combine a discrete version of the Fuller and Tabor multi-asperity model [162] and the solution as proposed by Muller [215], on a per asperity basis. Aforementioned theoretical treatises [191, 223, 333] share several observations: obviously adhesive hysteresis is enhanced with load rate. This is inherent to the assumption by Gent and Schultz [207–209]; the works by Ciavarella and Papangelo [223, 333] share the observation that at low retraction rates, the pull-off force increases due to roughness-induced enhancement by mechanical instabilities. With increased retraction rate, the rate-dependent effect "strengthens" [223] and the force-displacement curves collapse on a unique asymptote, that of a smooth adhesive Hertzian. The only mechanism of interfacial toughening that remains at retraction rates several times the characteristic frequency is thus due to viscous dissipation alone. The theoretical treatises [191, 223, 333] also contradict each other: where the pull-off force increases with (roughness) amplitude following Ciavarella and Papangelo [333], and Papangelo and Ciavarella [223]; the pull-off force is negligibly affected by the root-mean square roughness following Violano *et al.* [190, 191]. With viscous losses implicitly considered via the assumption by Gent and Schultz ([207–209]) [223], and the theoretical treatises by Ciavarella [193] with a cohesive zone model, report a dependence on pre-load as well. However, it is still unknown how surface roughness affects the dependence of the pull-off force on the maximum applied load [191]. The results indicate that, in the presence of viscoelasticity [190, 191] at low retraction rates, roughness increases the pull-off load (negligibly according to some authors [190, 191], significantly according to others [223, 333]). Whether this happens at high retraction rates as well is more controversial [223, 333]. Ciavarella and Papangelo [223, 333] find that roughness-induced dissipation disappears with retraction rate, viscous dissipation "dominates" instabilities and contact mechanics approach that of a smooth contact with viscous dissipation. They [223, 333] speculate that viscoelasticity "effectively dampens" [333] the roughness-induced elastic instabilities, *i.e.* reduces roughness induced adhesive hysteresis. Obviously unstable jumps do exist with viscous dissipation present. The first subquestion thus is: *What is the source of dissipation between stable, static equilibria in soft matter contacts?*.

Recently, much attention is dedicated to the study of the pull-off load in smooth, adhesive viscoelastic contacts [135, 193, 221, 337]. Viscoelastic stiffening tends to promote long-range adhesive behaviour [190, 193, 205, 335]. Violano and Afferante [337] elucidate the effects of long- and short-range adhesion on the pull-off force. They [337] find that in the limit of long-range adhesion: the unloading velocity has little effect on the pull-off force, and is close to the prediction by Bradley [196] for rigid bodies. The contact mechanics are thus characterised by uniform jump-out of contact under displacement control; the pull-off force is independent of the retraction rate; and, marked viscous dissipation occurs in the bulk of the material. Aforementioned observations oppose those for short-range adhesion, where for low and moderate retraction rates, dissipation is limited to a small volume close to the contact edges [229]. Violano and Afferante find [337] in accordance with Jiang *et al.* [135] and us [335] that the pull-off force (the effective work of adhesion in the latter work [335]) is limited by the effective Tabor/Maugis parameter. Ciavarella *et al.* [339] calculate the upper bound of this pull-off load. They [339] qualitatively reproduce the pull-off loads at high retraction rates by Müser and Persson [205] once the range of adhesion is adjusted by a corrective factor. We will show that roughness-induced mechanical instabilities reappear with increased retraction

rate. The second subquestion thus is: *When do mechanical instabilities occur in soft matter contact between stable, quasi-static equilibria?.*

Outline

In the following, we contribute to a better understanding of the interplay between roughness, viscoelasticity and adhesion by means of a simple two-dimensional numerical model, which has the strength that the dissipation is an emergent behaviour. The model builds on the work by Van Dokkum and Nicola [340], and Van Dokkum *et al.* [335], who study the indentation and retraction of a smooth, rigid cylinder from a viscoelastic half-plane by means of Green's function molecular dynamics [341]. To simplify the problem, roughness is modelled as a single wavelength wave superimposed on the profile of a rigid cylinder, that retracts from the viscoelastic half-plane. By changing retraction rate from two different initial loads and with two different instantaneous moduli, we compute the contact area and the load. We determine the contribution of viscous dissipation and mechanical instabilities in adhesive hysteresis by comparing with the JKR-solutions [172, 192] and the opening of a Mode I crack [217, 218]. Pull-off is analysed via an adjusted, Maugis calculation of the contact area and load, alike Johnson and Greenwood [201] and Ciavarella *et al.* [339].

5

5.2 Problem Definition

The problem considered in this chapter is the retraction of a rigid, wavy, infinitely long, cylindrical indenter from a viscoelastic half-plane, as represented schematically in Fig. 5.1. The cylindrical indenter, that is assumed to be much stiffer than the substrate, has a profile

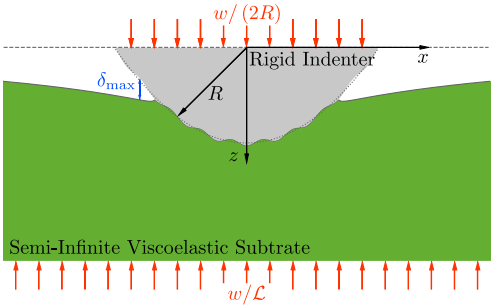

Figure 5.1: A rigid indenter with radius R in contact with a viscoelastic substrate for an applied load w. Adhesion is controlled by the interaction length $\delta_{\max}$. The image is stretched in the z-direction for clarity.

$$h(x,t) = h_0(t) + \frac{x^2}{2R} - A\cos\left(\frac{2\pi x}{\zeta}\right), \tag{5.1}$$

where the first term characterises a rigid body translation, the second the profile of a Hertzian cylinder with radius R and the third a sinusoidal waviness, superimposed on the cylindrical profile, with amplitude A, wavelength ζ and time t. The substrate is assumed to be initially flat and semi-infinite. The material is taken to be incompressible and viscoelastic in shear. For simplicity, the viscoelastic behaviour is modelled by means of the Zener model [342].

Hence, the creep function of the equivalent elastic modulus is

$$E^*(t) = E_0^* + \left(E_\infty^* - E_0^*\right) e^{-\frac{t}{\tau}}, \tag{5.2}$$

where E_0^* is the relaxed effective modulus, that characterises the response when the deformation rate $\dot{u} \sim 0$; E_∞^* the instantaneous effective modulus, that characterises the response in the limit $\dot{u} \to \infty$; and, τ the relaxation time. Here the overdot $\dot{\bullet}$ indicates the derivative of $\bullet$ with respect to the dimensional time t.

The Dugdale-Maugis model [194, 197] is used to describe the adhesive interaction between the indenter and the (visco)elastic substrate. This model [194, 197] specifies an adhesive traction σ_a whenever the gap (width) between the two bodies, $g(x,t)$, is positive but smaller than or equal to the interaction length δ_{max}. The adhesive contact is characterised by the relaxed Maugis parameter

$$\lambda_0 = \frac{\Delta\gamma_0}{\delta_{max}} \left(R / \left(\Delta\gamma_0 \left(E_0^*\right)^2 \right) \right)^{1/3}, \tag{5.3}$$

5

where $\Delta\gamma_0 = \sigma_a \delta_{max}$ is the relaxed work of adhesion. Interpenetration is prevented through a hard-wall constraint. The boundary conditions, which describe the interfacial interaction, are

$$\begin{aligned} g(x,t) = 0, &\quad p(x,t) < \sigma_a, &&\text{intimate contact;} \\ 0 < g(x,t) \leq \delta_{max}, &\quad p(x,t) = \sigma_a, &&\text{adhesive annulus;} \\ g(x,t) > \delta_{max}, &\quad p(x,t) = 0, &&\text{out of contact,} \end{aligned} \tag{5.4a}$$

with the gap

$$g(x,t) = h(x,t) - u(x,t), \tag{5.4b}$$

where $u(x,t)$ indicates the normal displacements of the (visco)elastic substrate. The normal pressure at the interface is indicated by $p(x,t)$. By convention, pressure is defined positive when compressive. The contact area a_c is defined as the area in intimate contact where the gap $g(x,t) = 0$.

5.3 Theory

Before presenting recent theory, let us revisit analytical results that aid the following analyses. The load in wavy adhesive line contact [172] in the relaxed and short-range adhesion limits is

$$\bar{w}_0 = \frac{\pi}{4}\bar{a}_c^2 - \sqrt{2\pi\bar{a}_c} + \pi\alpha\bar{a}_c \mathrm{J}_1\left(\frac{2\pi\bar{a}_c}{\beta}\right), \tag{5.5a}$$

with the normalised load $\bar{w} = w / \left(RE_0^* \Delta\gamma_0^2\right)^{1/3}$, and normalised amplitude and wavelength,

$$\alpha = \frac{\pi A E_0^*}{\zeta} \left(\frac{R}{\left(E_0^*\right)^2 \Delta\gamma_0} \right)^{1/3}; \qquad \text{and,} \qquad \beta = \zeta \left(\frac{E_0^*}{R^2 \Delta\gamma_0} \right)^{1/3}, \tag{5.5b}$$

respectively, where $\bar{a}_c = a_c / \left(R^2\Delta\gamma_0 / E_0^*\right)^{1/3}$ is the normalised contact area and $\mathrm{J}_1(\bullet)$ the first Bessel function of order one. The first two terms on the right-hand side of Eq. (5.5a)

correspond with the two-dimensional JKR-solution [192] (See *e.g.* [177, 201]) and the third one incorporates the effect of waviness. Equation (5.5) holds only for a connected, intimate contact area. For a smooth cylindrical indenter ($\{\alpha,\beta\}=\{0,-\}$), that separates from an elastic substrate, JKR-theory [201] gives the contact area at pull-off

$$(\bar{a}_c)_{\mathrm{PO}}^{\mathrm{JKR}} = \left(2R^2\Delta\gamma_0/\left(\pi E_0^*\right)\right)^{1/3}, \tag{5.6a}$$

with the load,

$$\bar{w}_{\mathrm{PO}}^{\mathrm{JKR}} = -(3/4)(4\pi E_0^* R\Delta\gamma_0^2)^{1/3}, \tag{5.6b}$$

that are finite and negative (tension), respectively, when adhesion allows for the indenter to pull on the substrate. Equations (5.5) and (5.6) serve as the relaxed limits with short-range adhesion in the following analysis.

Turning our attention to short-range adhesion in the instantaneous limit, we obtain the closed-form solution of the load-area relationship in wavy contact as well. A straightforward analysis (see *e.g.* [183]) shows that the maximum effective work of adhesion reached due to viscous dissipation is $\Delta\gamma_{\mathrm{eff}} \sim f_r\Delta\gamma_0$, with the modulus ratio $f_r = E_\infty^*/E_0^*$. This corresponds with an elastic material with the instantaneous effective modulus E_∞^* at the contact edges [335]. The increased adhesion provided for by viscous dissipation is traditionally described by an effective work of adhesion $\Delta\gamma_0 \le \Delta\gamma_{\mathrm{eff}} \le f_r\Delta\gamma_0$ (see *e.g.* [333]). In the instantaneous limit, the instantaneous work of adhesion is thus constant with $\Delta\gamma_\infty \equiv \Delta\gamma_0 f_r$. Since viscous dissipation is concentrated near the edges of contact, the bulk is still characterised by the relaxed effective modulus E_0^*. One thus recovers elastic behaviour, albeit with an effective work of adhesion $\Delta\gamma_{\mathrm{eff}} \sim \Delta\gamma_\infty$ in the instantaneous limit. Guduru's solution for the elastic contact with the instantaneous effective modulus E_∞^*, in the second term on the RHS of Eq. (5.5a), is one lower limit to the viscoelastic load-area curves. In the following, we refer to this solution as the instantaneous limit with short-range adhesion, because viscoelastic contact tends towards this limit at high retraction rates, as we show in the following.

Greenwood and Johnson [183] indicate that, since the traction at the peeling edges is infinite in the JKR-theory, the stress and strain rates are infinite for any finite retraction rate. Therefore, any viscous material around the peeling edge is in the instantaneous limit. They [183] note that this is against observations and therefore, suggest to use a more realistic description of the traction outside of intimate contact, which accounts for the fact that the stress peak at the peeling edges is finite and adhesion acts over a finite range, with interaction ranges $0 < \delta_{\max}$. In any case, due to stiffening in the adhesive annulus, the effective Maugis parameter λ_{eff} [335] becomes smaller than the relaxed Maugis parameter λ_0 and larger then the instantaneous Maugis parameter

$$\lambda_\infty \equiv \frac{\Delta\gamma_0}{\delta_{\max}}\left(R/\left(\Delta\gamma_0\left(E_\infty^*\right)^2\right)\right)^{1/3}. \tag{5.7}$$

There is thus the need to account for viscous dissipation in the edges of contact and its influence on the (finite) range of adhesion, which Ciavarella *et al.* [339] recently attempted.

Ciavarella *et al.* [339] consider the contact between a smooth cylindrical indenter and a viscoelastic, adhesive half-plane, *i.e.* with normalised parameters $\{\alpha,\beta\}=\{0,-\}$. The basic equations in the relaxed limit are given in Baney and Hui [343] and the explicit evaluation is presented by Johnson and Greenwood [201]. Following Johnson and Greenwood [201],

we use the superposition principle and ensure the normal separation $g(a_c m) = \delta_{\max}$ at the edge of the adhesive annulus, with ratio $m = a_a/a_c$. This normal separation at the edge of the adhesive annulus is

$$\lambda_0 \bar{a}_c^2 \bar{g}_0^H(m) + \lambda_0^2 \bar{a}_c \bar{g}_0^A(m) = 1, \tag{5.8a}$$

where,

$$\begin{aligned} \bar{g}_0^H &= \frac{1}{2}\left(m\sqrt{m^2-1} - \cosh^{-1}(m)\right); \quad \text{and,} \\ \bar{g}_0^A &= \frac{4}{\pi}\left(\sqrt{m^2-1}\cosh^{-1}(m) - m\ln(m)\right), \end{aligned} \tag{5.8b}$$

are the gaps, $\bar{g} = g_c/\left(R^2\Delta\gamma_0/E_0^*\right)^{1/3}$, outside of and an adhesionless Hertzian contact and at the edge of an attractive annulus, respectively. The normalised load is

$$\bar{w} = \frac{\pi \bar{a}_c^2}{4} - 2\lambda_0 \bar{a}_c \sqrt{m^2-1}, \tag{5.8c}$$

where the first term on the RHS is the Hertzian load, and the second term the adhesive contribution. In the JKR-limit, with ratio $m \sim 0$ and relaxed Maugis parameter $\lambda_0 \sim \infty$, we obtain the first two terms on the right-hand side of Eq. (5.5a); and, in the rigid limit, the pull-off load is $\bar{w}_{PO}^{PO} = 2\sqrt{2}\sqrt{\lambda_0}$ and intimate contact area $(a_c)_{PO}^{rigid} = 0$.

Ciavarella *et al.* [339] incorporate viscous dissipation by modifying Eq. (5.8) in a "*Schapery*" approximate sense. They [339] only modify the condition of critical gap size (5.8a) by replacing the effective elastic modulus E_0^* in the definition of the adhesive gap g_0^A by a creep function equivalent to Eq. (5.2). They [339] "*considered the remote bulk material to be in a relaxed state even during unloading, which is the correct assumption in view of obtaining upper bounds for the pull-off load*". In the instantaneous limit, the second term on the LHS of Eq. (5.8a) then reads $\lambda_0^2 \bar{a}_c \bar{g}_0^A(m)/f_r$. However, the Hertzian gap g^H outside of intimate contact depends on the equivalent elastic modulus E^* in the contact area as well.

For the remainder of this analysis, we consider solely the viscoelastic response in the instantaneous limit. In Hertzian/cylindrical contact, the mixed boundary value problem is solved by removing the singularity at the edges of contact (See *e.g.* Barber [344]). The normalised load per unit cylinder length in the intimate contact area thus is

$$\bar{p}_0^H(\bar{x}) = -\frac{2\bar{w}_0^H}{\pi\lambda_0}\frac{\sqrt{\bar{a}_c^2 - \bar{x}^2}}{\bar{a}_c^2}, \tag{5.9}$$

with the normalised pressure and normalised x-coordinate,

$$\bar{p} = \frac{\delta_{\max} p}{\Delta\gamma_0}; \quad \text{and,} \quad \bar{x} = x/\left(R^2\Delta\gamma_0/E_0^*\right)^{1/3}, \tag{5.10}$$

respectively, where $\bar{w}_0^H = \pi\bar{a}_c^2/4$ is the Hertzian load on the cylinder in the relaxed limit. The surface displacement's gradient under plane strain condition outside of intimate contact, *i.e.* $\bar{a}_c \le \bar{x}$, thus becomes

$$\frac{\partial}{\partial\bar{x}}\bar{u}(\bar{x}) = -\frac{2\lambda_0}{\pi f_r}\int_{-\bar{a}_c}^{\bar{a}_c}\frac{\bar{p}_0^H(\bar{x}')}{\bar{x}-\bar{x}'}\,\mathrm{d}\bar{x}' = \frac{1}{f_r}\left(\bar{x} - \sqrt{\bar{x}^2 - \bar{a}_c^2}\right). \tag{5.11}$$

Here, we make the assumption that the viscoelastic response inside the contact area is in the instantaneous limit as well. This is equivalent to one substituting the creep function, alike Ciavarella *et al.* [339], in the definition of the Hertzian gap g^{H} where the load, $\bar{w}_0^{\mathrm{H}}$, remains in the relaxed limit. Integrating Eq. (5.11) and applying the appropriate boundary condition at the edge of intimate contact (*i.e.*, $\lim_{\bar{x}\to\bar{a}_c^+}\ \bar{g}^{\mathrm{H}} = 0$), the normalised separation at the edge of the adhesive annulus is

$$\lambda_0\bar{a}_c^2\bar{g}_0^{\mathrm{H}}(m) + \lambda_0^2\bar{a}_c\bar{g}_0^{\mathrm{A}}(m) = f_r. \tag{5.12}$$

The semi-analytical solution of Eqs. (5.8c) and (5.12) is a limit of the Maugis analysis, where the adhesive response in the instantaneous limit. In the following, we refer to this solution as the instantaneous limit with finite-range adhesion.

In Fig. 5.2, the theoretical load-area and scaled load-scaled area curves for smooth and wavy contact in the relaxed and instantaneous limits are given; the solid and dashed lines indi-

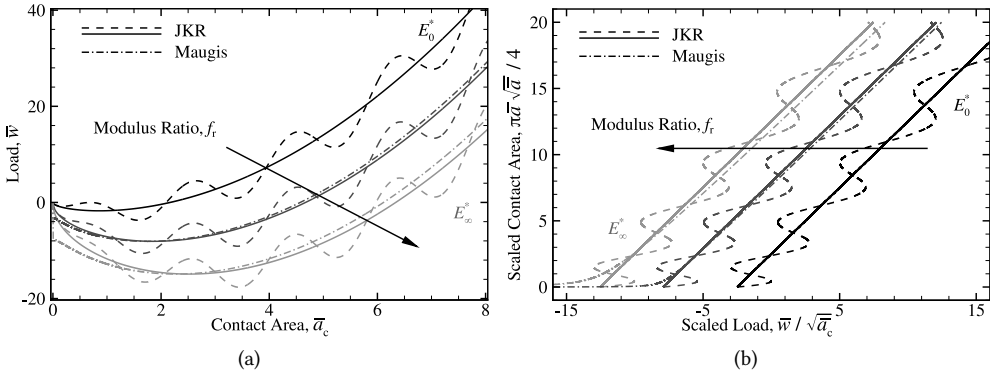

Figure 5.2: (a) The normalised load $\bar{w}$ as a function of the normalised contact area $\bar{a}_c$ and (b) the scaled area $\pi\bar{a}_c\sqrt{\bar{a}_c}/4$ as a function of the scaled load $\bar{w}/\sqrt{\bar{a}_c}$ for smooth (solid line) and wavy ((dashed)-dotted lines) contact, and adhesion is short-range with a relaxed Maugis parameter $\lambda_0 = 7$. The black lines indicate the relaxed limit E_0^*, the gray lines the instantaneous limits E_∞^* and the black arrow an increase in modulus ratio modulus ratios f_r =10 and 25 across grey coloured lines.

cate the short-range adhesive limit, $\lambda_0 \sim \infty$, and the dashed-dotted line finite-range adhesion, $3 \leq \lambda_0$ [201]. In the relaxed limit E_0^* and/or for the modulus ratio $f_r \sim 1$, the responses with a finite and an infinitesimal range of adhesion coincide when $3 << \lambda_0$ [201]. The difference between the responses with a finite and infinitesimal range of adhesion, in the instantaneous limit E_∞^*, increases with modulus ratio f_r and relaxed Maugis parameter λ_0 [335]. The former load-area response differs most from short-range adhesive, cylindrical contact, when the intimate contact area $\bar{a}_c < 3$, *i.e.*, near pull-off.

A characteristic of load-controlled adhesive experiments with short-range adhesion is that pull-off and/or mechanical instabilities occur for a finite intimate contact area $0 << (\bar{a}_c)_{\mathrm{PO}}$ upon retraction, where the slope $\mathrm{d}\bar{w}/\mathrm{d}\bar{a}_c$ changes sign. An increase in load $\bar{w}$ with decreasing contact area $\bar{a}_c$ is thus not observed during retraction. Juxtaposed to elastic adhesive contact, mechanical instabilities solely occur when the load-area response meets the instantaneous limit in the presence of viscous dissipation [345]. The grey lines in Fig. 5.2 are these instan-

taneous limits. Larger loads $\bar{w}$ and smaller contact areas $\bar{a}_c$ are thus observed in the presence of viscoelasticity, than in elastic contacts.

The dashed-dotted grey lines in Fig. 5.2 are a second instantaneous limit, with a finite range of adhesion. The pressure inside intimate contact is that of a Hertzian in the relaxed limit, and the deformation in the adhesive annulus is in the instantaneous limit. Due to stiffening in the adhesive annulus, the effective Maugis parameter λ_{eff} becomes smaller [335]. The vanishing, finite contact area at increasing load, is a characteristic of this transition form the JKR-limit to the rigid limit. This becomes clearest in Fig. 5.2b of the scaled area-scaled load curves with contact areas $\bar{a}_c < (a_c)_{\text{PO}}^{\text{JKR}}$ and loads $\bar{w}_{\text{PO}}^{\text{JKR}} < \bar{w}$. The contact's response changes from short- to finite-range adhesion. We expect that the latter's instantaneous limit is approached at vanishing contact area $(a_c)_{\text{PO}} \sim 0$. The instantaneous limit with finite range adhesion thus is the second limit we use to analyse the intimate contact area $(\bar{a}_c)_{\text{PO}}$ and load $\bar{w}_{\text{PO}}$ at pull-off in the following.

5.4 Numerical Method

5

The numerical model adopted is the one presented by Van Dokkum and Nicola [340], that employs the Green's Function Molecular Dynamics (GFMD) technique and discrete Fourier transform [346] to achieve an efficient algorithm. The GFMD technique is a boundary-element method that permits one to reduce the dimensions of the problem such that only the profile of the substrate is modelled. At each temporal increment Δt, the equilibrium normal displacement of the profile is found by means of the following relation in Fourier space:

$$\tilde{p}(q,t) + \tau \dot{\tilde{p}}(q,t) = -8|q| \left(E_0^* \tilde{u}(q,t) + \tau E_\infty^* \dot{\tilde{u}}(q,t) \right), \tag{5.13}$$

coupled to the imposed boundary conditions. Here, the overscript tilde $\tilde{\bullet}$ indicates the Fourier transform of $\bullet$, with the wavenumber q. Equation (5.13) is integrated in the time domain semi-analytically within each constant, dimensional time-step Δt. We thus avoid storing the whole history of normal pressures and displacement, which is necessary for a direct numerical integration. Each dimensionless time-step $\Delta \bar{t}$, the position (Störmer-)Verlet algorithm [347] is used to compute, through damped dynamics, the new normal displacement of the equispaced nodes n_x that discretise the profiles. Adhesion is here implemented using a first-order approximation in the gap, in a manner similar to that presented by Medina and Dini [158]. The dimensionless time-step $\Delta t = \Delta t_{\max}/50$, with the maximum time-step $\Delta t_{\max} = \tau(1 - 1/f_r)$, and spatial discretization $n_x = 2^{15}$ ensure convergence for the physical parameters we choose.

The cylinder's radius $R = \mathcal{L}/10$, with the periodic width $\mathcal{L}$. The ratio $\mathcal{L}/R$ is chosen sufficiently large so that the results are unaffected by the inherent periodicity of the discrete Fourier transform [346]. The normalised parameters $\{\alpha, \beta\} = \{0, -\}$ (*i.e.* smooth contact), and $\{1.46, 1.87\}$ (*i.e.* wavy contact), unless specified differently. The modulus ratios are $f_r = 10$ and 25, where the relaxed effective modulus E_0^* and the relaxation time τ are kept constant. The relaxed Maugis parameter $\lambda_0 = 7$ ensures short-range adhesive contact in the relaxed limit [201]. The problem is studied by controlling the load rate $\dot{w}(t) = \frac{\partial}{\partial t} \int p(x,t)\, \mathrm{d}x$ at the contact.

First, we indent the substrate elastically, with the relaxed effective modulus E_0^*, up to maximum loads $\bar{w}_{\max} = 20$ and 40. This is equivalent to indenting a viscoelastic substrate

and prescribing an infinite waiting time, so the substrate fully relaxes after indentation, but computationally tractable. Subsequently, the indenter is retracted by reducing the load at a constant load rate $\dot{w}$. The normalised retraction rates $\dot{\bar{w}} \times 10^4 = \dot{w}\tau / \left(RE_0^* \Delta\gamma_0^2\right)^{1/3} = 300, 120, 60, \cdots, 0.03, 0.012, 0.006$ and ~ 0 (*i.e.* elastic).

5.5 Results and Discussion

In Fig. 5.3, the load $\bar{w}$ as a function of the contact area $\bar{a}_c$ is presented for smooth and wavy contact, with maximum loads $\bar{w}_{max} = 20$ and 40; in Figs. 5.3a,c, and 5.3b,d, the load-area curves

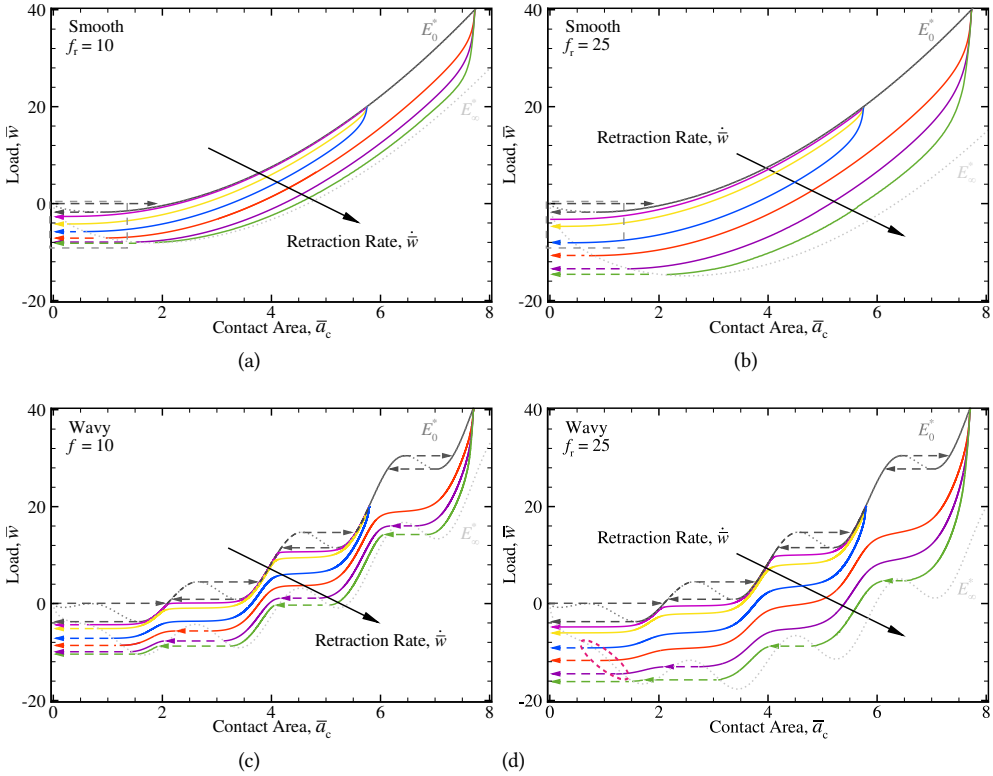

Figure 5.3: The normalised load $\bar{w}$ as a function of the normalised contact area $\bar{a}_c$ for (a, b) smooth ($\{\alpha, \beta\} = \{0, -\}$) and (c, d) wavy ($\{\alpha, \beta\} = \{1.47, 1.87\}$) contact, with modulus ratios (a, c) $f_r = 10$ and (b, d) 25, and maximum normalised loads $\bar{w}_{max} = 20$ and 40. The loading rate $\dot{\bar{w}} \sim 0$ (*i.e.* elastic), and retraction rates $\dot{\bar{w}} \times 10^4 =$0.06, 0.3, 3, 12, 60 and 300 increase across solid coloured lines as indicated by the black arrow. The dark grey dotted line indicates the relaxed and the light grey dotted line the instantaneous limit with short-range adhesion. Unstable jumps are indicated by coloured arrows with coloured, dashed lines.

are given with modulus ratios $f_r = 10$ and 25, respectively. The relaxed and instantaneous limits with short-range adhesion are indicated by dark and light grey dotted lines, respectively. The elastic result (*i.e.*, loading rate $\dot{\bar{w}} \sim 0$) during indentation and retraction, with effective elastic modulus E_0^*, is indicated by a solid, dark grey line.

Both elastic and viscoelastic contacts are characterised by adhesive hysteresis, but their origins differ. We quantify adhesive hysteresis as the difference between elastic loading, indicated by dark grey line, and retraction with a finite rate, as indicated by coloured lines. In elastic contact, it is the dissipation of energy in the mechanical instabilities that causes adhesive hysteresis [123], as these elastic jumps upon retraction occur at lower loads than whilst indenting. All mechanical instabilities are indicated by coloured arrows with dashed lines, that correspond in their colour with the given retraction rate. For smooth contact the mechanical instability coincide with jump in- and out-of-contact, while in wavy contact mechanical instabilities occur during retraction as well. In viscoelastic contact, both mechanical instabilities and viscoelasticity contribute to adhesive hysteresis.

The viscoelastic curves fall below the relaxed limit, *i.e.*, a larger contact area is found for the same load, which indicates that adhesion is stronger than in elastic contact: the load-area curves for smooth contacts, in Figs. 5.3a and b, follow a path parallel to the JKR solution [192], characterised by an increased effective work of adhesion $\Delta\gamma_{\text{eff}}$ after an initial transient period [186, 335]; and, the load-area curves for wavy contact, in Figs. 5.3c and d, shift to lower loads with respect to the reference solution by Guduru (5.5) as well. As expected, one observes a monotonic trend; the load-area curve approaches the relaxed limit at low retraction rates and the instantaneous limit at high retraction rates. As the modulus ratio increases so does the adhesive hysteresis for a given retraction rate between Fig. 5.3a and b, and 5.3c and d. Notable is that in wavy contacts with retraction rates $\dot{\bar{w}} \times 10^{-4} \leq 3$, mechanical instabilities are absent during retraction, except for pull-off. For loads above the instantaneous limit and below the relaxed limit, a finite yet quick area reduction is observed. At high retraction rates $12 \leq \dot{\bar{w}} \times 10^{-4}$, mechanical instabilities do occur. We address these two observations in the following.

5.5.1 Wavy Contact

In Fig. 5.4, the particular case of retraction rate $\dot{\bar{w}} \times 10^4 = 12$ is presented, in wavy contact, with modulus ratio $f_{\text{r}} = 10$ and maximum load $\bar{w}_{\text{max}} = 20$; the load-area curve is presented in Fig. 5.4a together with the elastic realisation (*i.e.*, retraction rate $\dot{w} \sim 0$) as reference.

The elastic solution is characterised by an unstable jump around $\bar{a}_{\text{c}} \approx 5$ as marked by a yellow circle, where Guduru's analytical solution (5.5a) has a local minimum. This elastic mechanical instability, however, does not occur in the adhesive, viscoelastic wavy contact. This is in line with what was observed by *e.g.* Ciavarella [333] and is rationalised as follows: in an elastic material, the only equilibrium positions are given by the relaxed limit (dark grey dotted lines in Figs. 5.3 and 5.4). For a viscoelastic material, however, an infinite number of such solutions exist as the effective work of adhesion $\Delta\gamma_{\text{eff}}$ is allowed to vary freely between $\Delta\gamma_0$ and $f_{\text{r}}\Delta\gamma_0$. Therefore, at least the whole load-area region between the relaxed and instantaneous limits with short-range adhesion (*i.e.* between the dark and light grey dotted lines in Figs. 5.3 and 5.4) provides for stable, quasi-static equilibria.

To better understand what happens upon the retraction of the wavy, adhesive cylinder, the pressure profiles are presented in Fig. 5.4b at the loads $\bar{w} = 5.6$, 3.7 and -1.6, which correspond with the coloured dot-shaped markers in Fig. 5.4a. All the pressure profiles look qualitatively similar, with smooth oscillations that match the waviness of the indenter, and a large attractive normal pressure spike at the edge of contact. When the contact area recedes upon retraction, high pressure rates $\dot{\bar{p}} \equiv \delta_{\text{max}}\tau\dot{p}/\Delta\gamma_0$ are confined to the edges of the contact,

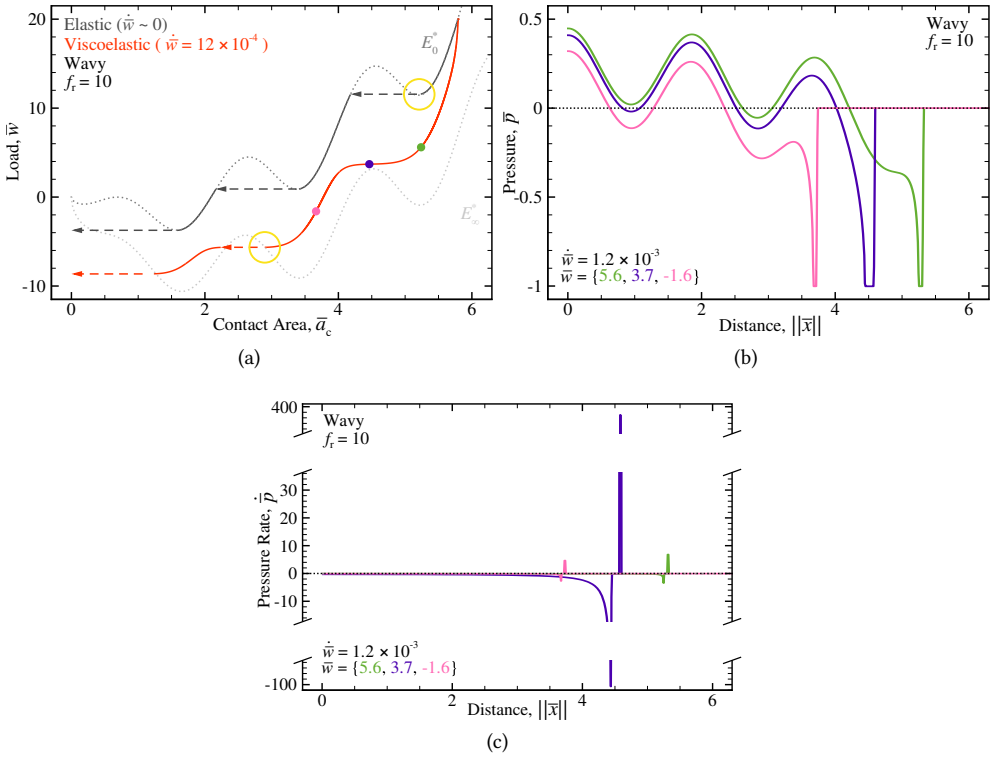

Figure 5.4: (a) The normalised load $\bar{w}$ as a function of the normalised contact area $\bar{a}_c$ for wavy contact ($\{\alpha, \beta\} = \{1.46, 1.87\}$), with maximum normalised load $\bar{w}_{max} = 20$, retraction rates $\dot{\bar{w}} \sim 0$ and $1.2 \cdot 10^{-3}$, and modulus ratio $f_r = 10$. (b) Pressure, (c) and pressure rate profiles for the normalised loads $\bar{w} = 5.6$, 3.7 and -1.6 as indicated by differently coloured, dot-shaped markers in (a).

as shown in Fig. 5.4c. This is consistent with the common assumption in literature, that the viscous dissipation is concentrated at the edges of intimate contact. Of course, this holds true only when the retraction rate does not exceed a given *a priori* unknown threshold; and when adhesion is short-range.

It is interesting to observe in Fig. 5.4b that the sizes of the adhesive annuli are different at different loads $\bar{w}$. The load $\bar{w} = 3.7$, as indicated by the purple curves in Figs. 5.4b, has the widest adhesive annulus of all loads we investigate. This is because the purple profile in Fig. 5.4b corresponds to a point, indicated with a purple dot-shaped marker on the load-area curve in Fig. 5.4a, with the smallest slope $d\bar{w}/d\bar{a}_c$: a minute reduction in the applied load $\bar{w}$ leads to a large drop in the contact area. Therefore, the contact area reduction, $-\dot{a}_c$, is highest at that point, which leads to an increase in normal pressure rate that stiffens the substrate locally. This increase holds the surfaces closer together by additional viscous dissipation, and a mechanical instability is absent. These observations are inline with the description of a crack tip in a viscoelastic solid by Greenwood and Johnson [183].

Mechanical instabilities during retraction, in wavy contact, solely occurs when the

viscoelastic load-area response meets the instantaneous limit with short-range adhesion; the effective work of adhesion $\Delta\gamma_{\text{eff}}$ approaches the instantaneous work of adhesion $\Delta\gamma_\infty$. The load can no longer decrease with contact area reduction and the mechanical instability ensues, as marked by a yellow circle at the intimate contact area $\bar{a}_c \approx 3$ and the load $\bar{w} \approx -6$ in Fig. 5.4a. Quasi-static stable contact is attained again with the intimate contact area $\bar{a}_c \approx 2.25$ for the same load. This mechanical instability constitutes roughness-induced dissipation.

In Fig. 5.5, the load-area curves in wavy contact for retraction rate $\dot{\bar{w}} \times 10^4 = 12$, and modulus ratios $f_r = 10$ and 25 are presented; the maximum load $\bar{w}_{\max} = 40$, and the elastic

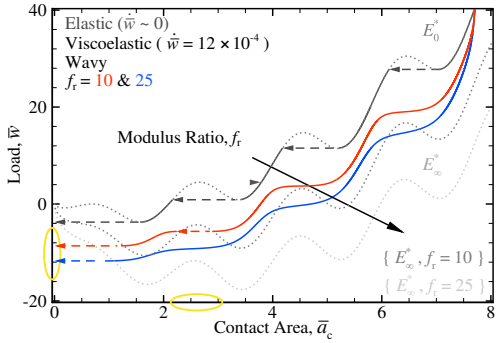

Figure 5.5: The normalised load $\bar{w}$ as a function of the normalised contact area $\bar{a}_c$ for modulus ratios f_r =10 and 25 in wavy contact ($\{\alpha, \beta\} = \{1.46, 1.87\}$), with maximum normalised load $\bar{w}_{\max} = 40$, and retraction rates $\dot{\bar{w}} \sim 0$ and $\dot{\bar{w}} = 1.2 \cdot 10^{-3}$.The dark and light grey dotted lines indicate the instantaneous limits with short-range adhesion for modulus ratios f_r =10 and 25, respectively, as indicated by the black arrow.

realisation (*i.e.*, retraction rate $\dot{w} \sim 0$) is added as reference. The relaxed and both instantaneous limits with short-range adhesion are indicated by dark and light grey, dotted lines, respectively. The numerical results out of Figs 5.3c and d are combined here for comparison's sake.

For the given retraction rate and increasing modulus ratio, the magnitude of adhesive hysteresis increases: the loads at pull-off are $\bar{w}_{\text{PO}} \approx -8$ and -12 for modulus ratios $f_r = 10$ and 25, respectively, as marked by a vertical yellow ellipse. The load $\bar{w}$ decreases with increased modulus ratio f_r for a given contact area a_c as well [333]; the number of mechanical instabilities decreases with increased modulus ratio; a mechanical instability occurs for modulus ratio $f_r = 10$, whose range of intimate contact areas $2 \lessapprox \bar{a}_c \lessapprox 3$ is marked by a horizontal yellow ellipse. For modulus ratio $f_r = 25$, a rapid yet constant, intimate contact area reduction is observed for this contact area range. The maximum work of adhesion, $\Delta\gamma_0 f_r$, increases with the modulus ratio, so the pull-off load $\bar{w}_{\text{PO}}$ decreases in the instantaneous limits E_∞^*. The magnitude of the observed adhesion increases, yet the magnitude of roughness-induced dissipation reduces with increased modulus ratio f_r.

Mechanical instabilities are not all damped in viscoelastic wavy contacts, they do occur when the load-area curve traverses the instantaneous limit with short-range adhesion. These instabilities are indicated by coloured arrows with coloured dashed lines who's colour corresponds with the given retraction rate in Figs. 5.3c and d, and 5.4a and 5.5. We note that quasi-static equilibrium, is obtained beyond the instantaneous limit because the range adhesion increases with stiffening in the edges of contact [335]. This becomes most apparent

in our results when the modulus ratio increases from $f_r = 10$ to 25 in Fig. 5.3c and d. Since stiffness is bounded by the instantaneous effective modulus E^*_∞, mechanical instabilities occur at a finite intimate contact areas as highlighted in Fig. 5.3d by an hot pink coloured, dashed ellipse. These effects of viscoelasticity on the observed adhesion and observed roughness-induced dissipation is discussed in the following.

5.5.2 Viscoelastic Effects

In Fig. 5.6, the cases of retraction rates $\dot{\bar{w}} \times 10^4 = 0.006, 6$ and 60, and modulus ratios $f_r = 10$ and 25 are presented, in smooth ($\{\alpha, \beta\} = \{0, -\}$) and wavy ($\{\alpha, \beta\} = \{1.47, 1.87\}$) contacts; the

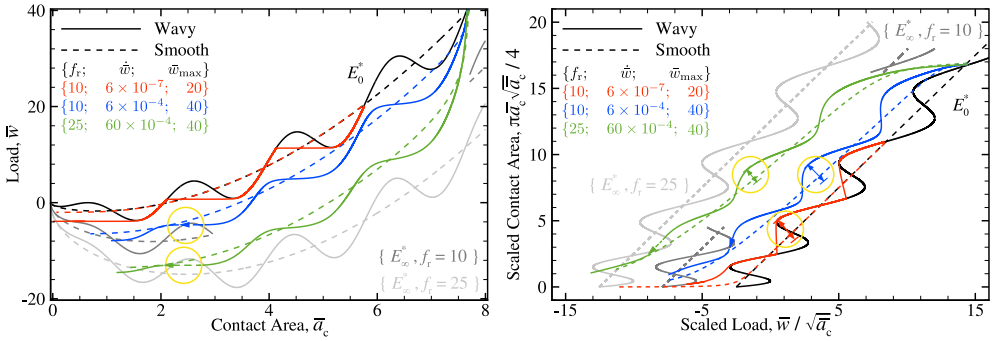

Figure 5.6: (a) The normalised load $\bar{w}$ as a function of the contact area $\bar{a}_c$ and (b) the scaled contact area $\pi\bar{a}_c\sqrt{\bar{a}_c}/4$ as a function of the scaled load $\bar{w}/\sqrt{\bar{a}_c}$ for smooth ($\{\alpha, \beta\} = \{0, -\}$) and wavy ($\{\alpha, \beta\} = \{1.47, 1.87\}$) contacts, with modulus ratios, retraction rates and maximum loads $\{f_r; \dot{\bar{w}}; \bar{w}_{max}\}$=$\{10; 6\times10^{-7}; 20\}$, $\{10; 6\times10^{-4}; 40\}$ and $\{25; 60\times10^{-4}; 40\}$. Part of the instantaneous limit for modulus ratio f_r =10 and arrows indicated jump-out-of-contact in Fig. 5.3 are omitted for clarity's sake. The double-headed arrows in (b) illustrate the local size of the load-area envelope [155].

maximum loads $\bar{w}_{max}$ are 20 with retraction rate $\dot{\bar{w}} \times 10^7 = 6$ and modulus ratio $f_r = 10$, and $\bar{w}_{max} = 40$ with rates $\dot{\bar{w}} \times 10^4 = 6$ and 60, for clarity's sake. We choose to compare the latter two retraction rates for one of each modulus ratio $f_r = 10$ and 25 because the load-area curves display a single mechanical instability. Those are indicated in Fig. 5.6 by coloured arrows and highlighted by yellow circles in Fig. 5.6a. In Figs. 5.6, the analytical and numerical result for both smooth ($\{\alpha, \beta\} = \{0, -\}$) and wavy ($\{\alpha, \beta\} = \{1.47, 1.87\}$) contacts are combined, and indicated by dashed and solid lines, respectively. For our choice of modulus ratios $f_r = 10$ and 25, the reduction in load-area envelope [155] is not readily noticeable for the same retraction rate $\dot{\bar{w}} \times 10^4 = 12$ in Fig. 5.5. The definition of load-area envelope originates from the work by Kesari and Lew [155]. They [155] expand Guduru's solution [172] asymptotically for very small wavelength of the waviness and obtain an envelope which touches the local maxima and minima of the load-approach curve. We omit part of the instantaneous limit, with short-range adhesion, for modulus ratio $f_r = 10$ for clarity's sake as well.

In Fig. 5.6a, the load $\bar{w}$ as a function of the contact area $\bar{a}_c$ is presented; and, in Fig. 5.6b, the scaled contact area $\pi\bar{a}_c\sqrt{\bar{a}_c}/4$ is given as a function of the scaled load $\bar{w}/\sqrt{\bar{a}_c}$. In wavy contact, the local envelope curves for the highest retraction rate $\dot{\bar{w}} \times 10^4 = 60$ is smaller than for $\dot{\bar{w}} \times 10^7 = 6$ and 600, and the elastic result. Herein, the local envelope is a line

that is tangential to all points of intersection with the scaled load-scaled area curve with a minimum of two points of intersection. This is a method to compare the waviness in the load-area curves between different retraction rates, wavy roughnesses and modulus ratios. The coloured, double headed arrows in Fig 5.6b, that are highlighted by yellow coloured circles, indicate the local size of the load-area envelopes. These arrows are visual aids to facilitate further comparison between different retraction rates $\dot{\bar{w}} \times 10^4 = 0.006, 6$ and 60, and modulus ratios $f_r = 10$ and 25, respectively.

The size of the local envelopes decreases with retraction rate and modulus ratio, which is rationalised as follows: the difference in retraction rate between "damped" elastic mechanical instabilities and the remainder of the retraction period decreases with increased viscous dissipation. The contact area reduction with time is readily inferred from Fig. 5.6a, noting that the retraction rate $\dot{\bar{w}}$ is constant for the given line colour. The contact area velocity, $\dot{a}_c$, thus decreases with increasing retraction rate, which increases viscous dissipation. Viscous dissipation increases for the given relaxation time τ with modulus ratio f_r as well. In turn, the load-area curve in wavy contact approaches that of smooth contact with increased modulus ratio but not necessary for the same retraction rate. The latter is clearest between the load-area responses in smooth and wavy contacts, as indicated by dashed and solid lines, respectively, in Fig. 5.6a. Our numerical results are in partial agreement with the speculation [333], that viscoelasticity reduces the effect of wavy roughness with increased retraction. Herein, mechanical instabilities do occur for modulus ratio $f_r = 25$ and retraction rates $60 \leq \dot{\bar{w}} \times 10^4$ in Fig. 5.3d.

For the lowest retraction rate $\dot{\bar{w}} \times 10^7 = 6$ and wavy contact, elastic mechanical instabilities are absent, except for pull-off. One might expect that with viscoelastic theory, the strict elastic solution is obtained at extremely low loading rates [333]. However, for the elastic result, as such independent of loading rate, an infinite speed of the receding contact edges is attained at mechanical instabilities. Herein, when viscous dissipation is confined to the edges of contact and a function of the receding contact's velocity, the effective work of adhesion $\Delta\gamma_{\text{eff}}$ increases with contact edge's velocity $\dot{a}_c/2$ [335]. The contact area velocity $\dot{a}_c$ is then finite because of the viscous dissipative component in the edges' equation of motion; when viscous dissipation is present a quasi-static stable equilibrium is attained. The only reason the quasi-static equilibrium becomes unstable is cause viscous dissipation is finite (See Sec. 5.5.1). Looking *e.g.* at previous works [223, 333], the instantaneous work of adhesion is infinite, so their [223, 333] models omit finite stiffening at the contacts' edges. For modulus ratio $f_r = 10$ and retraction rate $\dot{\bar{w}} \times 10^4$=12, part of adhesive dissipation is roughness-induced (See Fig. 5.3c). Wherefore with finite stiffening, we chose two different retraction rates to compare between two different modulus ratios in a meaningful manner. The occurrence of pull-off, at infinitesimal loading rates, might thus be due in part to meeting the instantaneous limit in the contact edges as well.

In Fig. 5.7, the scaled load $\bar{w}/\bar{w}_{\text{PO}}^{\text{JKR}}$ is given as a function of the scaled contact area $\bar{a}_c/(\bar{a}_c)_{\text{PO}}^{\text{JKR}}$ in smooth contact ($\{\alpha, \beta\} = \{0, -\}$) with modulus ratios $f_r = 10$ and 25; the results and limits in Fig. 5.7a and b, indicated by dotted and solid coloured lines, are equivalent for those in Fig. 5.3a and 5.3b, respectively; the dashed-dotted, light grey line delineates quasi-static equilibria in the instantaneous limit with a finite range of adhesion (See Sec. 5.3); and, the plots' range is indicated by grey dashed rectangles in Figs. 5.3a and b as well. We limit the following observations to the lowest retraction rates $\dot{\bar{w}} \times 10^4 = 0.006, \cdots, 3$. Furthermore,

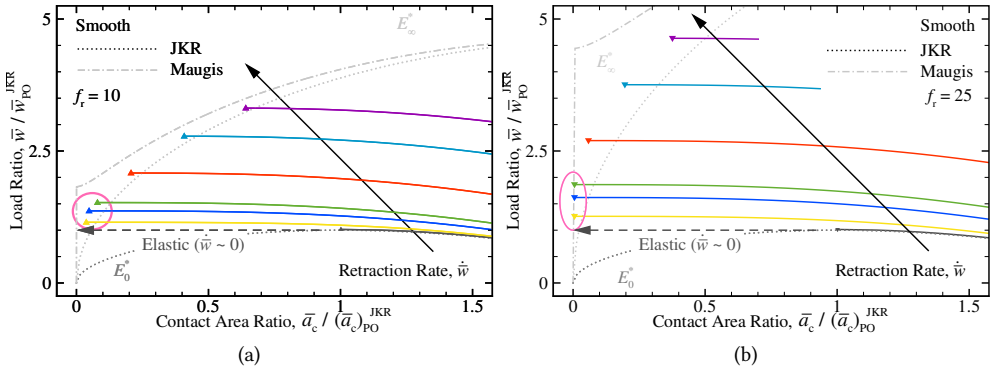

Figure 5.7: The scaled load $\bar{w}/\bar{w}_{PO}^{JKR}$ is given as a function of the scaled contact area $\bar{a}_c/(\bar{a}_c)_{PO}^{JKR}$ in smooth contact ($\{\alpha,\beta\}=\{0,-\}$) with modulus ratios (a) $f_r = 10$ and (b) 25. The retraction rate $\dot{\bar{w}}\sim 0$ (*i.e.* elastic), and $\dot{\bar{w}}\times 10^6 =$0.6, 3, 6, 30, 120 and 300 increases as indicated by the black arrow; the elastic mechanical instability is depicted by a dark grey arrow as a reference. The dark and light grey dotted lines indicate the relaxed and instantaneous with short-range adhesion (5.5), and the light grey dashed-dotted line the instantaneous limit with finite-range adhesion (5.12).

5

we omit the arrows with coloured dashed lines, that indicate jumps, for clarity's sake, expect for the the elastic result (*i.e.* retraction rate $\dot{\bar{w}} \sim 0$).

Pull-off is indicated on the scaled load-scaled contact area curves by coloured delta and gradient symbols in Figs. 5.7a and b, for modulus ratios $f_r = 10$ and 25, respectively. As expected, the pull-off loads tend towards the relaxed, JKR-limit with vanishing retraction rate (*i.e.* $\bar{w}_{PO} \sim \bar{w}_{PO}^{JKR}$). However, pull-off on the load-area curve resides between: the load-area relationship in the instantaneous limit for short-range adhesion (5.5); and, the load-area relationship with a finite range of adhesion (5.12), which includes a vanishing contact area at pull-off (*i.e.* $(a_c)_{PO} \sim 0$).

Once the contact area decreases below the minimum of adhesive elastic contact, *i.e.*, $a_c < (a_c)_{PO}^{JKR}$, the contact area reduction and viscous dissipation increase. The relative size of the adhesive annulus, a_a/a_c, increases with equivalent modulus E^*. The stiffening of the edges of contact with viscous dissipation increase the range of adhesion, whereby quasi-static equilibrium is attainable beyond the instantaneous limit with short-range adhesion. Hence the theoretical, maximum observed range of adhesion increases, which allows adhesive viscoelastic contacts to attain smaller intimate contact areas then one might expect from elastic short-range adhesive theory [335]. The difference between the obtained minimum contact area $(a_c)_{PO}$, and the short-range adhesive viscoelastic contact in the instantaneous limit, $(a_c)_{PO}^{JKR}$, increases with modulus ratio f_r. We thus find a vanishing contact area, $(\bar{a}_c)_{PO} \approx 0$, with retraction rates $\dot{\bar{w}}\times 10^7 = 6,\ 30$ and 60, and modulus ratio $f_r = 25$, which is indicated by a vertical pink ellipse in Fig. 5.7b.

The adhesive pull-off behaviour changes from short-range adhesion, to more rigid adhesive behaviour with modulus ratio f_r. This is in line with the observations by Müser and Persson [205] that an increase in instantaneous modulus, the pull-off transitions from crack-propagation to "*quasi-uniform*" bond breaking and the limit by Ciavarella *et al.* [339] at high retraction rates. However, we find that the presence of viscous dissipation governs the

effective range of adhesion, and in turn the contact area $(a_c)_{PO}$ at pull-off with a vanishing retraction rate and the smallest instantaneous Maugis parameter $\lambda_\infty = 1.5$ in this chapter as well. So the presence of viscous dissipation governs the observed range of adhesion for all retraction rates. To the best of our knowledge this has not been reported in literature before.

5.5.3 Work of Adhesion

When adhesion is short-range, the edge of contact is treated as a crack in an infinite elastic solid [194]. The works [229, 335, 336, 348] show that the solutions for a Mode I crack in an infinite viscoelastic solid, by Greenwood [334], and Persson and collaborators [217, 218], quantify the retraction of an adhesive, smooth Hertzian from a viscoelastic half-plane. We use our method, as championed in Van Dokkum *et al.* [335], to determine the effective work of adhesion $\Delta\gamma_{\text{eff}}$ during retraction. In Fig. 5.8, the effective work of adhesion $\Delta\gamma_{\text{eff}}$ is given as a function of the absolute contact area rate $\|\dot{\bar{a}}_c\|$, with the rate $\dot{\bar{a}}_c = \dot{a}_c\tau/\left(R^2\Delta\gamma_0/E_0^*\right)^{1/3}$. The

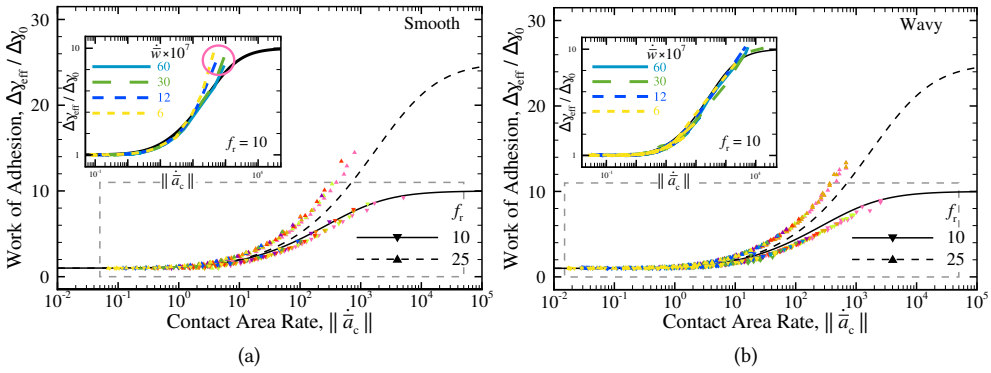

Figure 5.8: The scaled effective work of adhesion $\Delta\gamma_{\text{eff}}/\Delta\gamma_0$ as a function of the absolute contact area rate $\|\dot{\bar{a}}_c\|$ in (a) smooth ($\{\alpha,\beta\} = \{0,-\}$) and (b) wavy ($\{\alpha,\beta\} = \{1.47, 1.87\}$) contact with retraction rates $\dot{\bar{w}}\times10^4$=0.006, 0.012,0.03, 0.06, 0.012, 0.3, 0.6, 1.2 and 3, and modulus ratios $f_r = 10$ and 25. The black (dashed) lines indicate the solution by Persson and Brenner [217], with the solid's strength $\sigma_0 = \sigma_a$.

results in Fig. 5.8a correspond with smooth contact ($\{\alpha,\beta\} = \{0,-\}$) in Figs. 5.3a and b; and, the results in Fig. 5.8b with wavy contact ($\{\alpha,\beta\} = \{1.47, 1.87\}$) in Figs. 5.3c and d, without mechanical instabilities. The solid and dashed black lines indicate the solution by Persson and Brenner [217], with the solid's strength $\sigma_0 = \sigma_a$ and modulus ratios $f_r = 10$ and 25, respectively. Instead of the JKR solution [192], we use the solution by Guduru (5.5) for wavy contact, with effective modulus E_0^* as the reference solution [335]. Symbols are use for comparison purposes between smooth and wavy contact. Where in the latter case, the contact area velocity $\dot{a}_c$ oscillates (See Sec. 5.5.2). These symbols are limited to the "steady-state" period, that is independent of the initial contact, and sufficiently far from pull-off where the contact area decelerates, *i.e.* $\ddot{a}_c < 0$.

In smooth contact with modulus ratio $f_r = 10$, the numerical results align with the solution by Persson and Brenner [217], as we showed before [335]. With modulus ratio $f_r = 25$, the effective work of adhesion $\Delta\gamma_{\text{eff}}$ increases as a power-law with the absolute contact area rate $\|\dot{\bar{a}}_c\|$ as well. As expected, the effective work of adhesion $\Delta\gamma_{\text{eff}}$ tends to the instantaneous

work of adhesion $\Delta\gamma_\infty$ at high rates $10^4 < ||\dot{\bar{a}}||$. Notable is that these observations hold for wavy contact in Fig. 5.8b.

The inserts in Fig. 5.8 display the effective work of adhesion $\Delta\gamma_{\text{eff}}$ for the lowest loading rates $\dot{\bar{w}} \times 10^7 = 6,\ 12,\ 30$ and 60, and modulus ratio $f_r = 10$. The area of each insert is indicated by a light grey, dashed rectangle in their respective figure. Note that the transient up to pull-off is shown in the inserts in Fig. 5.8 but omitted from the main figure. In smooth contact, the load-area rate response is a monotonic increase in the contact area rate $||\dot{\bar{a}}_c||$ with decreasing load $\bar{w}$ till pull-off. In wavy contact, the load-area response alternate between: periods of increased area reduction rate, that correspond with the "damped" elastic mechanical instabilities of the elastic result; and, periods in which the contact area reduces in a slower manner. The oscillations in the contact area velocity $\dot{a}_c$ are readily inferred by one from Fig. 5.6a, noting that the retraction rate $\dot{\bar{w}}$ is constant for the given line colour. In wavy contacts, the acceleration in contact area reduction induces an increase in the effective work of adhesion $\Delta\gamma_{\text{eff}}$, which allows for a quasi-static stable contact to be attained and the elastic mechanical instability is avoided. This corresponds with the observations we make from Fig. 5.4b and c, which confirms the speculation by Ciavarella and Papangelo [223, 333] that viscoelasticity "effectively dampens" the elastic mechanical instabilities, at least at low retraction rates.

The effective work of adhesion at pull-off is highlighted by a pink circle in the insert in Fig. 5.8a, and the same instants are marked on the load-area in Fig. 5.7a, by a pink circle as well. The effective work of adhesion $\Delta\gamma_{\text{eff}}$ increases with the absolute contact area rate $||\dot{\bar{a}}_c||$ toward the instantaneous work of adhesion $\Delta\gamma_\infty$ in the inserts of Fig. 5.8, and even slightly surpass it. This confirms that mechanical instabilities, with vanishing retraction rate, are due to meeting the instantaneous limit in the contact's edges. The observed adhesive contact mechanics at pull-off are thus altered from static, elastic contact by viscous dissipation at low retraction rates, where the adhesive annulus now stiffens.

5.5.4 Pull-Off

A common way to assess how much waviness and viscoelasticity enhance hysteresis is to look at how the pull-off load increases [333]. In Fig. 5.9a, the scaled pull-off load $\bar{w}_{\text{PO}}/\bar{w}_{\text{PO}}^{\text{JKR}}$ is presented as a function of the retraction rate $\dot{\bar{w}}$, for normalised parameters $\{\alpha, \beta\} = \{0, -\}$ (*i.e.* smooth contact), and $\{1.46, 0.93\}$, $\{1.46, 1.87\}$, and $\{2.93, 1.87\}$ (*i.e.* wavy contacts); the pull-off loads are indicated with plus-shaped coloured markers; the relaxed limit is given by plus-shaped coloured markers as a reference and indicated by "El" as well; and, the solid coloured lines are guides to the eyes.

We consider first a smooth indenter (blue curve, with $\{\alpha, \beta\} = \{0, -\}$) and reproduce the JKR results in the relaxed limit. In the instantaneous limit, definition (5.6b) holds as well, provided that the work of adhesion is replaced by the instantaneous work of adhesion $\Delta\gamma_\infty$. Indeed, the load at pull-off $\bar{w}_{\text{PO}}$ is a power function of the retraction rate $\dot{\bar{w}}$ [205] and tends asymptotically to the expected value $\bar{w}_{\text{PO}} \sim f_r^{2/3} \bar{w}_{\text{PO}}^{\text{JKR}}$. For wavy contact, we see that the ratio $\bar{w}_{\text{PO}}/\bar{w}_{\text{PO}}^{\text{JKR}}$ increases even in the relaxed limit, consistent with the elastic results provided by Guduru [172], who shows that waviness enhances adhesion. An increase in normalised amplitude α increases the amplitude of the load-area curve and hence allows larger pull-off loads to be reached. An increase in normalised wavelength β has a similar but more moderate effect. When viscoelasticity is considered, a further increase in the pull-off load is observed.

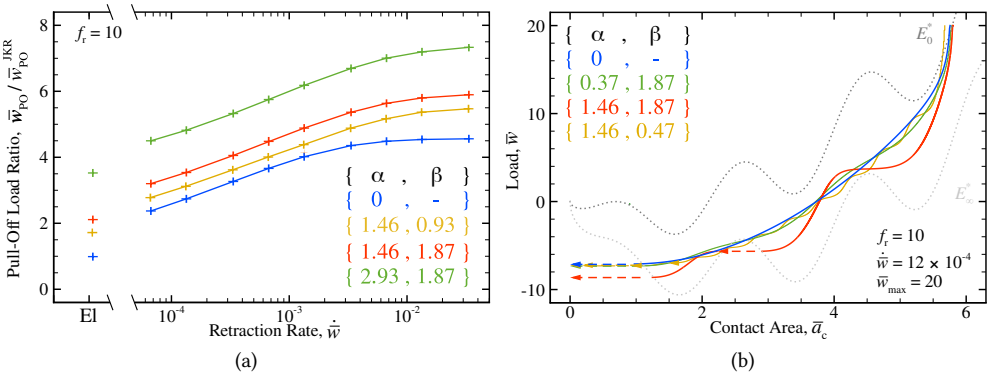

Figure 5.9: (a) The scaled, normalised pull-off load $\bar{w}_{PO}/\bar{w}_{PO}^{JKR}$ as a function of the retraction rate $\dot{\bar{w}}$ and (b) the normalised load $\bar{w}$ as a function of the normalised contact area $\bar{a}_c$ with retraction rate $\dot{\bar{w}} \times 10^4 = 12$ for the maximum load $\bar{w}_{max} = 20$, modulus ratio $f_r = 10$. The normalised parameters are (a) $\{\alpha, \beta\} = \{0, -\}$, $\{1.46, 0.93\}$, $\{1.46, 1.87\}$ and $\{2.93, 1.87\}$, and (b) $\{0, -\}$, $\{0.37, 1.87\}$, $\{1.46, 1.87\}$ and $\{1.46, 0.47\}$. In (a), the relaxed limit ($\dot{\bar{w}} \sim 0$) is indicated by plus-shaped coloured markers; in (b) the dotted, dark and light grey lines indicate the relaxed and instantaneous limits, respectively, with normalised amplitude $\alpha = 1.46$ and normalised wavelengths $\beta = 1.87$, and the coloured arrows indicate unstable jumps.

Viscous dissipation allows for attaining higher tensile loads than in elastic contact. So the pull-off force increases with viscous dissipation as well, which is as expected [205]. The effect of normalised amplitude α and wavelength β is analogous to that observed for elastic contact: the normalised amplitude α controls the amplitude of the load-area oscillations; and, the normalised wavelength β the wavelength of these load-area oscillations. This is by the same mechanism as in elastic contact, but now it is the increase in the instantaneous limit's load-area oscillations (See Sec. 5.3).

For all values of normalised amplitude α and normalised wavelength β, the load-rate curves shift to higher loads. Most notable is that the viscoelastic results in smooth contact, scaled with the increase in pull-off load in wavy elastic contact are close to the numerical results. For example, focusing on the results for normalised parameters $\{\alpha, \beta\} = \{2.93, 1.87\}$ and $\{1.46, 1.87\}$ indicated in red and green solid lines, respectively, we find that the increase in pull-off load $\bar{w}_{PO}$ compared with smooth contact ($\{\alpha, \beta\} = \{0, -\}$) is similar, in the presence, as in the absence of, viscous dissipation. This show that, as previously hypothesised by Ciavarella and Papangelo [333], the effects of waviness and viscoelasticity on pull-off appear nearly independent and additive, in short-ranged adhesive contact.

The effect of the normalised amplitude α and normalised wavelength β on the viscoelastic contact response is presented in Fig. 5.9b for retraction rate $\dot{\bar{w}} \times 10^{-4} = 12$ and normalised parameters $\{\alpha, \beta\} = \{0, -\}$, $\{0.37, 1.87\}$, $\{1.46, 1.87\}$ and $\{1.46, 0.47\}$. The differences between load-area curves are minimal for the given set of surface roughness parameters, when mechanical instabilities are absent, and they approach the response for smooth contact in blue as well. This thus supports the analytical results by Ciavarella and Papangelo [333] as well, where wavy contact approaches an equivalent smooth contact with retraction rate. We showed the local envelope of the given load-area curve reduces with a combined increase of retraction rate and modulus ratio in Sec. 5.5.2. So we suspect there are set

of roughness parameters where viscoelastic effects are much stronger, and the load-area curve approaches that of a give representative smooth contact with increased retraction rate and instantaneous modulus. Ciavarella and Papangelo [333] observe that viscoelasticity dominates over roughness in inducing dissipation during retraction as well. While the effect of waviness does not disappear herein, we show that its contribution to adhesive hysteresis seem additive. Hence, it is not far fetched to imagine a set of parameters where viscoelastic effects are much stronger (by considering larger values of modulus ratio $25 << f_r$ and small root-mean-square height roughness) and the load-area curve approaches that of a give representative smooth contact. However, this still has to be shown rigorously for realistic roughnesses [150], hence remains a challenge for the future.

5.6 Conclusions

In this chapter, we consider the adhesive hysteresis in soft matter contacts. The viscoelasticity is considered using the Zener model, and roughness is simplified to a single wavelength wave, superimposed on the profile of a rigid, cylindrical indenter. By studying the load-area curves during retraction of the indenter, we find, for the first time, that for low and moderate loading rates viscoelasticity "effectively dampens" the adiabatic mechanical instabilities caused by waviness. The results presented in this chapter show that both waviness and viscoelasticity increase the effective work of adhesion during retraction and hence adhesive hysteresis.

We make the following observations:

- viscous dissipation is the source of dissipation between the stable, static equilibria in adhesive, wavy viscoelastic contacts before pull-off;
- roughness-induced mechanical instabilities are absent for a given range of finite loading rates, and the wavy contact mechanics approaches that of an equivalent smooth contact with a combined increase in retraction rate and instantaneous modulus;
- roughness-induced mechanical instabilities reappear between stable, (quasi-)static equilibria when the contact stiffens to the instantaneous limit with acceleration of the edges of intimate contact.

These observations confirm the speculations by Ciavarella and Papangelo [223, 333] on the effect of viscous dissipation on wavy contact mechanics at least up to moderate retraction rates and short-range adhesion.

Our results demonstrate that, in general, two mechanisms of interfacial toughening are present: viscous and roughness-induced dissipation. The latter can be either in the form of a mechanical instability at high retraction rates or in the form of a fast quasi-static reduction of the contact area where the elastic mechanical instability is dampened. Whether the contact area reduction is very fast or occurs through an unstable mechanical jump, the result in terms of energy loss are similar when gauged by the addition of wavy elastic and smooth viscoelastic loads at pull-off. We, however, show that the effective work of adhesion $\Delta\gamma_{\text{eff}}$ tends towards the instantaneous work of adhesion $\Delta\gamma_\infty$ because mechanical instabilities only reappear when the instantaneous limit is traversed. Surprisingly, the pull-off loads are affected marginally by the instantaneous work of adhesion at pull-off for vanishing retraction rates, while the intimate contact area deviates noticeably from the smooth elastic contact. Both observations

on the load and area at pull-off coexist because of the rapid area reduction near pull-off whereby the load increases negligibly. So we conclude that viscoelasticity governs adhesive hysteresis, even in the presence of roughness-induced mechanical instabilities both in the relaxed and instantaneous loading limits. Our results are limited by the simplicity of the descriptions of viscoelastic substrate, adhesive interaction, surface roughness and loading conditions. Moreover, additional work is required to establish whether our conclusion extends to realistic rough contacts. However, one implication of this chapter is that for low loading rates, the origin of adhesive hysteresis, in existing, experimental results of soft matter contact, at least of patterned surfaces, might need to be reassessed. It remains up to future investigations to study the combination of realistic roughnesses and dissipation of the viscoelastic substrate.

6

On the Quasi-Static Response of a Base-Excited System subject to Static, Viscous and Dry Friction

Often the dynamic response of an engineering system subject to frictional dissipation is approximated by means of their quasi-static response. The validity of this approximation is here evaluated for the simple case of a base-excited single degree-of-freedom mass-spring-damper system with static and dry friction. To this end, the closed-form expression for its trajectory is contrasted with that obtained by neglecting inertia.

This chapter is based on the scientific article: Van Dokkum, J. S., On the Quasi-Static Response of a Base-Excited System with Static, Viscous and Dry Friction, (In preparation).

NOMENCLATURE

Variable	Definition	Dimension (mass M, length L and time t)
A & B	dimensionless amplitudes	–
c	viscous dissipation	Mt^{-1}
C	cosine	–
C_1, C_2 & C_3	integration constants	–
Ch	hyperbolic cosine	–
e	Euler's number	–
E	exponent	–
F_p	Coulomb friction force	MLt^{-2}
k	spring constant	Mt^{-2}
m	mass	M
N & M	system parameters	–
ω	frequency	t^{-1}
p	phase angle	–
P	dimensionless dissipation	–
r & q	normalised frequencies	–
S	sine	–
Sh	hyperbolic sine	–
t	time	t
T	dimensionless time	–
T_0	dimensionless period	–
x	mass trajectory	–
x'	mass displacement	L
X_0	dimensionless steady-state amplitude	–
X_d	dimensionless dissipative forces	–
X_f	dimensionless Coulomb friction force	–
X_v	dimensionless viscous force	–
y	base excitation	–
y'	base displacement	L
Y	excitation amplitude	L
z	damping ratio	–

6.1 INTRODUCTION

In this chapter, we consider a base-excited single degree-of-freedom mass-spring-damper system with Coulomb friction between the mass and a datum. The mass-spring system is practicable because it is the simplest system with just a single system parameter. However, it fails to track the dynamic response when a system is (near-)critically or over-damped. Den Hartog [349] presented the closed-form solution for the steady-state zero-stop response of a harmonically excited mass-spring system with Coulomb friction. They [349] show both theoretically and by experiment that, depending on system parameter, the mass moves continuously or comes to rest during parts of the oscillatory period. Hong and Liu [350] revisit aforementioned system, considering base-excitation, and obtain the dynamic response to simple harmonic loading. They [350] categorise the steady-state motions of the given

mass-spring system with zero to twelve stops. Papangelo and Ciavarella [234] neglect the inertia term in the equation of motion of the harmonically excited mass-spring system, and universally obtain two stops per oscillatory period. Their solution [234] thus does not correspond to any of the dynamic solutions towards the quasi-static loading limit. Still, the steady-state amplitude is non-trivially captured by their [234] static solution up to, but excluding frequencies when the dynamic solution is characterised by more than two stops per oscillatory period. Moreover, the solution under the static assumption (no inertia and no viscous damping) attains infinite acceleration when motion of the mass initiates, which is trivially unphysical. For an exhaustive comparison between the dynamic and (quasi-)static solution of a single degree-of-freedom mass-spring system, we refer to the work by Papangelo and Ciavarella [234] as well.

Levitan [351] analyses the mass-spring-damper system with harmonic base-excitation, including for the first time the Coulomb friction force, and assuming that viscous damping depends on the relative motion between the mass and the base. They [351] use a Fourier series approximation for the Coulomb friction force, which introduces a systematic error. The significance of base- *vs.* mass-excitation is that for (numerical) modelling efforts the trajectory of a mass is *a priori* unknown; only the excitation (alike base-excitation with viscous forces) are known. Hundal [352] considers a base-excited system with and without viscous damping, but now the static and dry friction forces oppose the relative motion between mass and a datum. This system where the trajectory of the mass is *a priori* unknown, *i.e.* base-excited with Coulomb friction between the mass and a datum, is most relevant in multi-scale modelling. They [352] give the closed-form solution for continuous motion of the mass and a semi-analytical solutions for two stops of finite duration per oscillatory period. The latter is known to occur for certain combinations of system parameters. Viscous dissipation is thus present while the mass is sessile and depends on the number of stops of finite duration per oscillatory period, which stands juxtaposed to mass-excitation where viscous forces are zero when the base and mass are at rest. Note that two stops or more stops of a finite duration are estimates because the trajectory, the number of stops per period and their duration differ and depend on system parameters, initial conditions and loading frequency. Papangelo and Ciavarella [234] show to solely have two stops per oscillatory period for finite Coulomb friction forces and significant damping [234]. The dynamic trajectory displays more than two stops per oscillatory period without significant damping. Moreover, the numerical dynamic solution is close to the static trajectory for viscous dissipation solely when critically damped. The number of stops per oscillatory period under the quasi-static assumption is not yet studied rigorously.

It is of interest to know for what viscous, static and dry-type friction forces the solution under quasi-static assumptions (qualitatively) approaches the dynamic solution in the limit of quasi-static loading, and for what loading frequencies with over-damped motion as well. Virtually all works subsequent to Hundal [352] solely solve the equation of motion numerically by means of a given time-marching scheme, *e.g.* [234, 353], or a piecewise analytical solution, *e.g.* [234, 354, 355]. A notable exception is the work by Lopéz *et al.* [356], who [356] consider excitation of the datum and under-damped motion of the mass. We are interested though in the closed-form analytical solutions for base-excitation with generic viscous damping. There is thus the need for an exact expression for the initial boundary conditions because numerical solutions are inexact for over-damped steady-state motion

with generic initial conditions. Hence we present a comprehensive set of (semi-)analytical solutions of dynamics and under the (quasi-)static assumption.

OUTLINE

In the present chapter, we consider a base-excited single degree-of-freedom mass-spring-damper system with Coulomb friction between the mass and a datum. We use the phase-plane method to obtain the steady-state response under the quasi-static assumption, which we call the quasi-static solution in the following. We revisit the continuous and two stop per period dynamic solutions by Hundal [352] and correct and simplify their phase-plane method. Their [352] cumbersome transition condition from continuous motion of the mass to one with two stops of finite duration per oscillatory period is refined. A numerical solver for piecewise ordinary differential equations in Mathematica [289] is used to verify the analytical results and the transition to more than two stops of finite duration per oscillatory period, whereof no analytical expressions exist in the presence of viscous dissipation.

We present quantitative comparisons between the quasi-static and the dynamic solution in frictional problems with viscous and Coulomb friction. The quantities under analysis are the steady-state amplitude, the phase shift, the phase-plane and the number of stops and dissipation per oscillatory period. When inertial forces are neglected, the estimate of two stops with finite duration per period is shown to hold for finite viscous and/or Coulomb friction forces. Towards the quasi-static loading limit, we show the quasi-static solution does approach the under-damped dynamic solution with viscous dissipation. Likewise, the quasi-static solution approaches the dynamic solution with Coulomb friction force, for a given over-damped system. We find that dissipation, and thus hysteresis and observed friction are underestimated for any finite excitation frequency under the quasi-static assumption.

6.2 PROBLEM DEFINITION

We consider the steady-state response of a single degree-of-freedom mass-spring-damper system with static and dry friction, and harmonic base-excitation $y' = Y\cos(\omega t + p)$, with excitation frequency ω. Here Y is the excitation amplitude and p an *a priori* unknown phase angle. A schematic representation of the system is given in Fig. 6.1. The equation of motion

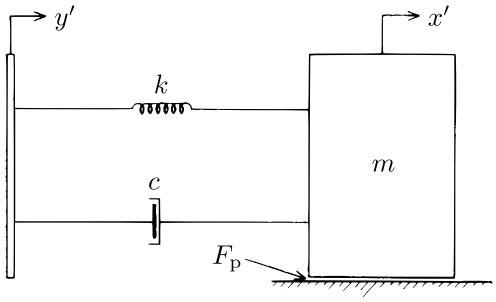

Figure 6.1: Schematic representation of a single degree-of-freedom mass-spring-damper system with static and dry friction forces F_p (Adapted from [352]).

reads

$$m\ddot{x}' + c\dot{x}' + kx' + F_{\mathrm{p}}\left(\dot{x}'\right) = c\dot{y}' + ky', \tag{6.1}$$

where m is the mass, c the viscous dissipation, k the spring constant and F_{p} the Coulomb friction force. When the mass is in motion $F_{\mathrm{p}}\left(\dot{x}'\right) \equiv F_{\mathrm{p}}\mathrm{Sgn}\left(\dot{x}'\right)$, with $\mathrm{Sgn}(\bullet) = -1$ and 1 for $\bullet < 0$ and $0 < \bullet$, respectively. When the mass is at rest and the applied force is insufficient to overcome static friction, the magnitude of the static friction force is given by

$$F_{\mathrm{p}}(0) = c\dot{y}' + k(y' - x'). \tag{6.2}$$

Here the static and dry friction forces have the same maximum magnitude, *i.e.* we model Coulomb friction. We now rewrite Eq. (6.1) in a non-dimensional form, *i.e.*

$$\ddot{x} + 2z\dot{x} + x + X_{\mathrm{f}}(\dot{x}) = \cos(rT + p) - 2rz\sin(rT + p), \tag{6.3}$$

with dimensionless time, normalised amplitude, dimensionless Coulomb friction force and normalised frequency

$$T \equiv \omega_{\mathrm{n}} t; \qquad x = \frac{x'}{Y}; \qquad X_{\mathrm{f}}(\dot{x}) \equiv \frac{F_{\mathrm{p}}\left(\dot{x}'\right)}{kY}; \quad \text{and,} \qquad r \equiv \frac{\omega}{\omega_{\mathrm{n}}}, \tag{6.4}$$

where

$$\omega_{\mathrm{n}} \equiv \sqrt{\frac{k}{m}}; \quad \text{and,} \quad z \equiv \frac{c}{2\sqrt{km}}, \tag{6.5}$$

are the natural frequency and the damping ratio, respectively. We hypothesise that the mass is in motion for $0 \leq T < T_0$, and at rest for $T_0 \leq T < \pi/r$. Hence during $0 < T < T_0$, the system is described by Eq. (6.3), and in the remainder

$$X_{\mathrm{f}}(\dot{x} \to 0) = \cos(rT + p) - 2rz\sin(rT + p) - x. \tag{6.6}$$

When $\dot{x} \leq 0$, the equation of motion (6.3) becomes

$$\ddot{x} + 2z\dot{x} + x = X_{\mathrm{f}} + \cos(rT + p) - 2rz\sin(rT + p), \tag{6.7}$$

and the general solution is

$$x = e^{-Tz}(C_1\cosh(qT) + C_2\sinh(qT)) + X_{\mathrm{f}} + A_{\mathrm{s}}\sin(rT + p) + A_{\mathrm{c}}\cos(rT + p), \tag{6.8}$$

with parameters

$$q = \sqrt{z^2 - 1}; \qquad A_{\mathrm{s}} = \frac{2r^3 z}{1 - 2r^2 + r^4 + 4r^2 z^2}; \quad \text{and,} \quad A_{\mathrm{c}} = \frac{\left(1 - r^2 + 4r^2 z^2\right)}{1 - 2r^2 + r^4 + 4r^2 z^2}, \tag{6.9}$$

where C_1 and C_2 are integration constants. The last two terms on the right-hand-side of Eq. (6.8) represent the steady-state harmonic response of the system in the absence of Coulomb friction, with the square steady-state amplitude:

$$A^2 \equiv A_{\mathrm{s}}^2 + A_{\mathrm{c}}^2 = \frac{1 + (2zr)^2}{\left(1 - r^2\right)^2 + (2zr)^2}. \tag{6.10}$$

The imposed boundary conditions are

$$x(0) = X_0, \quad \text{and} \quad \dot{x}(0) = 0; \tag{6.11a}$$

and,

$$x(T_0) = -X_0, \quad \text{and} \quad \dot{x}(T_0) = 0, \tag{6.11b}$$

where X_0 is the dimensionless steady-state amplitude. Together with the dimensionless period T_0 this allows one to satisfy the latter boundary conditions. The phase angle p thus is the phase shift between the base-excitation and the trajectory of the mass, the dependent variable, and is fully defined by the steady-state amplitude X_0 and the dimensionless period T_0. *Vice versa*, it is trivial that the dimensionless steady-state amplitude X_0 and dimensionless period T_0 are independent of the phase angle p that one excites the base with. In case of continuous motion the mass reverses its direction of motion in the limit $T_0 \sim \pi/r$. This is in line with the estimates by Den Hartog [349] when viscous dissipation is absent and Hundal [352], who includes viscous dissipation. We are aware of the potential emergence of different dynamic steady-state solutions or non-periodic solutions beyond the boundary conditions (6.11). The numerical approach in the present work does allow one to explore them. However, such solutions are not explored because they are beyond the scope of this work, *i.e.* highlighting differences between the dynamic and the quasi-static solution.

6.3 Quasi-Static Solution

We follow the same approach as outlined by Hundal [352] for the dynamic solution, but now apply it with the quasi-static approximation, by neglecting acceleration. The equation of motion (6.7) for $0 \leq T < T_0$ becomes

$$2z\dot{x} + x = X_\mathrm{f} - 2rz\sin(rT + p) + \cos(rT + p), \tag{6.12}$$

with the general solution

$$x = C_3 e^{-T/(2z)} + X_\mathrm{f} + \cos(rT + p), \tag{6.13}$$

where C_3 is an integration constant as well. In the absence of static and dry-friction, the mass is in continuous motion. When the static friction force $F_\mathrm{p} \geq kY$, the mass is sessile. The interesting cases fort the current analysis are those where the Coulomb friction force $0 < F_\mathrm{p} < kY$, thus the range $0 \leq X_\mathrm{f} \leq 1$ of dimensionless static and dry-friction forces. We consider the range $0 \leq X_\mathrm{f} \leq 1$, where the limiting cases are those of continuous motion and mass at rest.

6.3.1 Static Solution: without viscous dissipation

Taking the damping ratio as $z = 0$ in Eq. (6.12), and substituting the boundary condition (6.11a), we find the phase angle

$$\cos(p) = X_0 - X_\mathrm{f}, \tag{6.14}$$

which is equivalent to the force balance at $T = 0$. By substituting the phase angle p, applying the boundary conditions (6.11b) and rearranging the results as trigonometric functions of phase angle p, we obtain

$$A_{11}\sin(p) + A_{12}\cos(p) = B_1; \quad \text{and,} \quad A_{21}\sin(p) + A_{22}\cos(p) = B_2, \tag{6.15}$$

with

$$A_{11} = \mathrm{S}_{r0}; \qquad A_{12} = -\mathrm{C}_{r0}; \qquad B_1 = X_0 + X_\mathrm{f}; \tag{6.16a}$$

$$A_{21} = \mathrm{C}_{r0}; \qquad A_{22} = S_0; \qquad B_2 = 0, \tag{6.16b}$$

where $\mathrm{S}_{r0} \equiv \sin(rT_0)$ and $\mathrm{C}_{r0} \equiv \cos(rT_0)$. By virtue of the Pythagorean identity (*i.e.* $\sin(\bullet)^2 + \cos(\bullet)^2 = 1$, with scalar $\bullet$), we obtain the closed-form expression for the amplitude $X_0 = 1 - X_\mathrm{f}$; and, using boundary conditions (6.11b), we find the dimensionless time

$$\cos(rT_0) = 2X_\mathrm{f} - 1. \tag{6.17}$$

These results (6.14) and (6.17) are equivalent to those obtained by Papangelo and Ciavarella [234] for a system with solely Coulomb friction. We use them to normalise our results and initiate semi-analytical solutions in the following as well.

6.3.2 Continuous Motion

Taking the damping ratio $z > 0$; substituting the boundary conditions (6.11) with half the oscillatory period $T_0 = \pi/r$ in the general solution (6.13); and, rearranging the results as trigonometric functions of phase angle p, we obtain two equations in the form of Eq. (6.15) with

$$A_{11} = 0; \qquad A_{12} = 1; \qquad B_1 = X_0 + \left(\frac{2}{E'+1} - 1\right) X_\mathrm{f}; \tag{6.18a}$$

$$A_{21} = \frac{2rz}{E'}; \qquad A_{22} = 1; \qquad B_2 = X_0 - X_\mathrm{f}, \tag{6.18b}$$

where the exponent $E' \equiv e^{-\frac{\pi}{2rz}}$. The closed-form expression of the dimensionless steady-state amplitude thus is

$$X_0 = \sqrt{1 - \left(\frac{E' X_\mathrm{f}}{rz(1+E')}\right)^2} - \frac{X_\mathrm{f}}{1 + \dfrac{2E'}{(1-E')}}, \tag{6.19}$$

and the phase angle,

$$\cos(p) = \sqrt{1 - \left(\frac{E' X_\mathrm{f}}{rz(1+E')}\right)^2}. \tag{6.20}$$

6.3.3 Two Stops per Period

The force balances at dimensionless times $T = 0$ and $T = T_0$ are

$$X_0 = \cos(p) - 2rz\sin(p) + X_\mathrm{f}, \tag{6.21a}$$

and

$$X_0 = 2rz\sin(rT_0 + p) - \cos(rT_0 + p) - X_\mathrm{f}, \tag{6.21b}$$

respectively. Rearranging Eq. (6.21) as trigonometric functions of p, we obtain the two equations in the form of Eq. (6.15) with

$$A_{11} = -2rz; \qquad A_{12} = 1; \qquad B_1 = X_0 - X_\mathrm{f}; \tag{6.22a}$$

$$A_{21} = 2rz\mathrm{C}_{r0} + \mathrm{S}_{r0}; \qquad A_{22} = 2rz\mathrm{S}_{r0} - \mathrm{C}_{r0}; \qquad B_2 = X_0 + X_\mathrm{f}. \tag{6.22b}$$

Note that Eqs. (6.21a) holds for two stops per period in the dynamic case as well. The square steady-state amplitude thus is

$$X_0^2 = \mathrm{S}_{r0}^2 \left(\frac{2r^2 z^2}{1+\mathrm{C}_{r0}} - \frac{1+\mathrm{C}_{r0}-2X_\mathrm{f}^2}{2\left(1+\mathrm{C}_{r0}\right)^2} \right). \tag{6.23}$$

The amplitude is a function of the system parameters, r, z and X_f, and the unknown dimensionless period T_0. It is intuitive that the steady-state amplitude is independent of the phase angle p. Hence we only need to find the dimensionless period T_0 that satisfies Eq. (6.11).

Substituting the boundary conditions (6.11) in the general solution (6.8); and, after rearranging the results as trigonometric functions of phase angle p, we obtain two equations in the form of Eq. (6.15) with

$$A_{11} = 2rz\left(1+E_0'\right)+\mathrm{S}_{r0}; \qquad A_{12} = -(1+\mathrm{C}_{r0}); \qquad B_1 = 2X_\mathrm{f}; \tag{6.24a}$$

$$A_{21} = \mathrm{C}_{r0}-E_0'; \qquad A_{22} = \mathrm{S}_{r0}; \qquad B_2 = 0, \tag{6.24b}$$

where $E_0' \equiv e^{-\frac{T_0}{2z}}$. We reduce Eq. (6.15) to a single equality of the unknown dimensionless period T_0, *i.e.*

$$\frac{\left(\left(1+\mathrm{C}_{r0}\right)\left(E_0'-1\right)-2rz\left(1+E_0'\right)\mathrm{S}_{r0}\right)^2}{1+\left(E_0'\right)^2-2E_0'\mathrm{C}_{r0}} = 4X_\mathrm{f}^2, \tag{6.25}$$

and the phase shift is

$$\cos(p) = \frac{2\left(\mathrm{C}_{r0}-E_0'\right)X_\mathrm{f}}{\left(1+\mathrm{C}_{r0}\right)\left(E_0'-1\right)-2rz\left(1+E_0'\right)\mathrm{S}_{r0}}. \tag{6.26}$$

Equation (6.25) is solved numerically for the unknown dimensionless period T_0, which is then substituted in Eqs. (6.23) and (6.26), to obtain the dimensionless steady-state amplitude X_0 and phase shift p, respectively.

Limit of Continuous Motion: substituting the results (6.19) and (6.20) in Eq. (6.13); taking the derivative with respect to time t; and, using the boundary conditions (6.11), we obtain two equalities that are only satisfied in the limits $z \sim \infty$ and/or $X_\mathrm{f} \sim 0$. The solution for continuous motion thus is solely valid for a rigid connection between base and mass, and/or in the absence of Coulomb friction. The number of stops per oscillatory period is thus limited to a maximum of two under the quasi-static assumption. This is why we limit the dynamic solutions to at most two stops per oscillatory period in the following as well.

6.4 Dynamic Solution

We follow the approach as outlined by Hundal [352] for the dynamic solution as well.

6.4.1 Continuous Motion

We apply the boundary conditions (6.11) with half the oscillatory period, $T_0 = \pi/r$, to the general solution (6.8), and rearranging the results as trigonometric functions of phase angle p,

we obtain two equations in the form of Eq. (6.15) with

$$A_{11} = A_\mathrm{s} - rA_\mathrm{c}\frac{\mathrm{Sh}_q}{K}; \quad A_{12} = A_\mathrm{c} + rA_\mathrm{s}\frac{\mathrm{Sh}_q}{K}; \quad B_1 = X_0 + X_\mathrm{f}\left(\frac{2q}{EK} - 1\right); \tag{6.27a}$$

$$A_{21} = A_\mathrm{s} - rA_\mathrm{c}\left(2z - \frac{K}{\mathrm{Sh}_q}\right); \quad A_{22} = A_\mathrm{c} + rA_\mathrm{s}\left(2z - \frac{K}{\mathrm{Sh}_q}\right); \quad B_2 = X_0 - X_\mathrm{f}, \tag{6.27b}$$

with

$$K \equiv z\mathrm{Sh}_q + q\mathrm{Ch}_q + qE^{-1}, \tag{6.27c}$$

where $\mathrm{Sh}_q \equiv \sinh\left(\frac{\pi q}{r}\right)$, $\mathrm{Ch}_q \equiv \cosh\left(\frac{\pi q}{r}\right)$ and $E \equiv e^{-\frac{\pi z}{r}}$. The closed-form expression of the amplitude is

$$X_0 = \sqrt{A^2 - N^2X_\mathrm{f}^2} - MX_\mathrm{f}, \tag{6.28}$$

with the two system parameters:

$$M \equiv \frac{1 - E^2 - 2zq^{-1}E\mathrm{Sh}_q}{1 + E^2 + 2E\mathrm{Ch}_q}; \quad \text{and,} \quad N \equiv \frac{2q^{-1}r^{-1}E\mathrm{Sh}_q}{1 + E^2 + 2E\mathrm{Ch}_q}. \tag{6.29}$$

Equation (6.29) is equivalent to the result Hundal [352] obtains, and corresponds to his figure 5 on page 376 in print, though equation (14) on page 374 erroneously omits the addition of EC_q in the denominator of M. The phase shift is

$$\cos(p) = \frac{A_\mathrm{s}X_\mathrm{f}}{A^2}N + A_\mathrm{c}\sqrt{\frac{1}{A^2} - N^2\frac{X_\mathrm{f}^2}{A^4}}. \tag{6.30}$$

6.4.2 Two Stops per Period

Combining the boundary conditions (6.11) and the force balance (6.21a), we substitute the results in the general solution (6.8). Subsequently, rearranging the results as trigonometric functions of phase angle p, we obtain two equations in the form of Eq. (6.15) with

$$\begin{aligned}
A_{11} &= A_\mathrm{s}C_{r0} - A_\mathrm{c}S_r - 2rz - (A_\mathrm{s} + 2rz)E_0\mathrm{Ch}_{q0} + \left(rA_\mathrm{c} - zA_\mathrm{s} - 2rz^2\right)q^{-1}E_0\mathrm{Sh}_q;\\
A_{12} &= 1 + A_\mathrm{c}C_r + A_\mathrm{s}S_r + (1 - A_\mathrm{c})E_0\mathrm{Ch}_q + (z - rA_\mathrm{s} - zA_\mathrm{c})q^{-1}E_0\mathrm{Sh}_{q0};\\
B_1 &= -2X_\mathrm{f};
\end{aligned} \tag{6.31a}$$

$$\begin{aligned}
A_{21} &= A_\mathrm{c}q\mathrm{Ch}_{q0} + (A_\mathrm{s} - rzA_\mathrm{c} + 2rz)r^{-1}\mathrm{Sh}_{q0} - (A_\mathrm{c}C_{r0} + A_\mathrm{s}S_{r0})E_0^{-1}q\\
A_{22} &= (A_\mathrm{c} + rzA_\mathrm{s} - 1)r^{-1}\mathrm{Sh}_{q0} - qA_\mathrm{s}\mathrm{Ch}_{q0} + (A_\mathrm{s}C_{r0} - A_\mathrm{c}S_{r0})E_0^{-1}q;\\
B_2 &= 0,
\end{aligned} \tag{6.31b}$$

where $\mathrm{Sh}_{q0} \equiv \sinh(qT_0)$, $\mathrm{Ch}_{q0} \equiv \cosh(qT_0)$ and $E_0 \equiv e^{-zT_0}$.

Equalities (6.15) are solved numerically for the unknown dimensionless period T_0 and phase angle p by Hundal [352]. No one reproduced his method, to the best of our knowledge, because the steady-state response must be independent of phase angle p via the phase-plane method. *Vice versa*, phase shift p is uniquely defined by the period T_0. With the Pythagorean identity though, we reduce Eq. (6.15) to a single equality with the unknown dimensionless period T_0 as a function of the system parameters, r, z and X_f. This equality is solved

numerically. From Eq. (6.15), the phase shift is

$$\sin(p) = \frac{2A_{22}X_f}{A_{12}A_{21} - A_{11}A_{22}}; \quad \text{and,} \quad \cos(p) = -\frac{2A_{21}X_f}{A_{12}A_{21} - A_{11}A_{22}}, \tag{6.32}$$

and after Eq. (6.21a), the amplitude X_0 is given by

$$X_0 = \left(1 - \frac{2A_{21}}{A_{12}A_{21} - A_{11}A_{22}} - \frac{4rzA_{22}}{A_{12}A_{21} - A_{11}A_{22}}\right) X_f, \tag{6.33}$$

and is obtained with the then known period T_0.

Limit of Continuous Motion: the limit $T_0 \to \pi/r$ marks the transition from two stops of finite duration per period (*i.e.* $T_0 < \pi/r$) to continuous motion with half the oscillatory period. The transition is thus uniquely defined by the frequency r for system parameters z and X_f, and period $T_0 = \pi/2$. We equate the cosines transforms of the phase shift p in Eq. (6.30) and (6.32), and find the dimensionless boundary frequency $r_{2\to0}$ by means of numerical root-finding. Aforementioned methodology removes the need of differentiation of the general solution (6.8), and the numerical solution of both period T_0 and phase shift p [352].

6.5 Results and Discussion

In Fig. 6.2, the dimensionless steady-state amplitude X_0 is presented as a function of the dimensionless excitation frequency r for damping ratios $z = 1/10,\ 1/5,\ 3/10,\ 2/5$ and $1/2$, and dimensionless Coulomb friction forces $X_f = 0,\ 1/5,\ 2/5,\ 3/5,\ 4/5$ and 1, after Fig. 5 on page 376 by Hundal [352]. The dynamic results are indicated by solid and dashed, and quasi-static results by dashed-dotted lines. The solid lines indicate continuous motion, while the dashed(-dotted) lines indicate two stops of finite duration per oscillatory period. The (dashed-dotted) black lines indicate the results in absence of Coulomb friction, *i.e.* $X_f = 0$. The black dashed-dotted line under the quasi-static assumption is the exception and corresponds with continuous motion (See Sec. 6.4.2). In the absence of Coulomb friction, dynamic motion is continuous as well.

As expected, our dynamic results correspond to those by Hundal [352]. For finite Coulomb friction, the trajectory transitions from two stops per period to continuous motion with increased dimensionless excitation frequency r, which is indicated with a light grey dotted line in Fig. 6.2. At low dimensionless frequencies $r < 0.3$ and damping ratios $z < 1/2$ more than two stops per oscillatory period occur. The minimum dimensionless boundary frequency $r_{\bullet\to2}$ by which the numerical root search of T_0 converges are indicated with coloured crosses in Fig. 6.2. The (maximum) dynamic amplitude(s) for more than two stops per oscillatory period are not depicted in Fig. 6.2.

Under the quasi-static assumption, resonance around the natural frequency, $r \sim 1$, is absent and the dimensionless steady-state amplitude $X_0 \leq 1$. The dimensionless steady-state amplitude is zero when the Coulomb friction force is greater than the applied force, $\sqrt{1+(2zr)^2} \leq X_f$ [352] with inertia; and, under the quasi-static assumption, the steady-state amplitude is zero when $1 \leq X_f$. The quasi-static results for $X_f = 1$ are depicted in Fig. 6.2 by orange coloured dashed-dotted lines with the dimensionless amplitude $X_0 = 0$. Towards the quasi-static loading limit, the quasi-static dimensionless steady-state amplitude X_0 approaches the dynamic solution with damping ratios z and dimensionless Coulomb friction force X_f.

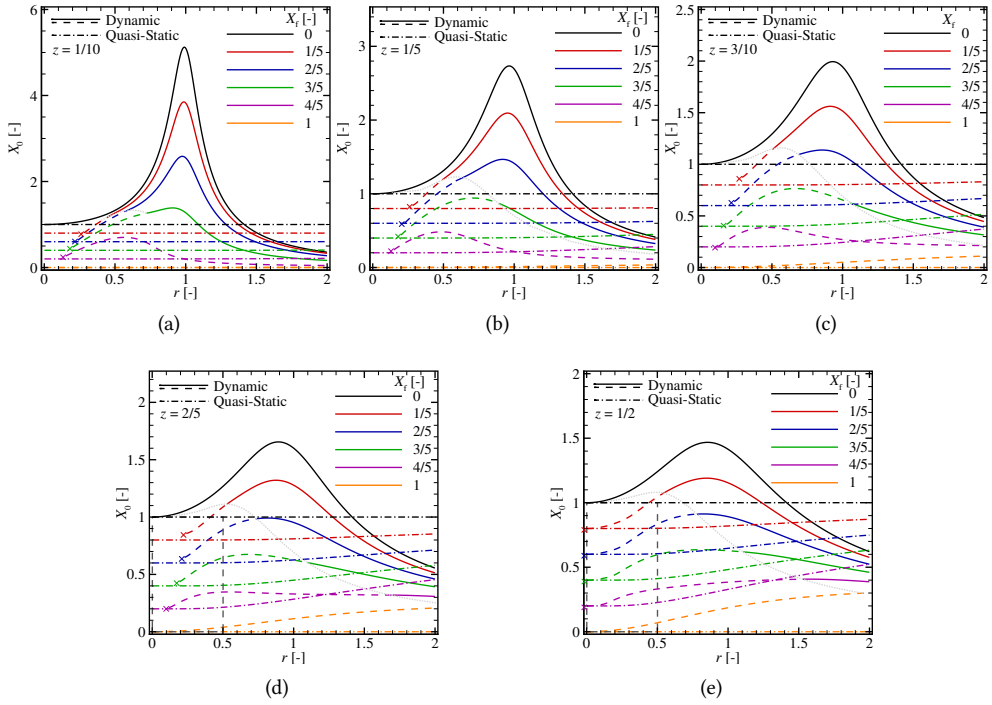

Figure 6.2: The dimensionless steady-state amplitude X_0 as a function of the dimensionless excitation frequency r for damping ratios (a) $z = 1/10$, (b) $1/5$, (c) $3/10$, (d) $2/5$ and (e) $1/2$, with dimensionless Coulomb friction forces $X_f = 0$, $1/5$, $2/5$, $3/5$, $4/5$ and 1. The solid lines indicate continuous motion and the dashed(-dotted) lines two stops of finite duration per oscillatory period, except for Coulomb friction force $X_f = 0$. The coloured crosses indicate the dimensionless boundary frequency $r_{\bullet\to 2}$.

It is of interest to investigate the differences on the phase-plane as well. The dimensionless amplitudes X_0 under the quasi-static assumption approaches the dynamic result with dimensionless Coulomb friction force X_f. The same does not necessarily hold for the velocity $\partial x'/\partial t$ though. We inspect the dimensionless boundary frequency $r_{\bullet\to 2}$, where the trajectory changes from multiple stops (indicated with $\bullet$) to two stops of finite duration per oscillatory period in accordance with results by the semi-analytical and our numerical method. The method whereby the numerical results are obtained is given in Appendix E.

In Fig. 6.3, the dimensionless velocity $\partial x/\partial T$ is presented as a function of the dimensionless trajectory x for damping ratios $z = 1/10$, $1/5$, $3/10$, $2/5$ and $1/2$, and dimensionless Coulomb friction forces $X_f = 1/5$, $2/5$, $3/5$ and $4/5$, with dimensionless excitation frequency $r = r_{\bullet\to 2}$. The dimensionless boundary frequencies $r_{\bullet\to 2}$ are indicated by coloured crosses in Fig. 6.2. We elect to only present the top half of the phase-plane, *i.e.* motion in the positive direction from the negative steady-state amplitude $-X_0$, exploiting the point symmetry around the origin of the phase-plane. Patterns and line colours are consistent with those in Fig. 6.2. Results without Coulomb friction force are omitted because these are represented by circles on the phase-plane. Numerical results are added and indicated

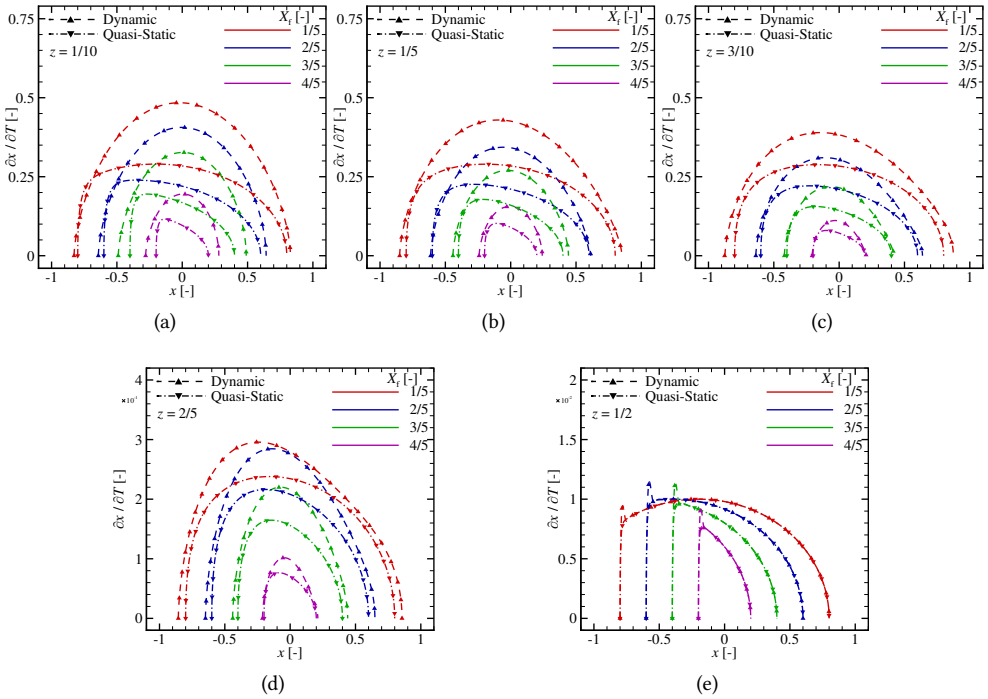

Figure 6.3: The dimensionless velocity $\partial x/\partial T$ at the dimensionless excitation frequency $r_{\bullet\to 2}$ (depicted by same coloured crosses in Fig. 6.2) is presented as a function of the dimensionless trajectory x for damping ratios (a) $z = 1/10$, (b) $1/5$, (c) $3/10$, (d) $2/5$ and (e) $1/2$, with dimensionless Coulomb friction forces $X_f = 1/5$, $2/5$, $3/5$ and $4/5$.

by coloured triangle and gradient symbols, which correspond with the dynamic and the quasi-static solution, respectively. This shows that our analytical results are physical, *e.g.* not a numerical artefact of the root-finding algorithm [289], and thus a trajectory with two stops of finite duration per oscillatory period is correct.

Even thought the steady-state amplitude approaches the quasi-static amplitude with damping ratio $z < 1/2$ and dimensionless Coulomb friction force X_f, velocity and trajectory remain distinctly different. The velocity, and in turn the trajectory, of the solution under the quasi-static assumption and dynamic solution differ up to a factor of two. For increasing damping ratio the agreement between dynamic and quasi-static solutions improve; for $1/2 \leq z$, the velocity and trajectory coincide, except a minor oscillation of the dynamic results after motion of the mass initiates, which is obviously absent from the quasi-static solution.

The present analytical results are in agreement with our numerical method, and present method reproduces the semi-analytical results as presented by Hundal in his seminal work [352]. Our analytical results are obtained more readily compared to the numerical piece-wise solution and the original semi-analytical solution [352] though. Notable is that damping ratios above $1/2 \leq z$ are difficult to achieve experimentally [356], which severely limits the validity and use of the quasi-static assumption in most physical problems even with viscous damping

towards the quasi-static loading limit.

6.5.1 Quasi-Static Loading Limit

In order to investigate whether the dynamic solution in the quasi-static loading limit is the same as the quasi-static solution, we plot the scaled dimensionless amplitude $(X_0-(1-X_f))/(1-X_f)$, combining the dynamic results for damping ratios $z=2/5$, $1/2$ and $3/4$, and solely up to half the natural frequency $r\leq 1/2$, in Fig. 6.4a. The converged numerical result for the smallest

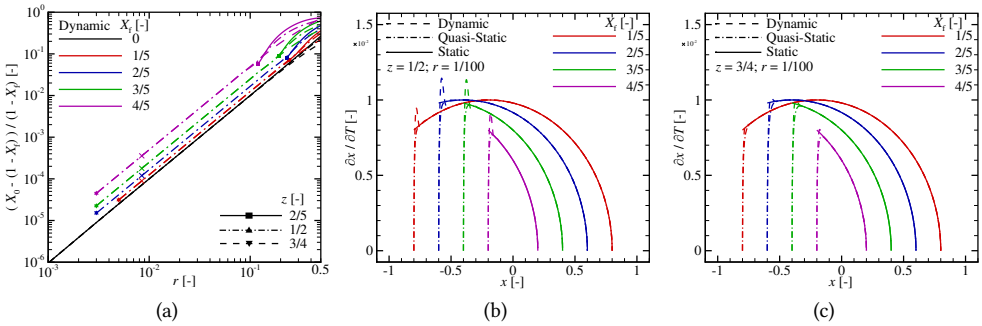

Figure 6.4: (a) Log-Log plot of the scaled dimensionless amplitude $(X_0-(1-X_f))/(1-X_f)$ as a function of the dimensionless excitation frequency r for damping ratios $z=2/5$, $1/2$ and $3/4$, with dimensionless Coulomb friction forces $X_f=0$, $1/5$, $2/5$, $3/5$ and $4/5$. (b-c) The dimensionless velocity $\partial x/\partial T$ is presented as a function of the dimensionless trajectory x for damping ratios (b) $z=1/2$ and (c) $3/4$, with dimensionless excitation frequency $r=1/100$ that is indicated by coloured crosses in (a).

dimensionless excitation frequency $r\approx 2\times 10^{-3}$ (by numerical root-finding) are indicated with a square, triangle and delta symbol for damping ratios $z=2/5$, $1/2$ and $3/4$, respectively. The solid, dashed-dotted and dashed line correspond with damping ratios $z=4/5$, $1/2$ and $3/4$ as well. The dashed and dash-dotted lines for the damping ratios $z=1/2$ and $3/4$ cover each other for the majority of the dimensionless excitation frequency range $r\lessapprox 10^{-1}$. The quasi-static results are omitted because it is trivial that the static equals the quasi-static amplitude in the quasi-static loading limit *i.e.* $X_0\sim(1-X_f)$. The area of Fig. 6.4a is indicated with dashed dark-grey rectangles in Figs. 6.2d and 6.2e, and in Fig. 6.5a of the dimensionless steady-state amplitude X_0 as a function of the dimensionless frequency r and damping ratio $z=3/4$.

In Figs. 6.4b and 6.4c, the dimensionless velocity $\partial x/\partial T$ is presented as a function of the dimensionless trajectory x for damping ratios $z=1/2$ and $3/4$, respectively, with dimensionless Coulomb friction forces $X_f=1/5$, $2/5$, $3/5$ and $4/5$, for the quasi-static loading frequency $r=1/100$. The dashed and dashed-dotted lines indicate the dynamic and quasi-static solution, respectively, which coincide for nearly the whole phase-plane. The solid line indicates the static solution and covers the dashed(-dotted) lines over its whole phase-plane. Moreover, the line colours and the patterns correspond to those in Figs. 6.2 and 6.4a, respectively, where the loading frequency $r\approx 1/100$ is indicated with coloured crosses in the latter figure.

The minor oscillation of the dynamic results, after the motion of the mass initiates, decreases with increased damping ratio z. This oscillation is absent from the solution

under quasi-static assumptions. Hence coincidence between velocity and trajectory of dynamic, quasi-static and static solution increases with damping ratio z as well. The static solution attains infinite acceleration when motion of the mass initiates and thus is unphysical. Contrarily, in the presence of finite viscous damping with damping ratio $1/2 \leq z$, acceleration is finite and captured by the quasi-static solution. Apart from aforementioned differences, the dynamic, quasi-static and static solution coincide over the majority of the phase-plane. The trajectory of damped dynamic motion is closely approached by the quasi-static solution with damping ratio $1/2 \leq z$ and finite dimensionless Coulomb friction forces $0 \leq X_f < 1$ in the (quasi-)static loading limit.

6.5.2 Damped Motion

The system parameter space is vast with dimensionless Coulomb friction force $0 \leq X_f \leq \sqrt{1+(2zr)^2}$ for damping ratio $0 \leq z$ and dimensionless frequency $0 \lesssim r$. We are interested in (near-)critically and over-damped motion, wherefore we consider damping ratios $z = 3/4,\ \sim 1,\ 5/4,\ 3/2$ and $7/4$ in the following. The present solutions in Secs. 6.3 and 6.4 are valid for all system parameters which lead to at most two stops of finite duration per oscillatory period. While Hundal [352] focuses on cases where damping ratio $z \leq 1/2$, here we extend our study to larger damping ratios because the quasi-static assumption is used for (near) over-damped engineering problems as well.

In Fig. 6.5, the dimensionless amplitude X_0 is presented as a function of the dimensionless excitation frequency r for large damping ratios, namely $z = 3/4, \sim 1, 5/4, 3/2$ and $7/4$. We choose throughout the present work $X_f = 99/100$ for the semi-analytical quasi-static solution, that we indicate with dimensionless Coulomb friction force $X_f \sim 1$, while the dynamic results retain the dimensionless Coulomb friction force of unity. The quasi-static result for Coulomb friction $X_f \sim 1$ is indicated with a dark-grey dashed-dotted line in Fig. 6.5.

As expected, the dimensionless amplitude X_0 obtained with the quasi-static solution approximates the dynamic solution with viscous damping ratio $1 < z$ (*i.e.* over-damped motion). Unexpectedly, the same holds with increased Coulomb friction force X_f, for under-damped motion (*e.g.*, $z = 3/4$ and $X_f \sim 1$), which is non-trivial. The quasi-static solution approaches the dynamic trajectory qualitatively and dimensionless amplitude X_0 quantitatively for a given over-damped system and with increased Coulomb friction force $X_f \lesssim 1$. Dynamic motion changes qualitatively with excitation frequency r; the amplitude decreases with increased excitation frequency, and dynamic motion is continuous around and above the natural frequency $r \lessapprox 1$. This dimensionless boundary frequency $r_{2\to 0}$ is indicated with coloured crosses in Fig. 6.5.

In Fig. 6.6, the normalised phase shift p/π between base- and mass-trajectory is presented as a function of the dimensionless excitation frequency r for damping ratios $z = 1/2, \sim 1$ and $3/2$. The choice of pattern and line colour corresponds to those in Figs. 6.2 and 6.5. The quasi-static result for Coulomb friction $X_f \sim 1$ is indicated with a dark-grey dashed-dotted line as well.

The observations made with Fig. 6.5 on the steady-state dimensionless amplitudes X_0 hold for the phase shift p as well. The quantitative differences in phase shift p between the quasi-static and the dynamic solution, at and above the natural frequency, are more pronounced than the differences in the dimensionless steady-state amplitudes X_0 in Figs. 6.2 and 6.5 though. The dynamic solution approaches free oscillation when the phase shift p

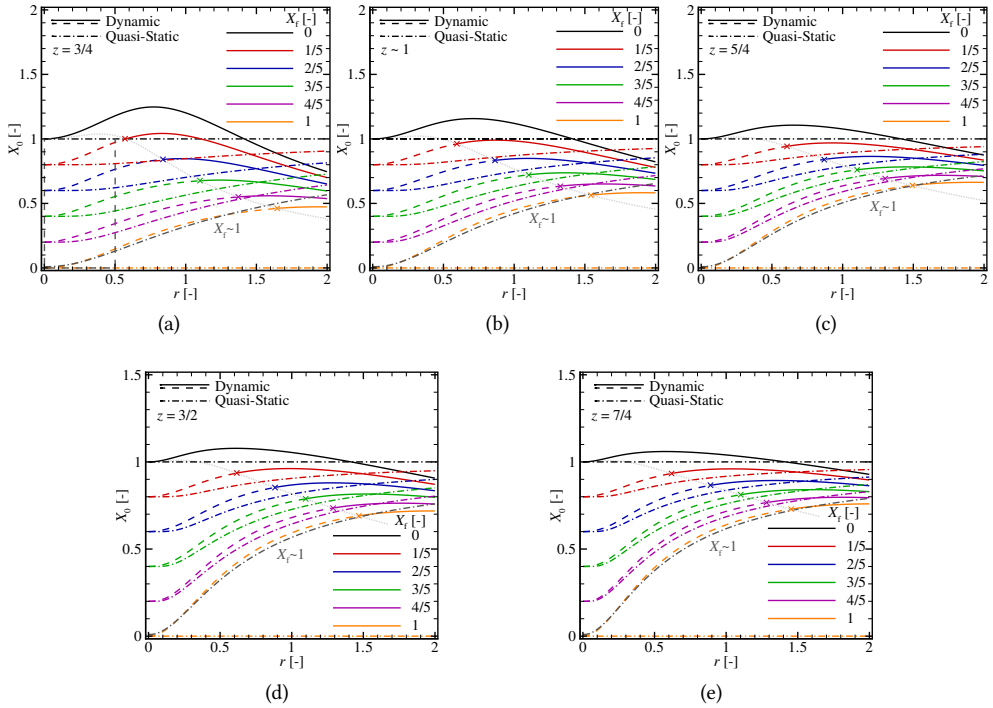

Figure 6.5: The dimensionless amplitude X_0 as a function of the dimensionless frequency r for damping ratios (a) $z = 3/4$, (b) ~ 1, (c) $5/4$, (d) $3/2$ and (e) $7/4$, with dimensionless Coulomb friction forces $X_f = 0$, $1/5$, $2/5$, $3/5$, $4/5$ and 1. The solid lines indicate continuous motion and the dashed(-dotted) lines two stops of finite duration per oscillatory period, except for Coulomb friction force $X_f = 0$. The coloured crosses indicate the dimensionless boundary frequency $r_{2\to0}$.

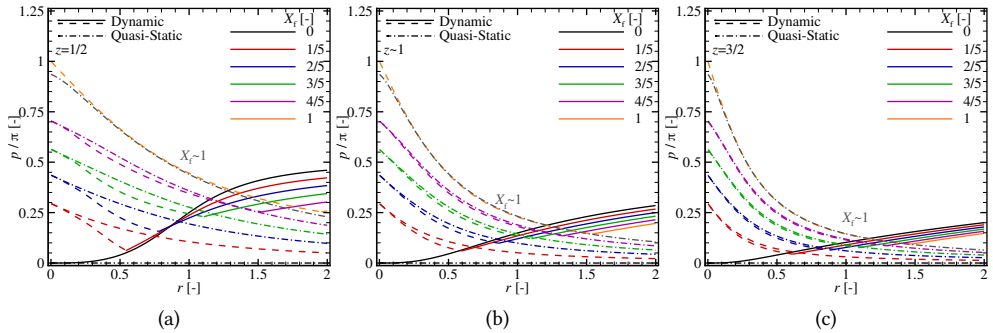

Figure 6.6: The normalised phase shift p/π is presented as a function of the dimensionless excitation frequency r for damping ratios (a) $z = 1/2$ (b) ~ 1 and (c) $3/2$, with dimensionless Coulomb friction forces $X_f = 0$, $1/5$, $2/5$, $3/5$, $4/5$ and 1. The solid lines indicate continuous motion and the dashed(-dotted) lines two stops of finite duration per oscillatory period, except for Coulomb friction force $X_f = 0$.

increases with excitation frequency r and dynamic motion becomes continuous. The dimensionless boundary frequency $r_{2\to0}$ thus corresponds with the change of gradients sign between phase shift p and dimensionless frequency r in Fig. 6.6. However, the quasi-static solution presents always two stops per oscillatory period except in the absence of Coulomb friction, *i.e.* $X_f = 0$.

The dimensionless boundary frequency $r_{2\to0}$ between the dynamic solution with two or more stops of finite duration per oscillatory period and continuous motion is provided in Fig. 6.7. At dimensionless frequencies below the dimensionless boundary frequency, *i.e.* $r < r_{2\to0}$,

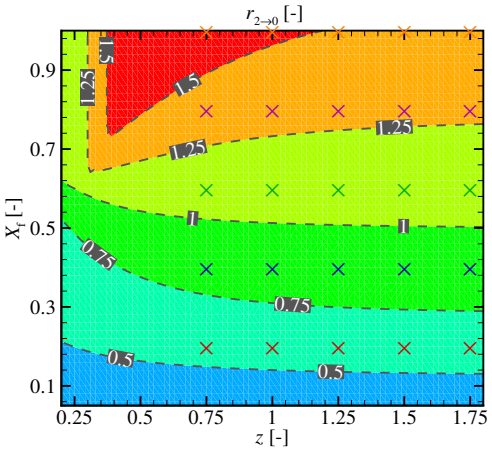

Figure 6.7: The dimensionless boundary frequency $r_{2\to0}$ between two stops of finite duration per oscillatory period and continuous motion as a function of damping ratio z and dimensionless Coulomb friction force X_f. The dashed grey iso-lines indicate the constant dimensionless frequencies $r_{2\to0} = 1/2, 3/4, 1, 5/4$ and $3/2$. The coloured crosses correspond with the same coloured crosses in Fig. 6.5.

as indicated by dashed dark-grey iso-lines of constant dimensionless frequency, the trajectory contains at least two stops of finite duration per oscillatory period. The coloured areas indicate the given ranges of dimensionless boundary excitation frequencies which are bounded by at most two selected iso-lines. Above the dimensionless boundary frequency $r_{2\to0} \leq r$ dynamic motion is continuous. The system parameter ranges of Fig. 6.7 are bound by the convergence of the numerical root-finding method. The result in Fig. 6.7 is a quick reference for the qualitative agreement between the dynamic and quasi-static solution. Quasi-Static motion is solely continuous in the absence of Coulomb friction and/or a rigid connection between the base and mass (See sec. 6.4.2). The dimensionless boundary frequency $r_{2\to0}$ thus bounds qualitative agreement between quasi-static and dynamic trajectories; and, at dimensionless frequencies $r_{2\to0} < r$, the phase shift p continuous to decrease under the quasi-static assumption but increases in the dynamic results.

In Fig. 6.8, the dimensionless velocity $\partial x/\partial T$ is presented as a function of the dimensionless trajectory x for damping ratios $z = 3/4, \sim 1, 5/4, 3/2$ and $7/4$, and dimensionless Coulomb friction forces $X_f = 1/5, 2/5, 3/5, 4/5$ and ~ 1. We choose the dimensionless excitation frequency $r = r_{2\to0}$ as indicated by coloured crosses in Figs. 6.5 and 6.7. The choice of pattern and line colour corresponds with those in Fig. 6.5 as well. Numerical results are added and indicated with coloured triangle and gradient symbols similar to Fig. 6.3.

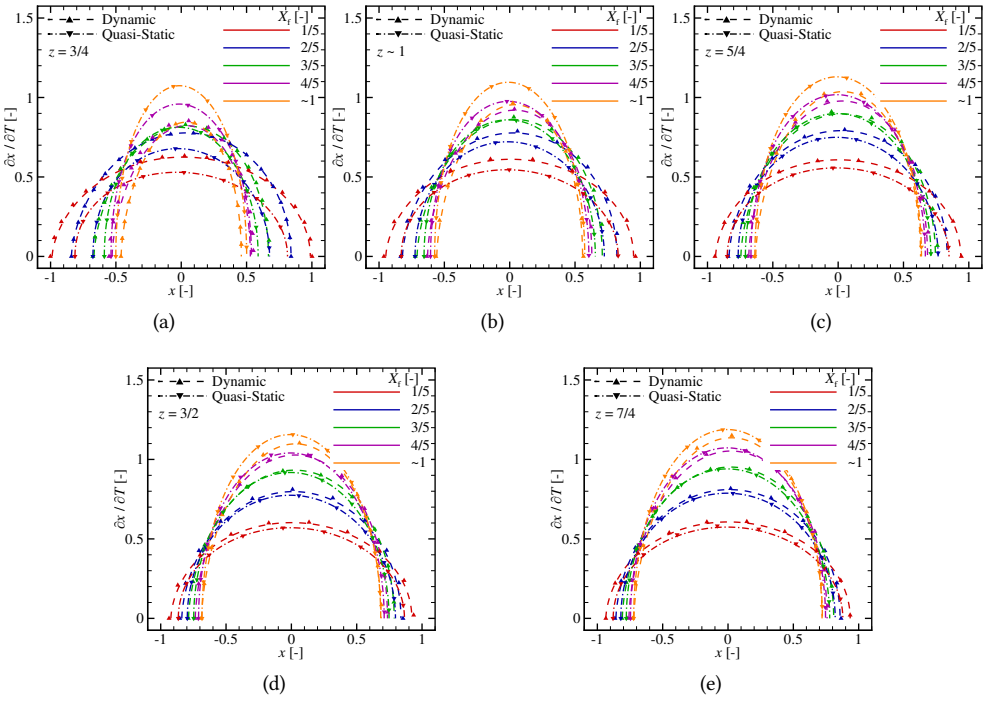

Figure 6.8: The the dimensionless velocity $\partial x/\partial T$ at the dimensionless excitation frequency $r_{2\to 0}$ (depicted by same coloured crosses in Figs. 6.5 and 6.7) is presented as a function of the dimensionless trajectory x for damping ratios (a) $z = 3/4$, (b) ~ 1, (c) $5/4$, (d) $3/2$ and (e) $7/4$, with dimensionless Coulomb friction forces $X_f = 0$, $1/5$, $2/5$, $3/5$, $4/5$ and ~ 1.

The same observations as made on Fig. 6.3 hold here, but now the velocity, and in turn the trajectory, of the quasi-static and dynamic solution differ up to a factor fourth instead of two. Even thought the dynamic dimensionless steady-state amplitude X_0 and phase shift p approaches the quasi-static steady-state results with damping ratio $z < 1/2$ and dimensionless Coulomb friction force X_f (See Figs. 6.5 and 6.6), velocity and trajectory remain distinctly different for damped motion, *i.e.* $1/2 \leq z < 3/2$. For critically and over-damped motion, *i.e.* $1 \leq z$, the dynamic velocity and the trajectory are close to symmetric around $x \approx 0$, and the differences between dynamic and quasi-static solution decrease with damping ratio z and dimensionless Coulomb friction force X_f as well. Notable is that the analytical and numerical results correspond for critically and over-damped motion, which is solely possible with the correct analytical initial boundary conditions of steady-state amplitude X_0 and phase shift p (See Introduction 6.1).

The differences between the quasi-static and the dynamic trajectory decrease solely with increased damping ratio $1 < z$, which is although limited to the given excitation frequency range up to about the natural frequency, *i.e.* $r \lessapprox 1$. Above the natural frequency, the quasi-static solution is at most a lower-order estimate cause of its two stops of finite duration per oscillatory period, and the differences in steady-state amplitude X_0 and phase shift p

increase with excitation frequencies $1 < r$ as well (See Figs. 6.5 and 6.6).

6.5.3 DISSIPATION

The major difference between the present base-excited system and a mass-excited system is that viscous dissipation is present in the former even when the mass is sessile. The dimensionless dissipation per period thus is

$$P = 2\left(\int_0^{T_0} X_{\mathrm{d}} \frac{\partial x\left(T'\right)}{\partial T'}\,\mathrm{d}T' + \int_{T_0}^{\pi/2} -X_{\mathrm{v}} \frac{\partial y\left(T'\right)}{\partial T'}\,\mathrm{d}T'\right), \tag{6.34}$$

with the dimensionless dissipative forces,

$$X_{\mathrm{d}}(T) \equiv X_{\mathrm{v}}(T) - X_{\mathrm{f}}(T), \tag{6.35}$$

and the dimensionless viscous force,

$$X_{\mathrm{v}}(T) = 2z\dot{x}(T) + 2rz\sin(rT + p), \tag{6.36}$$

where $y = y'/Y$ is the dimensionless base-excitation. For dimensionless times $0 \le T < T_0$, the mass is in motion ($\dot{x} < 0$) and sessile for $T_0 \le T < \pi/r$.

The dimensionless dissipation per oscillatory period in the absence of Coulomb friction thus is

$$P = \frac{2\pi z r^3}{1-(2-4z^2)r^2 + r^4}, \tag{6.37}$$

and under the quasi-static assumption the base-excitation and mass trajectory are in phase thus no viscous dissipation is present (See Eq. (6.13)). In the static limit, *i.e.* in the absence of inertia and viscous damping, the dimensionless dissipation is trivially $P = 4(1 - X_{\mathrm{f}})X_{\mathrm{f}}$. Moreover, when the mass is sessile during the whole oscillatory period the dimensionless dissipation $P = 2\pi rz$ and solely due to viscous damping under base-excitation.

In Fig. 6.6, the dimensionless dissipation per oscillatory period P is presented as a function of the dimensionless excitation frequency r for damping ratios $z = 1/2$, ~ 1 and $3/4$; the choice of pattern and line colour corresponds to those in Fig. 6.6.

The dimensionless dissipation displays one or two maxima, which correspond with viscous dissipation while the mass is sessile, and viscous and Coulomb friction near resonance, at low dimensionless frequencies $r < 1$ and higher frequencies $1 \lessapprox r$, respectively. For under-damped motion with damping ratio $z = 1/2$, the maxima seem to coalesce at the natural frequency, *i.e.* $r \approx 1$. Unexpected, the maximum due to viscous dissipation with a sessile mass is virtually independent of the damping ratio z (Compare the maxima of a given dashed coloured line across Figs. 6.9a-6.9c). This is readily rationalised as the sessile period decreases with damping ratio, while the viscous dissipation increases with the mass sessile. Moreover, dissipation near resonance decreases with damping ratio z and Coulomb friction force X_{f} because the phase shift p decreases with excitation frequency r (See Fig. 6.6). As expected, dissipation under the quasi-static assumption approaches the dynamic solution in the quasi-static loading limit. Furthermore, the dimensionless dissipation attains the maximum at low dimensionless frequencies $r < 1$ for dimensionless dry-friction forces $3/5 \lessapprox X_{\mathrm{f}} < 1$. For Coulomb friction forces $X_{\mathrm{f}} \lessapprox 3/5$, dissipation decreases monotonically with loading frequency, as the period with sessile mass decreases with Coulomb force X_{f}.

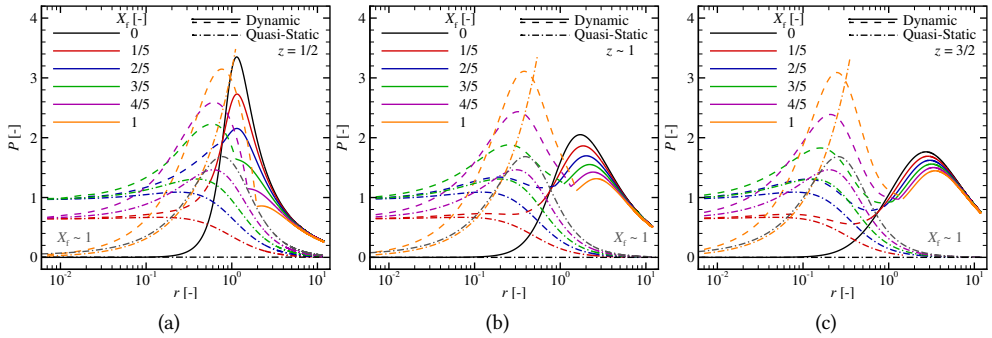

Figure 6.9: Log-Linear plot of the dimensionless dissipation P as a function of the dimensionless frequency r for damping ratios (a) $z = 1/2$, (b) ~ 1 and (c) $3/2$, with dimensionless Coulomb friction forces $X_f = 0$, $1/5$, $2/5$, $3/5$, $4/5$ and 1. The solid lines indicate continuous motion and the dashed(-dotted) lines two stops of finite duration per oscillatory period, except for Coulomb friction force $X_f = 0$. The quasi-static result for Coulomb friction $X_f \sim 1$ is indicated with a dark-grey dashed-dotted line.

Under the quasi-static assumption, dissipation is always under-predicted compared to the dynamic solution because the main source of dissipation is base-excitation while the mass is sessile. Indeed viscous dissipation is absent when the mass is in phase with the base trajectory and thus does not contribute to the friction forces. Solely for a sessile mass during the whole of the oscillatory period, dissipation increases monotonically, *i.e.* $P = 2\pi rz$ with $1 \leq X_f$. This holds for the dynamic results with dimensionless Coulomb friction forces $\sqrt{1+(2zr)^2} \leq X_f$ as well (not shown in Fig. 6.9).

The dissipative contribution of viscous damping due to a sessile mass obviously increases with Coulomb friction force X_f as the period the mass is in motion T_0 decreases. When the loading frequency increases above the natural frequency: for one, the period the mass is sessile $T_0 \leq T \leq \pi/r$ vanishes and/or decrease rapidly for the dynamic and quasi-static solution, respectively; moreover, the transient contribution (*i.e.* the phase shift p between base and mass when motion initiates from rest) and/or amplitude X_0 decrease or saturate with dimensionless excitation frequency r as well (See Figs. 6.2 and 6.6). It is thus clear that when the quasi-static assumption is used in, *e.g.* multi-scale modelling at the mesoscale, the dissipation, and in turn hysteresis and thus the macroscopically observed friction are underestimated. Which emphasises that special care and consideration is needed when one chooses to use the quasi-static assumption in the presence of Coulomb friction. Not solely in the static loading limit, as previously mentioned by Papangelo and Ciavarella [234], but for (over-)damped motion as well.

6.6 Conclusions

In this chapter, we present closed-form analytical expressions for a base-excited single degree-of-freedom mass-spring-damper system with Coulomb friction between the mass and a datum, with and without considering inertial forces. The derivation is performed with the simplification of the phase-plane method by Hundal [352], yet the final semi-analytical solutions are more comprehensive. The quasi-static and dynamic solutions are contrasted

quantitatively to highlight notable differences.

On the quasi-static assumption:

- the steady-state amplitude and the phase shift of damped dynamic motion are approximated with viscous dissipation $\sqrt{km} \leq c$ and Coulomb friction forces $0 \leq F_\mathrm{p} < kY$ in the quasi-static loading limit, and at least down to loading frequency $10^{-2}\sqrt{k/m}$ in the present work;

- the trajectory has two stops per oscillatory period for a finite Coulomb friction force $0 < F_\mathrm{p} < kY$ and is continuous with a rigid connection between the base and the mass;

- the trajectory is close to the dynamic solution for significantly over-damped motion, $2\sqrt{km} \leq z$, although for a limited range of loading frequencies, $\approx 0 \cdots \sqrt{k/m}$, with two stops of finite duration per oscillatory period;

- for excitation frequencies above the natural frequency, $\sqrt{k/m} < \omega$, the steady-state amplitude is a low-order approximate because the dynamic trajectory is continuous;

- dissipation is under-predicted because the main source of dissipation is base-excitation while the mass is sessile.

Even if the excitation frequency is low, for instance $10^{-1}\sqrt{k/m}$, the dissipation is underestimated by $5 \cdots 40$ % under the quasi-static assumption with respect to the dynamic solution, which depends on viscous damping and Coulomb friction.

On the dynamic solution:

- the system parameters and loading frequency of the boundary between continuous motion and two stops of finite duration per oscillatory is uniquely defined by the period that the mass is in motion;

- the dynamic trajectory is close to the trajectory under the quasi-static assumption, with viscous dissipation $\sqrt{km} \leq c$ and quasi-static loading frequencies down to $\omega = 2 \times 10^{-3}\sqrt{k/m}$ in the present work;

- The quasi-static solution is absent for $kY \leq F_\mathrm{p} \leq \sqrt{c^2\omega^2/k^2 + 1}$ while the mass is still mobile due to inertia;

- dissipation attains one or two maxima due to Coulomb friction and/or viscous dissipation around and above, or solely below, the natural frequency $\sqrt{k/m}$, respectively.

7

General Discussion

7.1 Part I: Inelasticity in Metals

The fundamental understanding on the effects of dislocation network geometry on the pre-, at- and post-yield material behaviour is illustrated. Summarising, we treat the relationships between the inelastic deformation and the dislocation network structure, and mechanical properties of anelasticity, yield and plastic flow. The obtained knowledge will aid in the future design of forming methods [28] and micro-mechanical systems [29]. We contribute by incorporating dislocation densities with varying dislocation character in predictions of the anelastic deformation of metal crystallites with a generic Poisson's ratio; and, with a seamless, unified stress-strain treatment, that combines the three deformation mechanisms of elastic bond stretching, stable and unstable dislocation glide.

Dislocation character has major effects on both the apparent elastic constants and yield points. This suggests that reassessment of previous studies on aforementioned topics is appropriate. Current limitations on the description of *e.g.* the distribution of dislocation links lengths, (far-field) elastic interaction and equivalent isotropic elasticity, are readily lifted by the Dislocation Dynamic Method [233]. This is however limited by load rate and dislocation density. Even so, the model in Chapter 2 is of engineering interest in higher scale computational methods under static loading conditions. The elastic-anelastic constitutive model takes account of anisotropic effects on a per-grain basis and presents a significant step towards modelling of crystallographically textured cubic materials. The model's ulterior application is to use experimental results to obtain information on the geometry [4–7] of an *a priori* unknown dislocation network. We find that near-incompressible materials and aluminium are promising candidates for future experimental research. The former is of interest because the influence of dislocation character is maximised with an increase in Poisson's ratio (See Sec. 2.3.3); the latter because aluminium has near-isotropic elasticity and a high stacking fault energy, which promotes the bowing-out of dislocation segments.

The physical interpretation of yield is the transition from mechanically recoverable to mechanically irrecoverable deformation. The novel yield criterion in Chapter 3 encompasses both the local behaviour of individual dislocation links and the global dislocation interactions that constitute hardening. This yield criterion allows us to analyse uniaxial tensile force-displacement curves and present the following findings: experimental verification that the flow strength is predicted by Taylor-type equations; and, a physics-informed connection between the geometry of the dislocation network and the Taylor relationships' constant.

The Taylor relationships' constant is a measure of the combined forest interactions and junction strengthening, akin to Kubin *et al.* [35]. Here, a proportionality between dislocation density and average dislocation link length is an effective measure of junction strengthening on the crystallite level, that changes with plastic strain through forest interactions. We thus refine the physical interpretation of the constant in the Taylor relationship to the theoretical asymptotic lower limit of the dislocation network geometry (See Sec. 3.6.4). Finally, where previously thought impossible [5], we rationalise the change in initial apparent elastic constants with thermomechanical processing [28, 38, 41, 275–278]. The now known evolution of the inverse proportionality between average segment length and dislocation density allows for hardening models to be further improved. One ulterior application of present, novel interpretation of yield and our unified model is to predict inelastic deformation by means of full-field crystal plasticity modelling [357].

This year Zhou *et al.* [358] experimentally confirm the dislocation bow-out mechanism

for anelasticity in single- and bi-crystals of Tantalum. Moreover, the initial apparent moduli ("Loop Width" in their work [358]) have a minimum under uniaxial tension in the ⟨100⟩-crystallographic direction and maxima in the ⟨110⟩ and ⟨111⟩ tensile-directions, which is in accordance with our single crystallite dislocation bow-out model (See Sec. 2.2.2). This confirmation is significant in view of the applicability of the single metallic crystallite model in Chapter 2. Notable is that they [358] report that dissipation is larger in single- and bi-crystals than in commercial, polycrystalline metals. This stands juxtaposed to the notion that the non-local internal stresses that arise from plastic strain gradients, particularly those from microstructural inhomogeneity, increase the magnitude of anelastic deformation [7, 38]. Moreover, Zhou *et al.* [358] find that the initial apparent moduli and initial plastic modulus are proportional. This is also in line with the static unified inelastic model that we present in Chapter 3.

The results and conclusions that we present in Part I extend to the following aspects:

pre-yield mechanical behaviour of complex steels is of engineering interest [38, 41, 278]. Recently, the pre-yield mechanical behaviour of Dual-Phase is experimentally investigated by Li and Wagoner [7], and Vitzthum *et al.* [38]. The unified inelastic model is readily implemented in a composite model, alike Mughrabi [359, 360]. This is a method to account for the inelastic accommodation between constituents. However the remaining challenge is the identification of the structural variables (See Sec. 3.2), and their evolution with local deformation, in each crystalline constituent. One potential method to alleviate this is the experimental measurement of the lattice strain in each constituent by high-energy synchrotron transmission measurements [38];

single crystallite mechanical behaviour is one input to full-field crystal plasticity modelling [357]. Hence the unified inelastic model is readily adapted in a discrete framework that is suitable for numerical integration. However, the remaining challenge is the numerical integration of the resulting stiff, non-linear equation of dislocation motion [273]. This stiffness is the result of the several orders of magnitude difference between rate of dislocation events and (quasi-)static loading, that is of engineering interest. A reduced equation of motion must be formulated, that retains the high non-linearity yet improves computational tractability;

activation, glide and ensuing dislocation-density increase on individual slip-systems are postdictions in work-hardening models of single metallic crystallites [35]. This holds for the most recent dislocation dynamics results by Akhonzadeh *et al.* [32] and Katzer *et al.* [361] as well. We find that unification of an existing single-crystallite hardening model [35] with the bow-out model of pre-yield inelastic deformation [273] poses reliable predictions [362]. This unified approach [362] accounts for both the influence of dislocation network geometry and pre-yield compliance, that effect initiation of unstable dislocation glide. There is currently, however, no consensus on the dislocation mechanism that controls unstable dislocation glide. Known is that the activity of a specific mechanism depends on the system size and load rate, *e.g.* single-arm sources in micro-pillars [363, 364]; zipping and unzipping mechanisms at high strain rates [365]; and, cross-slip and glissile junctions for low dislocation densities [366]. Each mechanism has an associated anelastic strain contribution that must be accounted for, which poses one route to a unified approach;

quantitative connection between the key microstructural features of the dislocation network and inelastic metals deformation was lacking [8]. Nowadays the consensus is that the dislocation segments follow a length distribution [8, 11, 361, 363, 367, 368]. The exact form might be exponential as the result of a one-dimensional Poisson's process by junction formation [8, 32, 361, 368]; Log-Normal as proposed by Shishvan and Van der Giessen [367]; or, the result of a random distribution of pinning points in a finite size domain by Parthasarathy *et al.* [363]. The recognised evolution of the inverse proportionality between average segment length and dislocation density (See Sec. 3.6.4) is thus a significant step towards a model of link-length distribution evolution with inelastic strain. Especially, this link-length evolution must be incorporated in future coarse-grained field theories of dislocation dynamics or full-field crystal plasticity models [8]. Coarse-grained field theories under quasi-static loading conditions, where a range of initial segment lengths are activated simultaneously [11, 236–238] exist for almost fifty years. Most recently, Wijnen *et al.* [364] investigate small-scale experiments on single crystals with a full-field crystal plasticity model, where flow is based on the underlying distribution of the dislocation source sizes [364]. Moreover, Ye *et al.* [368] model the mobile dislocation density as the number fraction of activated segment lengths as a function of the line stress. However, the change in inelastic compliance before global yield, which controls the local activation of dislocation links and global flow peri-yield, is not considered as of yet.

7.2 Part II: Yield Point Phenomenon

Plastic flow in the Lüders front maximises global dissipation and vanishes parallel to it, which are the characteristics of the Lüders front. Lüders bands form oblique to the tensile direction, and the angle between loading axis and the Lüders front depends on material properties, specimen geometry and test conditions. Chapter 4 presents a macromechanical model of the Lüders front, where the Lüders front orientation and the observed lower yield strength depend on the difference between the material's upper and lower yield strengths, as well as in-plane condition. The obtained knowledge aids in the measurements on the yield point phenomenon [67] and suppression thereof via industrial, post-process rolling [81].

An alternative mechanism for the rotation of the Lüders front is the change in heterogeneous stress state across, and the confinement in, the Lüders front. This alternative is complementary to the dependencies on compressibility [313, 320], plastic anisotropy [318] and loading/gripping conditions [300], which were reported previously [120]. For thin tensile specimens Lüders bands align perpendicular to the loading axis, which reduces the bending moment [120], and with the magnitude of the stress concentration at the Lüders front [64, 65]. The latter we verify in Sec. 4.6.1 for the first time to the authors' knowledge. We expect that when the tensile specimen thickness increases the Lüders bands angle with respect to the loading axis sharpens, because the in-plane plastic strain decreases [310]. In the limit of the plane strain state, the Lüders front will form on a plane at 45 degrees angle with respect to the loading axis (See Secs. 4.3.1 and 4.5.2).

The numerical results in Chapter 4 are in line with the hypothesis that the Lüders band is parallel to the direction of zero extension and plastic shear perpendicular to the Lüders front is negligible compared with the Lüders strain. The former holds inside the Lüders band in the numerical results in Sec. 4.5.3 while the latter does not (See 4.6.2 as well).

Whereof the outcome is an experimental method to approximate the constitutive parameters by the common-place uniaxial tensile test. The novelty is a simple methodology with the force-displacement and Lankford coefficients [322] to obtain material properties independent of test conditions. However the difference between estimated and material properties that we discuss in Sec. 4.6.2 must be diminished by an accurate description of flow inside the Lüders band in the future.

The results and conclusions that we present in Part II extend to the following aspects:

experimental validation of the macroscopic modelling framework and the characteristics of the Lüders front that we introduce (See Sec. 4.2) remains tentative. An initial step towards validation is presented by Van der Heijde and Samad [330, 331]. They [330, 331] present the effect of tensile specimen thickness on the Lüders front orientation. However, the influence of the true upper and lower yield strengths on the Lüders front angle are not yet experimentally verified. Seminally, Hanai *et al.* [369] experimentally show that the difference between the flow strength before paint bake-hardening, and the lower observed yield strength after, increases with carbon and nitrogen content. Kim *et al.* [101] report that the Lüders strain increases with the ratio between carbon content and dislocation density. They [101] however omit the lower observed yield strength and compare different annealing times. With an increase in annealing time the upper yield strength is thought to increase. Even so, their [101, 369] results are in line with our macroscopic model but omit to report the orientation of the Lüders bands. This year, Qiu *et al.* [370] examine the global and local deformation behaviours of four ferrite–pearlite steels with various carbon contents via extensometer and digital image correlation techniques. They [370] report that the observed upper and lower yield strengths increase with carbon content. However, the Lüders strain decreases with the increase in pearlite volume fraction. This increase in volume fraction facilitates the generation of mobile dislocations by a greater area of ferrite/cementite-interfaces. They [370] do not to report the Lüders band morphology during yield elongation though. Hence there is currently the clear need for experimental measurements of the Lüders band morphology in low carbon steel with different interstitials contents during yield point elongation. Together with measurement of the true lower yield strength, this might verify the characteristics of the Lüders front;

little is known and reported on the effects of crystallographic texture, or *vice versa* inelastic anisotropy, on the Lüders band morphology. The only works that the authors are aware of, which experimentally connects rolling texture with the Lüders band inclination, are by Daniel *et al.* [312] and Savoie *et al.* [307] for cold-rolled steel and aluminium, respectively. They [307, 312] report that the contraction ratio and thus the Lüders front angle change between the rolling and the transverse directions. Yu *et al.* [329] report that the Portevin-Le Chatelier band's orientation is constant, due to crystallographic texture invariance during tensile loading. Tokuoka and Saito [318] derive the Lüders front angle as a function of the difference in angle between the principal axis of anisotropy and the uniaxial tensile direction. Most recently, Cazacu and Rodríquez-Martínez [328] theoretically investigate the orientation of plastic necks in specimens taken from orthothropic metallic sheets that are subjected to uniaxial tension, which is similar to the analysis by Tokuoka and Saito [318]. These solu-

tions [318, 328] do not account for the stress concentration at the Lüders front due to the upper and lower yield strengths though. When these models do so they might lead to methods of crystallographic texturing that minimise yield elongation;

a lot is known and reported on the effect of experimental measurement method on the yield point phenomenon. Seminally, the effects of surface treatment [67] and test equipment stiffness [371] are investigated. Less well-known are the effects of loading/gripping conditions [120, 300] beyond the introduction of a moment before tensile testing [62]. Because in-plane plastic flow and shear components are non-zero, unless the stress state is uniaxial in the Lüders band, the testing device constrains. This increases the moments during tensile loading; moments are maximised when the lateral displacements are constrained. Similarly, the propagation of Lüders fronts keeps the tensile specimen straighter, when they are antisymmetrically oriented across the dog-bone specimen, and the moments are reduced compared with a single Lüders band [53]. When single Lüders bands are studied, which is preferable because the local strain rate changes with number of bands [300], the device must thus allow for lateral displacements. Otherwise, multiple Lüders bands nucleate (which obviously depends on surface finish) and/or the Lüders bands might rotate, which has currently multiple recognised reasons [53, 74, 120, 300, 372]. There is thus the need for a dedicated tensile test method and methodology, similar to the work by Vadoulakis *et al.* [373], to meaningfully compare experimental results;

the rigid-plastic mechanical model is at the basis of our macromechanical framework. The elastic deformation is neglected, which has the merit of simplicity and continues to be applied in modelling sheet metals forming [374]. Even so, localisation is known to depend on softening [327] as well. Throughout our numerical results the softening (tangent) modulus is kept constant. Secondly, only the Lüders front is modelled while the stress state changes throughout the Lüders band, which leads to local changes in in-plane plastic flow and shear. The numerical results capture this change in plastic shear, that we find is up to a hundredth of the Lüders strain and is thus neglected in our proposed experimental methodology (See Sec. 4.6). Thirdly, we omit the (applied) boundary conditions that impose an in-plane moment, and traction-less boundaries on the sides of the tensile specimen. We choose the geometry and applied deformation rate in the numerical approach (See Fig. 4.4) that minimise boundary conditions' effects while retaining computational tractability. Hence the future step is the use of an elastic-plastic material, mechanical model [327] in our analysis, which will allow for a more meaningful comparison with the numerical results (than in Sec. 4.6.1) and accounts for the elastic contraction in front of the Lüders front.

7.3 Part III: Dissipative Contacts

Two mechanisms of interfacial toughening are present in rough, soft matter contacts: viscous and roughness-induced dissipation. Chapter 5 demonstrates that the latter is either in the form of a mechanical instability at high retraction rates or in the form of a fast quasi-static reduction of the contact area where the elastic mechanical instability is dampened. Whether the contact area reduction is very fast or occurs through an unstable mechanical jump, the result in terms of energy loss are similar when gauged by the addition of wavy elastic

and smooth viscoelastic loads at pull-off. We, however, show that the effective work of adhesion tends towards the instantaneous work of adhesion because mechanical instabilities only reappear when the instantaneous limit is traversed. The obtained knowledge aids in the design and/or interpretation of experiments, and improvement of existing numerical methods [150].

Surprisingly, the pull-off loads are affected marginally by the instantaneous work of adhesion at pull-off for vanishing retraction rates, while the intimate contact area deviates noticeably from the smooth elastic contact. Both observations on the load and area at pull-off coexist because of the rapid area reduction compared with the retraction rate near pull-off. Whereby the load increases negligibly compared with the instantaneous limit. So we conclude that viscoelasticity governs adhesive hysteresis even in the presence of roughness-induced mechanical instabilities, both in the relaxed and instantaneous loading limits.

With Chapter 6 one is able to assess the difference between the dynamic and the quasi-static solution in engineering problems with viscous, static and dry friction. Insight is engendered to the validity of neglecting inertial forces from frictional problems. We present quantitative measures of the differences between the quasi-static and the dynamic solution in frictional problems with viscous, static and dry friction, by steady-state amplitude, phase shift, phase-plane, and the number of stops and dissipation per oscillatory period.

When inertial forces are neglected, the estimate of two stops with finite duration per period is shown to hold for finite viscous and/or Coulomb friction forces. Towards the quasi-static loading limit, the quasi-static solution does approach the under-damped dynamic solution with viscous dissipation. Likewise, the quasi-static solution approaches the dynamic solution, for a given over-damped system, with Coulomb friction force. However, when inertia is accounted for, motion is continuous around and above the natural frequency. Which is not provided for by the quasi-static solution.

The dissipation per oscillatory period attains one or two maxima, which correspond with viscous dissipation for a sessile mass, and viscous and Coulomb friction near resonance, respectively. Under the quasi-static assumption, dissipation decreases monotonically with loading frequency or attains a single maximum. The latter maximum corresponds to viscous dissipation while the mass is sessile. Notable is that the observed friction is underestimated for any finite excitation frequency under the quasi-static assumption with a mobile mass.

We engender new insight into the validity of omitting inertial forces from problems with finite viscous, static and dry-type frictional forces and formulate a general rule as follows: *The dynamic solution in the presence of Coulomb friction between mass and datum, and base-excitation, is approached by the solution under the quasi-static assumption with viscous dissipation; at loading frequencies far below the natural loading frequency, with near critical viscous dissipation; and, for over-damped motion with Coulomb friction force and a limited range upto about the natural frequency.*

In Chapter 6, we give the range of system parameters and loading frequencies for which the solution under the quasi-static assumption closely tracks the dynamic trajectory and the observed friction is qualitatively approached. The ulterior motive of Chapter 6 is to guide future (multi-scale) numerical modelling efforts. For example, modelling interface friction due to viscous and adhesive dissipation in reciprocating sliding contacts with roughness present over multiple length-scales [142, 190, 340, 375, 376], and the hysteretic deformation of metals [7, 279].

In Chapter 5, we consider quasi-static loading conditions and thus ignore inertia of the viscoelastic substrate [340]. The present results at vanishing retraction rate are thus the limiting solution for which cases inertia can be ignored. We speculate that inertia of the substrate allows for mechanical instabilities at vanishing retraction rates as well. Our results are thus limited by the simplicity of the descriptions of viscoelastic substrate, adhesive interaction, surface roughness and loading conditions.

Results and conclusions that we present in Part III implicate that for low loading rates, the origins of hysteresis in existing experimental results of soft matter contact, at least of patterned surfaces, need to be reassessed. It remains up to future investigations to study the combination of realistic roughnesses, dissipation and inertia of the viscoelastic substrate. Additional work is required to establish whether our conclusions already extend to realistic rough contacts. A higher surface roughness generally leads to more viscoelastic deformation [150] thus to more dissipation, and reduces the number of contacts, which lowers adhesion. Hence trends in the adhesive hysteresis with real surface roughness present are currently moot (See Sec. 1.4 as well).

The final, recognised research path pertains to finite viscoelastic bodies sizes [219]. In his numerical work, Attard [377] finds that the pull-off force is independent of the maximum indentation depth, except for "relatively small" initial loads in viscoelastic, smooth, adhesive Hertzian contacts. The works by Van Dokkum *et al.* [335] and Pérez-Ràfols *et al.* [345] report no initial load dependency for retraction rates that are low compared with the relaxation time, and large initial intimate contact areas. More recently, realisations of smooth Hertzian contact on a viscoelastic half-space by means of Finite Element modelling efforts [135, 348] show that the pull-off force depends on the initial indentation depth (or equivalently maximum contact area). Notably, they [348, 378] introduce an corrective factor into the theory by Persson and Brenner [217, 218] that accounts for the finite value of the contact radius at the start of unloading. The (aforementioned) numerical realisations [205, 229, 335, 337, 348, 377] are limited to smooth cylindrical/Hertzian indenters though. This year, Müser and Nicola [150] highlight the necessity for studies that reproduce hysteresis when viscoelasticity and roughness-induced multistability both contribute substantially. This highlights the need and the relevance of explicitly modelling the viscoelastic solids [150]. Hence together with the conclusions in Part III we propose the following necessary steps: modelling finite viscoelastic substrate sizes [379]; including coupled, traction-separation interface laws [380]; extending with interfacial damage [381] and viscoelastodynamics [382]; and, bridging meso to the macro length-scales *e.g.* by (hybrid) multi-scale modelling [383, 384].

Appendices

A Frank-Read Source

A.I Equilibrium Shapes

The loci of the pinning points are given by

$$\left\{\frac{x_\alpha(\phi_\alpha)}{L},\frac{y_\alpha(\phi_\alpha)}{L}\right\}\equiv\left\{-\frac{\cos(\phi_\mathrm{i})}{2},\frac{\sin(\phi_\mathrm{i})}{2}\right\}, \tag{A.1a}$$

and

$$\left\{\frac{x_\beta(\phi_\beta)}{L},\frac{y_\beta(\phi_\beta)}{L}\right\}\equiv\left\{\frac{\cos(\phi_\mathrm{i})}{2},-\frac{\sin(\phi_\mathrm{i})}{2}\right\}. \tag{A.1b}$$

Hence the scaled integration constants are

$$\frac{C_1}{L}=-\frac{\tau_\mathrm{c}}{8\tau'_{xz}}(4\sin(\phi_\alpha)+\nu\sin(\phi_\alpha)+\nu\sin(3\phi_\alpha))-\frac{\cos(\phi_\mathrm{i})}{2}, \tag{A.2a}$$

and

$$\frac{C_2}{L}=-\frac{\tau_\mathrm{c}}{8\tau'_{xz}}\left(4\cos(\phi_\beta)-5\nu\cos(\phi_\beta)+\nu\cos(3\phi_\beta)\right)-\frac{\sin(\phi_\mathrm{i})}{2}. \tag{A.2b}$$

Combining Eqs. (A.1) and (A.2), we give the coordinates along the dislocation loop as

$$\frac{x(\phi)}{L}\equiv\frac{\tau_\mathrm{c}}{8\tau'_{xz}}((4\sin(\phi)+\nu\sin(\phi)+\nu\sin(3\phi))-(4\sin(\phi_\alpha)+\nu\sin(\phi_\alpha)+\nu\sin(3\phi_\alpha)))-\frac{\cos(\phi_\mathrm{i})}{2}; \tag{A.3a}$$

$$\frac{y(\phi)}{L}\equiv\frac{\tau_\mathrm{c}}{8\tau'_{xz}}\left((4\cos(\phi)-5\nu\cos(\phi)+\nu\cos(3\phi))-\left(4\cos(\phi_\beta)-5\nu\cos(\phi_\beta)+\nu\cos(3\phi_\beta)\right)\right)-\frac{\sin(\phi_\mathrm{i})}{2}. \tag{A.3b}$$

Using Eqs. (A.6) and (A.9), we obtain the normalised equilibrium shape of the initial RHS dislocation segment as

$$\frac{x(\phi)}{L}=\frac{4\sin(\phi)+\nu\sin(\phi)+\nu\sin(3\phi)}{2(4\sin(\Delta\phi_\mathrm{s})+\nu\sin(\Delta\phi_\mathrm{s})+\nu\sin(3\Delta\phi_\mathrm{s}))}; \tag{A.4a}$$

$$\frac{y(\phi)}{L}=\frac{4\cos(\phi)-5\nu\cos(\phi)+\nu\cos(3\phi)-(4\cos(\Delta\phi_\mathrm{s})-5\nu\cos(\Delta\phi_\mathrm{s})+\nu\cos(3\Delta\phi_\mathrm{s}))}{2(4\sin(\Delta\phi_\mathrm{s})+\nu\sin(\Delta\phi_\mathrm{s})+\nu\sin(3\Delta\phi_\mathrm{s}))}, \tag{A.4b}$$

and the normalised equilibrium of the initial positive edge dislocation segment as

$$\frac{x(\phi)}{L}=\frac{4\sin(\phi)+\nu\sin(\phi)+\nu\sin(3\phi)-(4\cos(\Delta\phi_\mathrm{e})+\nu\cos(\Delta\phi_\mathrm{e})-\nu\cos(3\Delta\phi_\mathrm{e}))}{2(4\sin(\Delta\phi_\mathrm{e})-5\nu\sin(\Delta\phi_\mathrm{e})-\nu\sin(3\Delta\phi_\mathrm{e}))}; \tag{A.5a}$$

$$\frac{y(\phi)}{L}=\frac{4\cos(\phi)-5\nu\cos(\phi)+\nu\cos(3\phi)}{2(4\sin(\Delta\phi_\mathrm{e})-5\nu\sin(\Delta\phi_\mathrm{e})-\nu\sin(3\Delta\phi_\mathrm{e}))}. \tag{A.5b}$$

A.II Pure Character Angles

For initial pure screw character segments, Eq. (2.6) is rewritten as

$$\frac{\tau'_{xz}}{\tau_c} = \sin(\Delta\phi_s) + \nu\sin(\Delta\phi_s) - \nu\sin^3(\Delta\phi_s). \tag{A.6}$$

We are interested in the difference angle $\Delta\phi_{\bullet}$ as an explicit function of the shear stress τ_{xz}, for which we substitute $s \equiv \sin(\Delta\phi_{\bullet})$. Rearranging Eq. (A.6), we find a convenient form to determine the three roots s_g, with subscript $g = 0, 1$ and 2, being

$$0 = s_g^3 - \left(1 + \frac{1}{\nu}\right) s_g + \frac{1}{\nu}\frac{\tau'_{xz}}{\tau_c}. \tag{A.7}$$

The three real-valued roots of a cubic equation [385]

$$0 = r^3 + pr + q, \tag{A.8a}$$

are

$$r_g \equiv 2\sqrt{-\frac{p}{3}}\cos\left(\frac{1}{3}\cos^{-1}\left(\frac{3q}{2p}\sqrt{-\frac{3}{p}}\right) - \frac{2\pi g}{3}\right), \qquad \text{when} \qquad p < 0. \tag{A.8b}$$

Substituting Eq. (A.7) in Eq. (A.8) and noting $\sin(\Delta\phi_s) \in [-1, 1]$, we find $g = 1$ and the explicit equation of the difference angle for the stable equilibrium shape $\Delta\phi_s$.

For initial pure edge character segments, Eq. (2.11) is rewritten as

$$\frac{\tau_{xz}}{\tau_c} = \frac{1}{4(1-\nu)}\left(4\sin(\Delta\phi_e) - 5\nu\sin(\Delta\phi_e) - \nu\sin(3\Delta\phi_e)\right), \tag{A.9a}$$

and

$$\frac{\tau_{xz}}{\tau_c} = \frac{\sin(\Delta\phi_e)}{1-\nu} - \frac{2\nu\sin(\Delta\phi_e)}{1-\nu} + \frac{\nu\sin^3(\Delta\phi_e)}{1-\nu}. \tag{A.9b}$$

Rearranging Eq. (A.9b), we find a convenient form to determine the three roots s_g of the cubic equation:

$$0 = s_g^3 + \left(\frac{1}{\nu} - 2\right) s_g + \frac{(\nu-1)}{\nu}\frac{\tau_{xz}}{\tau_c}, \tag{A.10}$$

which is of the same form as Eq. (A.8a), but with $p \geq 0$, since $\nu \leq 1/2$. The single real-valued and two complex-valued roots of the cubic equation (A.8a) [385] for $p > 0$ are

$$r_g = 2\sqrt{\frac{p}{3}}\sinh\left(\frac{1}{3}\sinh^{-1}\left(-\frac{3q}{2p}\sqrt{\frac{3}{p}}\right) + \frac{2i\pi g}{3}\right), \tag{A.11}$$

where i is the imaginary unit. Substituting Eq. (A.10) in Eqs. (A.8a) and (A.11), and noting $\sin(\Delta\phi_e) \in [-1, 1]$, we use $g = 0$ and find the explicit equation of the difference angle for the stable equilibrium shape $\Delta\phi_e$.

A.III Swept Areas

Considering a FR source with generic initial dislocation character ϕ_i, we substitute Eq. (A.2) in Eq. (2.4) and, noting

$$\begin{aligned}\frac{1}{L^2}\left(x(\phi)\frac{\partial y(\phi)}{\partial\phi}-y(\phi)\frac{\partial x(\phi)}{\partial\phi}\right)&=\frac{2-\nu+3\nu\cos(2\phi)}{32}\left(\frac{\tau_\mathrm{c}}{\tau'_{xz}}\right)^2(\cdots\\ \cdots\cos(\phi)&\left(2\nu\cos(\phi)+(4-5\nu)\cos\left(\phi_\beta\right)+\nu\cos\left(3\phi_\beta\right)+4\frac{\tau'_{xz}}{\tau_\mathrm{c}}\sin(\phi_\mathrm{i})\right)\cdots\\ \cdots+\sin(\phi)&\left(-2\nu\sin(\phi+(\nu+4)\sin(\phi_\alpha)+\nu\sin(3\phi_\alpha)+4\frac{\tau'_{xz}}{\tau_\mathrm{c}}\cos(\phi_i))\right)+2\nu-4\Bigg),\end{aligned}\tag{A.12}$$

obtain the normalised area swept out as

$$\begin{aligned}\frac{S\left(\phi_\alpha,\phi_\beta\right)}{L^2}&=\frac{1}{256}\left(\frac{\tau_\mathrm{c}}{\tau'_{xz}}\right)^2\left(16\left(2\left(\phi_\beta-\phi_\alpha\right)+4\sin\left(\phi_\alpha\right)\cos\left(\phi_\beta\right)-\sin\left(2\phi_\alpha\right)-\sin\left(2\phi_\beta\right)\right)\cdots\right.\\ &\cdots-8\nu\left(\sin\left(4\phi_\alpha\right)+\sin\left(4\phi_\beta\right)+4\left(\phi_\beta-\phi_\alpha-\sin\left(2\phi_\beta\right)+2\sin\left(\phi_\alpha\right)\cos\left(\phi_\beta\right)\right)\cdots\right.\\ &\cdots-2\left.\left(\sin\left(\phi_\alpha\right)\cos\left(3\phi_\beta\right)+\sin\left(3\phi_\alpha\right)\cos\left(\phi_\beta\right)\right)\right)\\ &+8\frac{\tau'_{xz}}{\tau_\mathrm{c}}\left(4\cos\left(\phi_\beta+\phi_i\right)-2\nu\cos\left(\phi_\beta+\phi_i\right)-2(2-\nu)\cos\left(\phi_\alpha+\phi_i\right)\cdots\right.\\ &\cdots+3\nu\left(\cos\left(\phi_i-\phi_\alpha\right)-\cos\left(\phi_i-\phi_\beta\right)\right)+\nu\left.\left(\cos\left(3\phi_\beta+\phi_i\right)-\cos\left(3\phi_\alpha+\phi_i\right)\right)\right)\\ &+\nu^2\left(4\left(\phi_\alpha-\phi_\beta\right)+3\sin\left(2\phi_\beta\right)+19\sin\left(2\phi_\alpha\right)+\sin\left(4\phi_\beta\right)+7\sin\left(4\phi_\alpha\right)-\sin\left(6\phi_\alpha\right)-\sin\left(6\phi_\beta\right)\right)\cdots\\ &\cdots+4\left(\sin\left(\phi_\alpha\right)\cos\left(3\phi_\beta\right)+\sin\left(3\phi_\alpha\right)\cos\left(3\phi_\beta\right)\right)-20\left(\sin\left(\phi_\alpha\right)\cos\left(\phi_\beta\right)+\sin\left(3\phi_\alpha\right)\cos\left(\phi_\beta\right)\right)\Big)\Big).\end{aligned}\tag{A.13}$$

Hereby, the normalised area swept by the RHS screw FR source is

$$\begin{aligned}\frac{S_\mathrm{s}\left(\Delta\phi_\mathrm{s}\right)}{L^2}=&\frac{1}{32\left(2+\nu+\nu\cos\left(2\Delta\phi_\mathrm{s}\right)\right)^2\sin^2\left(\Delta\phi_\mathrm{s}\right)}\left(\left(32-32\nu-4\nu^2\right)\Delta\,\phi_\mathrm{s}\cdots\right.\\ &\left.\cdots-\left(16-32\nu-3\nu^2\right)\sin\left(2\Delta\phi_\mathrm{s}\right)-\left(8\nu-\nu^2\right)\sin\left(4\Delta\phi_\mathrm{s}\right)-\nu^2\sin\left(6\Delta\phi_\mathrm{s}\right)\right),\end{aligned}\tag{A.14}$$

and for the positive edge FR source

$$\begin{aligned}\frac{S_\mathrm{e}\left(\Delta\phi_\mathrm{e}\right)}{L^2}=&\frac{1}{32\left(\nu\cos\left(3\nu+2\Delta\phi_\mathrm{e}\right)-2\right)^2\sin^2\left(\Delta\phi_\mathrm{e}\right)}\left(\left(32-32\nu-4\nu^2\right)\Delta\phi_\mathrm{e}\cdots\right.\\ &\left.\cdots-\left(16-19\nu^2\right)\sin\left(2\Delta\phi_\mathrm{e}\right)+\left(8\nu-7\nu^2\right)\sin\left(4\Delta\phi_\mathrm{e}\right)-\nu^2\sin\left(6\Delta\phi_\mathrm{e}\right)\right).\end{aligned}\tag{A.15}$$

Equations (A.14) and (A.15) are equivalent to the swept areas Cash and Cai [30] obtained apart from different definitions of difference angle. The area swept $S(\Delta\phi)$ is given in Fig. A.1. For the ease of comparison with Figs. 2.3a and 2.3b, the swept areas, which correspond to line stresses $\tau_{xz}/\tau_\mathrm{c}$=$\tau'_{xz}/\tau_\mathrm{c}$= 1/10, 9/10 and 1 are indicated with (coloured) triangle, square, circle and gradient symbols as well in Fig. A.1.

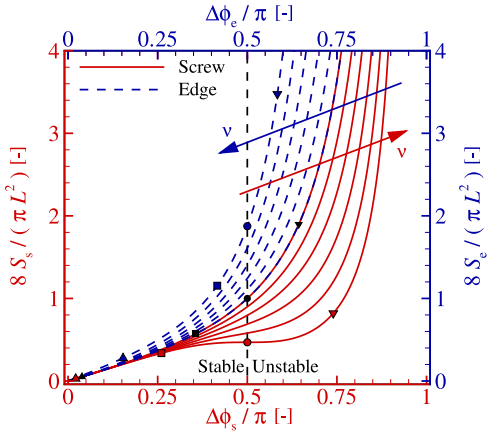

Figure A.1: The normalised swept-out areas $8S_s/(\pi L^2)$ and $8S_e/(\pi L^2)$ as a function of the normalised difference angles $\Delta\phi_s/\pi$ and $\Delta\phi_e/\pi$ for Poisson's ratios $\nu = 0,\ 1/10,\ 1/5,\ 3/10,\ 2/5$ and $1/2$. The coloured arrows indicate an increase in Poisson's ratio ν across equivalently coloured lines.

B Taylor Factor

Using the principle of virtual work, we require that the rate of external anelastic work is equivalent to the rate of internal anelastic work across k slip systems, *i.e.*

$$\boldsymbol{\sigma} : \frac{\partial \boldsymbol{\epsilon}^{\text{an}}}{\partial t} \equiv \sum_k |\tau_{xz} \frac{\partial \gamma_{xz}^{\text{an}}}{\partial t}|, \tag{B.1}$$

where τ_{xz} and γ_{xz}^{an} are the shear stress and anelastic shear strain, respectively, and their magnitudes may vary between slip systems. It is convenient to express the rate of external anelastic work in terms of the principal deformation rates by

$$\frac{\partial W^{\text{an}}}{\partial t} = |\frac{\partial \epsilon_1^{\text{an}}}{\partial t}(\sigma_1 + \lambda\sigma_2 + (1-\lambda)\sigma_3)|, \tag{B.2a}$$

with contraction ratio $\lambda \equiv \partial\epsilon_2^{\text{an}}/\partial\epsilon_1^{\text{an}}$ and conservation of volume during dislocation glide, *i.e.*

$$\frac{\partial \epsilon_2^{\text{an}}}{\partial t} + \frac{\partial \epsilon_2^{\text{an}}}{\partial t} + \frac{\partial \epsilon_2^{\text{an}}}{\partial t} \equiv 0, \tag{B.2b}$$

where $|\frac{\partial \epsilon_1^{\text{an}}}{\partial t}| \geq |\frac{\partial \epsilon_2^{\text{an}}}{\partial t}| \geq |\frac{\partial \epsilon_3^{\text{an}}}{\partial t}|$ are the absolute principal strain rates. In a virtual tensile test, there is a single principal stress component and we rewrite Eq. (B.1) as a function of the normal stress

$$\sigma \frac{\partial \epsilon^{\text{an}}}{\partial t} = \sum_k |\tau_{xz} \frac{\partial \gamma_{xz}^{\text{an}}}{\partial t}|. \tag{B.3a}$$

Following Van Liempt and Sietsma [4] and using the Taylor factor M, we relate the normal stress to the resolved shear stress τ in each grain by

$$M \equiv \frac{\sigma}{\tau} = \sum_k \frac{\partial \gamma_{xz}^{\text{an}}}{\partial \epsilon^{\text{an}}}. \tag{B.3b}$$

Furthermore, we assume: (1) each grain is subjected to a normal stress parallel to the tensile axis [255]; (2) all orientations are equally likely [255]; (3) the resolved shear stress τ is the same in each grain [4]; and (4), each grain extends by the same amount along the tensile axis [254]. Integrating the right-hand side of Eq. (B.3b) with the boundary condition $\gamma_{xz}^{\mathrm{an}}(0) \equiv 0$ for no applied principal strain, we obtain

$$\tau = \frac{\sigma}{M}, \qquad \text{and} \qquad \epsilon^{\mathrm{an}} = \frac{1}{M}\sum_k \gamma_{xz}^{\mathrm{an}}. \tag{B.4}$$

C Inelastic Shear

The normalised anelastic shear strain is

$$\bar{\gamma}_k^{\mathrm{an}}(\bar{\tau}) \equiv \gamma_k^{\mathrm{an}} \frac{\langle l_k \rangle}{b} = \frac{1}{8\alpha_k^2 (\bar{\tau}_k)^2} \left(2\sin^{-1}(\bar{\tau}_k) - \sin\left(2\sin^{-1}(\bar{\tau}_k)\right)\right), \tag{C.1}$$

where the normalised shear stress is

$$\bar{\tau}_k \equiv \frac{\tau_k}{\tau_k^{\mathrm{c}}} = \frac{\tau_k \langle l_k \rangle}{b\mu}, \tag{C.2}$$

with the maximum line stress $\tau_k^{\mathrm{c}} \equiv b\mu/\langle l_k \rangle$. The normalised anelastic tangent modulus is

$$\frac{\Theta_k^{\mathrm{an}}}{\mu} \equiv \left(\frac{\partial \bar{\gamma}_k^{\mathrm{an}}}{\partial \bar{\tau}_k}\right)^{-1} = \frac{2\alpha_k^2 (\bar{\tau}_k)^2}{\dfrac{1}{\sqrt{1-(\bar{\tau}_k)^2}} - \dfrac{1}{\bar{\tau}_k}\sin^{-1}(\bar{\tau}_k)}. \tag{C.3}$$

Equation (3.19) is a separable differential equation for the plastic shear strain:

$$\int_{\gamma_k^{\mathrm{pl}}(\tau_k^{\mathrm{y}})}^{\gamma_k^{\mathrm{pl}}(\tau_k)} \mathrm{d}\gamma' = \int_{\rho_k(\tau_k^{\mathrm{y}})}^{\rho_k(\tau_k)} \left(\frac{\langle \beta_k \rangle}{\alpha_k b}\sqrt{\rho'} - \frac{\langle \xi_k \rangle}{b}\rho'\right)^{-1} \mathrm{d}\rho', \tag{C.4}$$

where $\tau_k^{\mathrm{y}} \leq \tau_k^{\mathrm{c}}$ is the yield strength. The normalised plastic shear strain for a finite shear stress is

$$\bar{\gamma}_k^{\mathrm{pl}} = \frac{2}{\hat{q}_k} \ln\left(\left(1 - \frac{\hat{q}_k \bar{\tau}_k^{\mathrm{y}}}{\langle \beta_k \rangle}\right) \Big/ \left(1 - \frac{\hat{q}_k \bar{\tau}_k}{\langle \beta_k \rangle}\right)\right), \tag{C.5}$$

with a dimensionless parameter $\hat{q}_k \equiv \langle \xi_k \rangle / \langle l_k \rangle$ that is detailed in Sec. 3.3.1. The normalised hardening modulus is

$$\frac{\Theta_k^{\mathrm{pl}}}{\mu} \equiv \left(\frac{\partial \bar{\gamma}_k^{\mathrm{pl}}}{\partial \bar{\tau}_k}\right)^{-1} = \frac{\langle \beta_k \rangle}{2}\left(1 - \frac{\hat{q}_k \bar{\tau}_k}{\langle \beta_k \rangle}\right). \tag{C.6}$$

D Stage-II Work-Hardening

The majority of stage-II work-hardening models have the form:

$$\frac{\partial \rho}{\partial \epsilon_{\mathrm{pl}}} \approx C_1 \sqrt{\rho\left(\epsilon_{\mathrm{pl}}\right)} - C_2 \rho\left(\epsilon_{\mathrm{pl}}\right), \tag{D.1}$$

where C_1 and C_2 are constants with units m^{-1} and no dimension, respectively. Equation (D.1) describes the development of the dislocation density as a function of the true plastic principal strain ϵ_{pl}. Note that glide plane and slip system remain unspecified here, and the dislocation properties are omitted for clarity; the type of dislocation density varies between theories. Equation (D.1) is identical in form to Vetter's version of Bergström's equation, that considers the immobile dislocation density alone [386, 387], and the proto-statistical storage model by Kocks (See Sec. 3.2.2), that originally treats forest dislocations [10]. Combining the (classic) Taylor relationship for the flow strength, $\sigma \sim \alpha' M \mu b \sqrt{\rho}$, and Eq. (D.1), the plastic tangent modulus Θ_{pl} is

$$\Theta_{\mathrm{pl}}\left(\epsilon_{\mathrm{pl}}\right) \approx \frac{1}{2}\alpha' C_1 M \mu b - \frac{1}{2} C_2 \sigma\left(\epsilon_{\mathrm{pl}}\right). \tag{D.2}$$

The saturation stress σ_{s} thus is

$$\sigma_{\mathrm{s}} \equiv \lim_{\epsilon_{\mathrm{pl}} \to \infty} \sigma\left(\epsilon_{\mathrm{pl}}\right) \sim \frac{\alpha' C_1 M \mu b}{C_2}. \tag{D.3}$$

Rewriting Eq. (3.19) as a function of the true plastic principal strain ϵ_{pl}, and comparing the result with Eqs. (D.2), we find

$$\beta \approx \frac{\alpha' C_1 b}{M}; \quad \text{and,} \quad \xi \approx \frac{C_2 b}{M}, \tag{D.4}$$

where ξ is the effective junction length. Equation (D.3) is then used to determine the saturation stress σ_{s} by linear regression on the plastic tangent modulus, and Eq. (D.4) for comparison with the here summarised seminal approach.

E Numerical Solution of Piecewise Equations of Motion

We use Mathematica [289] to verify the analytical results in present manuscript, which is feasible for over-damped motion as well cause the initial dimensionless amplitude $x(0) = X_0$, velocity $\dot{x}(0) = 0$ and phase shift p between base-excitation and mass trajectory are *a priori* known. The Mathematica [289] code we use is given in Listing E.1. The variables correspond to those given in manuscript with the capitalisation and typesetting removed. Note that the given initial trajectory changes to stuck[-((2 **Pi**/r)] == 0 when the dynamic trajectory is continuous.

Example E.1: Mathematica code.

```
dynsys := {(x^\[Prime]\[Prime])[T] == If[stuck[T] == 1, 0, Cos[p + r T] - 2 r z
  Sin[p + r T] - Sign[Derivative[1][x][T]] xf - x[T] - 2 z
  Derivative[1][x][T]], x[-((2 Pi)/r)] == dynx0, x'[-((2 Pi)/r)] == 0.};
statsys := {2 z Derivative[1][x][T] == If[stuck[T] == 1, 0, Cos[staticp + r T]
  - 2 r z Sin[staticp + r T] - Sign[Derivative[1][x][T]] xf - x[T]], x[0] ==
  statx0, x'[0] == 0.};
dynstick = WhenEvent[x'[T] == 0, stuck[T] -> Boole[(Cos[p + r T] - 2 r z Sin[p
  + r T] -x[T])^2 < (xf)^2]];
dynslip = WhenEvent[(Cos[p + r T] - 2 r 5 z Sin[p + r T] - x[T])^2 > (Xf)^2,
  stuck[T] -> 0];
statstick = WhenEvent[(Cos[staticp + r T] - 2 r z Sin[staticp + r T] - x[T])^2
  <= (xf)^2, stuck[T] -> 1];
statslip = WhenEvent[(Cos[staticp + r T] - 2 r z Sin[staticp + r T] - x[T])^2 >
  (xf)^2, stuck[-((2 Pi)/r)] -> 0];
{dynpos, dynvel} = NDSolveValue[{dynsys, dynstick, dynslip, stuck[-((2 Pi)/r)]
  == 1}, {x, x'}, {T, -((2 Pi)/r), (2 Pi)/r}, DiscreteVariables -> stuck[T],
  Method -> {"ImplicitRungeKutta"}];
{statpos, statvel} = NDSolveValue[{statsys, statstick, statslip, stuck[-((2
  Pi)/r)] == 1}, {x, x'}, {T, -((2 Pi)/r), (2 Pi)/r}, DiscreteVariables ->
  stuck[T], Method -> {"EquationSimplification" -> "Residual"}];
```

Bibliography

References

[1] J.D. Eshelby. Dislocations as a cause of mechanical damping in metals. *Proceedings of the Royal Society of London. Series A. Mathematical and Physical Sciences*, 197(1050):396–416, 1949.

[2] J.S. Koehler and G. DeWit. Influence of elastic anisotropy on the dislocation contribution to the elastic constants. *Physical Review*, 116(5):1121, 1959.

[3] B.K. Agrawal and G.S. Verma. Dislocation Contribution to the Elastic Constants of Body-Centered Cubic Crystals. *Physical Review*, 127(2):501, 1962.

[4] P. van Liempt and J. Sietsma. A physically based yield criterion I. Determination of the yield stress based on analysis of pre-yield dislocation behaviour. *Materials Science and Engineering: A*, 662:80–87, 2016.

[5] Z. Arechabaleta, P. van Liempt, and J. Sietsma. Quantification of dislocation structures from anelastic deformation behaviour. *Acta Materialia*, 115:314–323, 2016.

[6] Z. Arechabaleta, P. van Liempt, and J. Sietsma. Unravelling dislocation networks in metals. *Materials Science and Engineering: A*, 710:329–333, 2018.

[7] D. Li and R.H. Wagoner. The Nature of Yielding and Anelasticity in Metals. *Acta Materialia*, page 116625, 2020.

[8] R.B. Sills, N. Bertin, A. Aghaei, and W. Cai. Dislocation networks and the microstructural origin of strain hardening. *Physical Review Letters*, 121(8):085501, 2018.

[9] D. Hull and D.J. Bacon. *Introduction to dislocations*, volume 37. Elsevier, 2011.

[10] D. Kuhlmann-Wilsdorf. Questions you always wanted (or should have wanted) to ask about work-hardening. *Materials Research Innovations*, 1(4):265–297, 1998.

[11] D. Kuhlmann-Wilsdorf. LEDS: Properties and effects of low energy dislocation structures. *Materials Science and Engineering*, 86:53–66, 1987.

[12] A.H. Cottrell. The properties of materials at high rates of strain. In *London Conference of Institute of Mechanical Engineers (IME, London, 1957)*, page 18, 1957.

[13] K. Srivastava, D. Weygand, D. Caillard, and P. Gumbsch. Repulsion leads to coupled dislocation motion and extended work hardening in bcc metals. *Nature Communications*, 11(1):1–8, 2020.

[14] F.C. Frank and W.T. Read Jr. Multiplication processes for slow moving dislocations. *Physical Review*, 79(4):722, 1950.

[15] F.C. Frank. The Frank—Read source. *Proceedings of the Royal Society of London. A. Mathematical and Physical Sciences*, 371(1744):136–138, 1980.

[16] M. Peach and J.S. Koehler. The forces exerted on dislocations and the stress fields produced by them. *Physical Review*, 80(3):436, 1950.

[17] P.M. Anderson, J.P. Hirth, and J. Lothe. *Theory of dislocations*. Cambridge University Press, 2017.

[18] J. Diehl. Zugverformung von Kupfer-Einkristallen. *International Journal of Materials Research*, 47(5):331–343, 1956.

[19] U.F. Kocks. Laws for work-hardening and low-temperature creep. *Journal of engineering materials and technology*, 98(1):76–85, 1976.

[20] U.F. Kocks and H. Mecking. Physics and phenomenology of strain hardening: The FCC case. *Progress in Materials Science*, 48(3):171–273, 2003.

[21] Y.U. Estrin and H. Mecking. A unified phenomenological description of work hardening and creep based on one-parameter models. *Acta Metallurgica*, 32(1):57–70, 1984.

[22] Y. Bergström and W. Roberts. A dislocation model for dynamical strain ageing of α-iron in the jerky-flow region. *Acta Metallurgica*, 19(11):1243–1251, 1971.

[23] Y. Bergström and H. Hallén. An improved dislocation model for the stress-strain behaviour of polycrystalline α-Fe. *Materials Science and Engineering*, 55(1):49–61, 1982.

[24] P. Van Liempt. Workhardening and substructural geometry of metals. *Journal of Materials Processing Technology*, 45(1-4):459–464, 1994.

[25] P. Van Liempt, M. Onink, and A. Bodin. Modelling the influence of dynamic strain ageing on deformation behaviour. *Advanced Engineering Materials*, 4(4):225–232, 2002.

[26] F. Roters, D. Raabe, and G. Gottstein. Work hardening in heterogeneous alloys - a microstructural approach based on three internal state variables. *Acta Materialia*, 48(17):4181–4189, 2000.

[27] A. Ma and F. Roters. A constitutive model for fcc single crystals based on dislocation densities and its application to uniaxial compression of aluminium single crystals. *Acta Materialia*, 52(12):3603–3612, 2004.

[28] A. Torkabadi, E.S. Perdahcıoğlu, V.T. Meinders, and A.H. van den Boogaard. On the nonlinear anelastic behavior of AHSS. *International Journal of Solids and Structures*, 151:2–8, 2018.

[29] S. Shao, M.M. Khonsari, J. Wang, N. Shamsaei, and N. Li. Frequency dependent deformation reversibility during cyclic loading. *Materials Research Letters*, 6(7):390–397, 2018.

[30] W.D. Cash and W. Cai. Dislocation contribution to acoustic nonlinearity: The effect of orientation-dependent line energy. *Journal of Applied Physics*, 109(1):014915, 2011.

[31] G. Schoeck. Dislocation theory of plasticity of metals. In *Advances in Applied Mechanics*, volume 4, pages 229–279. Elsevier, 1956.

[32] A. Akhondzadeh, R.B. Sills, N. Bertin, and W. Cai. Dislocation Density-Based Plasticity Model from Massive Discrete Dislocation Dynamics database. *Journal of the Mechanics and Physics of Solids*, pages 104–152, 2020.

[33] G.I. Taylor. The mechanism of plastic deformation of crystals. Part I.—Theoretical. *Proceedings of the Royal Society of London. A.*, 145(855):362–387, 1934.

[34] G. Saada. Sur le durcissement dû à la recombinaison des dislocations. *Acta Metallurgica*, 8(12):841–847, 1960.

[35] L. Kubin, B. Devincre, and T. Hoc. Toward a physical model for strain hardening in FCC crystals. *Materials Science and Engineering: A*, 483:19–24, 2008.

[36] A. Torkabadi. *Towards an Accurate Springback Prediction.* PhD thesis, University of Twente, 2018.

[37] J.S. Van Dokkum, C. Bos, S.E. Offerman, and J. Sietsma. Influence of dislocations on the apparent elastic constants in single metallic crystallites: an analytical approach. *Materialia*, 20:101178, 2021.

[38] S. Vitzthum, J.R. Kornmeier, M. Hofmann, M. Gruber, R. Norz, E. Maawad, J. Mendiguren, and W. Volk. In-situ analysis of the elastic-plastic characteristics of high strength dual-phase steel. *Materials Science and Engineering: A*, page 144097, 2022.

[39] G. Zhu, C. Yang, G. Shen, Y. Peng, and B. Shi. The asymmetric pre-yielding behaviour during tension and compression for a rolled AZ31 Mg alloy. *International Journal of Material Forming*, 15(3):1–12, 2022.

[40] J. Ma, H. Li, and M.W. Fu. Modelling of springback in tube bending: A generalized analytical approach. *International Journal of Mechanical Sciences*, 204:106516, 2021.

[41] J. Ma, H. Li, Z.R. He, H. Yang, and M.W. Fu. Complex unloading behavior of titanium alloy in cold and thermal-mechanical working. *International Journal of Mechanical Sciences*, 233:107672, 2022.

[42] G. Piobert, A.J. Morin, and I. Didion. Commission des principes du tir. *Mémorial de l'artillerie*, 5:501–552, 1842.

[43] W. Lüders. Über die äusserung der Elasticität an stahlartigen Eisenstäben und Stahlstäben, und über eine beim biegen solcher Stäbe beobachtete Molecularbewegung. *Dinglers Polytech J*, 5:18–22, 1860.

[44] R. Schwab and V. Ruff. On the nature of the yield point phenomenon. *Acta Materialia*, 61(5):1798–1808, 2013.

[45] J.W. Rudnicki and J.R. Rice. Conditions for the localization of deformation in pressure-sensitive dilatant materials. *Journal of the Mechanics and Physics of Solids*, 23(6):371–394, 1975.

[46] A.H. Cottrell and B.A. Bilby. Dislocation theory of yielding and strain ageing of iron. *Proceedings of the Physical Society. Section A*, 62(1):49, 1949.

[47] W.G. Johnston and J.J. Gilman. Dislocation velocities, dislocation densities, and plastic flow in lithium fluoride crystals. *Journal of Applied Physics*, 30(2):129–144, 1959.

[48] G.T. Hahn. A model for yielding with special reference to the yield-point phenomena of iron and related bcc metals. *Acta Metallurgica*, 10(8):727–738, 1962.

[49] Z.H. Cai, S.Y. Jing, H.Y. Li, K.M. Zhang, R.D.K. Misra, H. Ding, and Z.Y. Tang. The influence of microstructural characteristics on yield point elongation phenomenon in Fe-0.2C-11Mn-2Al steel. *Materials Science and Engineering: A*, 739:17–25, 2019.

[50] E.O. Hall. The deformation and ageing of mild steel: II characteristics of the Lüders deformation. *Proceedings of the Physical Society. Section B*, 64(9):742, 1951.

[51] R.A. Elliot, E. Orowan, T. Udoguchi, and A.S. Argon. Absence of yield points in iron on strain reversal after aging, and the Bauschinger overshoot. *Mechanics of Materials*, 36(11):1143–1153, 2004.

[52] J. Kim and D.-N. Kim. Computational studies for the yield-point phenomenon of metals. *Multiscale Science and Engineering*, 2(2):90–106, 2020.

[53] S. Kyriakides and J.E. Miller. On the Propagation of Lüders bands in Steel Strips. *Journal of Applied Mechanics*, 67(4):645–654, 2000.

[54] K.C. Park and J.B. Yoon. Analysis on the mechanism of fluting in the bending of low carbon steels. *Transactions of Materials Processing*, 16(4):317–322, 2007.

[55] F. Yoshida. A constitutive model of cyclic plasticity. *International Journal of Plasticity*, 16(3-4):359–380, 2000.

[56] A. Žerovnik, R. Kunc, and I. Prebil. Yield-point phenomenon in constitutive models of cyclic plasticity. *Computational Materials Science*, 49(3):473–482, 2010.

[57] A.M. Giarola, P.H.R. Pereira, P.A. Stemler, A.E.M. Pertence, H.B. Campos, M.T.P. Aguilar, and P.R. Cetlin. Strain heterogeneities in the rolling direction of steel sheets submitted to the skin pass: A finite element analysis. *Journal of Materials Processing Technology*, 216:234–247, 2015.

[58] M. Mazière and S. Forest. Strain gradient plasticity modeling and finite element simulation of Lüders band formation and propagation. *Continuum Mechanics and Thermodynamics*, 27(1):83–104, 2015.

[59] M. Mazière, J. Besson, S. Forest, B. Tanguy, H. Chalons, and F. Vogel. Numerical aspects in the finite element simulation of the Portevin–Le Chatelier effect. *Computer Methods in Applied Mechanics and Engineering*, 199(9-12):734–754, 2010.

[60] G.E. Moore et al. c. In *Electron devices meeting*, volume 21, pages 11–13. Washington, DC, 1975.

[61] A. Marais, M. Mazière, S. Forest, A. Parrot, and P. Le Delliou. Identification of a strain-aging model accounting for Lüders behavior in a C-Mn steel. *Philosophical Magazine*, 92(28-30):3589–3617, 2012.

[62] R. Schwab and A. Harter. Extracting true stresses and strains from nominal stresses and strains in tensile testing. *Strain*, 57(6):e12396, 2021.

[63] R. Schwab. Understanding the complete loss of uniform plastic deformation of some ultrafine-grained metallic materials in tensile straining. *International Journal of Plasticity*, 113:218–235, 2019.

[64] G.T. Van Rooyen. The stress and strain distribution in a propagating Lüders front accompanying the yield-point phenomenon in iron. *Materials Science and Engineering*, 3(2):105–117, 1968.

[65] G.T. Van Rooyen. Basic factors which influence the Lüders strain during discontinuous yielding. *Materials Science and Engineering*, 7(1):37–48, 1971.

[66] S. Beissel and T. Belytschko. On patterns of deformation in phase transformations and Lüders bands. *International Journal of Solids and Structures*, 33(12):1689–1707, 1996.

[67] E.O. Hall. *Yield point phenomena in metals and alloys*. Springer Science & Business Media, 2012.

[68] W.M. Lomer. The yield phenomenon in polycrystalline mild steel. *Journal of the Mechanics and Physics of Solids*, 1(1):64–73, 1952.

[69] Y.-L. Cai, S.-L. Yang, S.-H. Fu, and Q.-C. Zhang. The Influence of Specimen Thickness on the Lüders effect of a 5456 Al-based alloy: Experimental Observations. *Metals*, 6(5):120, 2016.

[70] G.E. Dieter and D. Bacon. *Mechanical metallurgy*, volume 3. McGraw-hill New York, 1976.

[71] B.B. Hundy. Inhomogeneous Deformation During the Temper Rolling of Annealed Mild Steel. *Journal of the Iron and Steel Institute*, 181:313 – 315, 1955.

[72] W.F. Hosford and R.M. Caddell. *Metal forming: mechanics and metallurgy*. Cambridge university press, 2011.

[73] B. Sun, Y. Ma, N. Vanderesse, R.S. Varanasi, W. Song, P. Bocher, D. Ponge, and D. Raabe. Macroscopic to nanoscopic in situ investigation on yielding mechanisms in ultrafine grained medium Mn steels: role of the austenite-ferrite interface. *Acta Materialia*, 178:10–25, 2019.

[74] S. Nagarajan, R. Narayanaswamy, and V. Balasubramaniam. A systematic approach for effective measurement of deformation front orientation accompanying plastic instability. *Results in Physics*, 15:102534, 2019.

[75] P. Ebenberger, P.J. Uggowitzer, S. Kirnstötter, B. Gerold, S. Zaefferer, and S. Pogatscher. Processing-controlled suppression of Lüders elongation in AlMgMn alloys. *Scripta Materialia*, 166:64–67, 2019.

[76] J.F. Hallai and S. Kyriakides. Underlying material response for Lüders-like instabilities. *International Journal of Plasticity*, 47:1–12, 2013.

[77] B. Çolak. How the skin-pass rolling reduction ratio affects the strain aging behaviour of low-carbon steel sheets. *Ironmaking & Steelmaking*, 48(10):1254–1260, 2021.

[78] J. Kim, K.-C. Park, and D.-N. Kim. Investigating the fluting defect in v-bending due to the yield-point phenomenon and its reduction via roller-leveling process. *Journal of Materials Processing Technology*, 270:59–81, 2019.

[79] R. Pearce. *Sheet metal forming*. Springer Science & Business Media, 1991.

[80] H.E. Theis. *Handbook of Metalforming processes*. CRC Press, 1999.

[81] R.D. Butler and D.V. Wilson. The mechanical behavior of temper rolled steel sheets. *Journal of the Iron and Steel Institute*, 201(1):16, 1963.

[82] J. Kim and D.-N. Kim. Robust stress integration algorithms for implicit elastoviscoplastic finite element analysis of materials with yield-point phenomenon. *International Journal of Mechanical Sciences*, 150:277–289, 2019.

[83] K.C. Park. Leveling of aged low carbon steel sheets in order to prevent shape defects after stamping. *Transactions of Materials Processing*, 24(4):241–247, 2015.

[84] T. Pepelnjak and B. Barisic. Analysis and elimination of the stretcher strains on TH415 tinplate rings in the stamping process. *Journal of Materials Processing Technology*, 186(1-3):111–119, 2007.

[85] H. Kantereit. Bake hardening behavior of advanced high strength steels under manufacturing conditions. Technical report, SAE Technical Paper, 2011.

[86] S. Holmberg and B. Nejabat. Numerical assessment of stiffness and dent properties of automotive exterior panels. *Materials & Design*, 25(5):361–368, 2004.

[87] J. Kim, H. Lee, K. Oh, D.-Y. Seok, S. Park, Y. Kang, and D.-N. Kim. Experimental and numerical investigation on the dent resistance of a dual phase steel originated from the yield-point phenomenon. *Journal of Materials Processing Technology*, 289:116929, 2021.

[88] V. Ballarin, M. Soler, A. Perlade, X. Lemoine, and S. Forest. Mechanisms and modeling of bake-hardening steels: Part I. Uniaxial tension. *Metallurgical and Materials Transactions A*, 40(6):1367–1374, 2009.

[89] J.S.H. Lake. Control of discontinuous yielding by temper rolling. *Journal of Mechanical Working Technology*, 12(1):35–66, 1985.

[90] J.W. Green. Skin Pass & Temper Rolling-A Review of Seminar organised by the Rolling Group of IoM. *Steel Times International*, 26(9):49, 2002.

[91] F. Yoshida, Y. Kaneda, and S. Yamamoto. A plasticity model describing yield-point phenomena of steels and its application to FE simulation of temper rolling. *International Journal of Plasticity*, 24(10):1792–1818, 2008.

[92] H. Kijima. Influence of roll radius on contact condition and material deformation in skin-pass rolling of steel strip. *Journal of Materials Processing Technology*, 213(10):1764–1771, 2013.

[93] H. Kijima. Influence of roll radius on roughness transfer in skin-pass rolling of steel strip. *Journal of Materials Processing Technology*, 214(5):1111–1119, 2014.

[94] D.J. Dingley and D. McLean. Components of the flow stress of iron. *Acta Metallurgica*, 15(5):885–901, 1967.

[95] S. Gao, M. Chen, M. Joshi, A. Shibata, and N. Tsuji. Yielding behavior and its effect on uniform elongation in IF steel with various grain sizes. *Journal of Materials Science*, 49:6536–6542, 2014.

[96] D.H. Johnson, M.R. Edwards, and P. Chard-Tuckey. Microstructural effects on the magnitude of Lüders strains in a low alloy steel. *Materials Science and Engineering: A*, 625:36–45, 2015.

[97] B. Mao and Y. Liao. Modeling of lüders elongation and work hardening behaviors of ferrite-pearlite dual phase steels under tension. *Mechanics of Materials*, 129:222–229, 2019.

[98] H. Shi, J. Li, J. Mao, and W. Lu. The elimination of the yield point phenomenon in a new zirconium alloy: Influence of degree of recrystallization on the tensile properties. *Scripta Materialia*, 169:28–32, 2019.

[99] D.H. Kim, J.-H. Kang, J.H. Ryu, and S.-J Kim. Effect of austenitization of cold-rolled 10 wt% Mn steel on microstructure and discontinuous yielding. *Materials Science and Engineering: A*, 774:138930, 2020.

[100] M.S. Mohsenzadeh and M. Mazinani. On the yield point phenomenon in low-carbon steels with ferrite-cementite microstructure. *Materials Science and Engineering: A*, 673:193–203, 2016.

[101] J.G. Kim, H.Y. Um, J.Y. Kang, H.J. Jeong, K.H. Choi, S.-H. Lee, S.-Y. Kim, J.-S. Chung, and H.S. Kim. Quantitative study on yield point phenomenon of low carbon steels processed by compact endless casting and rolling. *Materials Science and Engineering: A*, 734:408–415, 2018.

[102] V.M. Farber, O.N. Polukhina, D.I. Vichuzhanin, V.A. Khotinov, and S.V. Smirnov. A Study of Plastic Strain Before and on the Yield Plateau of Steel 08G2B by Correlation of Digital Images. Part II. Functioning of Flow Channels and Zones in them. *Metal Science and Heat Treatment*, 61:405–410, 2019.

[103] Y. Wang, Y. Tomota, T. Ohmura, W. Gong, S. Harjo, and M. Tanaka. Continuous and discontinuous yielding behaviors in ferrite-cementite steels. *Acta Materialia*, 196:565–575, 2020.

[104] R. Sarkar, A. Mukhopadhyay, P. Ghosal, T.K. Nandy, and K.K. Ray. A study on anomalous yield drop behaviour in modified beta titanium alloys. *Philosophical Magazine*, 100(4):399–425, 2020.

[105] R.S. Varanasi, S. Zaefferer, B. Sun, and D. Ponge. Localized deformation inside the Lüders front of a medium manganese steel. *Materials Science and Engineering: A*, 824:141816, 2021.

[106] X.T. Wang, H. Hamasaki, M. Yamamura, R. Yamauchi, T. Maeda, Y. Shirai, and F. Yoshida. A Study of High temperature viscoplastic deformation of beta titanium alloy considering yield-point phenomena. In *Key Engineering Materials*, volume 410, pages 177–185. Trans Tech Publ, 2009.

[107] A. Momeni, S.M. Abbasi, M. Morakabati, and A. Akhondzadeh. Yield point phenomena in TIMETAL 125 beta Ti alloy. *Materials Science and Engineering: A*, 643:142–148, 2015.

[108] H.B. Sun, F. Yoshida, M. Ohmori, and X. Ma. Effect of strain rate on Lüders band propagating velocity and Lüders strain for annealed mild steel under uniaxial tension. *Materials Letters*, 57(29):4535–4539, 2003.

[109] I. Jandrlić, S. Rešković, and F. Vodopivec. Determining the amount of Lüders band in niobium microalloyed steel. *Metalurgija*, 55(4):631–634, 2016.

[110] A.R. Khalifeh, A.D. Banaraki, H.D. Manesh, and M.D. Banaraki. Investigating of the tensile mechanical properties of structural steels at high strain rates. *Materials Science and Engineering: A*, 712:232–239, 2018.

[111] J. Ma, H. Liu, Q. Lu, Y. Zhong, L. Wang, and Y. Shen. Temperature-Dependent Macroscopic Mechanical Behaviors and Their Microscopic Explanations in a Medium Mn Steel. *Metallurgical and Materials Transactions A*, 51:5180–5186, 2020.

[112] J.-H. Shin, J.-S. Jeong, J. Lee, S.-D. Kim, J.H. Jang, J. Moon, H.-Y. Ha, and T.-H. Lee. Nitrogen-induced yield point phenomenon in an austenitic steel. *Materials Science and Engineering: A*, 774:138897, 2020.

[113] S. Nagarajan, N. Raghu, and B. Venkatraman. Advanced imaging for early prediction and characterization of zone of Lüders band nucleation associated with pre-yield microstrain. *Materials Science and Engineering: A*, 561:203–211, 2013.

[114] T. Brlić, S. Rešković, F. Vodopivec, and I. Jandrlić. Lüders bands at the beginning of the plastic flow of materials. *Metalurgija*, 57(4):357–359, 2018.

[115] H. Qiu, T. Inoue, and R. Ueji. Experimental measurement of the variables of Lüders deformation in hot-rolled steel via digital image correlation. *Materials Science and Engineering: A*, 790:139756, 2020.

[116] H. Qiu, T. Inoue, and R. Ueji. In-Situ observation of Lüders band formation in hot-rolled steel via digital image correlation. *Metals*, 10(4):530, 2020.

[117] D.E. Delwiche and D.W. Moon. Orientation of Lüders band fronts. *Materials Science and Engineering*, 7(4):203–207, 1971.

[118] N. Srinivasan, N. Raghu, and B. Venkatraman. Study on the deformation band characteristics in mild steel using digital image correlation. *Journal of Multidisciplinary Engineering Science and Technology*, 1(5):400–403, 2014.

[119] V.I. Danilov, V.V. Gorbatenko, L.B. Zuev, D.V. Orlova, and L.V. Danilova. Luders deformation of low-carbon steel. *Steel in Translation*, 47(10):662–668, 2017.

[120] V.S. Ananthan and E.O. Hall. Macroscopic aspects of Lüders band deformation in mild steel. *Acta Metallurgica et Materialia*, 39(12):3153–3160, 1991.

[121] D.E. Delwiche and D.W. Moon. Strain profile of a propagating Lüders front. *Materials Science and Engineering*, 9:347–354, 1972.

[122] C. Müller, M. Samri, R. Hensel, E. Arzt, and M.H. Müser. Revealing the coaction of viscous and multistability hysteresis in an adhesive, nominally flat punch: A combined numerical and experimental study. *Journal of the Mechanics and Physics of Solids*, page 105260, 2023.

[123] P.R. Guduru and C. Bull. Detachment of a rigid solid from an elastic wavy surface: Experiments. *Journal of the Mechanics and Physics of Solids*, 55(3):473–488, 2007.

[124] A. Sanner and L. Pastewka. Crack-front model for adhesion of soft elastic spheres with chemical heterogeneity. *Journal of the Mechanics and Physics of Solids*, 160:104781, 2022.

[125] S. Hong, G. Erdogan, K. Hedrick, and F. Borrelli. Tyre–road friction coefficient estimation based on tyre sensors and lateral tyre deflection: Modelling, simulations and experiments. *Vehicle System Dynamics*, 51(5):627–647, 2013.

[126] A. Genovese, F. Farroni, A. Papangelo, and M. Ciavarella. A discussion on present theories of rubber friction, with particular reference to different possible choices of arbitrary roughness cutoff parameters. *Lubricants*, 7(10):85, 2019.

[127] S. Hemette, J. Cayer-Barrioz, and D. Mazuyer. Thermal effects versus viscoelasticity in ice-rubber friction mechanisms. *Tribology International*, 162:107129, 2021.

[128] A. Tiwari, T. Tolpekina, H. van Benthem, M.K. Gunnewiek, and B.N.J. Persson. Rubber adhesion and friction: role of surface energy and contamination films. *Frontiers in Mechanical Engineering*, page 114, 2021.

[129] P. Yu, D. Zhang, Y. Ma, and J. Hong. Dynamic modeling and vibration characteristics analysis of the aero-engine dual-rotor system with Fan blade out. *Mechanical Systems and Signal Processing*, 106:158–175, 2018.

[130] P. Chizhik, M. Friedrichs, D. Dietzel, and A. Schirmeisen. Tribological analysis of contacts between glass and tungsten carbide near the glass transition temperature. *Tribology Letters*, 68(4):1–10, 2020.

[131] M.A. Meitl, Z.-T. Zhu, V. Kumar, K.J. Lee, X. Feng, Y.Y. Huang, I. Adesida, R.G. Nuzzo, and J.A. Rogers. Transfer printing by kinetic control of adhesion to an elastomeric stamp. *Nature Materials*, 5(1):33–38, 2006.

[132] H. Zhou, W. Qin, Q. Yu, H. Cheng, X. Yu, and H. Wu. Transfer printing and its applications in flexible electronic devices. *Nanomaterials*, 9(2):283, 2019.

[133] A. Martinez-Rivas, G.K. González-Quijano, S. Proa-Coronado, C. Séverac, and E. Dague. Methods of micropatterning and manipulation of cells for biomedical applications. *Micromachines*, 8(12):347, 2017.

[134] S. Neupane, N.A. Rivas, P. Losada-Pérez, J. D'Haen, H. Noei, T. Keller, A. Stierle, M. Rudolph, A. Terfort, O. Bertran, et al. A model study on controlling dealloying corrosion attack by lateral modification of surfactant inhibitors. *npj Materials Degradation*, 5(1):1–6, 2021.

[135] L. Jiang, M. Wu, Q. Yu, Y. Shan, and Y. Zhang. Investigations on the Adhesive Contact Behaviors between a Viscoelastic Stamp and a Transferred Element in Microtransfer Printing. *Coatings*, 11(10):1201, 2021.

[136] J. Shintake, V. Cacucciolo, D. Floreano, and H. Shea. Soft robotic grippers. *Advanced Materials*, 30(29):1707035, 2018.

[137] H. Yao, W. Yang, W. Cheng, Y.J. Tan, H.H. See, S. Li, H.P.A. Ali, B.Z.H. Lim, Z. Liu, and Benjamin C.K. Tee. Near–hysteresis-free soft tactile electronic skins for wearables and reliable machine learning. *Proceedings of the National Academy of Sciences*, 117(41):25352–25359, 2020.

[138] R. Coulson, C.J. Stabile, K.T. Turner, and C. Majidi. Versatile soft robot gripper enabled by stiffness and adhesion tuning via thermoplastic composite. *Soft Robotics*, 9(2):189–200, 2022.

[139] J.-W. Jeong, G. Shin, S.I. Park, K.J. Yu, L. Xu, and J.A. Rogers. Soft materials in neuroengineering for hard problems in neuroscience. *Neuron*, 86(1):175–186, 2015.

[140] R. Villey, C. Creton, P.-P. Cortet, M.-J. Dalbe, T. Jet, B. Saintyves, S. Santucci, L. Vanel, D.J. Yarusso, and M. Ciccotti. Rate-dependent elastic hysteresis during the peeling of pressure sensitive adhesives. *Soft Matter*, 11(17):3480–3491, 2015.

[141] A.G. Peressadko, N. Hosoda, and B.N.J. Persson. Influence of surface roughness on adhesion between elastic bodies. *Physical Review Letters*, 95(12):1–4, 2005.

[142] A. Tiwari, L. Dorogin, A.I. Bennett, K.D. Schulze, W.G. Sawyer, M. Tahir, G. Heinrich, and B.N.J. Persson. The effect of surface roughness and viscoelasticity on rubber adhesion. *Soft Matter*, 13(19):3602–3621, 2017.

[143] X. Li, D. Tao, H. Lu, P. Bai, Z. Liu, L. Ma, Y. Meng, and Y. Tian. Recent developments in gecko-inspired dry adhesive surfaces from fabrication to application. *Surface Topography: Metrology and Properties*, 7(2):023001, 2019.

[144] M.G. Mazzotta, A.A. Putnam, M.A. North, and J.J. Wilker. Weak bonds in a biomimetic adhesive enhance toughness and performance. *Journal of the American Chemical Society*, 142(10):4762–4768, 2020.

[145] K.L. Johnson. *Contact mechanics and adhesion of viscoelastic spheres*. ACS Publications, 2000.

[146] Y.-Y. Lin and C.Y. Hui. Mechanics of contact and adhesion between viscoelastic spheres: an analysis of hysteresis during loading and unloading. *Journal of Polymer Science Part B: Polymer Physics*, 40(9):772–793, 2002.

[147] B. Lorenz, B.A. Krick, N. Mulakaluri, M. Smolyakova, S. Dieluweit, W.G. Sawyer, and B.N.J. Persson. Adhesion: Role of bulk viscoelasticity and surface roughness. *Journal of Physics Condensed Matter*, 25(22), 2013.

[148] V.L. Popov. A Note by KL Johnson on the History of the JKR Theory. *Tribology Letters*, 69(4):1–3, 2021.

[149] A. Papangelo and M. Ciavarella. A criterion for the effective work of adhesion in loading and unloading of adhesive soft solids from rough surfaces. *Tribology Letters*, 69(1):1–10, 2021.

[150] M.H. Müser and L. Nicola. Modeling the surface topography dependence of friction, adhesion, and contact compliance. *MRS Bulletin*, pages 1–8, 2023.

[151] H.L. Costa, F.J. Profito, X. Zhang, and K.A. Thole. Optimizing the surface of manufactured components for friction, adhesion, and convective heat transfer. *MRS Bulletin*, pages 1–13, 2023.

[152] M.K. Ben-Larbi, R. Hensel, G. Atzeni, E. Arzt, and E. Stoll. Orbital debris removal using micropatterned dry adhesives: Review and recent advances. *Progress in Aerospace Sciences*, 134:100850, 2022.

[153] K. Kendall. *Molecular adhesion and its applications: the sticky universe*. Springer Science & Business Media, 2007.

[154] B.N.J. Persson and E. Tosatti. The effect of surface roughness on the adhesion of elastic solids. *The Journal of Chemical Physics*, 115(12):5597–5610, 2001.

[155] H. Kesari and A.J. Lew. Effective macroscopic adhesive contact behavior induced by small surface roughness. *Journal of the Mechanics and Physics of Solids*, 59(12):2488–2510, 2011.

[156] M. Ciavarella. On roughness-induced adhesion enhancement. *The Journal of Strain Analysis for Engineering Design*, 51(7):473–481, 2016.

[157] S. Dalvi, A. Gujrati, S.R. Khanal, L. Pastewka, A. Dhinojwala, and T.D.B. Jacobs. Linking energy loss in soft adhesion to surface roughness. *Proceedings of the National Academy of Sciences*, 116(51):25484–25490, 2019.

[158] S. Medina and D. Dini. A numerical model for the deterministic analysis of adhesive rough contacts down to the nano-scale. *International Journal of Solids and Structures*, 51(14):2620–2632, 2014.

[159] Y. Zhu, Z. Zheng, Y. Zhang, H.A. Wu, and J. Yu. Adhesion of elastic wavy surfaces: Interface strengthening/weakening and mode transition mechanisms. *Journal of the Mechanics and Physics of Solids*, 151:104402, 2021.

[160] B. Zappone, K.J. Rosenberg, and J. Israelachvili. Role of nanometer roughness on the adhesion and friction of a rough polymer surface and a molecularly smooth mica surface. *Tribology Letters*, 26(3):191–201, 2007.

[161] I.A. Lyashenko and R. Pohrt. Adhesion between rigid indenter and soft rubber layer: Influence of roughness. *Frontiers in Mechanical Engineering*, 6(July):1–10, 2020.

[162] K.N.G. Fuller and D. Tabor. The effect of surface roughness on the adhesion of elastic solids. *Proceedings of the Royal Society of London. A. Mathematical and Physical Sciences*, 345(1642):327–342, 1975.

[163] G.A.D. Briggs and B.J. Briscoe. The effect of surface topography on the adhesion of elastic solids. *Journal of Physics D: Applied Physics*, 10(18):2453, 1977.

[164] K.N.G. Fuller and A.D. Roberts. Rubber rolling on rough surfaces. *Journal of Physics D: Applied Physics*, 14(2):221, 1981.

[165] C.A. Dahlquist. Pressure-sensitive adhesives. *Treatise on adhesion and adhesives*, 2:219–260, 1969.

[166] C.A. Dahlquist. Tack. Adhesion Fundamentals and Practice. *London: McLaren and Sons Ltd*, pages 143–151, 1966.

[167] A. Pepelyshev, F.M. Borodich, B.A. Galanov, E.V. Gorb, and S.N. Gorb. Adhesion of soft materials to rough surfaces: Experimental studies, statistical analysis and modelling. *Coatings*, 8(10):1–17, 2018.

[168] M. Ciavarella, J.A. Greenwood, and J.R. Barber. Effect of tabor parameter on hysteresis losses during adhesive contact. *Journal of the Mechanics and Physics of Solids*, 98:236–244, 2017.

[169] M. Ciavarella, J. Joe, A. Papangelo, and J.R. Barber. The role of adhesion in contact mechanics. *Journal of the Royal Society Interface*, 16(151):20180738, 2019.

[170] A. Wang, Y. Zhou, and M.H. Müser. Modeling adhesive hysteresis. *Lubricants*, 9(2):17, 2021.

[171] M. Barquins and D. Maugis. Tackiness of elastomers. *The Journal of Adhesion*, 13(1):53–65, 1981.

[172] P.R. Guduru. Detachment of a rigid solid from an elastic wavy surface: Theory. *Journal of the Mechanics and Physics of Solids*, 55(3):445–472, 2007.

[173] G. Carbone, E. Pierro, and G. Recchia. Loading-unloading hysteresis loop of randomly rough adhesive contacts. *Physical Review E - Statistical, Nonlinear, and Soft Matter Physics*, 92(6):1–8, 2015.

[174] A.A. Griffith. VI. The phenomena of rupture and flow in solids. *Philosophical Transactions of the Royal Society of London. Series A*, 221(582-593):163–198, 1921.

[175] J.A. Greenwood. Reflections on and extensions of the Fuller and Tabor theory of rough surface adhesion. *Tribology Letters*, 65(4):1–12, 2017.

[176] Y.L. Chen, C.A. Helm, and J.N. Israelachvili. Molecular mechanisms associated with adhesion and contact angle hysteresis of monolayer surfaces. *Journal of Physical Chemistry*, 95(26):10736–10747, 1991.

[177] M.K. Chaudhury, T. Weaver, C.Y. Hui, and E.J. Kramer. Adhesive contact of cylindrical lens and a flat sheet. *Journal of Applied Physics*, 80(1):30–37, 1996.

[178] G.-P. Ostermeyer, V.L. Popov, E.V. Shilko, and O.S. Vasiljeva. *Multiscale Biomechanics and Tribology of Inorganic and Organic Systems: In Memory of Professor Sergey Psakhie*. Springer Nature, 2021.

[179] I.A. Lyashenko and V.L. Popov. Dissipation of Mechanical Energy in an Oscillating Adhesive Contact between a Hard Indenter and an Elastomer. *Technical Physics Letters*, 46(11):1092–1095, 2020.

[180] S. Perutz, E.J.. Kramer, J. Baney, C.Y. Hui, and C. Cohen. Investigation of adhesion hysteresis in poly(dimethylsiloxane) networks using the JKR technique. *Journal of Polymer Science, Part B: Polymer Physics*, 36(12):2129–2139, 1998.

[181] I. Etsion, Y. Kligerman, and Y. Kadin. Unloading of an elastic-plastic loaded spherical contact. *International Journal of Solids and Structures*, 42(13):3716–3729, 2005.

[182] Y. Kadin, Y. Kligerman, and I. Etsion. Unloading an elastic-plastic contact of rough surfaces. *Journal of the Mechanics and Physics of Solids*, 54(12):2652–2674, 2006.

[183] J.A. Greenwood and K.L. Johnson. The mechanics of adhesion of viscoelastic solids. *Philosophical Magazine A: Physics of Condensed Matter, Structure, Defects and Mechanical Properties*, 43(3):697–711, 1981.

[184] V. Vaenkatesan, Z. Li, W.P. Vellinga, and W.H. de Jeu. Adhesion and friction behaviours of polydimethylsiloxane - A fresh perspective on JKR measurements. *Polymer*, 47(25):8317–8325, 2006.

[185] G. Violano and L. Afferrante. Adhesion of compliant spheres: an experimental investigation. *Procedia Structural Integrity*, 24:251–258, 2019.

[186] G. Violano, A. Chateauminois, and L. Afferrante. A JKR-like solution for viscoelastic adhesive contacts. *Frontiers in Mechanical Engineering*, 7:25, 2021.

[187] G. Violano, G. Orlando, G.P. Demelio, and L. Afferrante. Adhesion of viscoelastic media: an assessment of a recent JKR-like solution. *IOP Conference Series: Materials Science and Engineering*, 1214(1):012038, 2022.

[188] L. Dorogin, A. Tiwari, C. Rotella, P. Mangiagalli, and B.N.J. Persson. Role of preload in adhesion of rough surfaces. *Physical Review Letters*, 118(23):238001, 2017.

[189] V. Acito, M. Ciavarella, A.M. Prevost, and A. Chateauminois. Adhesive contact of model randomly rough rubber surfaces. *Tribology Letters*, 67(2):1–10, 2019.

[190] G. Violano, A. Chateauminois, and L. Afferrante. Rate-dependent adhesion of viscoelastic contacts, Part I: Contact area and contact line velocity within model randomly rough surfaces. *Mechanics of Materials*, 160:103926, 2021.

[191] Gu. Violano, A. Chateauminois, and L. Afferrante. Rate-dependent adhesion of viscoelastic contacts. Part II: Numerical model and hysteresis dissipation. *Mechanics of Materials*, 158:103884, 2021.

[192] K.L. Johnson, K. Kendall, and A.D. Roberts. Surface energy and the contact of elastic solids. *Proceedings of the Royal Society of London. Series A*, 324:301–313, 1971.

[193] M. Ciavarella. An upper bound for viscoelastic pull-off of a sphere with a Maugis-Dugdale model. *Journal of Adhesion*, pages 1–14, 2021.

[194] D. Maugis. Adhesion of spheres: the JKR-DMT transition using a Dugdale model. *Journal of Colloid and Interface Science*, 150(1):243–269, 1992.

[195] B.V. Derjaguin, V.M. Muller, and Y.P. Toporov. Effect of contact deformations on the adhesion of particles. *Journal of Colloid and Interface Science*, 53(2):314–326, 1975.

[196] R.S. Bradley. LXXIX. The cohesive force between solid surfaces and the surface energy of solids. *The London, Edinburgh, and Dublin Philosophical Magazine and Journal of Science*, 13(86):853–862, 1932.

[197] D.S. Dugdale. Yielding of steel sheets containing slits. *Journal of the Mechanics and Physics of Solids*, 8(2):100–104, 1960.

[198] D. Tabor. Surface forces and surface interactions. In *Plenary and invited lectures*, pages 3–14. Elsevier, 1977.

[199] J.E. Jones. On the determination of molecular fields.-I. From the variation of the viscosity of a gas with temperature. *Proceedings of the Royal Society of London. Series A, Containing Papers of a Mathematical and Physical Character*, 106(738):441–462, 1924.

[200] J.E. Jones. On the determination of molecular fields.-II. From the equation of state of a gas. *Proceedings of the Royal Society of London. Series A*, 106(738):463–477, 1924.

[201] K.L. Johnson and J.A. Greenwood. A Maugis analysis of adhesive line contact. *Journal of Physics D: Applied Physics*, 41(15):155315, 2008.

[202] B.N.J. Persson. Nanoadhesion. *Wear*, 254(9):832–834, 2003.

[203] H. Gao and H. Yao. Shape insensitive optimal adhesion of nanoscale fibrillar structures. *Proceedings of the National Academy of Sciences*, 101(21):7851–7856, 2004.

[204] D. Maugis and M. Barquins. Fracture mechanics and adherence of viscoelastic solids. In *Adhesion and Adsorption of Polymers*, pages 203–277. Springer, 1980.

[205] M.H. Müser and B.N.J. Persson. Crack and pull-off dynamics of adhesive, viscoelastic solids. *Europhysics Letters*, 137(3):36004, 2022.

[206] J.F. Waters and P.R. Guduru. Mode-mixity-dependent adhesive contact of a sphere on a plane surface. *Proceedings of the Royal Society A: Mathematical, Physical and Engineering Sciences*, 466(2117):1303–1325, 2010.

[207] A.N. Gent and J. Schultz. Effect of wetting liquids on the strength of adhesion of viscoelastic material. *The Journal of Adhesion*, 3(4):281–294, 1972.

[208] A.N. Gent. Adhesion of viscoelastic materials to rigid substrates. II. Tensile strength of adhesive joints. *Journal of Polymer Science Part A-2: Polymer Physics*, 9(2):283–294, 1971.

[209] A.N. Gent and R.P. Petrich. Adhesion of viscoelastic materials to rigid substrates. *Proceedings of the Royal Society of London. A. Mathematical and Physical Sciences*, 310(1502):433–448, 1969.

[210] E.H. Andrews and A.J. Kinloch. Mechanics of elastomeric adhesion. *Journal of Polymer Science: Polymer Symposia*, 46(1):1–14, 1974.

[211] M. Barber, J. Donley, and J.S. Langer. Steady-state propagation of a crack in a viscoelastic strip. *Physical Review A*, 40(1):366, 1989.

[212] R.A. Schapery. A theory of crack initiation and growth in viscoelastic media. *International Journal of fracture*, 11(1):141–159, 1975.

[213] R.A. Schapery. A theory of crack initiation and growth in viscoelastic media II. Approximate methods of analysis. *International Journal of Fracture*, 11(3):369–388, 1975.

[214] E. Barthel and C. Frétigny. Adhesive contact of elastomers: effective adhesion energy and creep function. *Journal of Physics D: Applied Physics*, 42(19):195302, 2009.

[215] V.M. Muller. On the theory of pull-off of a viscoelastic sphere from a flat surface. *Journal of Adhesion Science and Technology*, 13(9):999–1016, 1999.

[216] W.G. Knauss. A review of fracture in viscoelastic materials. *International Journal of Fracture*, 196(1):99–146, 2015.

[217] B.N.J. Persson and E.A. Brener. Crack propagation in viscoelastic solids. *Physical Review E*, 71(3):036123, 2005.

[218] G. Carbone and B.N.J. Persson. Crack motion in viscoelastic solids: the role of the flash temperature. *The European Physical Journal E*, 17(3):261–281, 2005.

[219] B.N.J. Persson. Crack propagation in finite-sized viscoelastic solids with application to adhesion. *Europhysics Letters*, 119(1):18002, 2017.

[220] B.N.J. Persson. On opening crack propagation in viscoelastic solids. *Tribology Letters*, 69(3):1–8, 2021.

[221] D. Das and I. Chasiotis. Rate dependent adhesion of nanoscale polymer contacts. *Journal of the Mechanics and Physics of Solids*, 156:104597, 2021.

[222] M. Ciavarella. Improved Muller approximate solution of the pull-of of a sphere from a viscoelastic substrate. *Journal of Adhesion Science and Technology*, 35(20):2175–2183, 2021.

[223] A. Papangelo and M. Ciavarella. Adhesion enhancement in a dimpled surface with axisymmetric waviness and rate-dependent work of adhesion. *The Journal of Adhesion*, pages 1–16, 2021.

[224] G.A.C. Graham. Two extending crack problems in linear viscoelasticity theory. *Quarterly of Applied Mathematics*, 27(4):497–507, 1970.

[225] D. Baek, P. Hemthavy, S. Saito, and K. Takahashi. Evaluation of energy dissipation involving adhesion hysteresis in spherical contact between a glass lens and a PDMS block. *Applied Adhesion Science*, 5(1):1–11, 2017.

[226] W. Deng and H. Kesari. Depth-dependent hysteresis in adhesive elastic contacts at large surface roughness. *Scientific Reports*, 9(1):1–12, 2019.

[227] E. Kroner, D.R. Paretkar, R.M. McMeeking, and E. Arzt. Adhesion of flat and structured pdms samples to spherical and flat probes: a comparative study. *The Journal of Adhesion*, 87(5):447–465, 2011.

[228] Y. Lai, D. He, and Y. Hu. Indentation adhesion of hydrogels over a wide range of length and time scales. *Extreme Mechanics Letters*, 31:100540, 2019.

[229] L. Afferrante and G. Violano. On the effective surface energy in viscoelastic Hertzian contacts. *Journal of the Mechanics and Physics of Solids*, 158:104669, 2022.

[230] K. Chen, J. Han, X. Pan, and D.J. Srolovitz. The grain boundary mobility tensor. *Proceedings of the National Academy of Sciences*, 117(9):4533–4538, 2020.

[231] E. Van Der Giessen, P.A. Schultz, V.V. Bertin, N.and Bulatov, W. Cai, S.M. Csányi, G.and Foiles, M.G.D. Geers, C. González, M. Hütter, et al. Roadmap on multiscale materials modeling. *Modelling and Simulation in Materials Science and Engineering*, 28(4):043001, 2020.

[232] A.I. Vakis, V.A. Yastrebov, J. Scheibert, L. Nicola, D. Dini, C. Minfray, A. Almqvist, M. Paggi, S. Lee, G. Limbert, et al. Modeling and simulation in tribology across scales: An overview. *Tribology International*, 125:169–199, 2018.

[233] N. Bertin, R.B. Sills, and W. Cai. Frontiers in the Simulation of Dislocations. *Annual Review of Materials Research*, 50:437–464, 2020.

[234] A. Papangelo and M. Ciavarella. On the limits of quasi-static analysis for a simple Coulomb frictional oscillator in response to harmonic loads. *Journal of Sound and Vibration*, 339:280–289, 2015.

[235] G. DeWit and J.S. Koehler. Interaction of dislocations with an applied stress in anisotropic crystals. *Physical Review*, 116(5):1113, 1959.

[236] R. Gasca-Neri and W.D. Nix. A model for the mobile dislocation density. *Acta Metallurgica*, 22(3):257–264, 1974.

[237] A. Orlová. Two concepts of mobile dislocation density in creep at high temperatures. *Materials Science and Engineering: A*, 151(2):153–160, 1992.

[238] G.M. Pharr and W.D. Nix. Application of the methods of dislocation dynamics to describe plastic flow in both bcc and fcc metals. *Acta Metallurgica*, 27(3):433–444, 1979.

[239] I. Kovacs. The Critical Shear Stress needed for the Operation of a Dislocation Segment as a Frank-Read Source in Anisotropic Crystals. *physica status solidi (b)*, 3(1):140–144, 1963.

[240] W. Cai and William D. Nix. *Imperfections in crystalline solids*. Cambridge University Press, 2016.

[241] F. Yoshida, T. Uemori, and K. Fujiwara. Elastic–plastic behavior of steel sheets under in-plane cyclic tension–compression at large strain. *International Journal of Plasticity*, 18(5-6):633–659, 2002.

[242] L. Sun and R.H. Wagoner. Complex unloading behavior: Nature of the deformation and its consistent constitutive representation. *International Journal of Plasticity*, 27(7):1126–1144, 2011.

[243] R.O. Scattergood and D.J. Bacon. The Orowan mechanism in anisotropic crystals. *Philosophical Magazine*, 31(1):179–198, 1975.

[244] S.P. Fitzgerald. Frank–Read sources and the yield of anisotropic cubic crystals. *Philosophical Magazine Letters*, 90(3):209–218, 2010.

[245] S.P. Fitzgerald and S. Aubry. Self-force on dislocation segments in anisotropic crystals. *Journal of Physics: Condensed Matter*, 22(29):295403, 2010.

[246] S. Aubry, S.P. Fitzgerald, S.L. Dudarev, and W. Cai. Equilibrium shape of dislocation shear loops in anisotropic α-Fe. *Modelling and Simulation in Materials Science and Engineering*, 19(6):065006, 2011.

[247] S.P. Fitzgerald, S. Aubry, S.L. Dudarev, and W. Cai. Dislocation dynamics simulation of Frank-Read sources in anisotropic α-Fe. *Modelling and Simulation in Materials Science and Engineering*, 20(4):045022, 2012.

[248] W. Cai, A. Arsenlis, C.R. Weinberger, and V.V. Bulatov. A non-singular continuum theory of dislocations. *Journal of the Mechanics and Physics of Solids*, 54(3):561–587, 2006.

[249] See Supplemental Material for analysis and additional results. https://doi.org/10.1016/j.mtla.2021.101178.

[250] Q.-C. He and A. Curnier. A more fundamental approach to damaged elastic stress-strain relations. *International Journal of Solids and Structures*, 32(10):1433–1457, 1995.

[251] T. Böhlke and C. Brüggemann. Graphical representation of the generalized Hooke's law. *Technische Mechanik*, 21(2):145–158, 2001.

[252] J. Nordmann, M. Aßmus, and H. Altenbach. Visualising elastic anisotropy: Theoretical background and computational implementation. *Continuum Mechanics and Thermodynamics*, 30(4):689–708, 2018.

[253] E. Orowan. Problems of plastic gliding. *Proceedings of the Physical Society*, 52(1):8, 1940.

[254] A. Kochendorfer. *Reine und angewandte Metallkunde*. Springer Berlin, 1941.

[255] J.F.W. Bishop and R. Hill. XLVI. A theory of the plastic distortion of a polycrystalline aggregate under combined stresses. *The London, Edinburgh, and Dublin Philosophical Magazine and Journal of Science*, 42(327):414–427, 1951.

[256] H.J. Frost and M.F. Ashby. Deformation-mechanism maps for pure iron, two austenitic stainless steels, and a low-alloy ferritic steel. In *Fundamental Aspects of Structural Alloy Design*, pages 27–65. Springer, 1977.

[257] H.S. Zurob, C.R. Hutchinson, Y. Brechet, and G. Purdy. Modeling recrystallization of microalloyed austenite: effect of coupling recovery, precipitation and recrystallization. *Acta Materialia*, 50(12):3077–3094, 2002.

[258] N. Xiao, M. Tong, Y. Lan, D. Li, and Y. Li. Coupled simulation of the influence of austenite deformation on the subsequent isothermal austenite–ferrite transformation. *Acta Materialia*, 54(5):1265–1278, 2006.

[259] K. Levenberg. A method for the solution of certain non-linear problems in least squares. *Quarterly of Applied Mathematics*, 2(2):164–168, 1944.

[260] D.W. Marquardt. An algorithm for least-squares estimation of nonlinear parameters. *Journal of the society for Industrial and Applied Mathematics*, 11(2):431–441, 1963.

[261] D. Kuhlmann-Wilsdorf. Unified theory of stages II and III of workhardening in pure fcc metal crystals. Technical report, Virginia Univ., Charlottesville. School of Engineering and Applied Science, 1966.

[262] Z.A.D. Lethbridge, R.I. Walton, A.S.H. Marmier, C.W. Smith, and K.E. Evans. Elastic anisotropy and extreme Poisson's ratios in single crystals. *Acta Materialia*, 58(19):6444–6451, 2010.

[263] C.M. Kube. Elastic anisotropy of crystals. *AIP Advances*, 6(9):095209, 2016.

[264] E. Schmid. U. W. Boas: Kristallplastizität mit besonderer Berücksichtigung der Metalle, 1935.

[265] N.E.K.V.A. Brown and R.A. Ekvall. Temperature dependence of the yield points in iron. *Acta Metallurgica*, 10(11):1101–1107, 1962.

[266] A. De Vaucorbeil, W.J. Poole, and C.W. Sinclair. The superposition of strengthening contributions in engineering alloys. *Materials Science and Engineering: A*, 582:147–154, 2013.

[267] L. Kubin, R. Madec, and B. Devincre. Dislocation intersections and reactions in FCC and BCC crystals. *MRS Online Proceedings Library Archive*, 779, 2003.

[268] G. Po, Y. Cui, D. Rivera, D. Cereceda, T.D. Swinburne, J. Marian, and N. Ghoniem. A phenomenological dislocation mobility law for bcc metals. *Acta Materialia*, 119:123–135, 2016.

[269] C. Zener. Contributions to the theory of beta-phase alloys. *Physical Review*, 71(12):846, 1947.

[270] W. Voigt et al. *Lehrbuch der Kristallphysik*, volume 962. Teubner Leipzig, 1928.

[271] A. Reuß. Berechnung der Fließgrenze von Mischkristallen auf Grund der Plastizitätsbedingung für Einkristalle. *ZAMM-Journal of Applied Mathematics and Mechanics/Zeitschrift für Angewandte Mathematik und Mechanik*, 9(1):49–58, 1929.

[272] D.J. Dever. Temperature dependence of the elastic constants in α-iron single crystals: relationship to spin order and diffusion anomalies. *Journal of Applied Physics*, 43(8):3293–3301, 1972.

[273] A.A. Benzerga, Y. Bréchet, A. Needleman, and E. Van der Giessen. Incorporating three-dimensional mechanisms into two-dimensional dislocation dynamics. *Modelling and Simulation in Materials Science and Engineering*, 12(1):159, 2003.

[274] H. Mecking and U.F. Kocks. Kinetics of flow and strain-hardening. *Acta Metallurgica*, 29(11):1865–1875, 1981.

[275] K. Yamaguchi, H. Adachi, and N. Takakura. Effects of plastic strain and strain path on youngs modulus of sheet metals. *Metals and Materials*, 4(3):420–425, 1998.

[276] JA Benito, J Jorba, JM Manero, and A Roca. Change of young's modulus of cold-deformed pure iron in a tensile test. *Metallurgical and Materials Transactions A*, 36(12):3317–3324, 2005.

[277] R. Perez, J.A. Benito, and J.M. Prado. Study of the inelastic response of TRIP steels after plastic deformation. *ISIJ International*, 45(12):1925–1933, 2005.

[278] J.N. Chamakura, A.C. Riemslag, T.E. Reinton, V.A. Popovich, and J. Sietsma. The quantitative relationship between non-linear stress-strain behaviour and dislocation structure in martensitic stainless steel. *Acta Materialia*, 240:118364, 2022.

[279] B.E.N.A.T. Gurrutxaga-Lerma, D.S. Balint, D. Dini, and A.P. Sutton. The mechanisms governing the activation of dislocation sources in aluminum at different strain rates. *Journal of the Mechanics and Physics of Solids*, 84:273–292, 2015.

[280] Y. Estrin. Dislocation-density-related constitutive modeling. *Unified Constitutive Laws of Plastic Deformation*, 1:69–106, 1996.

[281] E. Voce. The relationship between stress and strain for homogeneous deformation. *Journal of the Institute of Metals*, 74:537–562, 1948.

[282] J.H. Palm. Stress-strain relations for uniaxial loading. *Flow, Turbulence and Combustion*, 1(1):198, 1949.

[283] U.F. Kocks, A.S. ARGON, and M.F. ASHBY. Thermodynamics and kinetics of slip. *Progress in Materials Science*, 19, 1975.

[284] E. Nes. Modelling of work hardening and stress saturation in FCC metals. *Progress in Materials Science*, 41(3):129–193, 1997.

[285] E. Nes, K. Marthinsen, and B. Holmedal. The effect of boundary spacing on substructure strengthening. *Materials Science and Technology*, 20(11):1377–1382, 2004.

[286] E. Demir. A physically based constitutive model for FCC single crystals with a single state variable per slip system. *Modelling and Simulation in Materials Science and Engineering*, 25(1):015009, 2016.

[287] R. Madec, B. Devincre, L. Kubin, T. Hoc, and D. Rodney. The role of collinear interaction in dislocation-induced hardening. *Science*, 301(5641):1879–1882, 2003.

[288] W.E. Jominy and A.L. Boegehold. A hardenability test for carburizing steel. *Transactions of the American Society for Metals*, 26:574–606, 1938.

[289] Wolfram Research, Inc. Mathematica, Version 13.2. Champaign, IL, 2022.

[290] A. Considère. Annales des ponts et chaussées. *Q*, 9(1):574–775, 1885.

[291] G. Ghosh and G.B. Olson. The isotropic shear modulus of multicomponent Fe-base solid solutions. *Acta Materialia*, 50(10):2655–2675, 2002.

[292] J.M. Rosenberg and H.R. Piehler. Calculation of the Taylor factor and lattice rotations for bcc metals deforming by pencil glide. *Metallurgical Transactions*, 2(1):257–259, 1971.

[293] R.E. Stoller and S.J. Zinkle. On the relationship between uniaxial yield strength and resolved shear stress in polycrystalline materials. *Journal of Nuclear Materials*, 283:349–352, 2000.

[294] H.J.C. Berendsen. *A student's guide to data and error analysis*. Cambridge University Press, 2011.

[295] J. Friedel. The mechanism of work-hardening and slip-band formation. *Proceedings of the Royal Society of London. Series A*, 242(1229):147–159, 1957.

[296] P. Lukáš and L. Kunz. Role of persistent slip bands in fatigue. *Philosophical Magazine*, 84(3-5):317–330, 2004.

[297] S.K. Paul. A critical review of experimental aspects in ratcheting fatigue: microstructure to specimen to component. *Journal of Materials Research and Technology*, 8(5):4894–4914, 2019.

[298] A. Sendrowicz, A.O. Myhre, I.S. Yasnikov, and A. Vinogradov. Stored and dissipated energy of plastic deformation revisited from the viewpoint of dislocation kinetics modelling approach. *Acta Materialia*, page 118190, 2022.

[299] B. Jaoul. Consolidation des polycristaux de fer et hypothèses sur l'origine du palier des courbes de traction. *Journal of the Mechanics and Physics of Solids*, 9(2):69–90, 1961.

[300] J.F. Butler. Lüders front propagation in low carbon steels. *Journal of the Mechanics and Physics of Solids*, 10(4):313–318, 1962.

[301] W. Sylwestrowicz and E.O. Hall. The deformation and ageing of mild steel. *Proceedings of the Physical Society. Section B*, 64(6):495, 1951.

[302] J.P. Burg and L.B. Harris. Tension fractures and boudinage oblique to the maximum extension direction: an analogy with Lüders' bands. *Tectonophysics*, 83(3-4):347–363, 1982.

[303] V.S. Ananthan and E.O. Hall. Shear and kink angles at the Lüders band front. *Scripta Metallurgica*, 23(7):1075–1078, 1989.

[304] D.W. Beardsmore, J.Q. da Fonseca, J. Romero, C.A. English, S.R. Ortner, J. Sharples, A.H. Sherry, and M.A. Wilkes. Study of Lüders phenomena in reactor pressure vessel steels. *Materials Science and Engineering: A*, 588:151–166, 2013.

[305] G. Pomey, M. Grumbach, and C. Rossard. Aspect des bandes de Piobert-Lüders sur des éprouvettes en tôle d'acier extra-doux recouvertes de vernis élastique. *Mémoires Scientifiques de La Revue de Metallurgie*, 4:243–522, 1964.

[306] X.G. Wang, L. Wang, and M.X. Huang. Kinematic and thermal characteristics of Lüders and Portevin-Le Châtelier bands in a medium Mn transformation-induced plasticity steel. *Acta Materialia*, 124:17–29, 2017.

[307] J. Savoie, J.J. Jonas, S.R. MacEwen, and R. Perrin. Evolution of r-value during the tensile deformation of aluminium. *Textures and Microstructures*, 23, 1970.

[308] H. Louche and A. Chrysochoos. Thermal and dissipative effects accompanying Lüders band propagation. *Materials Science and Engineering: A*, 307(1-2):15–22, 2001.

[309] Y.Z. Tian, S. Gao, L.J. Zhao, S. Lu, R. Pippan, Z.F. Zhang, and N. Tsuji. Remarkable transitions of yield behavior and Lüders deformation in pure Cu by changing grain sizes. *Scripta Materialia*, 142:88–91, 2018.

[310] A. Nadai. *Theory of Flow and Fracture of Solids; Volume 2.* New York, NY, McGraw-Hill Book Company Incorporated, 1963.

[311] T.Y. Thomas. On the inclination of plastic slip bands in flat bars in tension tests. *Proceedings of the National Academy of Sciences*, 39(4):257–265, 1953.

[312] D. Daniel, J.J. Jonas, and J. Bussiére. The elastic strain ratio, the Lüders strain ratio and the evolution of r-value during tensile deformation. *Textures and Microstructures*, 19, 1970.

[313] T.Y. Thomas. The effect of compressibility on the inclination of plastic slip bands in flat bars. *Proceedings of the National Academy of Sciences*, 39(4):266–273, 1953.

[314] T.Y. Thomas. The Lüders band problem. *Journal of Mathematics and Mechanics*, pages 17–27, 1958.

[315] T.Y. Thomas. Singular surfaces and flow lines in the theory of plasticity. *Journal of Rational Mechanics and Analysis*, 2:339–381, 1953.

[316] R.T. Hill. On discontinuous plastic states, with special reference to localized necking in thin sheets. *Journal of the Mechanics and Physics of Solids*, 1(1):19–30, 1952.

[317] J.-G. Park and M.-R. Kim. A Study on the Angle of Localization of a Metal Specimen under Uniaxial Tension with Plane Strain Condition. *Journal of the Computational Structural Engineering Institute of Korea*, 24(3):275–281, 2011.

[318] T. Tokuoka and M. Saito. Slip planes in orthogonally anisotropic flat bars in uniaxial stress tests. *Acta Mechanica*, 17(3):305–313, 1973.

[319] R. Hill. A theory of the yielding and plastic flow of anisotropic metals. *Proceedings of the Royal Society of London. Series A. Mathematical and Physical Sciences*, 193(1033):281–297, 1948.

[320] Y. Mengi, H.D. McNiven, and A.Ü. Erdem. A theory for the formation and propagation of Lüders bands in a plate subjected to uniaxial tension. *International Journal of Solids and Structures*, 11(7-8):813–825, 1975.

[321] J. Watterson. The future of failure: stress or strain? *Journal of Structural Geology*, 21(8-9):939–948, 1999.

[322] W.T. Lankford. New criteria for predicting the performance of deep drawing sheets. *Transactions of the American Society for Metals*, 42:1197, 1950.

[323] G.R. Irwin. Angle and Strain Relations in Flat-Plate Lüders' Bands. *Journal of Applied Mechanics*, 20:449–450, 1953.

[324] Dassault Systemes. ABAQUS/CAE User's Manual, Version 6.14. *Providence, RI: Dassault Systemes Simulia Corp*, 2014.

[325] J.A. Shaw and S. Kyriakides. Initiation and propagation of localized deformation in elasto-plastic strips under uniaxial tension. *International Journal of Plasticity*, 13(10):837–871, 1997.

[326] J. Besson, G. Cailletaud, J.-L. Chaboche, and S. Forest. *Non-linear mechanics of materials*, volume 167. Springer Science & Business Media, 2009.

[327] M.K. Neilsen and H.L. Schreyer. Bifurcations in elastic-plastic materials. *International Journal of Solids and Structures*, 30(4):521–544, 1993.

[328] O. Cazacu and J.A. Rodríguez-Martínez. Effects of plastic anisotropy on localization in orthotropic materials: new explicit expressions for the orientation of localization bands in flat specimens subjected to uniaxial tension. *Journal of the Mechanics and Physics of Solids*, 126:272–284, 2019.

[329] K. Yu, L. Hou, M. Guo, D. Li, D. Huang, L. Zhuang, J. Zhang, and P. Wu. A method for determining r-value of aluminum sheets with the Portevin-Le Chatelier effect. *Materials Science and Engineering: A*, 814:141246, 2021.

[330] J.H. van der Heijde. *The Effect of Specimen Thickness on the Lüders Phenomena in AISI 1524 Steel Alloy*. PhD thesis, Rochester Institute of Technology, 2022.

[331] J.H. van der Heijde and W.A. Samad. The Effect of Specimen Thickness on the Lüders Phenomena in AISI 1524 Steel Alloy: Experimental Observations Using DIC. *Experimental Mechanics*, pages 1–12, 2023.

[332] D.W. Moon. Considerations on the present state of Lüders band studies. *Materials Science and Engineering*, 8(4):235–243, 1971.

[333] M. Ciavarella and A. Papangelo. On the interaction of viscoelasticity and waviness in enhancing the pull-off force in sphere/flat contacts. *Tribology Letters*, 69(4):127, 2021.

[334] J.A. Greenwood. The theory of viscoelastic crack propagation and healing. *Journal of Physics D: Applied Physics*, 37(18):2557–2569, 2004.

[335] J.S. Van Dokkum, F. Pérez-Ràfols, L. Dorogin, and L. Nicola. On the retraction of an adhesive cylindrical indenter from a viscoelastic substrate. *Tribology International*, 164:107234, 2021.

[336] M.H. Müser. Google I/O 2021. Martin Müser. `https://youtu.be/tC9-oUV5dGA?t=1667`, October 2021.

[337] G. Violano and L. Afferrante. On the long and short-range adhesive interactions in viscoelastic contacts. *Tribology Letters*, 70(3):1–5, 2022.

[338] R.M. McMeeking, L. Ma, and E. Arzt. Bi-Stable Adhesion of a Surface with a Dimple. *Advanced Engineering Materials*, 12(5):389–397, 2010.

[339] M. Ciavarella, Q.-A. Wang, and Q. Li. Maugis-Tabor parameter dependence of pull-off in viscoelastic line Hertzian contacts. *The Journal of Adhesion*, pages 1–16, 2022.

[340] J.S. Van Dokkum and L. Nicola. Green's function molecular dynamics including viscoelasticity. *Modelling and Simulation in Materials Science and Engineering*, 27(7):075006, 2019.

[341] N. Prodanov, W.B. Dapp, and M.H. Müser. On the Contact Area and Mean Gap of Rough, Elastic Contacts: Dimensional Analysis, Numerical Corrections, and Reference Data. *Tribology Letters*, 53(2):433–448, 2014.

[342] S.P.C. Marques and G.J. Creus. *Computational viscoelasticity*. Springer Science & Business Media, 2012.

[343] J.M. Baney and C.Y. Hui. A cohesive zone model for the adhesion of cylinders. *Journal of Adhesion Science and Technology*, 11(3):393–406, 1997.

[344] J.R. Barber. *Contact mechanics*. Springer, 2018.

[345] F. Pérez-Ràfols, J.S. Van Dokkum, and L. Nicola. On the interplay between roughness and viscoelasticity in adhesive hysteresis. *Journal of the Mechanics and Physics of Solids*, 170:105079, 2023.

[346] M. Frigo and S.G. Johnson. The design and implementation of FFTW3. *Proceedings of the IEEE*, 93(2):216—-231, 2005.

[347] C. Störmer. Sur les trajectoires des corpuscules électrisés dans l'espace sous l'action du magnétisme terrestre, avec application aux aurores boréales. *Le Radium*, 9(11):395–399, 1912.

[348] G. Violano and L. Afferrante. Size effects in adhesive contacts of viscoelastic media. *European Journal of Mechanics-A/Solids*, page 104665, 2022.

[349] J.P. Den Hartog. Forced vibrations with combined Coulomb and viscous friction. *Transaction of the American Society of Mechanical Engineering*, 53(9):107–115, 1931.

[350] H.-K. Hong and C.-S. Liu. Coulomb friction oscillator: modelling and responses to harmonic loads and base excitations. *Journal of Sound and Vibration*, 229(5):1171–1192, 2000.

[351] E.S. Levitan. Forced oscillation of a pring-mass system having combined Coulomb and viscous damping. *the Journal of the Acoustical Society of America*, 32(10):1265–1269, 1960.

[352] M.S. Hundal. Response of a base excited system with Coulomb and viscous friction. *Journal of Sound and Vibration*, 64(3):371–378, 1979.

[353] V. Marchis and F. Vatta. A numerical approach on the combined viscous and Coulomb friction motion. *Mechanism and Machine Theory*, 20(3):171–180, 1985.

[354] E. Marui and S. Kato. Forced vibration of a base-excited single-degree-of-freedom system with Coulomb friction. *Journal of Dynamic Systems, Measurement, and Conrol*, 106:280–285, 1984.

[355] C.-S. Liu and W.-T. Chang. Frictional behaviour of a belt-driven and periodically excited oscillator. *Journal of Sound and Vibration*, 258(2):247–268, 2002.

[356] I. Lopez, J.M. Busturia, and H. Nijmeijer. Energy dissipation of a friction damper. *Journal of Sound and Vibration*, 278(3):539–561, 2004.

[357] F. Roters, M. Diehl, P. Shanthraj, P. Eisenlohr, C. Reuber, S.L. Wong, T. Maiti, A. Ebrahimi, T. Hochrainer, and H.O. Fabritius. DAMASK–the Düsseldorf advanced material simulation kit for modeling multi-physics crystal plasticity, thermal, and damage phenomena from the single crystal up to the component scale. *Computational Materials Science*, 158:420–478, 2019.

[358] G. Zhou, J. Tsai, T. Russell, E. Taghipour, R.H. Wagoner, D.T. Fullwood, and S. Niezgoda. Mesoscale Slip Behavior in Single Crystal and Bicrystal Tantalum. *Materialia*, 28:101730, 2023.

[359] H. Mughrabi. Dislocation wall and cell structures and long-range internal stresses in deformed metal crystals. *Acta Metallurgica*, 31(9):1367–1379, 1983.

[360] H. Mughrabi and T. Ungar. Long-range internal stresses in deformed single-phase materials: The composite model and its consequences. In *Dislocations in Solids*, volume 11, pages 343–411. Elsevier, 2002.

[361] B. Katzer, K. Zoller, D. Weygand, and K. Schulz. Identification of dislocation reaction kinetics in complex dislocation networks for continuum modelling using data-driven methods. *Journal of the Mechanics and Physics of Solids*, 168:105042, 2022.

[362] Y. Zheng. *Dislocation-based plasticity model by analysis of discrete dislocation dynamics*. PhD thesis, Delft University of Technology, 2021.

[363] T.A. Parthasarathy, S.I. Rao, D.M. Dimiduk, M.D. Uchic, and D.R. Trinkle. Contribution to size effect of yield strength from the stochastics of dislocation source lengths in finite samples. *Scripta Materialia*, 56(4):313–316, 2007.

[364] J. Wijnen, R.H.J. Peerlings, J.P.M. Hoefnagels, and M.G.D. Geers. A discrete slip plane model for simulating heterogeneous plastic deformation in single crystals. *International Journal of Solids and Structures*, 228:111094, 2021.

[365] N. Bertin, W. Cai, S. Aubry, A. Arsenlis, and V.V. Bulatov. Enhanced mobility of dislocation network nodes and its effect on dislocation multiplication and storage. *arXiv preprint arXiv:2210.14343*, 2022.

[366] M. Stricker, M. Sudmanns, K. Schulz, T. Hochrainer, and D. Weygand. Dislocation multiplication in stage II deformation of FCC multi-slip single crystals. *Journal of the Mechanics and Physics of Solids*, 119:319–333, 2018.

[367] S.S. Shishvan and E. Van der Giessen. Distribution of dislocation source length and the size dependent yield strength in freestanding thin films. *Journal of the Mechanics and Physics of Solids*, 58(5):678–695, 2010.

[368] C. Ye, G. Liu, K. Chen, J. Liu, J. Hu, Y. Yu, Y. Mao, and Y. Shen. Unified crystal plasticity model for fcc metals: From quasistatic to shock loading. *Physical Review B*, 107(2):024105, 2023.

[369] S. Hanai, N. Takemoto, Y. Tokunaga, and Y. Mizuyama. Effect of grain size and solid solution strengthening elements on the bake hardenability of low carbon aluminum-killed steel. *Transactions of the Iron and Steel Institute of Japan*, 24(1):17–23, 1984.

[370] H. Qiu, R. Ueji, and T. Inoue. Yield-Point Phenomenon and Plastic Bands in Ferrite–Pearlite Steels. *Materials*, 16(1):195, 2022.

[371] G. Welter and S. Gockowski. Influence of the Resiliency of the Test Machine and of the Loading Speed upon the Determination of the Yield Point for Mild Steel. *Metallurgica*, pages 143–148, 1938.

[372] R. Iricibar, J. Mazza, and A. Cabo. On the Lüders band front in mild steel—I. *Acta Metallurgica*, 25(10):1163–1168, 1977.

[373] I. Vardoulakis, M. Goldscheider, and G. Gudehus. Formation of shear bands in sand bodies as a bifurcation problem. *International Journal for Numerical and Analytical Methods in Geomechanics*, 2(2):99–128, 1978.

[374] J. Hu, Z. Marciniak, and J. Duncan. *Mechanics of sheet metal forming*. Elsevier, 2002.

[375] C. Putignano. Oscillating viscoelastic periodic contacts: A numerical approach. *International Journal of Mechanical Sciences*, 208:106663, 2021.

[376] G. Carbone, C. Mandriota, and N. Menga. Theory of viscoelastic adhesion and friction. *Extreme Mechanics Letters*, 56:101877, 2022.

[377] P. Attard. Interaction and deformation of viscoelastic particles. 2. Adhesive particles. *Langmuir*, 17(14):4322–4328, 2001.

[378] G. Violano, S. De Carolis, M.E. Palmieri, G. Carbone, L. Tricarico, G.P. Demelio, and L. Afferrante. Crack propagation in viscoelastic finite-sized solids: theory and experiments. In *IOP Conference Series: Materials Science and Engineering*, volume 1275, page 012043. IOP Publishing, 2023.

[379] S.P. Venugopalan, L. Nicola, and M.H. Müser. Green's function molecular dynamics: including finite heights, shear, and body fields. *Modelling and Simulation in Materials Science and Engineering*, 25(3):034001, 2017.

[380] Pérez-Ràfols F. and L. Nicola. Incipient sliding of adhesive contacts. *Friction*, pages 1–14, 2021.

[381] Z. He, Y. Yang, and H. Jiang. Modeling interfacial instability patterns during debonding a rigid spherical indenter from thin elastic films. *Journal of the Mechanics and Physics of Solids*, 169:105089, 2022.

[382] J. Liu, M. Latorre, and A.L. Marsden. A continuum and computational framework for viscoelastodynamics: I. Finite deformation linear models. *Computer Methods in Applied Mechanics and Engineering*, 385:114059, 2021.

[383] A. Al-Qudsi, L. De Lorenzis, and M. Scaraggi. A Hybrid Multiscale Approach for Rubber Contact. *Frontiers in Mechanical Engineering*, 8:814607, 2022.

[384] M. Paggi, J. Bonari, and J. Reinoso. From the pioneering contributions by wriggers to recent advances in computational tribology. *Current Trends and Open Problems in Computational Mechanics*, pages 385–393, 2022.

[385] G. Birkhoff and S. Mac Lane. *A survey of modern algebra*. Universities Press, 1998.

[386] R. Vetter and A. van den Beukel. Dislocation production in cold worked copper. *Scripta Metallurgica*, 11(2):143–146, 1977.

[387] P. van Liempt. *Yield and flow stress of steel in the austenitic state*. PhD thesis, Delft University of Technology, 2016.

List of Publications

2023 Van Dokkum, J. S., Bos, C., Offerman, S. E., Sietsma, J. Static Unified Inelastic model: dislocation-mediated deformation pre-, at- and post-yield. *Materialia*, 101694.

2022 Pérez-Ràfols, F., Van Dokkum, J. S., Nicola, L. On the Interplay between Roughness and Viscoelasticity in Adhesive Hysteresis, *Journal of the Mechanics and Physics of Solids*, 105079.

2022 Atreya, V., Van Dokkum, J.S., Bos, C., Santofimia, M.J. Effect of the anisotropy of martensitic transformation on ferrite deformation in Dual-Phase steels, *Materials and Design*, 110805.

2022 Shah, V, Sedighiani, K.S, Van Dokkum, J.S., Bos, C., Roters, F., Diehl, M. Coupling crystal plasticity and cellular automata models to study meta-dynamic recrystallization during hot rolling at high strain rates, *Material Science and Engineering: A*, 849, 143471.

2021 Van Dokkum, J. S., Bos, C., Offerman, S. E., Sietsma, J. Influence of dislocations on the apparent elastic constants in single metallic crystallites: an analytical approach. *Materialia*, 20, 101178.

2021 Van Dokkum, J. S., Pérez-Ràfols, F., Dorogin, L., Nicola, L. On the retraction of an adhesive cylindrical indenter from a viscoelastic substrate. *Tribology International*, 164, 107234.

2020 Salehani, M. K., van Dokkum, J. S., Irani, N., Nicola, L. On the load-area relation in rough adhesive contacts. *Tribology International*, 144, 106099.

2019 Van Dokkum, J. S., Nicola, L. Green's function molecular dynamics including viscoelasticity. *Modelling and Simulation in Materials Science and Engineering*, 27(7), 075006.

2018 van Dokkum, J. S., Salehani, M. K., Irani, N., Nicola, L. On the proportionality between area and load in line contacts. *Tribology Letters*, 66(3), 1-8.

2017 van Dokkum, J. Green's function molecular dynamics approach: Proportionality between area and load, *Master Thesis*, TU Delft repository.

About the Author

M.Sc. Jan Steven van Dokkum is born on the 18th of November 1990 in Heerenveen, the Netherlands. After finishing high school in 2009 at R.S.G. Steenwijk in Steenwijk, The Netherlands, he studied Mechanical Engineering at Delft University of Technology in Delft, The Netherlands. In 2013 he started the Master Materials Science and Engineering at Delft University of Technology as well. He graduated within the group of Prof. dr. M.Sc. Lucia Nicola on continuum mechanical modelling techniques in Tribology. Between 2017 and 2019 he worked as a researcher under the supervision of Prof. dr. M.Sc. Lucia Nicola on adhesive contact mechanics as well. Starting at the end of 2019 he partakes in a large project at Delft University of Technology with Tata Steel Europe under the supervision of Prof. dr. ir. Jilt Sietsma, Dr. ir. Sven Erik Offerman and Dr. ir. Cornelis Bos. The continuation of the former research, and achievements within the latter PhD project, are presented in this dissertation. Late fall 2023 Jan Steven van Dokkum will start as Post-Doc researcher on the friction of metamaterials in the Group of Prof. dr. M.Sc. David S. Kammer at Eidgenössische Technische Hochschule (ETH) Zürich.